ULTRAVIOLET AURORA AND AIRGLOW

Graham Geoffrey O'Connor, B.Sc. (Hons)

A Thesis

presented for the degree of

DOCTOR OF PHILOSOPHY

at the

University of Adelaide

Physics Department

March 1973

CONTENTS

SUMMARY

ULTRAVIOLET AURORA AND AIRGLOW

The Thesis presents the results of a program of investigations, based on rocket born experiments, into the characteristics of ultraviolet radiation in the upper atmosphere and the interaction of the radiation with atmospheric constituents.

Atomic hydrogen in the vicinity of the Earth scatters a part of the strong solar Lymanα flux into the night-time atmosphere to form the major component of the observed night-sky radiation in the vacuum ultraviolet. This airglow radiation is transported through many optical thicknesses in hydrogen before being absorbed by molecular oxygen. One part of this work was a study of the transport and absorption of the radiation below 120 km.

When fluxes of energetic protons or electrons are precipitated into the atmosphere, some of their energy appears as auroral radiation. Predictions had been made that a large portion of the emission would be in the ultraviolet region, and a program of measurements was undertaken to study the auroral ultraviolet radiation and its relationship to other auroral parameters.

Two series of rocket payloads were instrumented to make photometric studies of the ultraviolet aurora and airglow. Ionization chambers were used as the primary detectors in each payload, while radiation in associated wavelength bands was monitored by photomultiplier systems. A description is given of several different types of ionization chambers which were developed for use, both with and without gas multiplication, in these

measurements which covered the altitude range between 70 and135 km.

The auroral experiment payloads measured two dominant visible emissions for comparison with the ultraviolet intensities, while associate measurements were made by other experimenters. Ultraviolet radiation in the 105 nm to 135 nm range was detected in an active aurora against the diffuse background of the geocoronal Lymanα airglow. On the occasion reported, no aurorally associated Lymanα radiation was detected, and the activity appeared to be dominantly electron-excited.

Most of the radiation in excess of the airglow background was diffuse, but some discreet source regions, not all of them coincident with visible auroral forms, were observed. Calculations of the total ultraviolet and invisible energy in the observed auroral forms indicated that ultraviolet radiation fluxes do not transport as much of the input particle energy as had been suggested by some earlier predictions.

Measurements were made of the altitude and directional dependence of night-sky Lymanα airglow intensities, and the distributions observed with narrow field instruments have been found to be consistent with a simple model of the airglow spectrum and its absorption below 120 km. The measured absorption characteristics were used to relate the atmospheric densities of atomic hydrogen and molecular oxygen, and to derive density profiles of molecular oxygen. It is suggested that instruments of more specialized design, based on this exploratory work, should lead to improved measurements of these two atmospheric constituents.

The shape of the density profile of hydrogen in particular is of considerable interest because of the high loss-rate which has been predicted by photochemical models in the lower part of the measurement range, and the consequent sensitivity of the profile to diffusion effects.

The instruments used for the airglow observations were also used to measure the flux of Lymanα radiation from the moon. The derived value of lunar albedo at Lymanα has shown that the previously reported rapid decline of the lunar surface reflectivity through the mid-ultraviolet region does not continue through the vacuum ultraviolet part of the spectrum.

Some suggestions are made for continuation and extension of the program outlined in this Thesis.

This Thesis contains no material which has been accepted for the award of any other degree or diploma in any University. To the best of the author's knowledge and belief it contains no material previously published or written by another person, except where due reference has been made in the text.

(G.G. O'Connor)

ACKNOWLEDGEMENTS

The program of research reported in this Thesis covered two related aspects of upper atmospheric phenomena, namely aurora and airglow. Although most of the work was done in the Physics Department, University of Adelaide, each of the two sections of the work involved rocket launchings done in conjunction with organizations outside of the University.

The auroral experiments were conducted as part of the Modular Auroral Probe program which was instituted in the University of Texas at Dallas (formerly the Southwest Center for Advanced Studies) under the leadership of Professor W.J. Heikkila. The author is indebted to Professor Heikkila for the opportunity to participate in the program and for providing technical and financial support for the work. The efforts and assistance of many members of the staff of U.T.D. in overcoming the special problems of logistics and communication which arose through this participation are gratefully acknowledged. It is realized that, because of the great distances involved, the inclusion of these experiments in the program placed additional work loads and responsibilities on the vehicle preparation and launch teams.

Rocket vehicles were made available for the conduct of the airglow experiments through the Weapons Research Establishment at Salisbury, South Australia. The rocket flights were part of an extensive series in which the Physics Department has collaborated with groups within W.R.E., and were flown as part of the program of the Upper Atmosphere Research Group, under the direction of Mr. P.H.O. Pearson. The assitance and encouragement given by the members of that Group is much appreciated. Acknowledgement is also made of the assistance given by other members of Aerospace Division

in the design, construction and launching of the vehicles. The rocket program in the University was supported in part by a grant from the Department of Supply.

Several members of the staff of the Physics Department have given assistance in the form of discussion and information; in particular, Dr. P.J. Edwards provided supervision and guidance in the early part of the work, while Dr. B.H. Horton gave assistance throughout the program. The author is indebted also to the technical staff of the Space Physics Group, for their assistance with the design and construction of a large amount of flight instrumentation and ground equipment.

To Professor J.H. Carver, who supervised this project, appreciation is expressed for the guidance and assistance given throughout this work.

During the course of this work, the author was supported by a Postgraduate Studentship awarded by the Department of Supply.

CHAPTER 1 ULTRAVIOLET RADIATION IN THE ATMOSPHERE

1.1 Introduction

A major facet of the importance of the Earth's atmosphere is its function as an energy exchange and interaction region. The sun is the major energy source for terrestrial processes, with the energy being transported by radiation and energetic particle fluxes. A part is able to reach the Earth's surface directly, while the remainder interacts with the atmosphere. From the atmosphere, this energy is either returned to space or reaches the Earth's surface, mostly in a modified form. Ultraviolet radiation forms a large part of this interactive energy. This work deals mainly with the vacuum ultraviolet range of wavelengths between 100 nm and 200 nm.

Outside of the visible region, the apparent solar spectrum at the Earth's surface deviates from the black body distribution at both longer and shorter wavelengths; most of the depletion is due to absorption by constituent gases of the atmosphere. Although the atmosphere is a mixture of many gases, there are wavelength regions in which the absorption is known to be due almost entirely to one or two constituents. In the near infrared, the absorption bands of water vapour and carbon dioxide are most prominent; in the middle ultraviolet (200 - 300 nm) absorption by ozone is dominant; in the vacuum ultraviolet region (100 - 200 nm) the only major constituent which absorbs strongly is molecular oxygen. The Schumann-Runge dissociation continuum of oxygen extends from near 130 nm to near 180 nm, and the oxygen absorption

coefficient has pronounced structure both above and below this region. Nitric oxide photoionization at wavelengths shorter than 135 nm is important as a source of electrons in the atmosphere but contributes little to the total absorption because of the relatively low concentration of nitric oxide. Radiation with wavelengths less than 100 nm is capable of ionizing nitrogen and is therefore absorbed higher in the atmosphere than is the vacuum ultraviolet radiation which is the primary interest in this work. The specificity of absorption at certain wavelengths permits the determination of the densities of individual absorbing species. The application of this technique is discussed in Chapter 6.

Vacuum ultraviolet radiation reaching the atmosphere injects energy at altitudes above 70 km. Figure 1 indicates the range of heights involved, and the dominant absorbers. The height at which the incident vertical flux is attenuated by the factor "e" is shown as a function of wavelength. Vacuum ultraviolet radiation, as a major source of energy for upper atmospheric processes, produces ionization, dissociation and excited atomic and molecular species. A knowledge of the intensities of this radiation, and of the manner of its interaction is important to an understanding of atmospheric processes and energy balances.

The fluxes of energetic particles which reach the earth from the sun interact strongly with the atmosphere above heights of 100 km. Some of the energy which these particles deposit in the atmosphere appears as ultraviolet radiation. The partition of the energy of incident

particles depends on the nature of the primary particles, and the question of the relationship between these and resultant ultraviolet energy, and the transport of that energy, was the basis of the work undertaken in the part of this work concerned with auroras.

1.2 Absorption of Radiation in the Atmosphere

The lower limit of wavelengths accessible to ground-level observations is near 290 nm. For vacuum ultraviolet measurements, detectors must be taken to heights above those indicated in Figure 1.1 so that absorption, if not negligible, can at least be corrected for with acceptable accuracy.

The absorbing properties of the atmosphere, while complicating measurements of incident intensities, do provide a means of studying the atmosphere itself. Much information can be obtained by detailed study of the absorption characteristics. Radiation at any wavelength incident on a pure absorbing atmosphere is attenuated in a manner described by

$$I(h) = I_0 \exp\{-\sigma N\} \qquad (1a)$$

where I_0 is the intensity incident on the atmosphere

$I(h)$ is the intensity at height h

σ is the absorption cross section of the atoms or molecules at the particular wavelength

N is the total column density of absorbers above height h, along the path of the radiation

At any one wavelength, σ can be regarded as a constant characteristic

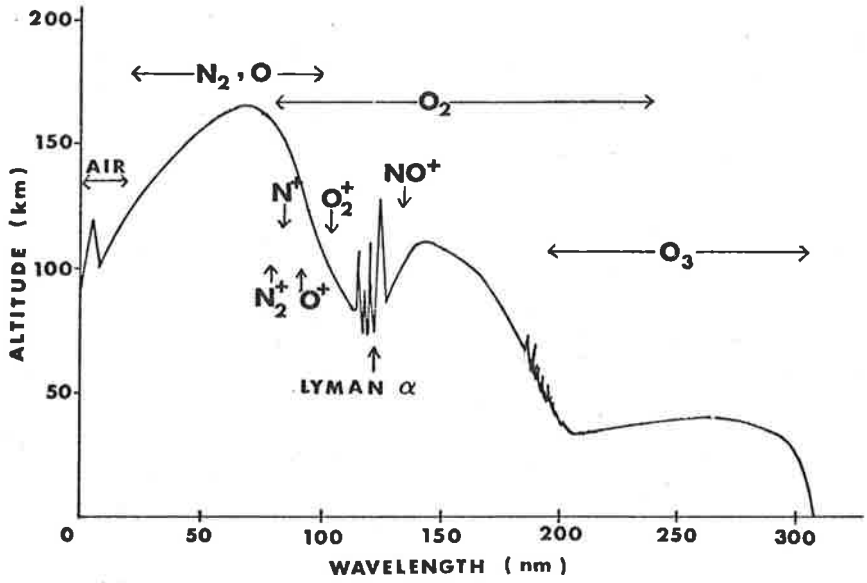

FIGURE 1.1 ATMOSPHERIC ABSORPTION HEIGHTS

(after Herzberg, 1965)

The curve shows the altitude at which vertically incident radiation is attenuated to $I/I_0 = 1/e$, i.e. unity vertical optical depth. Also included are the dominant absorbers and their ionization limits.

of one species if that species dominates the absorption. If not, at each height there is a combined effective absorber density and cross-section which can be used to calculate an effective cross-section. The expressions above are all functions also of wavelength.

The total column density, N(h), is found from the local number density, n(h), by integration along the radiation path. For radiation incident on a planar atmosphere at an angle χ from the vertical, the integral becomes

$$N(h) = \int_h^\infty n(h') \sec \chi \, dh' \qquad \text{(vertical integration)} \qquad (1b)$$

Thus, from (1a) and (1b)

$$I(h) = I_0 \exp \{-\sigma \int_h^\infty n(h') \sec \chi \, dh'\} \qquad (1c)$$

Taking logarithms and differentiating from (1c) gives

$$\frac{d}{dh} \ln I(h) = n(h) \, \sigma \sec \chi \qquad (1d)$$

$$\text{or, } n(h) = \frac{\cos\chi}{\sigma} \frac{d}{dh} \ln I(h) \qquad (1e)$$

Relationships derived in this manner enable height profiles of absorbing atmospheric species to be deduced from absorption profiles (Chapters 6, 7, 8). They also enable corrections to be made to measurements made at altitudes where absorption cannot be ignored.

The relationship (1e) refers only to pure absorption in a planar medium. Consideration of the effects of the curvature of the surface of the Earth, and of resonance absorption is given in later sections, (Chapters 6, 8).

1.3 Solar Radiation

In addition to the absorption bands mentioned above, the solar spectrum has other non-black-body features. At wavelengths longer than 160 nm Fraunhoffer absorption lines are found, while at shorter wavelengths emission lines of the elements are prominent. Between 120 nm and 160 nm, by far the most intense line in the solar spectrum is the Lymanα resonance line of atomic hydrogen. The incident flux of solar Lymanα radiation has been measured many times. Moderately large temporal variations have sometimes been indicated (Prag and Morse, 1970; Meier, 1969), and the mean flux is near 4.5×10^{-3} watts m^{-2}.

The solar Lymanα line has a complex profile due to absorption by solar, interplanetary and terrestrial atmospheric gases. The shape, as well as the total energy flux of the line is known to change with time. The width of the line is almost 0.1 nm, including two wings with a complex absorption core (Purcell and Tousey, 1960; Bruner and Parker, 1969; Figure 6.1).

The wavelength of Lymanα radiation coincides with a deep minimum in the molecular oxygen absorption cross-section of near $1 \times 10^{-24} m^2$ (Ogawa and Yamawaki, 1965). This means that most of the energy in this transmission window around the wavelength of Lymanα penetrates to well below 100 km, ionizing nitric oxide to form at least a major component of the D-Region. Details of the line profile of the solar Lymanα flux are important because of the resonant scattering of the core radiation by terrestrial hydrogen. The scattered radiation forms the strongest

component of the night airglow in the vacuum ultraviolet region (Morton, 1962). The contributions to the night sky ultraviolet radiation are discussed in Section 6.4.

1.4 Other Radiation Sources

During local night-time, when the atmosphere is shielded from the dominating direct solar radiation, other ultraviolet sources may be detected. The reflection of solar radiation by the moon has been measured in the middle ultraviolet above 200 nm (Carver et al., 1966; Lebedinsky et al., 1968). The observed spectral character of moonlight is similar to that of sunlight, but is modified by the lower effective reflectivity towards the short wavelength end of the measured spectra. The moon's radiation therefore affects the atmosphere in much the same way that sunlight does, and in any wavelength band the altitude profiles of absorption of solar and lunar radiation are similar. Because of the low flux levels, the measurement of the lunar reflectivity at wavelengths shorter than 200 nm is difficult.

The strength of the solar Lymanα emission makes feasible a determination of the lunar flux at this wavelength at least. Two of the experimental payloads described (in Chapters 7 and 8) were designed with the intention that (given suitable vehicle orientation near the apogee of the flights) the instruments would be able to measure the lunar flux at Lymanα.

At wavelengths other than Lymanα, stellar radiation has been observed from many discreet sources (Smith, 1967). Detection of distant sources

at Lymanα is complicated by resonance scattering in interstellar hydrogen and by the presence of strong airglow emissions from the geocorona surrounding the Earth.

Radiative emissions by atmospheric constituents are excited by one of four mechanisms:-

1. Resonance absorption of radiation from an external source (dominated by the sun).
2. Impact of energetic particles, notably protons and electrons.
3. Decay of metastable states in atoms and molecules excited during a previous period of solar illumination.
4. Recombination of electrons with ions formed during solar illumination.

The dominant airglow feature in the vacuum ultraviolet region arises from the resonance scattering of the large flux of solar Lymanα radiation by atomic hydrogen, mainly in the vicinity of the Earth. A study of the Lymanα airglow formed the basis of the work reported in Chapters 6, 7 and 8.

The mechanism 2 constitutes, by one definition, an aurora. The aurora in its most common forms is normally confined to near-polar regions. Auroras can be very variable in time and space, and involve large energy flux densities. Auroral emissions were the subject of part of this work and are discussed separately from airglow in Chapters 3, 4 and 5.

Mechanisms 3 and 4 do not appear to contribute significantly to

airglow emissions in the vacuum ultraviolet where photon energies are in excess of 5 electron volts.

1.5 Resonance Radiation

The discussion of atmospheric absorption in 1.2 concerned only pure absorption, in which each absorbed photon is permanently lost to the radiation field at the original photon wavelength. The absorbed energy may then appear as fluorescent radiation at a longer wavelength, or may be dissipated non-radiatively. Radiation which, after being absorbed by a group of atoms, is later re-emitted at the initial wavelength, is known as resonance radiation. The transition associated with resonance absorption is normally from the ground state of the atom (e.g. Lymanα), but other significantly populated states may be involved (e.g. the 130.2, 130.4, 130.6 nm resonance triplet in atomic oxygen). A gaseous species normally has a very large absorption cross-section in the vicinity of the resonance wavelength.

Resonance scattering of a beam of radiation tends to make the intensity isotropic, and modifies the transport of the radiation through the atmosphere so that the equations of 1.2 cannot be directly applied.

The optical depth, $\tau(h)$ for the radiation at any frequency is given by

$$\tau(h) = \int_h^\infty \sigma n(h')\, dh' \qquad \text{(vertical incidence)} \qquad (1f)$$

Where the optical depth is large, resonance radiation can become trapped by multiple scattering. Each photon entering the scattering region can effectively traverse the region many times before either

escaping upwards or being absorbed. The apparent flux measured by a detector within this region is magnified above the true net flux through the region. The effective absorption cross-sections of any true absorbing species are also greater than in a pure absorption situation. A detailed examination of this process is made in Chapter 6, and an application to atmospheric measurements is described in Chapter 8.

Resonance absorption is particularly important at two vacuum ultraviolet wavelengths which are included in the measurements described later. In the vicinity of Lymanα, photons are multiply scattered into the night time atmosphere. Only the radiation in the core of the solar emission line is scattered by the cool terrestrial hydrogen, but measurements have indicated that the night-sky radiation has a broad profile (Morton and Purcell, 1962). Relationships between the radiation in the core and in the wings of the night-sky Lymanα line are discussed in Chapters 6 and 8, and an absorption method of separating these two components is described. The two components behave differently in the absorbing region below 120 km because the atmosphere is optically thin to radiation in the wings, but is thick to the core radiation, of which resonance trapping occurs to a considerable degree.

Atomic oxygen in the ground state resonantly scatters radiation near 130.4 nm. Figure 2 shows some of the energy levels and transitions in atomic oxygen. This species is a major consituent above 100 km and there are very large optical depths for the 130.4 nm

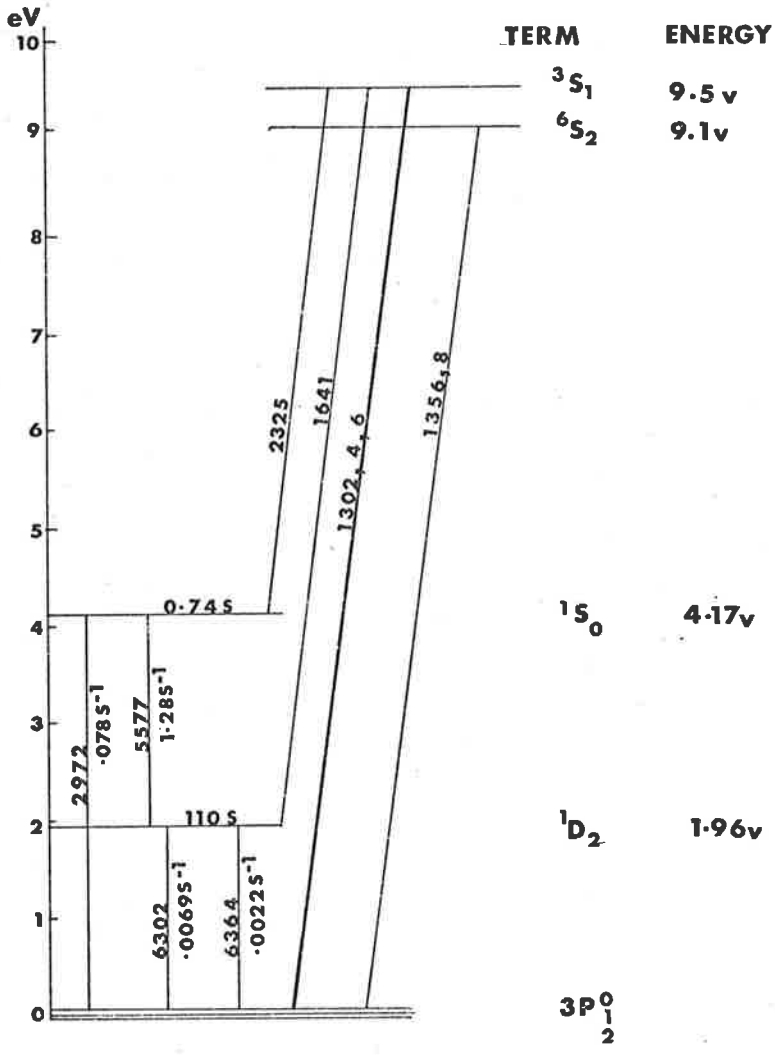

FIGURE 1·2 ENERGY LEVELS AND TRANSITIONS OF O I

resonance wavelengths above this height, (Fastie et al., 1964). Radiation in the 130.4 nm resonance lines has on some occasions been found to be a major part of the ultraviolet spectrum of auroras (Miller et al., 1968). The effects of the resonance trapping complicate the interpretation of signals from detectors spanning this wavelength range and apparent fluxes may not be a true indication of the intensity and location of the source (Donahue and Strickland, 1970). Resonance radiation in auroras is mentioned in more detail in Chapters 3 and 5.

1.6 Summary

Atmospheric properties relevant to the absorption and measurement of vacuum ultraviolet radiation have been outlined. In the 100 to 150 nm spectral region, total absorption occurs at altitudes above 65 km. Rocket measurement techniques are therefore required in order to study the important effects of this high altitude absorption.

Vacuum ultraviolet radiation is particularly important in the energy balance and in the chemistry of the upper atmosphere, because the photon energy is large enough to directly alter the chemical composition of the atmosphere by dissociation and ionization of both major and minor constituents.

Ultraviolet radiation either reaches the upper atmosphere from a distant source or is emitted locally as the result of an energy input of another form. Both energetic particle streams and radiation fluxes can provide the exciting energy input; in very general terms, the particles produce auroras, and the radiation excites the ultraviolet

airglow.

The purpose of this work is to provide more information on the generation and transport of atmospheric ultraviolet radiation which is classified, according to the exciting agent, as aurora or airglow. At the same time, more knowledge is sought of the sources of the exciting radiation, and of the composition of the upper atmosphere itself.

CHAPTER 2 ULTRAVIOLET RADIATION DETECTORS

The requirements and constraints governing the choice of detectors for rockets are discussed in this Chapter. Details are given of the design, construction and features of the detectors which were developed for this work. The procedures for testing and calibrating the detectors are described. Figures are given for the performance characteristics achieved by the ionization chambers, with reference to the special requirements for detectors used in small rocket instrumentation.

2.1 Properties of Detectors for Use in Rocket Experiments

The detectors used for the measurement of ultraviolet radiation, together with the associated components, had to meet several requirements for operation in the demanding environment of sounding rocket payloads. These included:-

(a) Mechanical ruggedness.

(b) High sensitivity: for rapid measurements from fast-moving vehicles.

(c) Spectral selectivity: to allow discrimination between emissions.

(d) Compactness: the available payload volumes placed severe restrictions on the size of the detectors, particularly when the experiment required that several be flown as a group.

(e) Temperature stability: during rapid heating to above 60^0C.

The above requirements determined the applicability of different methods of detecting ultraviolet radiation. Three physical effects which are useful for detection of radiation in the vacuum ultraviolet region (photon energy of 6 to 12 eV) are :-

(1) Photoelectric emission from surfaces.

(2) Fluorescence.

(3) Photoionization of gases.

(1) Photoelectric detectors often employ electron multiplication to amplify the small emission currents (photomultipliers, channeltrons). The multipliers, when mounted, require large volumes, while channeltrons employ high voltages and are susceptible to atmospheric poisoning at the height where measurements were required to be made. In addition, the long wavelength cutoffs of the cathodes are not sharp enough, or at suitable wavelengths, for the requirements of some of these experiments.

(2) Several materials are known which have a high efficiency for fluorescent conversion of ultraviolet to visible radiation. Fluoresence detection is most useful at wavelengths shorter than 100 nm where suitable entrance window materials may not exist for all applications. Spectral selectivity must then be achieved by the use of dispersing gratings or thin-film filters. A photomultiplier or photodiode is required to detect the fluorescent emission. An application of the thin-film filter technique is described briefly in Section 7.2.1.

(3) Photoionization of suitable gases has several advantages for ultraviolet radiation detection. When the resultant electrons are effectively collected and measured as a current, high detection efficiencies can be achieved. The molecular structure of some gases

causes them to have a sharply defined ionization threshold, where the ionization efficiency of radiation drops rapidly over a narrow wavelength range which is characteristic of the gas. Detectors employing the ionization of such gases then have sharply defined limits to the spectral response, and this property, together with compactness and ruggedness, led to the use of ionization chambers as the detectors in most of this work.

2.2 Principles of Ionization Chamber Operation

An ion chamber consists essentially of a volume of ionizable gas, a container for the gas with an area of a suitable window material, and a system of electrodes to collect the ions and electrons for measurement.

The three aspects of the generation of a signal current by the incident photon flux are treated separately below.

2.2.1 Absorption

A beam of radiation of a particular wavelength will be attenuated while passing through the chamber window. Materials which are suitable as windows for vacuum ultraviolet radiation detectors have a sharp transmission cutoff, with negligible transmission of wavelengths shorter than the limit. For each application the window material is chosen to give the desired short-wavelength limit to the chamber response.

The radiation which passes through the gas volume is absorbed at a rate determined by the gas pressure and its absorption coefficient

at that wavelength (in the same manner as described in 1.2). The absorption coefficient of the gas may vary over the range of wavelengths admitted to the chamber. Strongly absorbed wavelengths produce ions in the space immediately behind the window, and efficient ionization collection from this volume is thus important if the detector response is not to be excessively sensitive to gas pressure.

2.2.2 Ionization

Photons of energy exceeding the ionization threshold of the gas can ionize gas molecules on absorption. The ionization efficiency varies with wavelength and drops suddenly in the vicinity of the threshold. The efficiency near the threshold is dependent on temperature (Carver and Mitchell, 1967), so the long wavelength limit of the chamber response shifts slightly with temperature. In the middle of the response range, the ionization efficiency is not markedly temperature dependent. The photons able to enter the chamber through the window do not have enough energy to ionize more than one molecule, so the ionization efficiency is less than unity, and is known from laboratory measurements made previously by other investigators.

Radiation which is not strongly absorbed in the gas can reach the walls of the chamber and the collecting electrodes, where it may release photoelectrons from the surfaces. The resultant photoelectric current cannot be distinguished from the true ionization current. The most serious photoelectric effects are produced by radiation at wavelengths longer than the gas cutoff, as radiation shorter than

the window transmission limit can produce photoelectrons only outside of the chamber.

2.2.3 Charge collection

The ions and electrons are swept from the gas volume by the electric field between the conductors in contact with the gas. Most of the chambers used in this work had, as the collecting electrode, a rod fixed along the axis of the chamber. The other electrode was the side wall of the chamber.

The signal current from a chamber with constant radiation input depends on the bias voltage applied to it. When the applied voltage is less than about one volt, the signal current can actually oppose the applied bias. This is because the field is then not strong enough to collect much of the ionization charge, and the opposing photoelectric current dominates.

As the applied voltage is increased, the output current increases in the bias direction. At some voltage (typically 25 volts for the chambers used), the current becomes almost independent of the voltage. The field strength is sufficient to collect almost all of the ionization charge before recombination can occur. Below approximately 80 volts, no significant gas multiplication occurs, and one electron is collected in the signal circuit for each ionization event in the gas. A chamber run in this plateau region of the bias signal curve is said to be operating at unity gain (Figure 2.4). The sensitivity of the chamber at unity gain depends

only on the transmission of the window and the absorption coefficient and ionization efficiency of the gas at each wavelength.

At higher applied voltages the signal current again becomes voltage dependent as multiplication occurs within the gas. The degree of current amplification depends upon the composition and pressure of the gas, and on the field strength; a chamber operating under these conditions is said to be in gas gain mode. Operation of chambers at high voltages is discussed in 2.4.

Several different types of ion chambers were developed to meet the requirements of the experiments described in later sections. The following two Sections (2.3, 2.4) describe the features of the construction and operation of these chambers. The Sections 2.5, 2.6 and 2.7 describe the filling, testing and calibration procedures applied to the chambers.

2.3 Unity Gain Ion Chambers

The requirements of the experiment described in Chapter 4 were for chambers of several different spectral responses, to be operated at unity gain. The two designs used were almost identical externally, and were interchangeable in the payloads.

2.3.1 Chambers with copper bodies

The first was of the type described in Friedman et al, (1958) and of a design following Carver and Mitchell, (1964). The only modifications were the inclusion of a filter capacitor and an external shield around the signal electrode because the chambers were operated

in an unshielded location close to other circuitry. A diagram of one of these chambers is shown in Figure 2.1 and one is included in Figure 2.3.

The windows were cleaved ionic halide crystals (LiF, CaF_2 or BaF_2), between 1 and 2 mm in thickness, and 19 mm diameter. The entrance aperture, defined by the window support, was 13 mm diameter. A commercial grade "Araldite" epoxy was used to fix the windows. Although this had a relatively low limit on operating temperature (near 100^0C), it had the advantage of being sufficiently soft at room temperatures and above to minimise the chances of window cracking during heating. The expansion coefficients of the window materials were poorly matched to that of copper, and a hard epoxy would have transmitted excessive stresses. The epoxy did become harder at low temperatures, however, and some windows fractured during transit in very cold conditions. The glass bodied chambers adopted later (2.3.2) were not troubled by this problem. Some designs of ion chambers (Stober et al., 1963) have made use of silver window supports, but it was not found necessary in this application to resort to the more complex construction required to incorporate these support rings.

The chambers were evacuated and filled through annealed copper stems, and were sealed off by making cold weld pinch-seals in the stems. The gases used were nitric oxide, p-xylene and ethyl bromide. The filling procedure is described more fully in

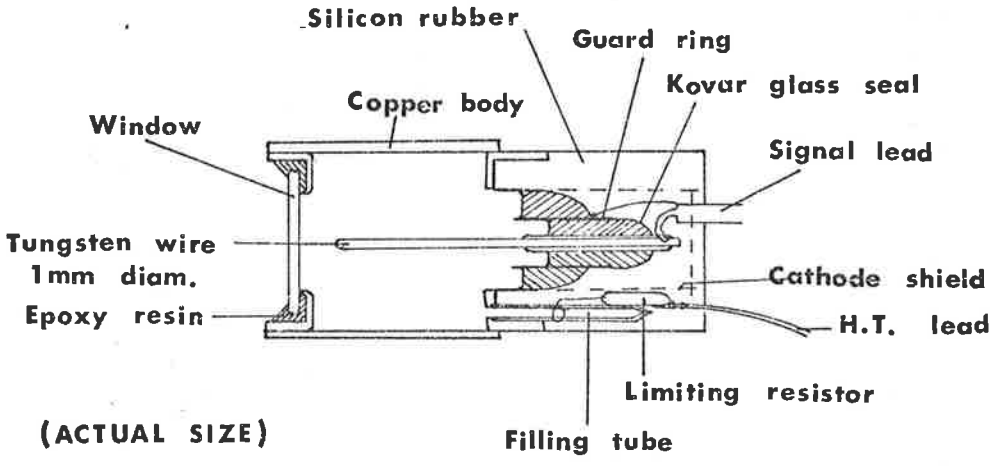

FIGURE 2·1 COPPER BODY UNITY GAIN ION CHAMBER

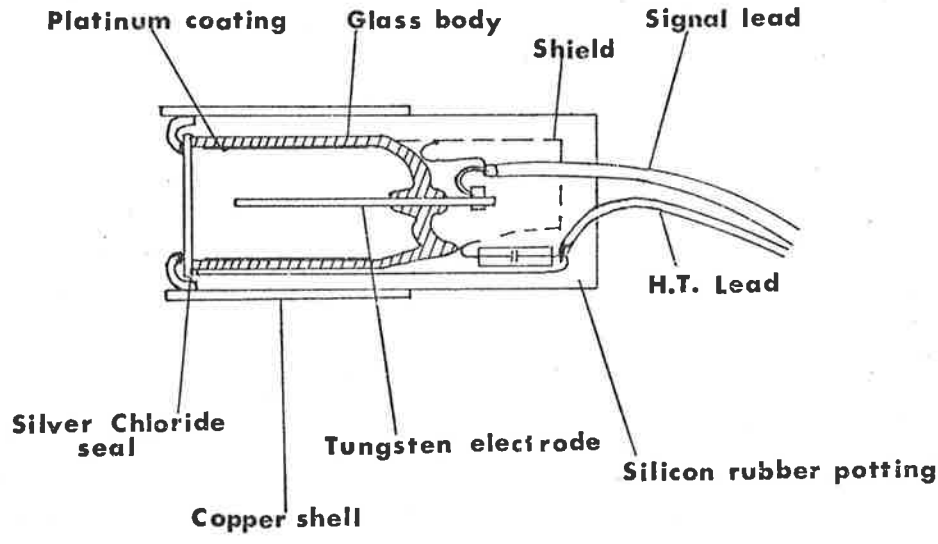

FIGURE 2.2 GLASS BODY UNITY GAIN ION CHAMBER

(ACTUAL SIZE)

Section 2.5.2.

The chambers were operated with the outer casing at +47 volts. This polarity confined the effects of photoelectric emission to the centre wire, which has a small cross-section for radiation entering at small angles to the chamber axis.

2.3.2 Chambers with glass bodies

The second type of chamber used for the unity gain applications is shown in Figures 2.2 and 2.3. The use of a glass body inside an earthed metal shield had several advantages. The glass body and silver chloride seal could be baked more thoroughly before filling than could the first type of chamber, and shielding reduced the sensitivity to the electrical noise generated by other circuits in in the payload. Chambers of this type were also found to be better able to withstand the stresses of vibration and shocks at low temperatures. The main elements of the structure are shown in Figure 2.2.

The glass seal-off was made in two stages to prevent gas migration during flame sealing. A rapid preliminary seal was made about two inches from the chamber body to separate it from the filling system. The chamber was again tested and, if satisfactory, was sealed again close to the rear of the body. After being tested and having leads attached, the chambers were potted with RTV850 into a copper shield of the same size as the bodies of the earlier chambers.

The testing and calibration procedures used for these and other

FIGURE 2.3 THREE TYPES OF ION CHAMBERS

The two large-diameter chambers were used at unity gain in the MAP auroral payload. At left is the copper bodied version; the chamber in the centre has a glass body inside the copper shell. The miniature gas-gain chamber at right has a glass body potted into the protective sleeve; the type was used on Aerobee 4.301 and C104.


16THS
10THS
HELIX
MRI.
MADE IN ENGLAND

chambers are described later in 2.6 and 2.7.

2.4 Gas Gain Ion Chambers

As mentioned in 2.2, there is a range of chamber operating voltages over which the output current is practically independent of the voltage. If the voltage is increased beyond this plateau region, the chamber sensitivity (current per incident photon) increases above the unity gain value. Electrons can acquire sufficient energy from the field to ionize further gas molecules, initiating an avalanche. Avalanche multiplication occurs most readily if the outer walls are biased negatively with respect to the centre electrode. The primary electrons produced in all parts of the gas volume then pass through the strong field region near the centre wire, where the avalanches occur. The degree of multiplication, or gas gain, at any voltage is measured as the ratio of the signal current at that voltage to the current when the chamber is operating in the centre of the plateau region. Typical gain curves for 13mm diameter nitric oxide chambers are shown in Figure 2.4.

Factors which have the most influence on the effective gas gain include applied voltage, gas pressure and composition, and electrode sizes and shapes. Figure 2.5 shows gain curves obtained for both miniature and standard sized glass chambers (2.4.2) at different pressures close to the usual filling pressure. At lower pressures the mean time between electron-gas collisons is greater, and the electron can acquire ionizing energies from a weaker applied field. Gas multiplication processes are discussed in detail by Wilkinson (1950).

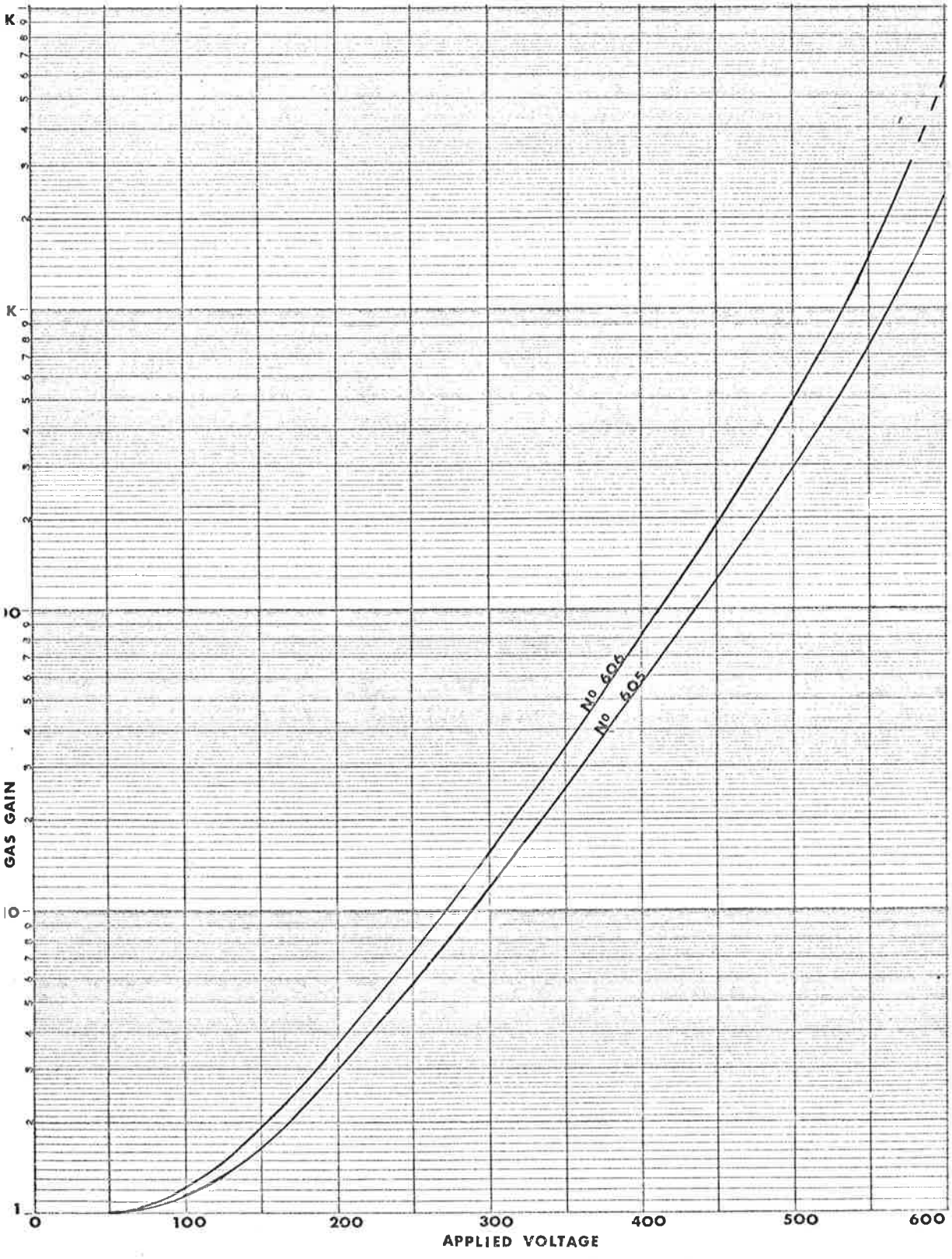

FIGURE 2·4 GAS GAIN CURVES OF GLASS CHAMBERS

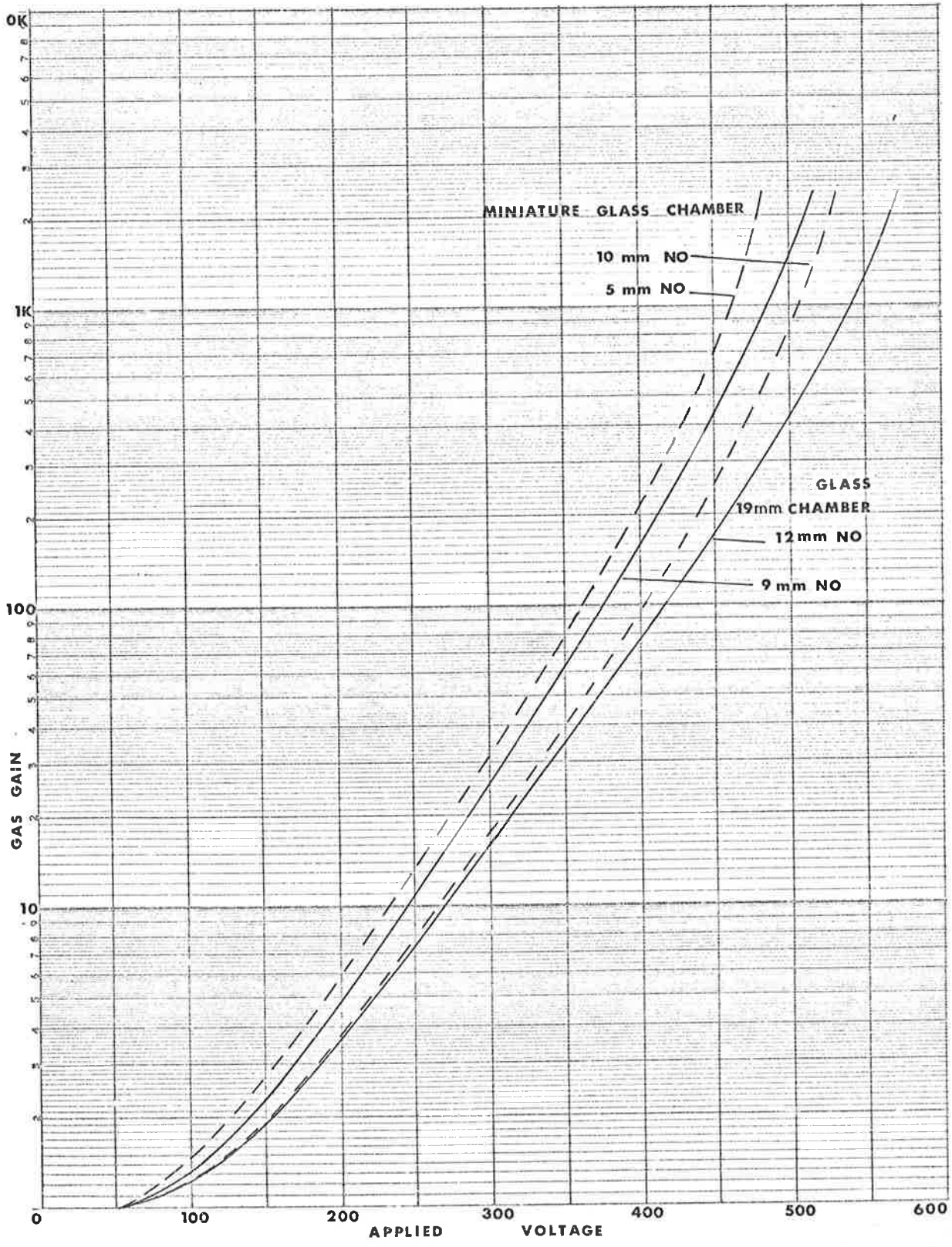

FIGURE 2.5 EFFECT ON GAS GAIN OF FILLING PRESSURE CHANGE

The region near the surface of the centre wire, having the highest electric field strength, is the most important in the multiplication process. Careful preparation of the surface of this electrode is necessary. During the construction of each gas gain chamber the surface of the wire was polished smooth to make the field uniform, elminating regions of local instability. Tungsten rod of 1 mm diameter was used in most of the chambers constructed. It was found best to grind and polish hemispherical ends on the wires. The complete rods were then electro-chemically polished. Drawn tungsten has a generally rough surface, but the etching removed the worst irregularities.

At excessively high voltages (where the curve in Figure 2.4 is broken), chambers either went into a quiet non destructive discharge, or flashed over violently emitting a light pulse and chemically changing the composition of the filling gas. Care had to be exercised during tests at very high voltages to limit the energy available to any discharges. The tests were done to ensure that an adequate margin of stable gain had been achieved.

As the gas temperature is increased, the percentage of molecules in a kinetically excited state increases, thus tending to lower the mean ionization threshold and to increase the gas gain. On the other hand, the mean time between collisions is reduced and also some increase in pressure due to absorbed gas driven off from internal surfaces is to be expected. The last two effects both reduce the gas gain, opposing the increase due to threshold lowering.

The effects of temperature on the gain characteristic are shown in Figure 2.6. The measurements were made on a 19 mm glass-lithium fluoride-nitric oxide chamber. The lower curve was taken after the chamber had been hot for twenty minutes. The gain had not returned exactly to the original characteristic when the final curve was measured, ten minutes after cooling. No further measurements were made to determine whether further recovery occurred over a much longer period of time. Because the chambers were not subjected to heating prior to flight, it was only the short term behaviour which was relevant to the conditions during rocket flight. The magnitude of the temperature effect was small enough for no significant problems to be expected over the duration of a flight in a small rocket reaching an altitude near 120 km. An ion chamber in an exposed position would be required to operate at above 50^0C for a maximum of three minutes, and in a protected location its internal temperature should remain below this value during the entire period.

Care was taken to ensure that no regions of local high field strength were created in the vicinity of the guard electrode. Its operating potential is close to that of the collecting anode, so the shape and position of the guard were selected to avoid instability and breakdown at its surface.

2.4.1 Miniature glass chambers

To meet the requirements of two of the airglow experiments (7.2.1, 7.2.2), a small type of ion chamber was developed.

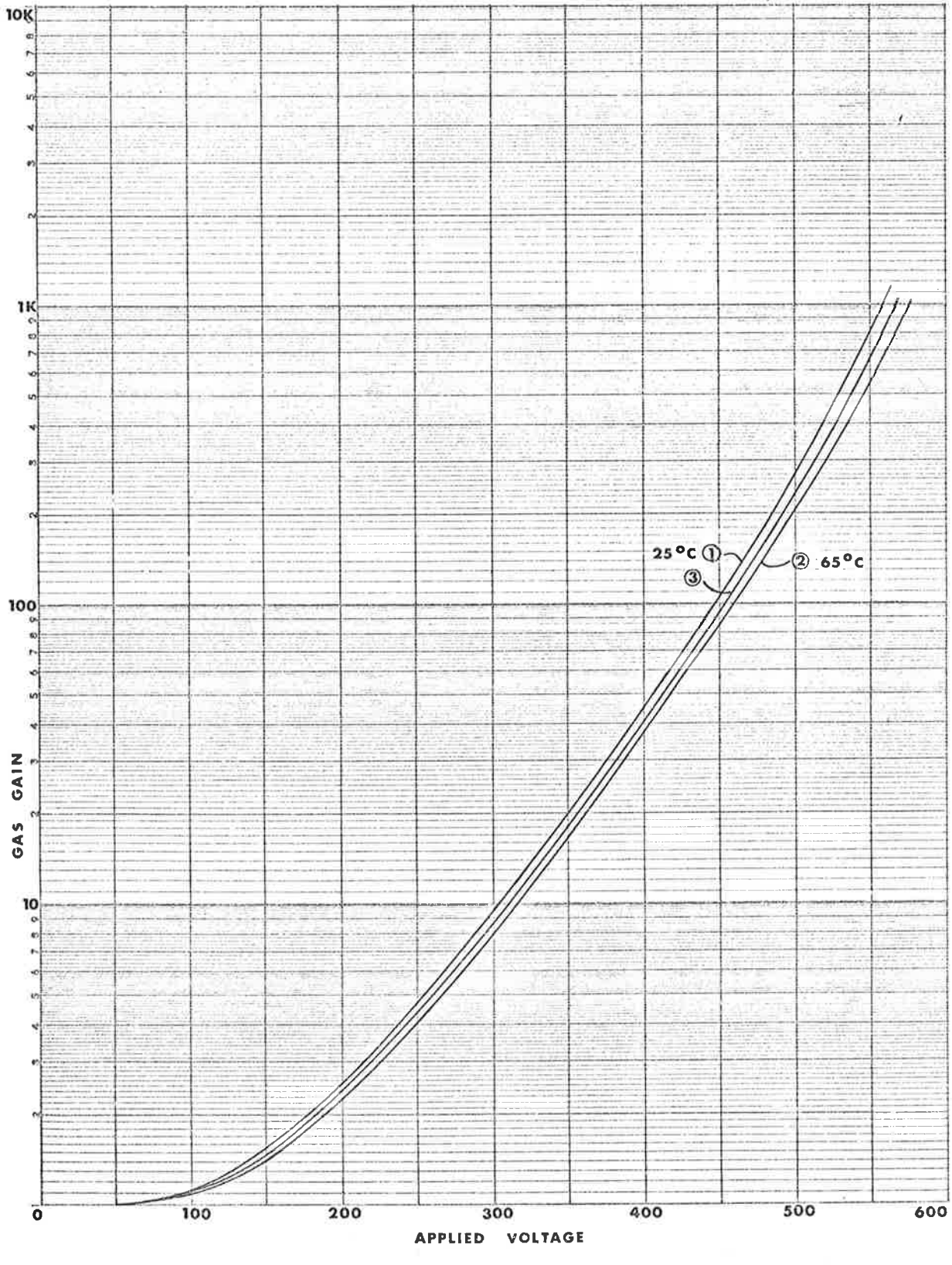

FIGURE 2.6 EFFECTS OF TEMPERATURE ON CHAMBER GAIN

Consideration of available space and weight precluded the use of larger chambers of a more standard design. The external form can be seen in Figure 2.3 and an annotated cross-section is given in Figure 2.8.

The basic feature of the construction are similar to those of the glass bodied unity gain chambers (2.3.2). The miniature chambers were not required to have an angular response as broad as that of the unity gain chambers, so the reduction in diameter did not entail very serious losses in photon absorption.

Typical gain-curves for this configuration of electrodes were given in Figure 2.5 in reference to the pressure dependence of gain. Despite the small volume of the gas, and the consequent large ratio of the surface area to volume within these chambers, the effect of temperature rises on the gas-gain characteristics was found to be small.

All of the miniature chambers were filled with nitric oxide gas at a pressure of 10 mm of mercury. Both lithium fluoride and calcium fluoride windows were fitted, as the chambers were required for detection of Lymanα radiation and for separation of this emission from any background of longer wavelength radiation. The spectral range of the chambers was 105 - 135 nm (lithium fluoride window) and 122 - 135 nm (calcium chloride window).

2.4.2 Dual ion chambers

The design of one of the experimental payloads incorporated

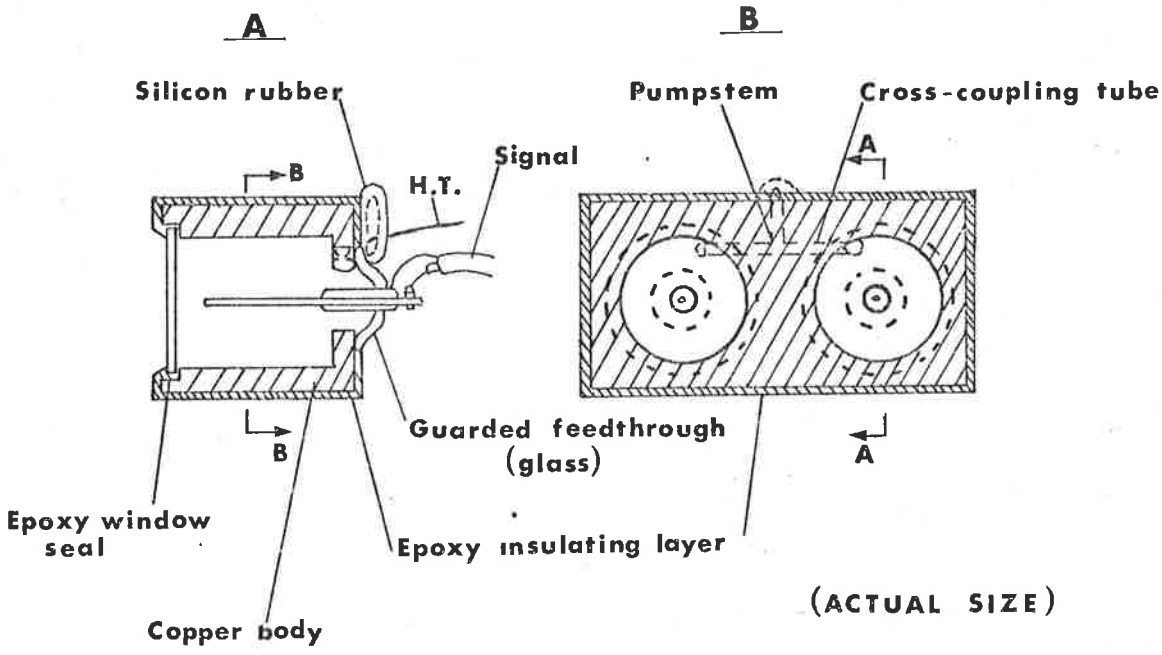

FIGURE 2.7 SECTIONS OF COPPER DOUBLE CHAMBER

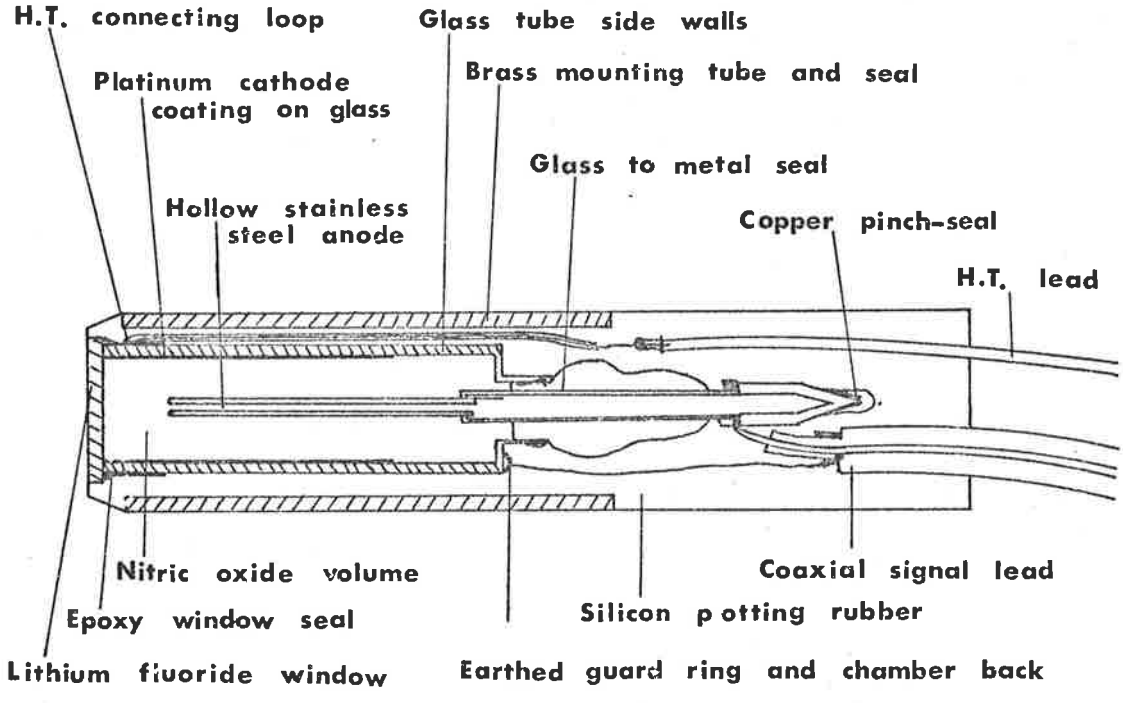

FIGURE 2·8 MINIATURE GAS-GAIN ION CHAMBER

a pair of ion chambers (7.2.3). As these were to be used for signal differencing, knowledge of the relative sensitivity of the two chambers at all wavelengths was important. The spectral response of the chambers could be measured in the laboratory, but some changes could be expected during the preparation and launch program. These changes would not have caused any significant problems in a single-channel application. However, since differencing was to be used, particular attention was paid to maintaining a constant relative sensitivity in the detectors at all wavelengths.

The spectral response of an ion chamber is determined by the properties of the window and the gas. The transmission curves of the window do not show any fine structure but the spectral response of the gas ionization exhibits structure. The detailed shape of the spectral response is not exactly the same for all chambers of the same type. There is some dependence on the condition of the gas and the filling system, and on the life history of the chamber. In nitric oxide chambers, effects had been observed from residual contamination by water vapour and other nitrogen oxides. Any other unidentified impurities with high absorption cross-sections could also effect the chamber response. Differences between chambers, and temporal changes in response and gas-gain, are due mainly to gas effects.

A dual chamber having two windows, two sets of collecting electrodes and a common gas volume was developed as a solution to

the problem of matching the spectral responses. Two methods of construction were investigated.

One type had two chambers machined into a copper block, with a connecting opening between them. Sections of one of these chambers are shown in Figure 2.7. The connecting opening between the two chambers was screened to prevent both optical and charge transfer coupling between the chambers. The copper block was potted in an epoxy resin as an insulator, while the copper filling stem and anode connections were protected by a silicone rubber compound.

The quantum efficiencies of the two chambers with dissimilar windows were different, even at the long wavelength end of the response range, as no attempt was made to match window transmissions by selection of individual window plates. As the shape of the response curves in the common sensitive region was determined by the gas, differences between window tranmissions could be corrected for by adjusting the respective amplifier gains. The gain characteristics of the twin chambers were found to be closely matched in a variety of operating conditions, which was the objective of the dual chamber development.

The other type of dual chamber consisted of a pair of glass chambers (of the type described in 2.3.2) fixed side by side between two supporting strips. Their filling stems formed flexible curves to a common filling and sealing stem. The complete structure was supported and insulated by silicone potting compound. The chamber

pair selected for flight was of this glass construction (Figure 7.4). The characteristics were similar to those of the copper type.

2.4.3 Standard size glass chambers

An improved version of the 19 mm window glass-body chamber was developed to meet the requirements of the experiment described in Chapter 9. Some of the chambers which had been used previously had shown a tendency to generate current pulses at a low repetition rate. The effect would only become noticeable several weeks after the chambers had been filled, and when the chambers were run at high gain. The pulses appeared when the chambers were not illuminated and, being suppressed by an ultraviolet input to the chambers, appeared to be caused by a charge build-up on the inside surface of the window. The resistivity of the window, although high, allowed a surface charge to build up when there was no radiative imput. The surface charged negatively towards the voltage applied to the cathode coating on the side-wall. As the charge build-up occurred, the field strength at the end of the anode increased. Particularly in the case of an aged chamber run at high gain, the field at the anode could become strong enough for a geiger type of pulse to be generated. Such a pulse could have been initiated by a nuclear decay within the chamber, or by cold emission of electrons from the walls.

To establish that the pulses were due to changes in the electric field connected to the window, a chamber was constructed with a metallic

mesh immediately behind the window. This screen maintained a constant potential across the front of the chamber, and greatly improved the stability of gas-gain operation.

An attempt was made to give the windows a conducting inside surface of vacuum-evaporated nichrome. It was found that, for the layer to have a useful conductivity after exposure to air, the thickness had to be so great that its attenuation of ultraviolet radiation was unacceptable. A striped pattern of aluminium was found to provide a suitable field with tolerable signal losses (15%). The evaporated coating was also used to define an entrance aperture of 13 mm diameter. Polished windows were used to enable an electrically continuous coating to be deposited.

Shorter anodes were also used to make the field distribution around the anode tip more uniform. With the modifications mentioned, the chambers could be operated with stable gains up to 10^4 for several months from the time of filling. (The voltage needed for a given gas gain increased slowly with time after the filling of the chamber; this was probably due largely to out-gassing of other gases from the walls, causing increased quenching. The operation of an aged chamber at gains near 10^4 would involve voltages near 800 volts, and there would be a consequent danger of flash-over of the insulation.) The gas gain required in the flight applications was much less than 10^4, but the ability of the chambers to operate stably and quietly at very high gain indicated that an ample safety margin had been achieved

for operation in the rocket environment. The gas gain curves (1, 2) in Figure 2.4 were measured on one of these striped window chambers. Chambers of this type are shown in Figure 2.9. The windows were fixed with epoxy because it was found that a slow reaction occurred between silver chloride and the evaporated coating on the window. Reliability of the window seal then became doubtful some time after the window had been fixed.

A firm continuous bond was required between the window edge and the potting compound to avoid risks of a corona discharge between the chamber body and the rocket body during flight. The bond was made with the sealant Dow-Corning RTV 3145 which was of a type least likely to contaminate the window surface during curing.

The above sections have outlined features of design and construction of the ion chambers employed in this work. In the following sections a description is given of the procedures for filling the chambers, and of the calibration and testing of the completed chambers.

2.5 Ion Chamber Filling

Although several gases have been found suitable for use in ion chambers (Carver and Mitchell, 1964), only nitric oxide, p-xylene and ethyl bromide were used in this work. The pressure of the filling gas was selected to give the chamber the maximum detection efficiency over the sensitive spectral range.

The absorption of radiation of any wavelength follows the form of

FIGURE 2.9 GAS-GAIN ION CHAMBERS AS USED IN C1014

The glass body is shown at the stage of first seal-off. The second seal was made at the constriction near the back of the body. The evaporated aluminium pattern of conductors can be seen on the window of the potted chamber.

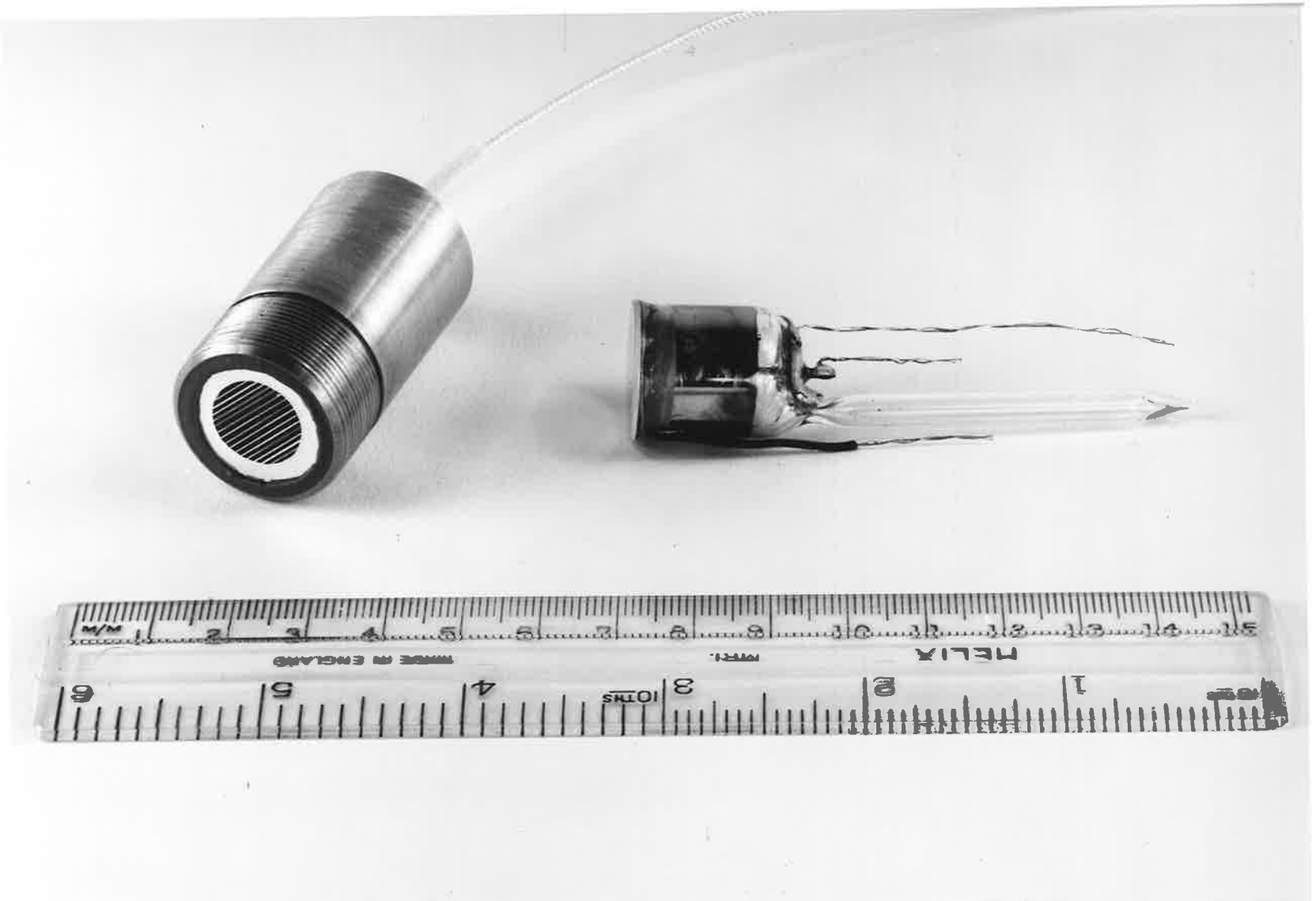
MADE IN ENGLAND
METRIC
10THS
6
5
4
3
2
1

equation (1a), and the ion production rate in the gas decreases exponentially over a path length determined by the gas pressure and its absorption coefficient for that wavelength. The gas pressure should be high enough to absorb most of the radiation in regions of low cross-section ($N\sigma>2$, preferably). However, the pressure should not be higher than necessary, or radiation for which σ is high will be absorbed too close to the window, where the collecting field is weaker and where recombination is more likely to occur.

In the case of each of the three gases mentioned, variation of σ across the relevant portions of the spectrum are not large (Watanabe, 1954; Carver and Mitchell, 1964). The response of a chamber to the undispersed radiation from a hydrogen discharge lamp therefore provided a valid measure of the overall chamber efficiency as the gas pressure was varied.

When chambers are filled to operate with gas gain, the changes in gas gain characteristics with pressure must also be considered. As the filling pressure is increased, the voltage required for a given gain is increased (Figure 2.5). The pressure should therefore be high enough to satisfy absorption conditions, but no higher, as excessive operating voltages increase the chances of break-down across insulators in the chamber and the supply circuitry.

2.5.1 Gas preparation

Ethyl bromide and p-xylene were obtained as AR grade reagents and no purification processes were required. They were introduced

to the filling system from a small phial of the liquid form, warmed slightly to fill the system with the vapour.

The nitric oxide was obtained from two sources. One was a cylinder of commercial gas. The other was the reaction of sodium nitrite with ferrous sulphate in an acid solution. In both cases, the gas was purified by passing in succession through traps filled with silica gel and with crushed glass, cooled to near -80^0C by immersion in a carbon tetrachloride-chloroform slush mixture (Figure 2.10). The gas was collected in glass bulbs, with breaker seals and "cold-finger" tubes, attached. The purification system, which had previously been baked out under vacuum, was constructed entirely of glass with no metal components which might react with the gas. When the receiving bulb had been filled to approximately 90% of atmospheric pressure, it was isolated and removed by flame seal.

The purification process was designed particularly to remove two contaminants which have strong absorption bands between 105 and 135 nm. They are water vapour, and the higher oxide N_2O_4 . The latter has a boiling point of 21^0C and a vapour pressure near 0.1 mm Hg at -80^0C. The vapour pressure of water at -80^0C is near 5×10^{-4} mm Hg.

In order to remove any contaminants (particularly water vapour) which might have outgassed from the walls of the glass bulbs during storage, the gas was further treated before the bulbs were attached to the chamber filling system. Each bulb was warmed while the attached "cold-finger" was immersed in a slush cooling mixture. The condensable

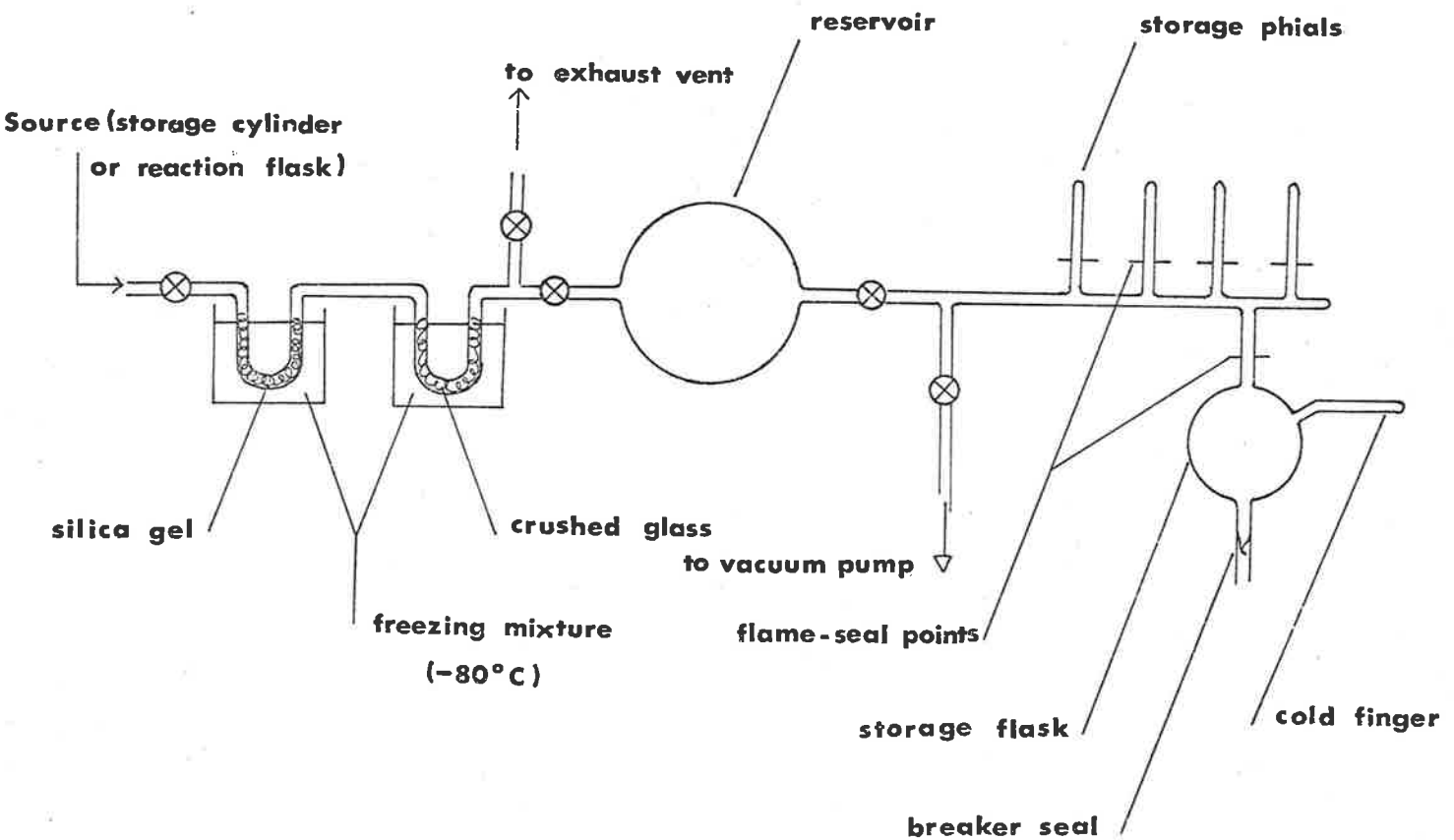

FIGURE 2.10 GAS PURIFICATION SYSTEM (NITRIC OXIDE)

contaminants were thereby concentrated in the finger, which was removed by flame seal-off.

Another method of gas storage was used in addition to the breaker-seal flasks. Attached to the collecting tube alongside of the flasks were a number of glass tube phials with drawn ends of the type used as breaker-seals. Each phial had a capacity of approximately 15 ml., and when filled with nitric oxide, was removed from the collecting tube by a flame seal-off. The gas contained in each phial was sufficient to fill one group of chambers on the filling system, and a fresh phial was used for each batch of chambers.

2.5.2 Chamber filling procedure

When the chambers had been assembled and tested for electrical leakage between electrodes, they were attached to the filling system. Those chambers with copper filling stems were attached by an epoxy joint; those with glass stems were glass blown directly onto the filling manifold.

The filling system was evacuated by an oil diffusion-rotary oil pump combination for several days, during which time the chambers and filling system were baked for periods at near 100^0C to remove absorbed gases from the tube walls.

A schematic diagram of the filling system is shown in Figure 2.11. There were two separate chamber mounting arms, so that groups of chambers could be pumped simultaneously and filled independently. There were two inlet points for nitric oxide, and one for other gases.

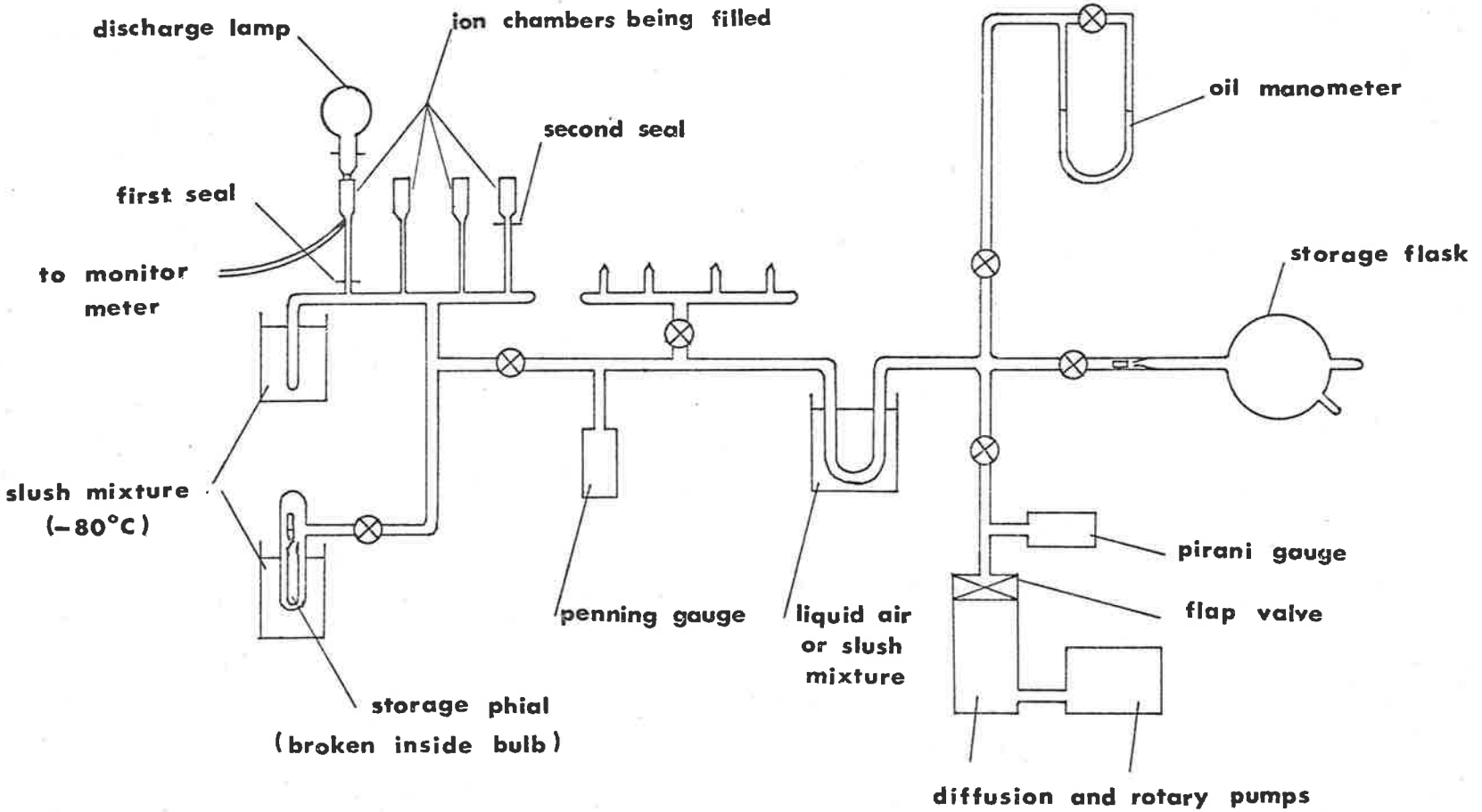

FIGURE 2.11 CHAMBER FILLING SYSTEM

The flasks of nitric oxide were joined permanently onto the filling system via a valve which controlled the admission of gas to the system after the flask seal had been broken open by a glass-coated steel slug.

Liquid air could not be used to cool vapour traps in the system while the filling gases were being admitted, as the boiling points of all of the gases are above liquid air temperatures. However, prior to gas admission, the central U- tube could be cooled with liquid air to aid the extraction of condensible vapours from the chambers.

The sensitivity of each chamber was monitored during gas admission, with a d.c. discharge between tungsten electrodes in hydrogen at a pressure of 4 Torr as the source. D.C. excitation was used as it produced no interference in the measuring circuitry. The lithium fluoride window of the lamp was placed in firm contact with the chamber window to minimise atmospheric absorption. Each chamber was operated at 50 volts and the output current was monitored as the gas was introduced. When the gas was free of impurities, the current rose to a maximum (for nitric oxide) at a gas pressure near 15 Torr, and did not change significantly as the pressure rose to 40 Torr. Contaminants in the gas would cause the sensitivity to drop as the chamber was overfilled. The chamber was left for about an hour at the required pressure to allow surface absorption to approach equilibrium.

After the soaking period, the gas was pumped away and more was introduced to a pressure slightly greater than that required for maximum sensitivity. Checks were made of the gas gain characteristic and, if this was satisfactory, the chamber was sealed off and simultaneously removed from the filling system.

The filling of chambers with gases other than nitric oxide was similar, except that the gas was vaporised from a warm phial of the liquid form. Cold traps could not be used for gases whose boiling points were not far below room temperature. Most of the gases used for filling chambers are very difficult to completely remove from surfaces, so separate filling systems were used for each gas to eliminate the risk of contamination by gas residues.

2.6 Testing of Ion Chambers

During the development and production phases of ion chamber manufacture, many tests and checks were made to ensure that they were optimised for performance in the conditions under which they would be operated. In addition to measurements of the performance of the chambers as radiation detectors, tests were made of their electrical characteristics and of their response to the heating, vibration and electrical interference which are found in the rocket environment.

2.6.1 Electrical properties

The construction had to be such as to allow the collection of minute signal currents (down to $\simeq 10^{-13}$ Amps) in very close proximity to the cathode and its connections which were at potentials up to

many hundreds of volts; this had to be done at ambient pressures where corona discharges readily occur. The anode feed-throughs used on the copper chambers all had guard rings in their structures, and the glass chambers had a platinum guard ring surrounding the anode on both the inside and the outside surfaces of the glass.

It was observed that an e.m.f. could be generated between the anode and guard ring if there was even a minute trace of acid flux absorbed into the glass surface. E.m.f.'s of up to one volt with a source impedance usually near 10^{11} ohms were observed. Even a much smaller e.m.f. would have been capable of introducing serious offsets into the low impedance amplifiers and care was taken to ensure cleanliness in the vicinity of the anode especially.

Measurements of leakage currents at 50 volts and 500 volts, and checks for e.m.f.'s were made at all stages of construction, filling and potting of the chambers. The measurements were made with Keithley Model 610 C electrometers. Typical leakage currents were 3×10^{-14} amps at 20^0C, and 6×10^{-14} amps at 50^0C.

The signal feed-throughs and connections were vacuum potted in silicon rubber to prevent leakage due to later contamination of the surfaces, or due to water vapour condensation during rocket ascent.

In most of the experiments, it was necessary to adjust the amplifiers to obtain the best high frequency response from the detectors. It was not possible to inject a test signal into the

amplifiers for this purpose by any form of electrical contact. The capacitive load on the input was critical, so the signal modulation had to be introduced optically by a modulated ultraviolet source. A circuit was constructed which could drive a discharge lamp to produce a square wave modulated output of variable frequency and modulation depth. The rise and fall times of the light output were less than 100μsec, which was more than adequate for this application. No overshoot in light output was observed, and when shielded the modulated lamp introduced a controlled precise signal with no capacitive coupling into the detector circuit.

2.6.2 Gain characteristics

The absolute calibration of the chambers was done with a vacuum monochromator, but quick checks were made of the continued operation of each chamber by measuring its response, at unity gain and at gas gain, to a hydrogen discharge lamp. The shape of the gain curve is a much more sensitive monitor of the effective gas pressure than is the unity gain response (Figure 2.5). The latter depends on the condition of the lamp and chamber windows (normally cleaned with acetone before testing), the lamp voltage and aging, the atmospheric humidity and the closeness of contact between the lamp and chamber window. The gain curve, being a measurement of ratios, is unaffected by the above factors if they are kept constant during the period of each test.

2.6.3 Water vapour absorption

The most troublesome contaminant in the chamber gases was water vapour. The effect of water vapour was most critical in the nitric oxide chambers intended for measurements of Lymanα. Water vapour has a series of absorption bands which spans the wavelength range of these chambers. One of these bands includes the wavelength of Lymanα (Watanabe and Zelikoff, 1953). Water penetrates the surfaces of glass and metals, and is very difficult to remove completely. Out-gassing from the chamber walls is accelerated by heating, so efforts were made to ensure that a negligible amount of vapour would be added to the nitric oxide during storage and during flight.

Absorption of Lymanα photons by water vapour produces no ionization, so an increase in the $[H_2O]:[NO]$ ratio reduces the quantum efficiency in the water absorption bands. The presence of water vapour is easily identified from the spectral response curve of a chamber around the absorption bands. Figure 2.12 shows the effect of a large amount of water vapour on the spectral response of a glass chamber near Lymanα. A measurement of the ratio of efficiencies at 121.5 nm and 123 nm was used as a quick check of the amount of water vapour absorption. The measurements required the use of a vacuum monochromator, but being a ratio, did not require an absolute flux calibration to be done simultaneously.

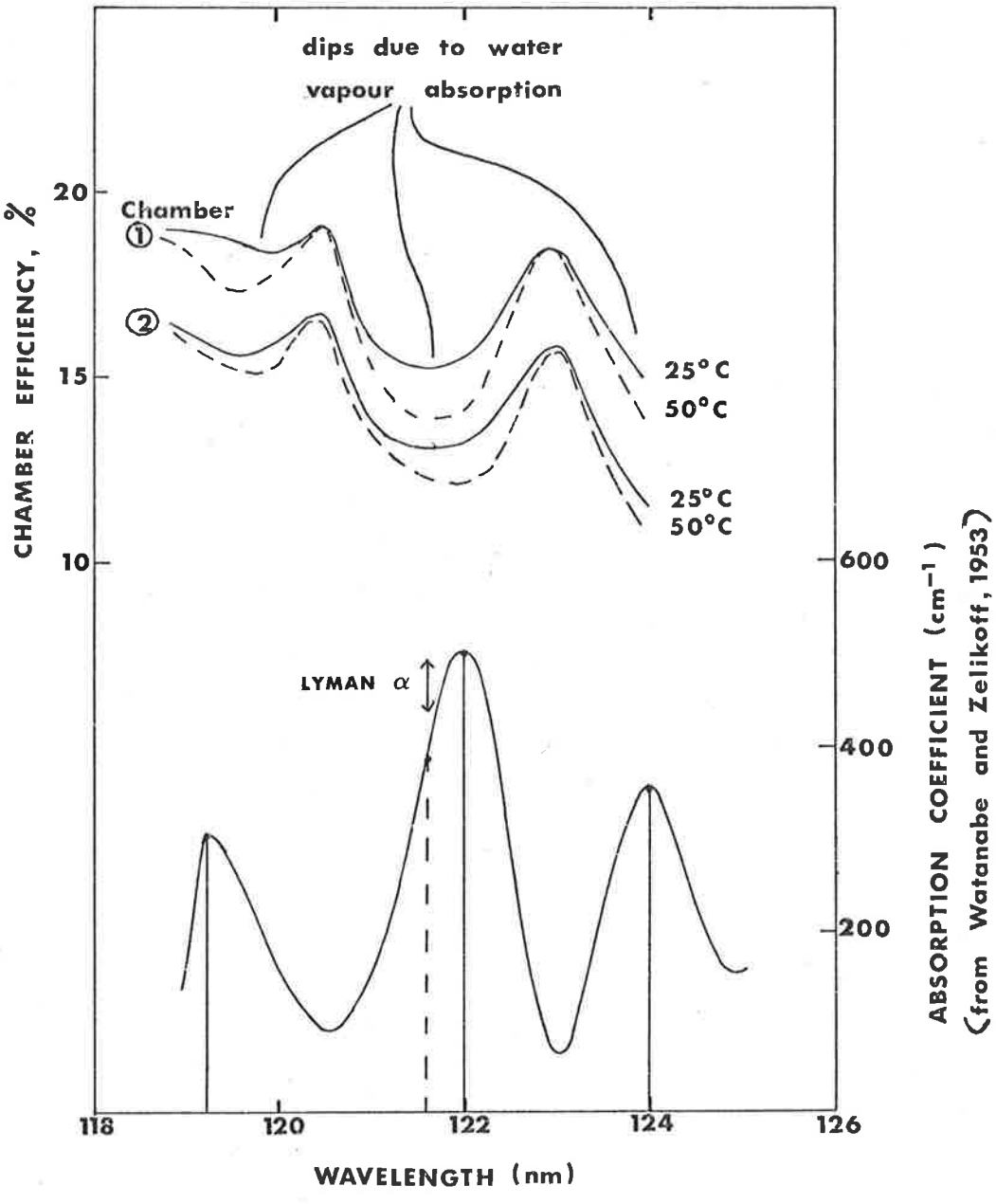

FIGURE 2.12 EFFECTS OF WATER VAPOUR ON SPECTRAL RESPONSE NEAR Ly α

2.6.4 Temperature

An investigation of the effects of temperature variations on ion chambers was reported by Carver and Mitchell (1967). Increases in temprature produced shifts in the cutoff at each end of the spectral response of the chamber, but in chambers with a broad central response region (e.g. Lithium Fluoride-Nitric Oxide) no change was reported in the central region efficiency. This result was verified, with the proviso that the chamber must be free of water vapour for temperature independence in the water absorption bands.

The gas gain of nitric oxide chambers was found to depend to a small degree on temperature. The curves of Figure 2.6, measured with a glass chamber and an undispersed lamp, show the effect to be partly reversible, and partly permanent, at least over a short recovery period. Nitric oxide is strongly absorbed onto the glass surfaces during flushing and filling, and heating causes some of this to out-gas, increasing the pressure and shifting the gain curve to higher voltages. Some of this may be slowly reabsorbed into the chamber walls.

2.6.5 Photoelectric response to longer wavelength radiation

The chambers had to be able to operate in large fluxes of middle ultraviolet (200 - 300 nm) radiation without producing a significant corresponding output. In the designs, attempts were made to minimise the photoemissive surfaces exposed to the incident radiation. In particular, in the glass chambers, the cathode surfaces were kept

well forward to avoid illuminiation and to make the field and the gas gain both low at the rear walls, where unabsorbed radiation would strike. The guard ring was also positioned to absorb a minimum of radiation.

The tests of middle ultraviolet response were made using Xenon and Mercury lamps illuminating a monochromator with 9 nm resolution. The spectral energy flux in the beam was measured with a Reeder quartz window thermopile. The response of the chambers, at gas gain, to this beam was measured with a Keithley electrometer. Near 250 nm, where the maximum photoelectric response to a solar type of spectrum would occur, the sensitivity was of the order of 10^{-12} amps per microwatt for a glass chamber. This was low enough to ensure that response to solar and lunar fluxes above 150 nm would be negligible. Some other types were not quite as good at rejection of middle ultraviolet.

2.6.6. Vibration

Tests were done on some of the ion chambers to confirm their ability to withstand the vibration of a rocket launching. These tests were performed at the Weapons Research Establishment, Salisbury. The vibration was sinusoidal at 15 g (RMS) from 2KHz down to 150 Hz, and at constant amplitude from 150 Hz down to 10 Hz. No damage was sustained by chambers using commercial feed-through assemblies, or to glass chambers with the thickened anode feed-through region as in Figure 2.2.

A gas gain chamber was vibrated, together with an amplifier, while operating at gains up to 500. The amplifier had a gain of 10^{11} volts per amp. and a rise time of 1.5 milliseconds. As was expected in such a sensitive system, the vibration produced an output signal variation; the sensitivity varied up to nearly 1 volt per g at resonant frequencies. Most of the signal was found to be due to vibration of the coaxial signal lead between the chamber and the amplifier. This lead was provided with a more secure support in the rocket structure. When the flight vibration levels, after motor burnout, were taken into account, the vibration sensitivity was found to be low enough for good signal detection.

2.7 Ion Chamber Calibration

2.7.1 Measurement of quantum efficiency

Measurements of the quantum efficiency of the ion chambers as an absolute calibration were done using a half-meter monochromator (McPherson Model 235), with a discharge through a continuous flowing stream of hydrogen as the source. The lamp was pumped through the entrance slits of the monochromator. With a grating of 1200 lines per mm, the slits were normally set for 0.5 nm resolution. The exit beam intensity was monitored by a photomultiplier viewing a grid coated with sodium salicylate phosphor which was positioned in the beam behind the exit slit.

The sensitivity of each ion chamber was compared with that of a standard parallel-plate ion chamber which could be attached

immediately behind the monitoring grid mentioned above. The standard chamber was used to determine absolutely the photon flux passing the monitor grid. The sensitivity of the monitoring system, in terms of output current per photon passing the grid, was then known. The calibration was normally done using the Lymanα emission line from the lamp, and the monitor was used to calculate the emergent beam strength during measurements on flight ion chambers at Lymanα and at other wavelengths. The transfer to other wavelengths was made by assuming the fluorescent efficiency of sodium salicylate to be independent of the exciting wavelength. Over the range of wavelengths used, this has been shown to be true, within adequate limits, for a freshly applied coating (Samson, 1964).

The standard ion chamber (Figure 2.13a) was of the single parallel plate type, with a sodium salicylate - photomultiplier combination as the detector of transmitted radiation. Measurements were made of the ionization current and the transmitted light signal over a range of gas pressures. When these were plotted against one other, the extrapolation to the axis, corresponding to total absorption in the gas, gave the ion current due to complete absorption without recombination (Figure 2.13b). The calibrations were normally done at Lymanα, using nitric oxide in the standard chamber. By assuming an ionization efficiency of 81% (Watanabe et al., 1967), the photon flux entering the chamber was calculated, and a measurement of the window transmission gave the flux in the beam passing the monitor grid.

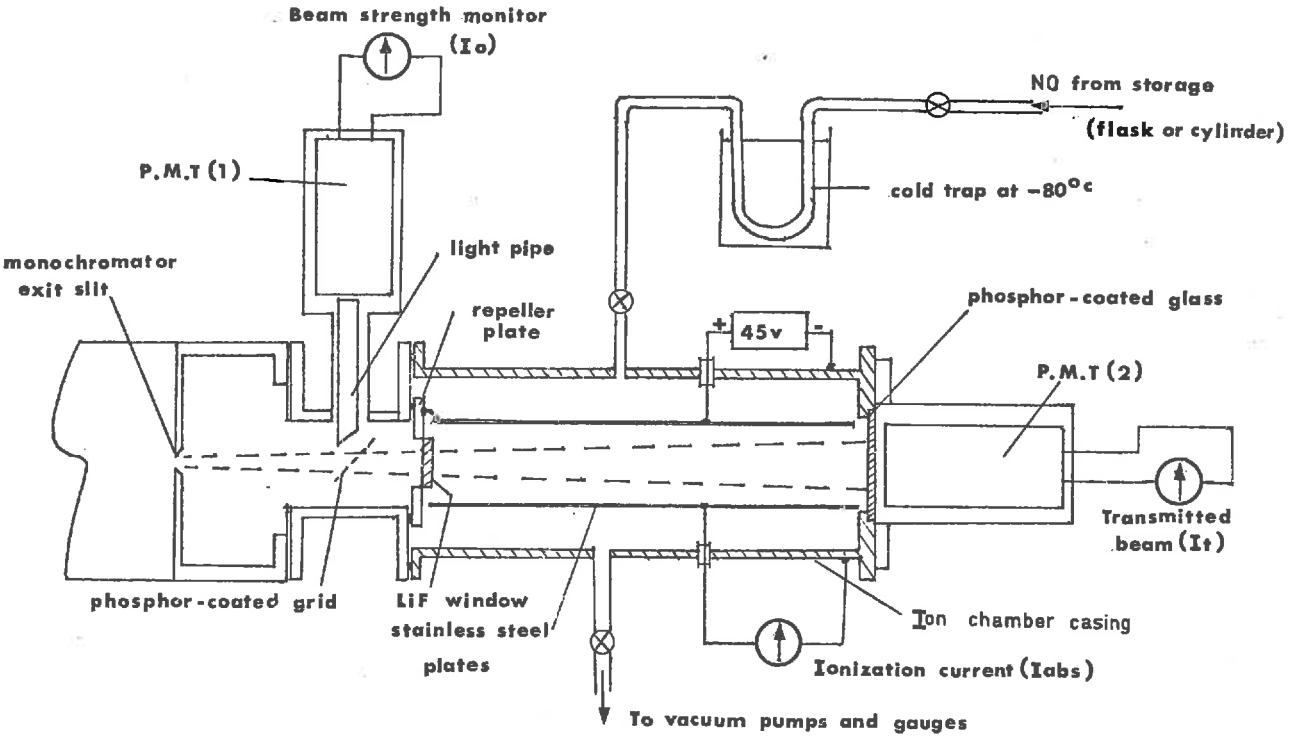

FIGURE 2·13a THE STANDARD ION CHAMBER CALIBRATION SYSTEM

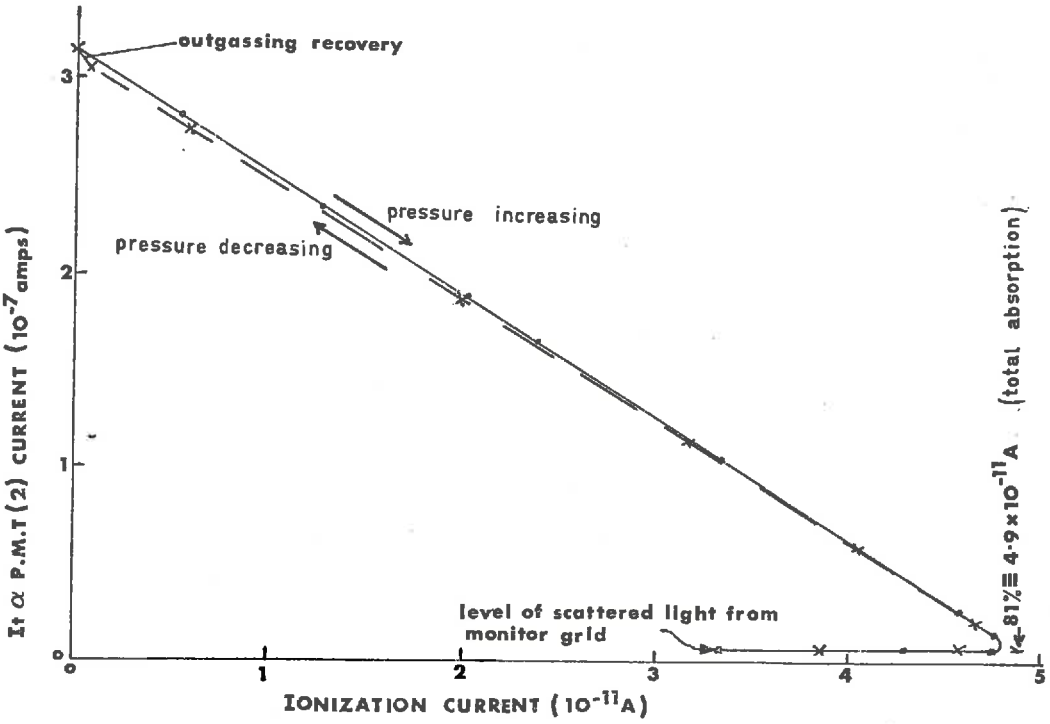

FIGURE 2·13b A CALIBRATION CURVE FOR THE STANDARD ION CHAMBER

The quantum efficiency of other chambers could then be determined by their response to the beam, with correction being made for beam strength variation as indicated by the monitor detector. The quantum efficiency measured in this way is the ratio of the number of electronic charges collected at the signal electrode, to the number of photons incident on the window. For calibration of those chambers insensitive to Lymanα, the monochromator beam strength at other wavelengths was related to that at Lymanα by reference to the monitor signal.

2.7.2 Spectral response measurements

The wavelength response of the chambers over their nominal range of sensitivity was measured, and when related to the absolute calibration, this gave the quantum efficiency for radiation at all wavelengths of interest. For most of the experimental applications, the efficiency was required to be known only at the wavelengths of certain atmospheric emission lines. However, complete spectral response curve were measured to indicate the purity of the gas. In particular, the presence of water vapour could readily be detected by its characteristic absorption spectrum (Figure 2.12).

Typical spectral response curves for the chambers used in this work are shown in Figure 2.14. These were measured on the unity gain type of chambers (2.3). The figure shows the chamber combination flown in the experiment reported in Chapter 5.

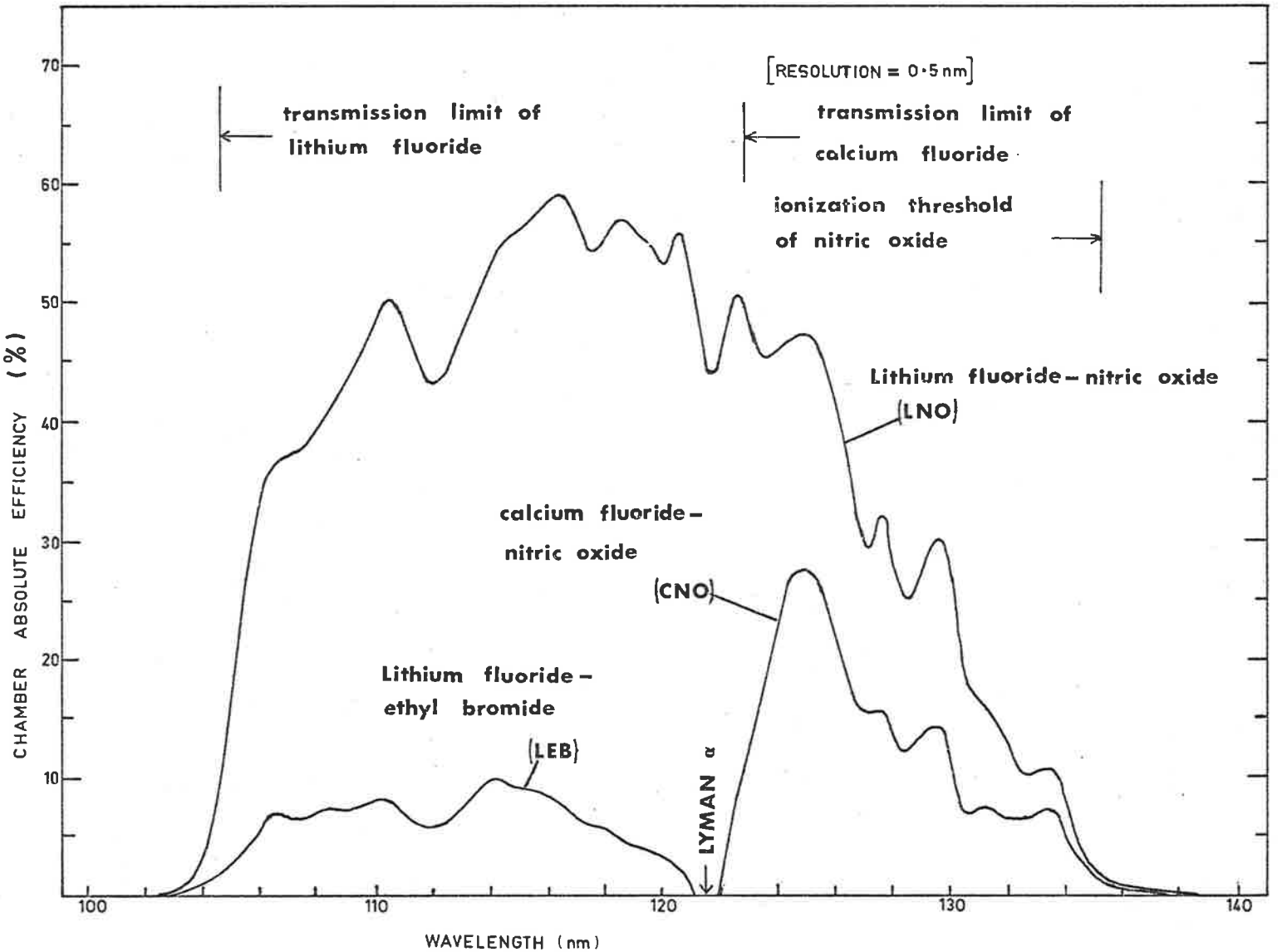

FIGURE 2.14 SPECTRAL RESPONSE OF THREE TYPES OF ION CHAMBERS

2.7.3 Angular response

In all of the payloads described later, the chambers were flown behind collimators or other optical elements which limited their fields of view. A knowledge was required of the uniformity of response at different angles of flux incidence within the fields. As quantum efficiencies were always measured at normal incidence to the chamber windows, correction had to be made for the reduced response to off-axis illumination.

Angular response measurements were made by using a broad-band discharge lamp in an evacuated chamber attached to the vacuum monochromator. Plots were made of the spatial profile of the monochromator beam to ensure that the cross-section was large enough to uniformly illuminate the chamber entrance apertures. Beam profiles taken at distance of 20 cm and 3 m from the exit slit are shown in Figure 2.15. The plots were made at Lymanα, using hydrogen in the lamp, with 0.5 nm resolution.

The divergence of the beam illuminating a half-inch diameter aperture at 30 cm from the slits was 2.5^0, and this limited the resolution obtainable. It was not necessary to seek higher resolution although some checks were made at a distance of 3 m (beam divergence = 0.25). The objective of the angular response tests was to determine the required correction functions for off-axis illumination at both unity and gas gain. Figure 2.16 shows measurements made on a gas gain chamber (2.4.3) at gains of 1 and 100. The two sets of curves

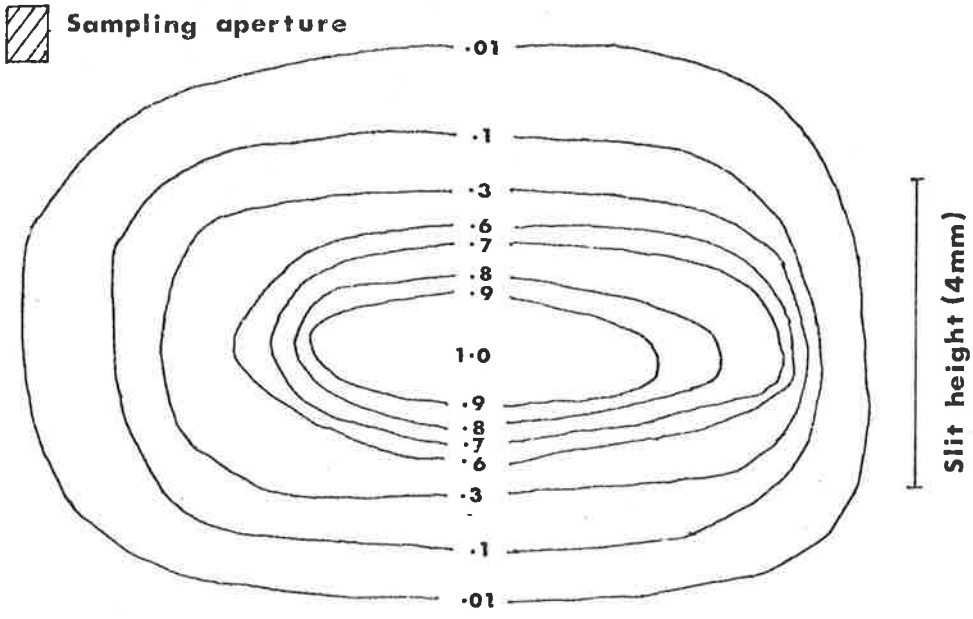

(a) 20 cm from slit

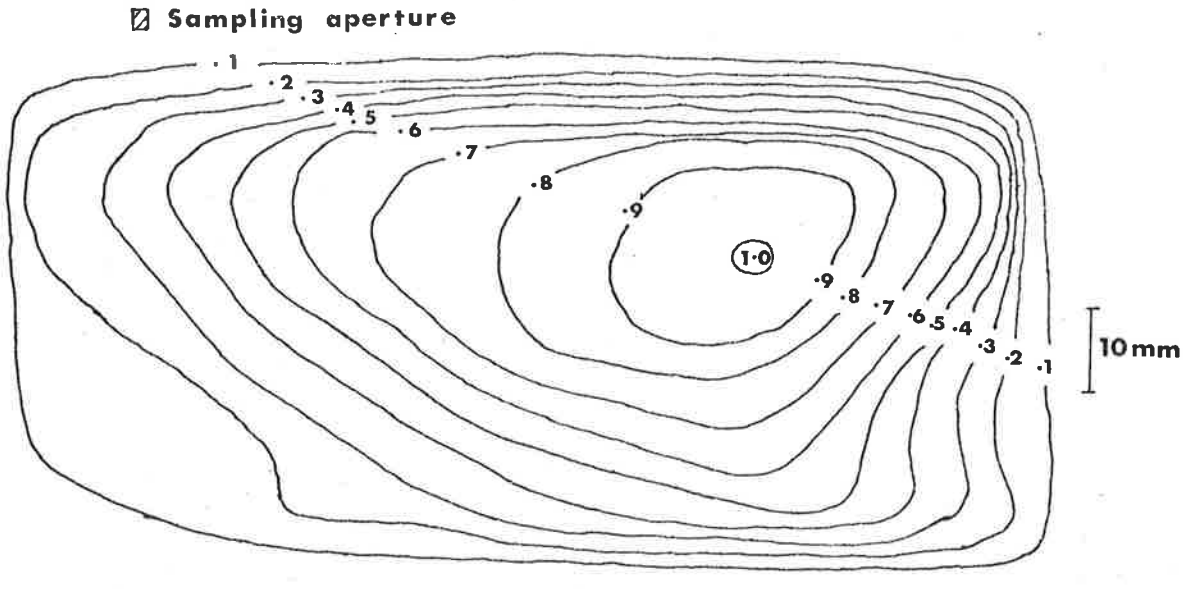

(b) 3m from slit

FIGURE 2·15 MONOCHROMATOR BEAM PATTERNS

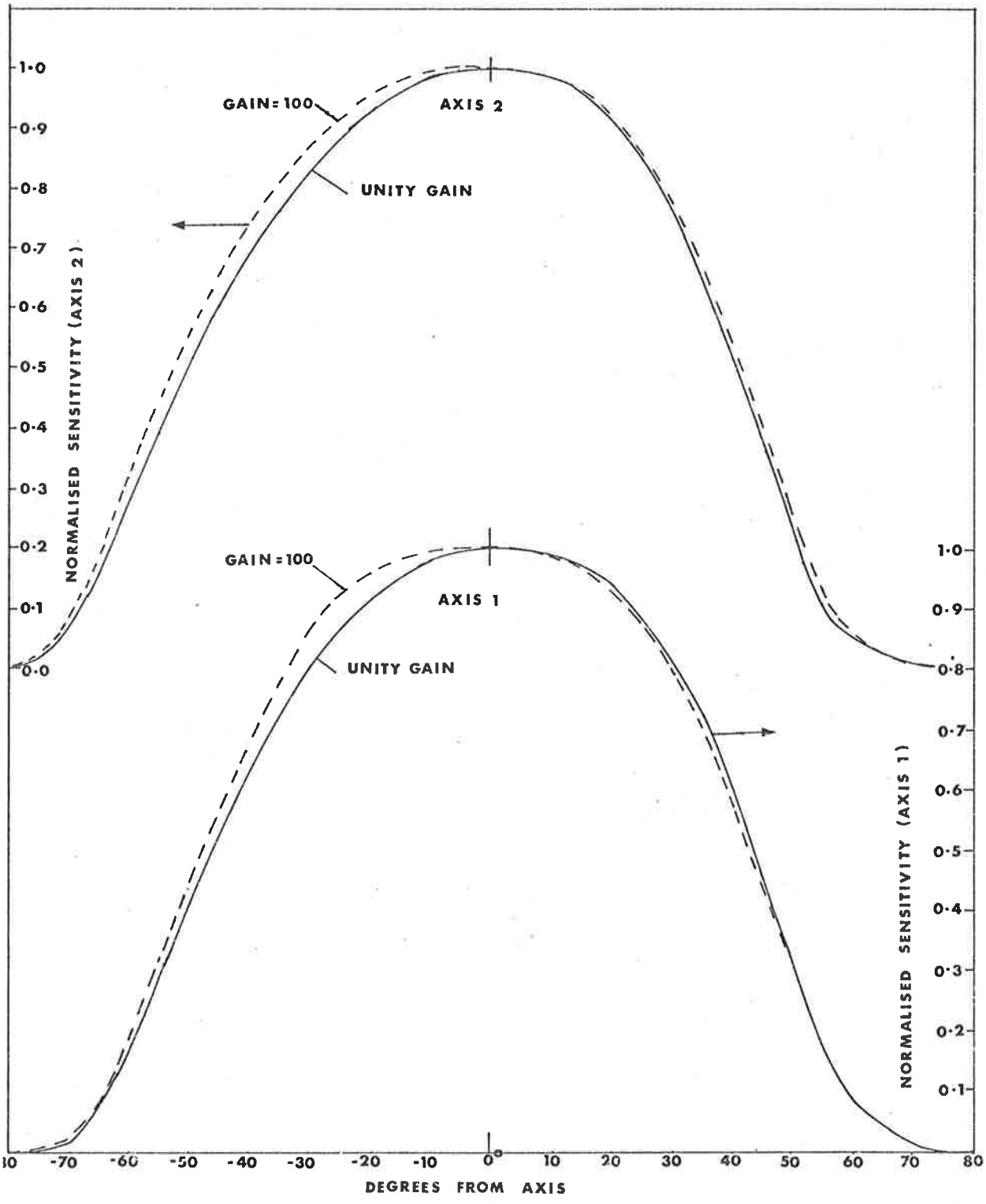

FIGURE 2·16 ANGULAR RESPONSE CURVE OF GLASS CHAMBER (2 AXES)

are almost identical. The deviations represent only a small difference in the total response integrated over the field of view used in the flight instruments.

2.8 Summary

Several types of ionization chambers have been constructed for use in rockets as detectors. They have important advantages of mechanical simplicity, compactness and ruggedness, together with high efficiency and low power requirements. Although ion chambers had been used before in rocket experiments, the chambers described have improved characteristics, particularly for small-volume multiple applications.

The rocket experimental payloads for which these chambers were designed are described in the following Chapters.

CHAPTER 3 ULTRAVIOLET AURORA

3.1 Introduction

Scientific observations of auroral displays have now been conducted for two centuries. Until comparatively recently, however, all of the observations and measurements had been made from the ground and were related to the characteristics of the visible radiation emitted from active regions.

Extensive catalogues have been compiled of those auroral emissions which have been spectrally classifed (Chamberlain, 1961a), but early observations were limited by atmospheric absorption to visible and near-visible wavelengths. The two emissions which normally dominate the visible spectrum are from molecular nitrogen (391.4 nm) and atomic oxygen (557.7 nm). These usually have approximately the same brightness (O'Brien and Taylor, 1964).

The unit which is most frequently used for measurement of auroral activity, namely the Rayleigh (R), came into use largely because of its applicability to ground based observations. One Rayleigh corresponds to an apparent emission rate of 10^6 photons per second from a 1 cm^2 column along the line of sight (or 10^{10} ph s^{-1} m^{-2} column). For isotropic emission in a medium with no absorption, the apparent surface brightness of an extended source is $\frac{10^6}{4\pi}$R ph cm^{-2} s^{-1} sr^{-1} for a column emission value of R rayleighs.

The many observations of visible emissions from the ground led to the concept of the 'auroral oval' as a zone (in each hemisphere) near 68^0 magnetic latitude, in which is found the greatest long-term average

of the frequency of auroras (Davis, 1967). The location of individual displays is influenced by the level of geomagnetic activity and the aurora tends to appear nearer the poles with greater geomagnetic activity (Bond and Jacka, 1963; Davis, 1963) and to extend over a broader latitude range.

Systematic studies of the altitude distribution of auroral emissions were initiated by Störmer (1965). The lower border is generally well defined, and near 110 km for weak activity, and as low as 95 km for intense forms. The upper border is less well defined, and varies from 120 km for N_2^+ (391.4 nm) (Miller et al., 1968) to several hundred kilometers for the 630 nm radiation which arises in transitions from the metastable ^2D state of atomic oxygen (Figure 1.2).

Because auroral processes occur near or above 100 km, with only a small fraction of the input energy becoming observable from the ground, most major developments in understanding the mechanisms involved have been made since the advent of rockets and satellites enabled measurements to be made within and above the emitting region. In particular, the vacuum ultraviolet emissions which were the main area of interest in this work are detectable only from altitudes above 70 km, and the history of their study is comparatively short.

3.2 Excitation Sources

The first positive indications of the mechanism of auroral excitation in emitting regions was obtained by Vegard (1939), followed by Meinel (1950), and Gartlein (1950). Their observations of Doppler-shifted

emissions from atomic hydrogen in the direction of the magnetic field indicated the existence of a precipitating flux of energetic protons. A lack of correlation between active visible auroras and the occurence of hydrogen emissions suggested the existence of another energy source, which was first identified positively by McIlwain (1960) as an energetic electron flux.

Measurements of much wider scope and greater detail have since been made by rocket and satellite borne experiments, one of the first examples of which was described by O'Brien et al., (1964). The majority of bright auroral emissions appear to be excited by electron impact, while proton auroras are less frequent and have an apparently independent distribution pattern (Eather and Sandford,1966).

Extremely monochromatic fluxes of electrons with energies of several keV have been observed on some occasions (McIlwain, 1960; Albert, 1967; Evans, 1968), in addition to a background flux with a more normal spectrum extending out to several tens of keV. Electrostatic fields were first suggested as the source of the energy of the electrons, (Evans, 1968) but more recent data obtained from satelllite instruments appears to be consistent with a Fermi acceleration process arising from field contraction in the neutral sheet region of the Earth's magnetospheric tail (Sharber and Heikkila, 1972). Electrons have in fact been observed out to large distances in the plasma sheet with energy distributions similar to those observed over precipitation regions (Bame et al., 1967; Akasofu et al., 1971; Hones et al., 1971).

Observable emissions account for only a small fraction of the energy input to auroral regions and the greater part of the energy must be transported away as both short and long wavelength radiation (Anderson, 1960; Vallance-Jones, 1971), as ionized and excited species (Hultqvist, 1965) or as kinetic energy. An extensive review of the distribution and dissipation of magnetospheric energy, for which auroral emission is but one sink, has been given by Cole (1966). The complexity of the energy dissipation paths, and the interdependence of alternative processes, means that a full understanding of the mechanisms must be based on measurements of an extensive range of atmospheric and magnetospheric parameters. In the part of this work concerned with auroral processes, the interest was concentrated on the vacuum ultraviolet emissions between 100 and 150 nm and their relationship to visible and particle excitation.

3.3 Predictions of Ultraviolet Aurora

By 1960, ground based spectroscopy had enabled an extensive array of auroral line and band systems in the visible, near infrared and near ultraviolet to be classified and measured in intensity. Chamberlain (1961a, b), after compiling a comprehensive listing of the features known at that time, made estimates of the intensities of those auroral emissions which were expected to be found in inaccessible parts of the spectrum but which had not at that time been observed. Working from known transition probabilities and observed visible and infrared line intensities, Chamberlain estimated that the total of ultraviolet

emissions from atomic oxygen and nitrogen would be approximately half of that in the green (557.7 nm) oxygen line, while the emission in the Vegard-Kaplan bands of molecular nitrogen would be twice the intensity of 557.7 nm. The estimates were based on the average characteristics of bright auroras of strength IBC III. (An aurora is classified as International Brightness Coefficient I, II, III or IV, for 1, 10, 100 and 1000 kR respectively of O_I (557.7 nm) radiation, measured in the zenith direction.) Chamberlain pointed out that even with generous estimates of ultraviolet intensities, the total radiation from the vacuum ultraviolet through to the infrared would still represent only a small fraction of the primary energy thought to be necessary for production of the observed amounts of 391.4 nm radiation from N_2^+. He suggested that the unaccounted energy might appear in other ultraviolet emissions which he had not included in his calculations.

At about the same time, Swings, Bosman-Crespin and Arpigny (1961), following a similar line of reasoning, produced an extensive list of ultraviolet emissions which they predicted might be found in auroras. They referred their estimates to the intensity of N_2^+ (391.4 nm) radiation, and suggested that the most prominent emissions between 100 and 200 nm wavelength would be at 102.6 nm and 130.4 nm (both from OI and both more intense than N_2^+ (391.4 nm)) and at 121.6 nm (from HI, at one third of the intensity at 391.4 nm). Their total background of minor components in the vacuum ultraviolet region was three times the intensity at 391.4 nm, and approximately one third of this lay

between 105 and 145 nm.

Green and Barth (1965) adopted a different approach, based on measured cross-sections for excitation and ionization of molecular nitrogen by electron impact. They considered the combined effect of primary, seconday and tertiary electrons in their contributions to each excited state. In their analysis they examined the energy degradation of 30 keV primary electrons. More recent measurements of electron spectra (Evans, 1968) have indicated that the majority of primary electrons responsible for an IBC III aurora would have energies much lower than 30 keV. However, because secondary collisions produce most of the excited molecules, the distribution between excited states is very much the same for primary electrons in the 6 - 10 keV range as for 30 keV electrons, and the predictions of emission intensities should be equally valid for excitation by less energetic electrons. Of the systems which are represented in the 100 to 150 nm range, Green and Barth predicted several thousand kilorayleighs in both the Lyman-Birge-Hopfield and the Birge-Hopfield systems of N_2 in an IBC III aurora. Such an intensity would have been an order of magnitude greater than the visible contributions.

In a later more detailed study, Stolarski and Green (1967) considered a composite atmosphere of N_2, O and O_2, and a range of primary energy from 30 keV down to 0.1 keV. Their predictions for the two ultraviolet systems mentioned above were lower by a factor of three, and some significant contributions from atomic oxygen were predicted. The major

atomic oxygen emissions in the range covered by the present work were expected to be at 130.4 nm (182 kR), 115.2 nm (106 kR) and 135.6 nm (92 kR) in an IBC III aurora excited by 10 keV electrons.

Model calculations such as those just mentioned had in general predicted very large amounts of radiation in the vacuum ultraviolet aurora, indicating the importance of measurements in the region to a complete understanding of the energy dissipation processes.

3.4 Previous Observations of Ultraviolet Aurora

The earliest reported detection of far ultraviolet radiation attributed to auroral activity was by Chubb et al., (1961), and since that time a number of observations have been made.

Fastie, Crosswhite and Markham (1961) made the first measurements with a scanning spectrophotometer in an IBC II aurora, and found several features which were considered to be the L-B-H system of molecular nitrogen (also Crosswhite et al., 1962). On a later flight improved data was obtained in the 141 to 221 nm range, where the L-B-H system of N_2 was positively identified (Isler and Fastie, 1965). Observed intensities in the vacuum ultraviolet region had been shown by these workers to be much lower than predicted theoretically.

Murcray (1966) on the other hand, had reported very large intensities between 105 and 135 nm wavelength. He used ionization chambers similar to some of those used in this work, but having a very wide field of view, so that he was unable to localize the source region. Murcray reported ultraviolet intensities as high as twenty times the intensity

at 557.7 nm and suggested that the emissions were mainly from atomic oxygen (130.4 nm) and molecular nitrogen (L-B-H, B-H and W-K systems). He also found some evidence that the ultraviolet and visible emitting regions were not coincident, but because of limitations in the instrument resolution, could not form any definite conclusions concerning the spatial distribution.

Miller et al., (1968) reported scanning spectrometer measurements covering the range 105 to 155 nm which showed the 130.4 nm atomic oxygen emission to be stronger than the simultaneous 391.4 nm intensity. From those bands of the N_2 (L-B-H) systems which were observed, the total system intensity was estimated to be only slightly less than the intensity at 391.4 nm.

3.5 The Objectives of these Auroral Measurements

The diverse results mentioned in the previous section show that, although at the commencement of this work some of the main features of the vacuum ultraviolet airglow had been identified, the intensities measured on different occasions had appeared to show such a great diversity that more comprehensive measurements were needed.

Some of the apparent disparity between reported ultraviolet intensities was probably due to the effects of using instruments with different fields of view to make measurements in the complex auroral forms, so that viewing conditions were not strictly comparable. There have since been more recent reports of other measurements which were made concurrently with this work, and they will be referred to in

the discussion of the results in Chapter 5.

The instruments described in the next Chapter were designed to measure the total intensities within a number of vacuum ultraviolet and visible wavelength ranges. The ultraviolet and visible radiation photometers were aligned with their axes parallel, and initially had the same acceptance angle, so that all of the detectors viewed the same region of space, allowing direct comparisons to be made between visible and ultraviolet emissions. During the course of the work, however, the fields of view of the ultraviolet detectors were enlarged to lower the threshold of detectable intensity. After this modification had been made, the visible photometers viewed the centre of the fields of the ultraviolet detectors.

Ionization chambers of the type described in Chapter 2 were used to detect the ultraviolet radiation because of their relatively high sensitivity, reliability, compactness and simplicity; all of which attributes were important in this particular application. Although each individual detector was relatively broad-band, suitable combinations of types of ion chambers (Table 4.1) were chosen to discriminate between those emissions which measurements such as those of Miller et al., (1968) had shown to be dominant in the spectral range that was covered.

Particular emphasis was placed on the separation of Hydrogen Lymanα radiation at 121.6 nm. This was known to be the dominant component in the non-auroral night sky vacuum ultraviolet spectrum where it is produced by geocoronal scattering (Chapters 6, 7, 8). Geocoronal airglow

must be taken into account in all measurements of far ultraviolet airglow, particularly at low levels of activity.

Lymanα radiation has a special significance in auroral measurements because of its predicted association with proton excited aurora. Discrimination between electron and proton auroras is normally made on the basis of measurements of visible hydrogen emissions. However, during daytime or even under bright moonlight such measurements are difficult or impossible. Lymanα measurements can provide a means of monitoring proton precipitation events and, in conjunction with other measurements of auroral parameters, could help to develop a better understanding of the proton aurora.

The design and specifications of the photometric instrumentation developed for these studies, and its relationship to other experiments flown in the same program, are described in the following Chapter, while Chapter 5 gives details of the results which have been obtained.

CHAPTER 4 THE AURORAL ULTRAVIOLET EXPERIMENT

4.1 The Modular Auroral Probe

4.1.1 Introduction

Auroral parameters are, in general, widely variable in time and space, and conditions are neither precisely predictable nor repeatable. The task of properly relating measurements made at different times or places is therefore difficult. With this in mind, the Modular Auroral Probe (MAP) programme was conceived and instigated in the Southwest Centre for Advanced Studies, Dallas, Texas (now incorporated as University of Texas at Dallas), under the leadership of Prof. W.J. Heikkila.

A rocket payload format was devised to provide a flexible means of combining a number of experimental packages from different laboratories, in order to make co-ordinated measurements of a wide range of parameters in auroral regions. Consideration was given in the design to rapid and easy checkout facilites so that, if required, payloads could be reflown soon after recovery. Successful recovery of the payloads was expected to enable a large number of flights to be made into a variety of auroral conditions.

Formation of the payload from separate packages of standard form allowed individual experiments to be easily removed and operated separately for testing, calibration and servicing. Modular construction and mounting of the packages enable different combinations of experiments to be grouped into payloads best suited to the requirements of the individual flights.

A basic set of experiments forming a payload comprised:-

Energetic Particle Detectors	Frequency Shift Capacitance Probe
Soft Electron Spectrometer	Langmuir Probe
Photometers	Pulse Receiver

This combination of instruments provided measurements over a wide range of proton, electron and alpha particle fluxes, and of the consequent radiation and ionization. The photometric measurements of auroral ultraviolet and visible radiation are the subject of this and the next Chapter. All of the measurements reported here were made by on-board photometers. Comparisons with ground based photometer data provided by range support facilities are mentioned in the appropriate parts of the discussion of the results.

A standard payload configuration is shown in Figure 4.1. The experimental packages and service units (power supplies, telemetry, interface logic and timing and control) were built into a vertical stack supported by a rack structure. This combination was inserted into the tubular skin section to which was attached the parachute recovery package and the nose cone. The payload was designed to be flown on the Nike-Apache two stage vehicle to about 140 km altitude.

4.1.2 Photometric measurements

Theoretical predictions and previously reported measurements of large fluxes of ultraviolet radiation in auroral forms had

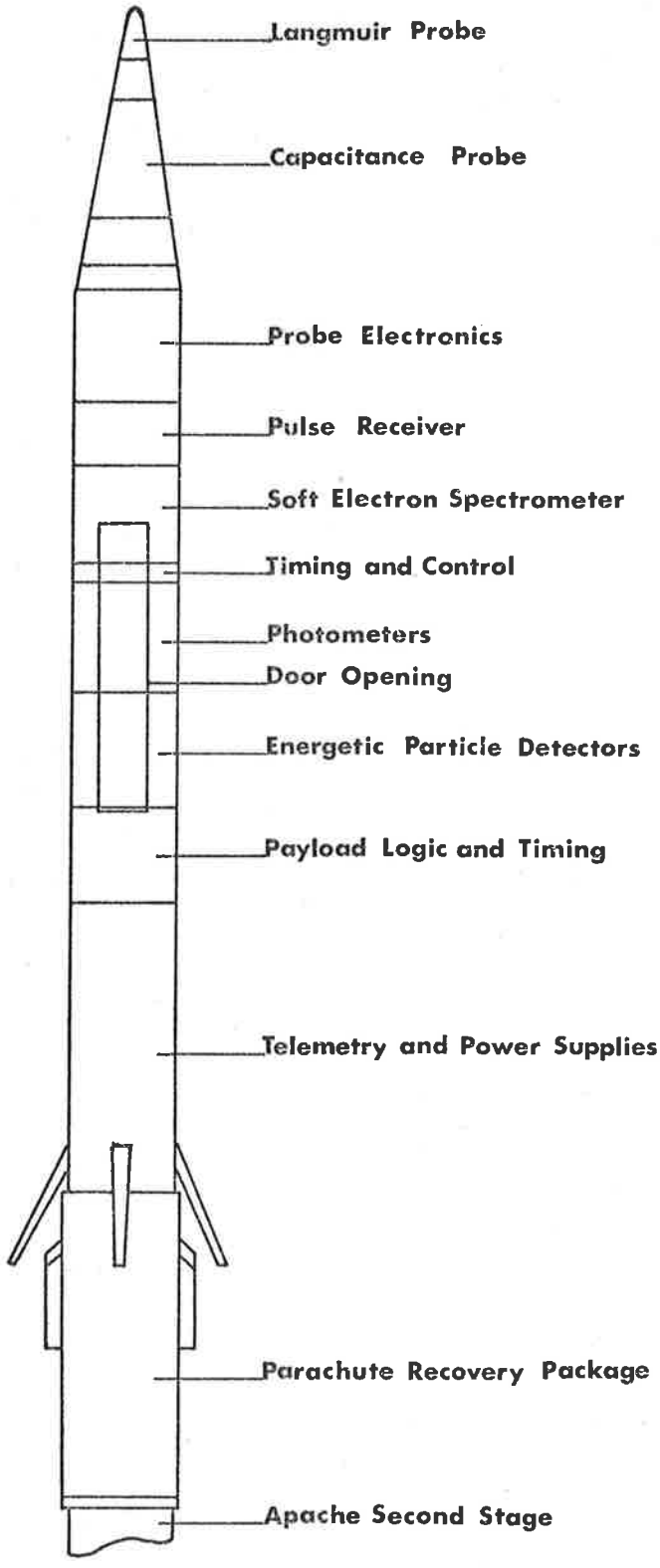

FIGURE 4.1 TYPICAL MAP PAYLOAD CONFIGURATION

indicated the importance of this spectral region in the energy-flow scheme. Accordingly, it was decided that the intensities of ultraviolet emissions, and their relationship to other parameters being measured, should be one of the aspects of auroral activity to be observed. Spatial distributions of the emissions, altitude profiles of the intensities, and spectral distribution of the radiation would be studied.

It was not feasible to construct a spectral scanning photometer to fit within the package, so wavelength discrimination in the ultraviolet region was obtained by the use of groups of ionization chambers with response bands selected to isolate the expected important emissions. The coarse spectral discrimination was then combined with altitude profile information to identify the components of the spectrum, and to determine the contributions from airglow emissions.

Visible radiation intensities were also measured for comparison with the ultraviolet observations, and as a means of relating the conditions during the flight to measurements made at other times. Ground based observations of the visible aurora can be misleading, particularly when the display has distinct localized emitting regions. Under these conditions, measurements of the intensity at the position of the rocket are most valuable.

The spatial and time resolution of the photometers was made

as high as the telemetry system would accept, to give maximum resolution of emission regions and to enable correlations between emission features and incoming particle fluxes to be detected. At the nominal spin rate of 5 rps, and with a telemetry sampling rate of 125 sps, each photometer in effect formed a series of integrals of intensity around approximately 15^0 of the detector scan circle.

4.2 The MAP Photometer Experiment

Five photometers with associated control and data handling systems formed the basis of the photometer package. Three ionization chambers covered bands in the vacuum ultraviolet region while filter-photomultiplier combinations monitored two visible emissions. Several combinations of ion chamber types were selected for different flight packages.

Figure 4.2 is a schematic of the photometer package systems. Provision was made for automatic calibration, both before and during flight, of all of the amplifiers and of the photomultipliers. The calibration cycle was triggered at 16 second intervals during flight by timing signals from the payload time base generator. No facility was provided for internal checks of ion chamber sensitivity because of the difficulty of providing a sufficiently stable small source.

The detector signals were amplified and accummulated in digital form for 8 millisecond periods before being transmitted through the pulse code-modulated telemetry modulator. Several aspects of the operation of the package were monitored via pulse amplitude modulated transmissions.

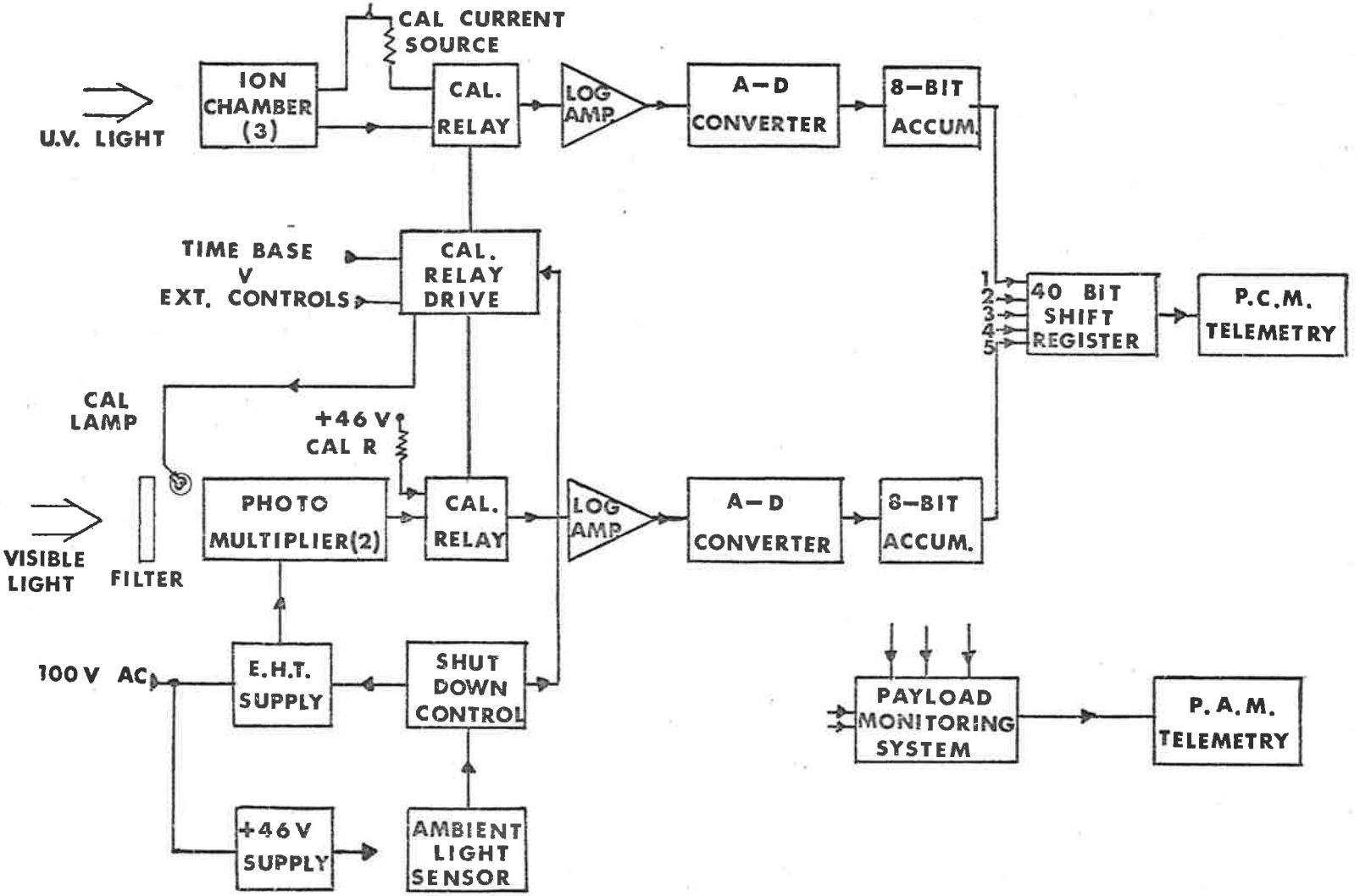

FIGURE 4.2 MAP PHOTOMETER PACKAGE SCHEMATIC

Figures 4.3 and 4.4 show the mechanical configuration of the package. All of the detectors were mounted with their viewing axes parallel, and at right angles to the rocket axis. They were protected during the launch phase by a cover which was released at 50 km. The logarithmic amplifiers, switching relays and detector power amplifiers were mounted alongside the detector block, while plug-in circuit cards held the signal processing and control electronics. Details of the design and function of the components of the photometer systems are given in the following Sections (4.2.1 to 4.2.5).

4.2.1 Visible radiation detectors

Photomultiplier-interference filter combinations were used to measure the intensities of the N_2^+ (391.4 nm) and O_I (557.7 nm) emissions within the fields of view defined by parallel tube collimators. In order to provide the positive output current required by the amplifiers, each photomultiplier network was supplied with both positive and negative voltages and the last dynode current was taken as the signal. In such a circuit, the dynode current is a factor of $\frac{G - 1}{G}$ times the anode current, where G is the gain of the last dynode stage. The factor is constant if the supplies are stable and the last stage voltage is high enough; both conditions were fulfilled by the circuit used.

Table 4.1 lists the specifications of the visible photometers and the calibrations applicable to the detectors on the flight

FIGURE 4.3 THE MAP PHOTOMETER PACKAGE

At bottom left can be seen the ion chamber collimators and the interference filters. The components of the system can be identified by reference to Figure 4.4. In the photograph, the digital electronics card has been removed.

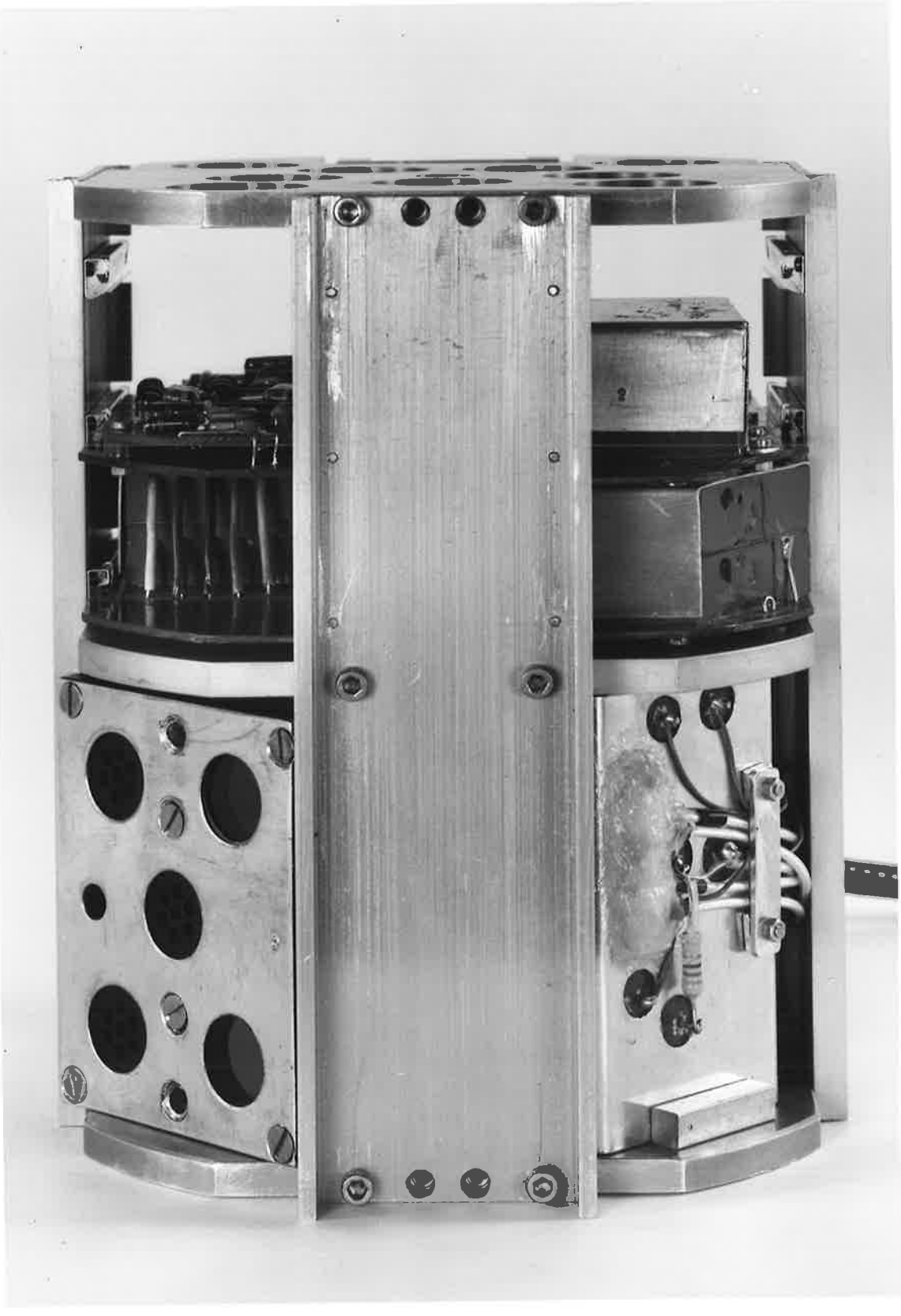

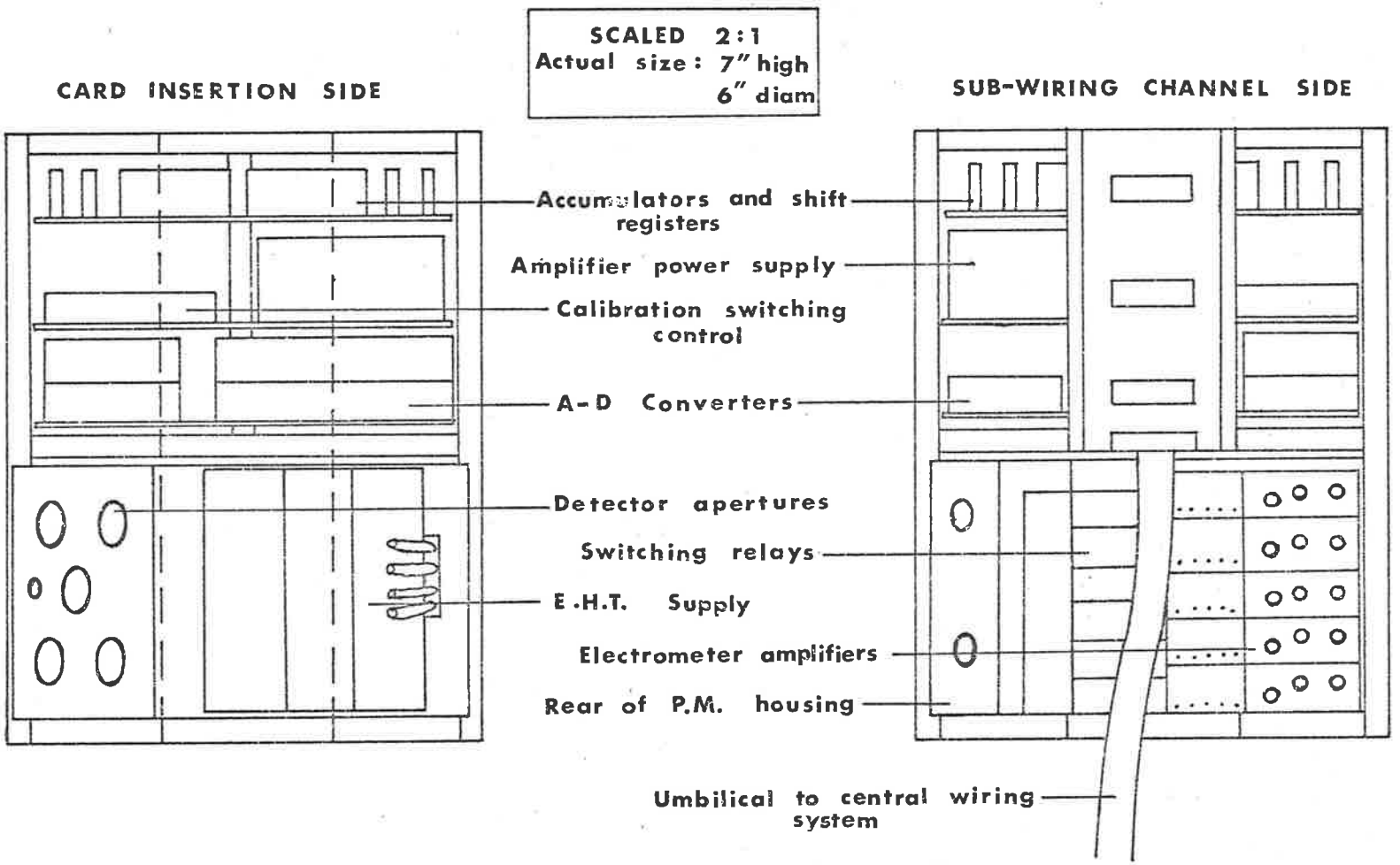

FIGURE 4.4 MAP PHOTOMETER MECHANICAL CONFIGURATION

number 14.443 which is referred to in the next Chapter.

TABLE 4.1 VISIBLE RADIATION DETECTOR SPECIFICATIONS

P.M. Tube Type	RCA 4460		
Cathode Type	S11		
Total Supply Voltage	1300 v		
Aperture Area	55 mm^2		
Angular Field of View (F.W.H.M.)	10^0		
Filters: Nominal Wavelength	391.4	557.7	nm
Passband Centre (actual)	392.0	557.4	nm
Passband Width (F.W.H.M.)	6.0	6.0	nm
Calibrated Sensitivity (50^0C) (Flight 14.443)	3.2×10^{-7} $\equiv 3.1 \times 10^8$	1.8×10^{-9} 5.5×10^8	Amps/kR kR/Amp

4.2.2 Ultraviolet detectors

Each payload carried three ionization chambers to measure intensities in selected ultraviolet wavelength bands. There was some overlap of their spectral response ranges, and signal differencing was used to separate emissions in overlapping and non-overlapping spectral regions. During the initial part of the program, the ion chambers were fitted with collimators identical to those on the photomultipliers. When the predicted signal levels were not received, the collimators were changed to increase both the collecting area and the angular field of view.

Although the sensitivities and response times of the u.v. detectors could have been improved by operating the chambers with internal gas gain, this idea was rejected because of the reduced measurement accuracy. The elapsed time between the last complete laboratory calibration of the chambers and the launch date was normally several months. Gas-gain characteristics of chambers are much more sensitive to deterioration in travel and storage than is the unity gain efficiency, so gas-gain operation would have introduced extra uncertainty in the sensitivities at the time of flight. All of the chambers were therefore operated at unity gain, even though the signal levels from some were near the limits of the amplifier capabilities.

Four different types of ion chambers were used in the MAP payloads, in groups of three selected from the types listed in Table 4.2.

TABLE 4.2 ION CHAMBERS USED IN MAP EXPERIMENTS

DESIGNATION	WINDOW	FILLING GAS	WAVELENGTH RANGE
LNO	LiF	NO	105 - 135 nm
CNO	CaF_2	NO	122 - 135 nm
LEB	LiF	Ethyl Bromide	105 - 120 nm
BAX	BaF_2	Xylene	135 - 147 nm

The first three types listed in the Table were fitted in the package which made the measurements described in the next Chapter. This group of chambers gave a good coverage of the region between 105 and 135 nm, but did not cover wavelengths longer than 135 nm (BAX range), where the L-B-H system of molecular nitrogen should be prominent.

The three chambers were chosen to separate hydrogen Lymanα radiation from emissions on either side of it in the spectrum. Previous dispersion measurements (Miller et al., 1968), had at times shown strong oxygen emission at 130.4 nm and, if present at the strength indicated, this emission would be the main contribution to the calcium fluoride-nitric oxide chamber signal. Dispersion instruments had shown only small intensities below 121 nm, but they may have been relatively intensitive in that region, thus failing to detect some short wavelength emissions. The lithium fluoride-ethyl bromide chamber was sensitive over the 105 - 120 nm range, and was intended to enable emissions in this region to be separated from those at Lymanα and longer wavelengths.

The specifications of the ultraviolet radiation detectors, with the figures appropriate to Flight 14.443, are summarised in Table 4.3. The spectral response curves of the three chambers from that payload are those shown in Figure 2.14.

4.2.3 Logarithmic amplifiers

Because of the wide range of intensities likely to be encountered in a series of auroral flights, each amplifier had to be capable of covering a range of four decades of detector signal currents. A logarithmic current to voltage conversion circuit was used to meet this requirement (Figure 4.5). The logarithmic function was derived from the positive-grid characteristics of the electrometer tube. The current ranges covered were nominally 10^{-12} to 10^{-8} A in the ion chmaber channels, and 10^{-9} to 10^{-5} A for the photomultipliers. Limiting circuits came into operation slightly short of the range ends to prevent multi-cycle operation of the digital accumulators (4.2.4).

Measurement and assessment of the effects of response time in nonlinear, current-driven amplifiers of the type used are complicated. The rise and fall times are different, and both of these depend upon the operating current levels and feedback neutralization. The flight amplifiers were adjusted to follow , up to 50 Hz repetition rate, a square wave test signal with a 2 : 1 current step at 2×10^{-11} A. Although the response time at signal levels below this was slower than that required to follow accurately the radiation fluctuations, this compromise between response time and stability was selected as the most appropriate for the operating conditions.

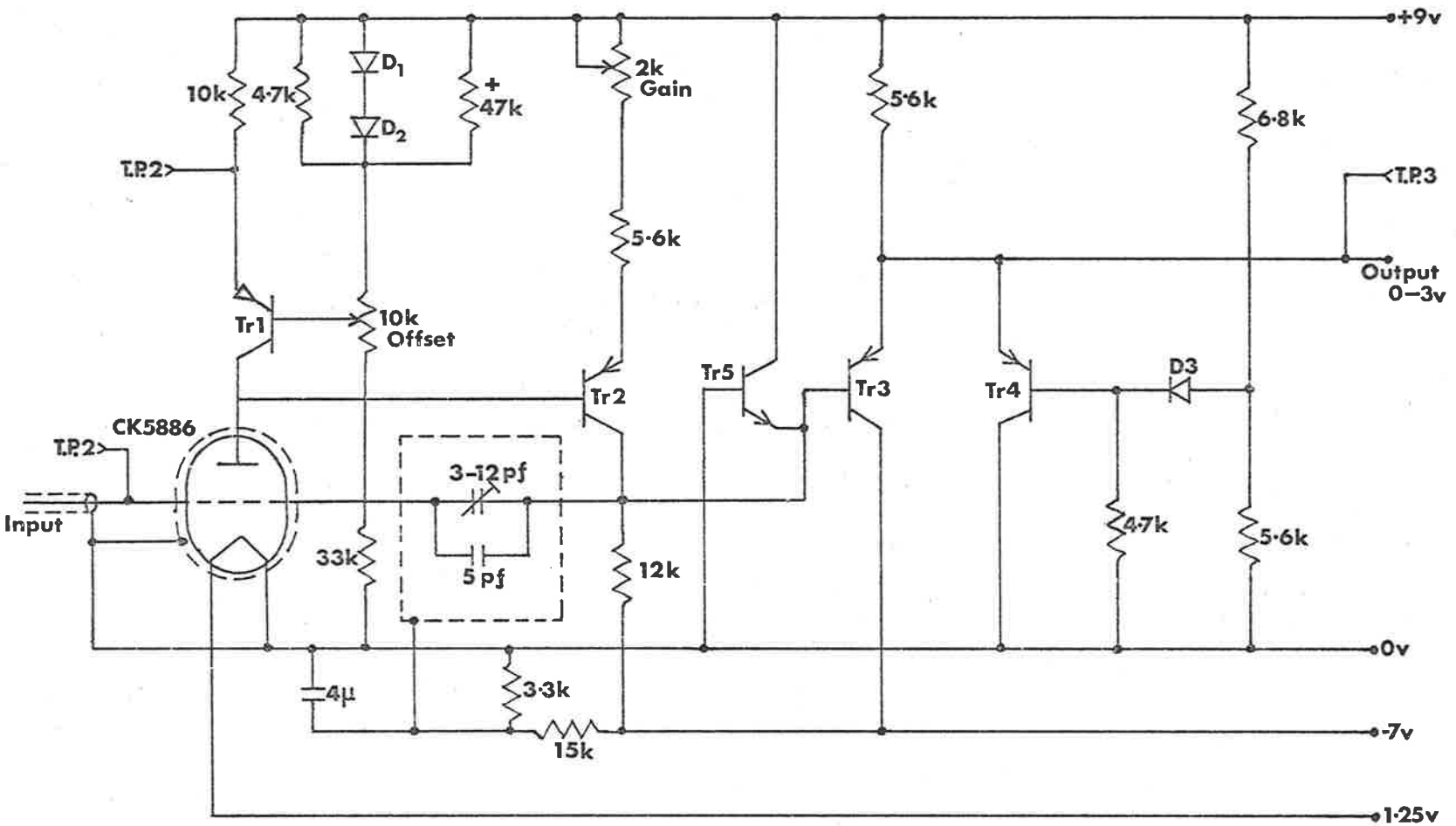

Tr1 – 4 2N3644 D1 – 3 OA202
Tr5 2N3694 + Selected For Zero Temp. Coeff.

FIGURE 4·5 LOGARITHMIC AMPLIFIER

TABLE 4.3 ULTRAVIOLET RADIATION DETECTORS

Entrance Aperture	1.27 cm^2		
Field of View	40^0 F.W.H.M. (circular)		
Operating Voltage	+47 Volts (unity gain)		
Chamber Type	LEB	LNO	CNO
Spectral Range	105 - 120 nm	105 - 135 nm	122 - 135 nm
Peak Efficiency	10%	59%	27%

4.2.4 Digital signal processing system

Voltage to frequency converters, driven by the analogue detector amplifiers, were used to derive suitable input signals for the digital data storage and transmission systems. Each linear voltage controlled oscillator produced a square-wave signal with frequency varying linearly from 32 kKz to 64 kHz for an amplifier output of 0v to 3 v. The number of pulses fed to each accumulator during the sampling period (8 ms) thus ranged from 256 to 512 over the range of the drive amplifier.

The top plug-in board held five accummulators with shift register storages and control and gating circuitry, and was designed and built by the staff of U.T.D. Each accummulated count was transferred to a storage register before the next sampling period commenced, and at the appropriate part of the telemetry frame, the

stored counts from the five detector channels were gated into the telemetry sub-modulator. The digitising error of one part in 256 (voltage) corresponded to ± 2% of the signal current referred to the amplifier input. This error was independent of whether the amplifier was operating at high or low levels.

4.2.5 In-flight calibration system

A calibrator was incorporated into each photometer package to enable periodic checks to be made on the operation and stability of the signal channels. At sixteen second intervals, relays were activated to disconnect the detectors from their amplifiers, and known currents from resistive sources were fed into the amplifiers for 100 milliseconds. This provided a one-point check of each main channel from the amplifier input to the data readout. A major fault in a channel would be indicated, but not necessarily located, by the calibration. Temperature drifts in each channel could be measured and allowed for, because the most temperature sensitive link was the logarithmic amplifier which, while drifting, maintained a constant volts-per-decade sensitivity. A single point calibration was therefore sufficient to allow any required corrections to be made. In practice, amplifier drifts during flight were found to be negligible.

The calibrator also switched on a miniature incandescent lamp which illuminated the photomultiplier faces via light-pipes for 150 milliseconds. This gave a measure of the photomultiplier sensitivities

to a broadband source, as the lamp light did not pass through the narrow band filters. The calibrator could be triggered or held continuously in either resistive source or lamp source mode by external control signals. This enabled calibration to be checked at any time until immediately before lift-off when external connections were isolated from the rocket.

4.3 Laboratory Calibration of the Photometers

4.3.1 Electronics

The amplifier input circuits had test-points into which selected currents were fed from Keithley 610 C instruments. Because the amplifier circuits did not use heavy overall d.c. feedback, the characteristic curves were determined by the electrometer grid characteristics. The transfer curve of each amplifier was plotted for each of the range settings used, and an amplifier most suited to the detector signal range was selected for each channel.

The analogue to digital converters were extremely linear and stable (± 0.01% per ^{0}C). Their input - output characteristics were set independently of the amplifiers so that, if a fault occurred, the converter boards could be interchanged between packages without requiring a recalibration to be done.

4.3.2 Photomultipliers

The photomultipliers were calibrated against an incandescent lamp which had been aged and calibrated for colour temperature and spectral energy density by the Australian National Standards

Laboratory. A series of metallic film neutral density filters was made to attenuate the standard lamp flux to the sensitivity range of the photomultipliers. These filters were made of evaporated nichrome, and their transmissions were measured on a Perkin-Elmer Model 137 UV spectrometer.

The response of the photomultipliers to the attenuated standard source was measured both with the cathodes bare, and with the multilayer flight filters fitted. A double check was then possible as the filters had been supplied with independent transmission curves measured on a Cary Model 14 spectrophotometer. The sensitivity of the multipliers was calculated by computing the wavelength integral of the product of the standard lamp spectral density, the relative cathode response function, and the transmissions of all filters and attenuators in the light path. The estimated errors in the calibrations were ± 25% absolute, and ± 10% relative between the two photomultipliers. Linearity was checked by using a combination of filters and lamp-detector separations. Significant non-linearities occurred only at signal currents exceeding the flight amplifier limits.

4.3.3 Ion chamber calibration

The ion chambers were calibrated by the procedures given in Section 2.7, except that these chambers were not tested or calibrated at gas gain. Calibrations were done at unity gain with the ion chamber walls at + 47 volts. Spectral response curves were taken at 0.5 nm intervals, with additional measurements at wavelengths where

strong line emissions were expected. While the sensitivity of the photomultiplier detectors was not expected to change significantly during the period between laboratory calibrations and the subsequent launch, the long term stability of the ion chambers was not so predictable. Over a period of several months some changes in sensitivity due to gas or window contamination were expected. It was found to be difficult to obtain accurate checks of sensitivity from preflight checks with portable discharge lamps. Better estimates of the in-flight chamber sensitivities were obtained from post flight calibrations on those occasions when the payloads were recovered without damage.

4.4 Environmental Testing of Payloads

4.4.1 Thermal

While on the launcher, the payload was heated by a warm airstream, so no requirement existed for operation or testing below normal laboratory temperatures (20^0C). The maximum temperature expected during flight in the interior of the payload at the photometer location was near 60^0C. Tests were made on the operation and drifts of the payload systems up to this temperature. The logarithmic amplifiers were the most temperature sensitive elements, but over this temperature range drifts were always less than 100 mv, and could be compensated for adequately by reference to the inflight calibrations.

4.4.2 Evacuation

Each photometer package, after being fitted with detectors, was placed in a vacuum chamber and operated under full power as the pressure was reduced to ensure that no corona discharges occurred from high voltage circuits in the pressure range around 1 Torr. The packages were operated continuously under vacuum for half an hour to prove that all components had ample margin for dissipation of heat when in a rarified atmosphere.

4.4.3 Vibration

All of the individual packages and an assembled payload were submitted to vibration before the first launching. Electrical power was not switched on during the vibration, but was applied for electrical function tests before and after the vibration. Vibration was done in three axes using both random and sliding tone sinusoidal excitation.

4.5 Summary

Four experimental packages, of the type described in the previous sections, were constructed for participation in a series of rocket borne experiments. Modifications and improvements were incorporated between flights, but the basic format remained unchanged. During the series of rocket flights, the ability of the photometer systems to make measurements over a range of auroral acitivty has been established.

The photometer packages featured five main detectors with aligned fields of view arranged to scan the spatial structure of auroral features

in a way not possible with larger forward viewing instruments. With this sytem, the relationships in strength and position of emissions within the five wavelength bands could be studied.

CHAPTER 5 RESULTS OF MAP AURORAL FLIGHTS

5.1 Flights of the MAP Payloads

5.1.1 Introduction

The MAP payload system was first flown in May, 1967 on a daytime test flight. Although the instruments performed satisfactorily, a failure occurred in the parachute deployment system, causing the payload to be destroyed, and the remaining three flights planned for the campaign were cancelled to allow development of an improved recovery system.

A second series of flights was made in February, 1969. Photometer packages were included in three payloads launched at night. On the first occasion, the aurora had faded before the rocket reached measuring altitudes. The photomultipliers received signals, but no ultraviolet fluxes above the thresholds were detected. The second flight of the series was made into an IBC II aurora. Once again, the photomultipliers operated as expected, but no ultraviolet radiation was detected. The level of ultraviolet intensities was apparently well below that which had been anticipated; a conclusion which was supported by data taken on a later flight and by other workers (Miller et al., 1968). During the ascent phase of the third flight of the series, a mechanical failure in the nose-cone occurred and the vehicle did not reach the required altitude.

A further flight of a MAP payload including a photometer package was made in April 1970, when the rocket was launched into a bright and very active aurora, and both visible and ultraviolet

emissions were detected. The results of the analysis of the data from this flight are presented in the following sections. A failure in the recovery system caused the payload to be extensively damaged on impact, so that post-flight tests and calibrations could not be done to check the operation and sensitivity of the detector systems.

5.1.2 MAP flight 14.443 - launch and flight conditions

The vehicle was launched at 0640 hrs on 16th April, 1970 (U.T.). Prior to launch, the ground magnetometers indicated a magnetic bay of approximately 100γ, and the riometer absorption was measured at 0.3 db. A scanning photometer at the Auroral Observatory indicated an intensity of near 100 kR of 557.7 nm emission for the brightest sections of the display. The all sky photographs (Figure 5.1) show the extent and activity of the emitting regions.

An apogee of 136 km was reached at 186 secs after launch, and 240 seconds of data from above 70 km were received. The photomultipliers registered auroral radiation from the time of cover release (+48 secs) and the ion chambers responded to radiation above 75 km. The payload rolled at a rate of 5 rps during ascent, and from +80 s precessed in a cone of 10^0 half angle. After the head had been severed from the second stage on the downleg (+216 s), it precessed in a cone of 23^0 half angle. The derivation of vehicle orientation is outlined in the following section.

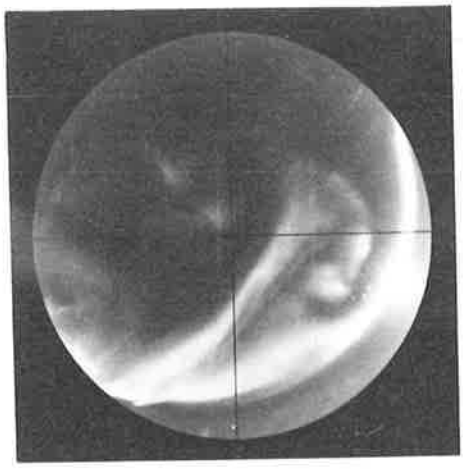

+60s

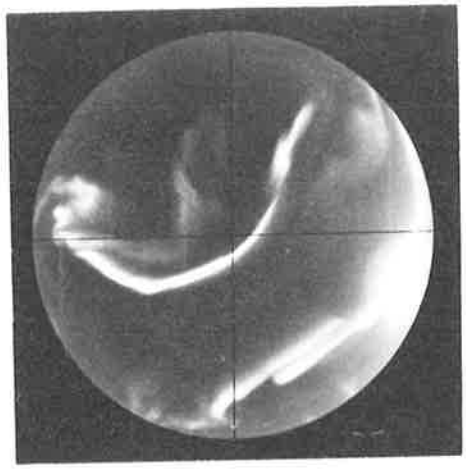

+240s

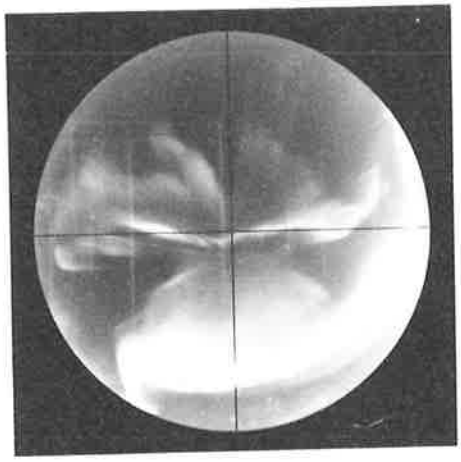

+120s

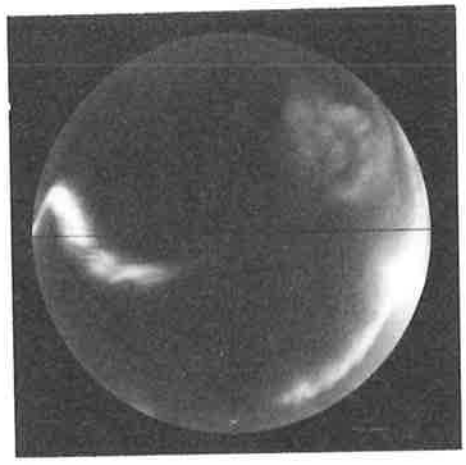

+300s

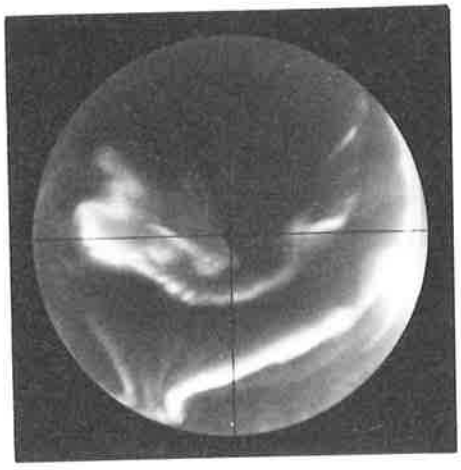

+180s

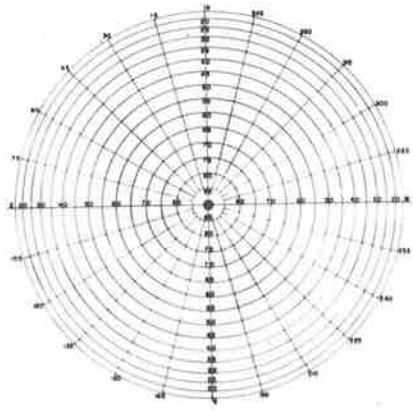

AZIMUTH/ELEVATION GRID

FIGURE 5·1 ALL-SKY PHOTOGRAPHS AT 60 sec INTERVALS

5. 1.3 Attitude solution

Three fluxgate magnetometers were carried to provide information on the attitude of the payload. Sensing heads were fixed at angles of 0^0, 90^0 and 45^0 to the rocket axis. In-flight calibration parameters for the 45^0 magnetometer were calculated at a number of flight-times by analysis of the telemetered signal. By using a method outlined by N. Eaker (private communication), based on a suggestion by Dr. J. Hugill of ESSA, the parameters were calculated from the flight data by an iterative process.

The output voltage of the magnetometer circuit was represented as

$$V = Vo + kB \cos\Theta$$

when the sensor made an angle of Θ with the Earth's magnetic field, $\underline{B}$. The instantaneous voltages V_1 and V_2 (Figure 5.2a) corresponded to the instants (t_1 , t_2) when the magnetometer, rocket axis and magnetic field were coplanar. Orthogonality of the vectors $\underline{m_1}$ and $\underline{m_2}$ (Figure 5.2b) meant that

$$\begin{aligned}(V_1 - V_0)^2 + (V_2 - V_0)^2 &= (kB \cos\Theta_1)^2 + (kB \cos \Theta_2)^2 \\ &= k^2B^2 \ (\cos^2\Theta_1 + \cos^2 \ (90 - \Theta_1)) \\ &= k^2B^2\end{aligned}$$

Several trial values of V_0 were selected, and the corresponding values of kB were calculated from the measured values of V_1 and V_2 at a number of times during a precession period. Interpolation in a (kB) vs (V_0) plot of the trial solution pairs gave the actual values of V_0

(a) Magnetometer Signal Waveform

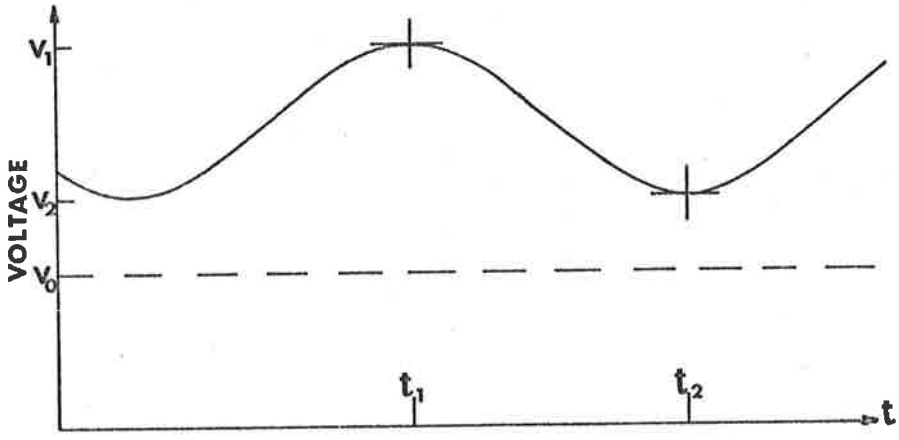

(b) Roll Circle of Angled Magnetometer

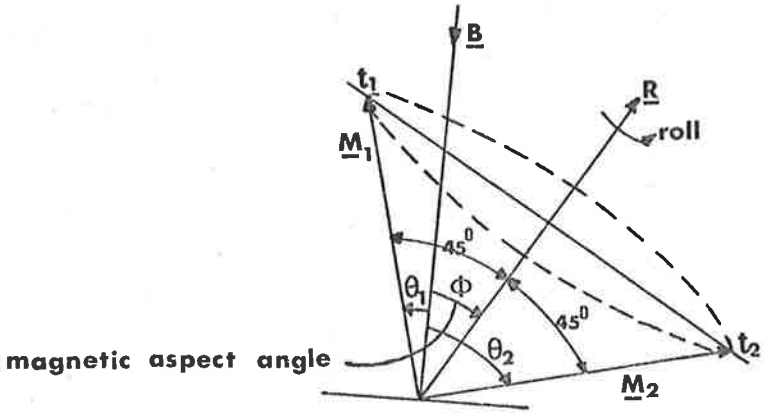

(c) Precession Cone of Rocket

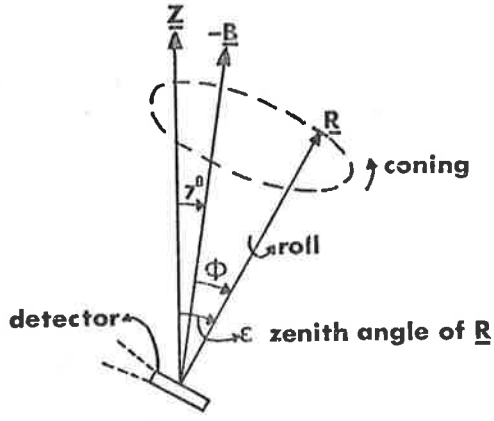

FIGURE 5-2 MAGNETOMETER SOLUTION DIAGRAMS

and kB to be used in the magnetometer data reduction. The above steps were repeated for several periods during the flight to correct for temperature drifts and for the change in bias due to payload separation.

The derived angle between the rocket roll axis and the magnetic field is plotted in Figure 5.3. As the dip angle of the field was 83^0, the curve also gives approximately the angle of the detector scan plane from the horizontal (this angle has been called ε and is shown in Figure 5.2c).

It had been intended to use the visible signals from both the auroral emissions and the moon as data for the attitude solution. Good signals from the moon, as an effective point source, would have greatly simplified the attitude solution. Figure 5.1 shows, however, that the moon (at 255^0 Az, $+26^0$ El) appeared in or near a bright auroral region for most of the flight, and intensity calculations confirmed that the lunar signal would have been difficult to distinguish in such a bright aurora, both at 391.4 nm and at 557.7 nm. Lunar signals could not therefore be used as a directional reference for this vehicle. Attitude data was also difficult to obtain from the auroral forms because of their variability and spatial distribution. Some of the observed properties of the ultraviolet airglow below 100 km (reported in Chapter 7 and 8) were used to derive attitude information from the airglow signals. A precise attitude solution was computed only for the period after +216 s (payload separation).

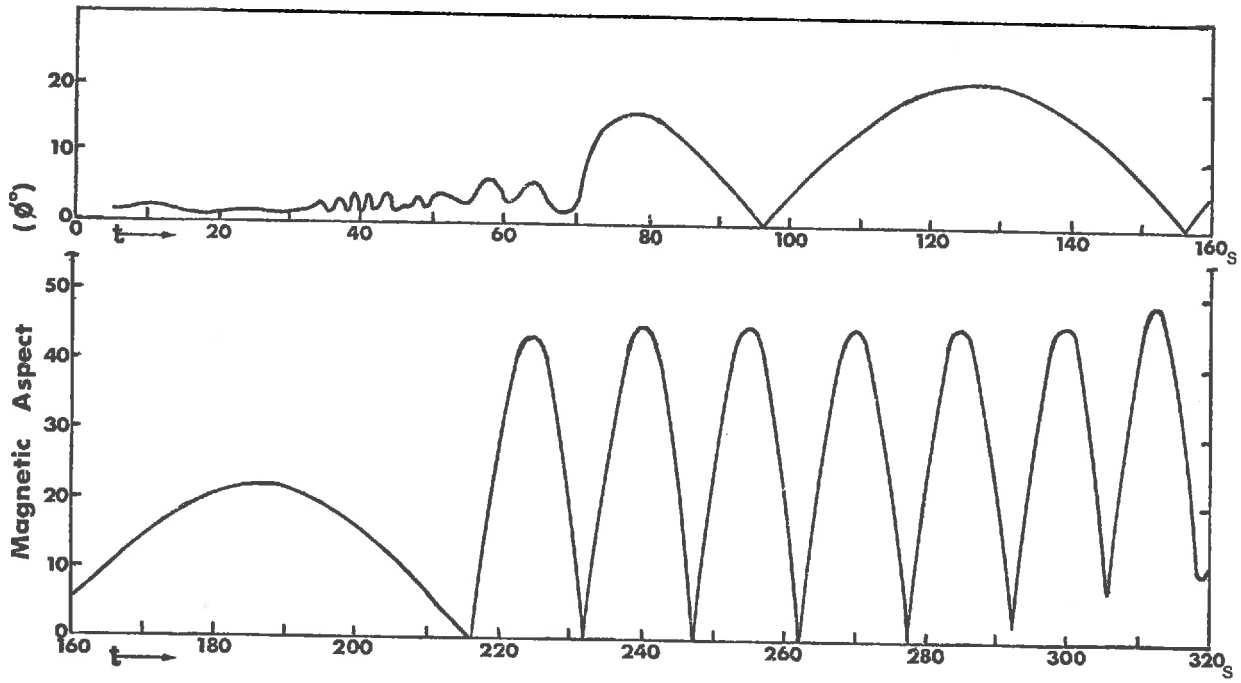

FIGURE 5.3 MAGNETIC ASPECT – 14·443

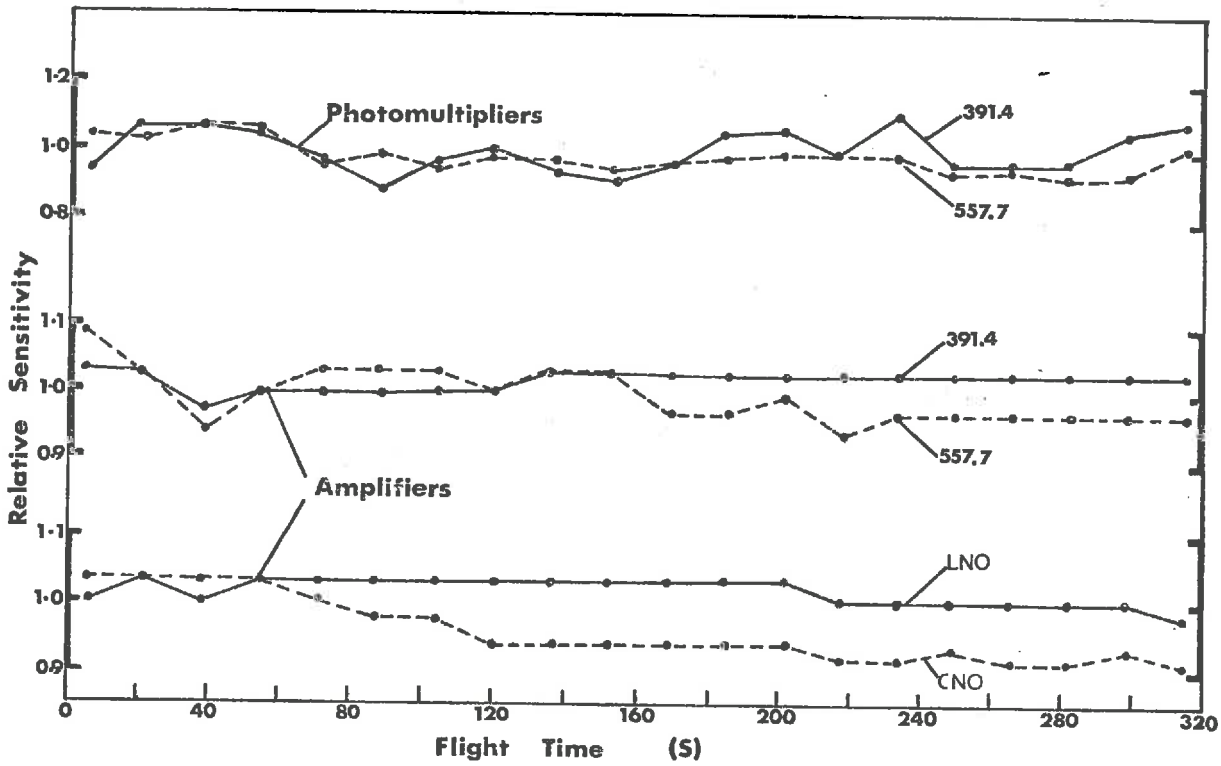

FIGURE 5.4 IN-FLIGHT CALIBRATIONS – 14.443

Between +216 s and about +305 s, the rocket precessed about a cone of 22.5^0 half angle, centred on (280^0 Az, $+68^0$ El), and passing within 1.5^0 of both the magnetic field and the zenith.

A study of the relationship between the ultraviolet and visible detector signals and the magnetic aspect during the period +80 s to +100 s indicated that between +80 s and +216 s, the axis of the precession cone lay within 8^0 of (180^0 Az, $+75^0$ El). For a precession cone centred within the stated limits, the scan plane inclination (ε) would have been between 10^0 and 28^0 at the times when the magnetic aspect angle was at a local maximum. After +216 s, ε was 40^0 at times of maximum magnetic aspect. This situation is referred to in Section 5.2.2. The times when the magnetic aspect, ϕ, was zero ($\underline{R}//\underline{B}$) and when the magnetic aspect was at a maximum (i.e. points 180^0 apart on the precession cone) were used for comparing measured intensities at different heights.

5.1.4 Instrument performance

Both photomultipliers and their data channels and two ion chamber channels performed satisfactorily and with adequate stability. In-flight calibration curves for the amplifiers and the two photomultipliers are shown in Figure 5.4. For logarithmic amplifiers of this type, with a four decade coverage, the drifts during flight (±5% referred to input) were satisfactory. The third ion chamber channel (LEB) showed neither signals nor calibration pulses, indicating that a fault had occurred in the data handling circuitry.

5.2 Auroral Ultraviolet Radiation

5.2.1 General characteristics of the ultraviolet detector signals.

The signal levels from both of the ion chambers were below the thresholds until the rocket reached 85 km, above which the LNO chamber (105 nm to 135 nm) showed a roll-modulated response. Signals received between 85 km and 100 km had a smooth variation around the detector scan circle. In that altitude range the radiation must have been predominantly hydrogen Lymanα, as this is the only prominent emission in the spectral range which can penetrate effectively below 95 km. The smoothness of the spatial distribution was characteristic of the airglow radiation which is treated in later Chapters (6, 7, 8). Figure 5.5 shows a series of traces taken from the telemetry records to illustrate the nature of the observed signals. On the logarithmic scale of the display, which covers four decades of signal current, the ratio of Imax/Imin around each spin scan is proportional to the height of the spin modulation of the waveform.

While the mean signal level increased with altitude, discreet localized sources began to appear above 100 km. Figure 5.5(b) shows a localized brightening of about 50% above the intensity from adjacent regions. Comparison with the photomultiplier signals showed that the greatest ultraviolet intensities did not always coincide with the brightest visible regions. Some part, but not all, of the apparent displacement may have been caused by the difference

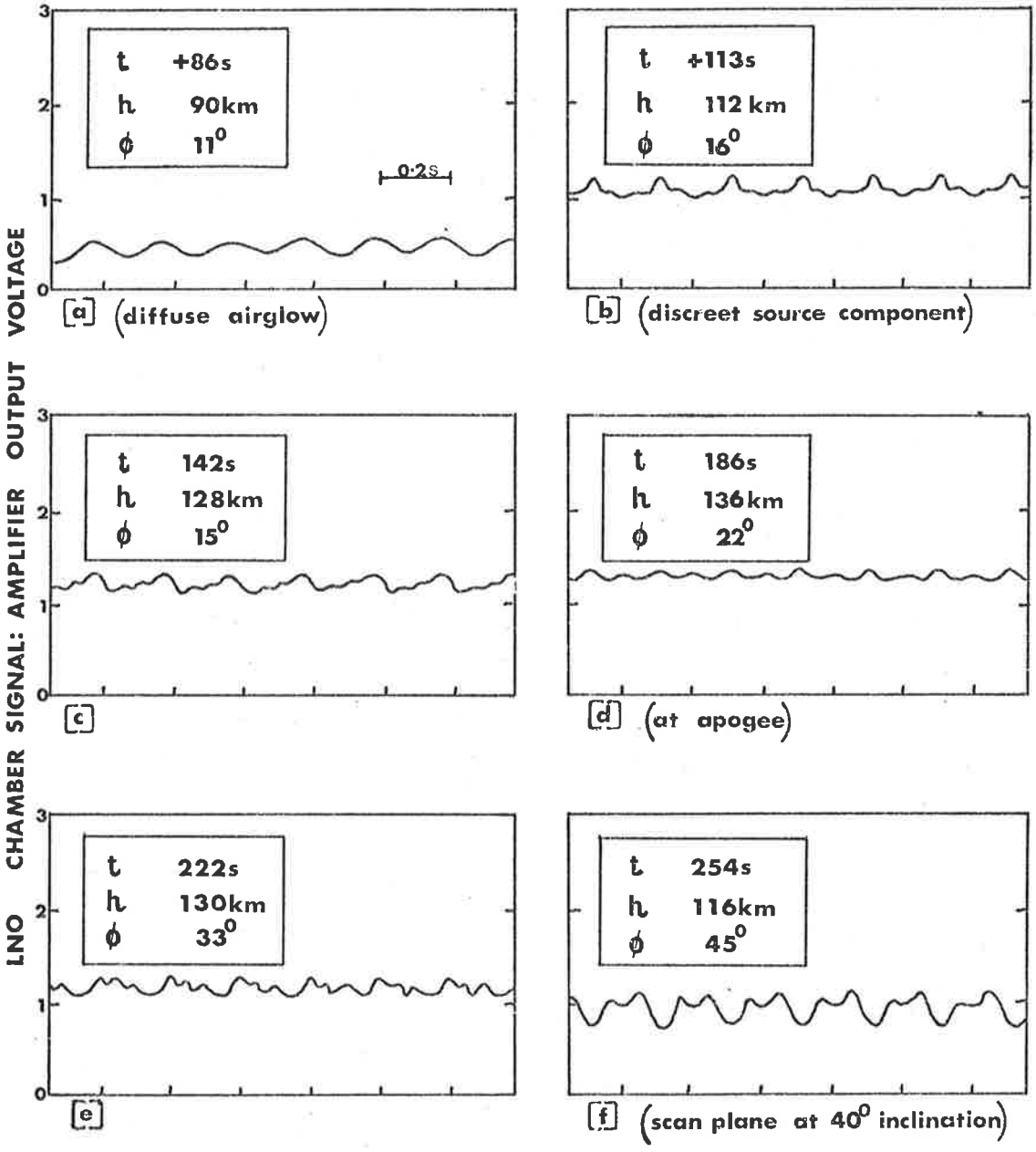

FIGURE 5·5 TELEMETRY TRACES FROM LNO ION CHAMBER CHANNEL

between the angular fields of the ion chambers and the photo-multipliers, especially when the detectors were viewing sharply defined auroral forms.

The highest ultraviolet intensities were recorded 15 seconds on either side of the time of rocket apogee (Figure 5.6). Modulation depth due to vehicle rotation was low for most of the upleg (Imax ≃ 1.5 Imin), but increased during the downleg so that Imax/Imin became as high as 3 at times. There were no parts of the sky which were very dark; this uniformity of the spatial distribution is characteristic of radiation which is subject to a large degree of resonance trapping. A more complete discussion of resonance radiation is given in Chapter 6 in reference to airglow distribution.

No localised sources were seen from below 104 km on the downleg, and the signal wave form reverted to the smooth shape shown in Figure 5.5(a). Because the attitude solution for this flight was incomplete, the bright ultraviolet regions could not be positively identified in the ground-base photographs of the auroral forms, and comparisons could be made only with the on-board measurements of visible intensity distributions.

Signals above the threshold level were first seen by the CNO ion chamber (122 nm to 135 nm) near +100 s (100 km). The signal level rose slowly until +160 s (132 km), the rose rapidly to a peak at +173 s (134.5 km). Changing vehicle attitude and auroral activity rather than increasing altitude, would have been responsible

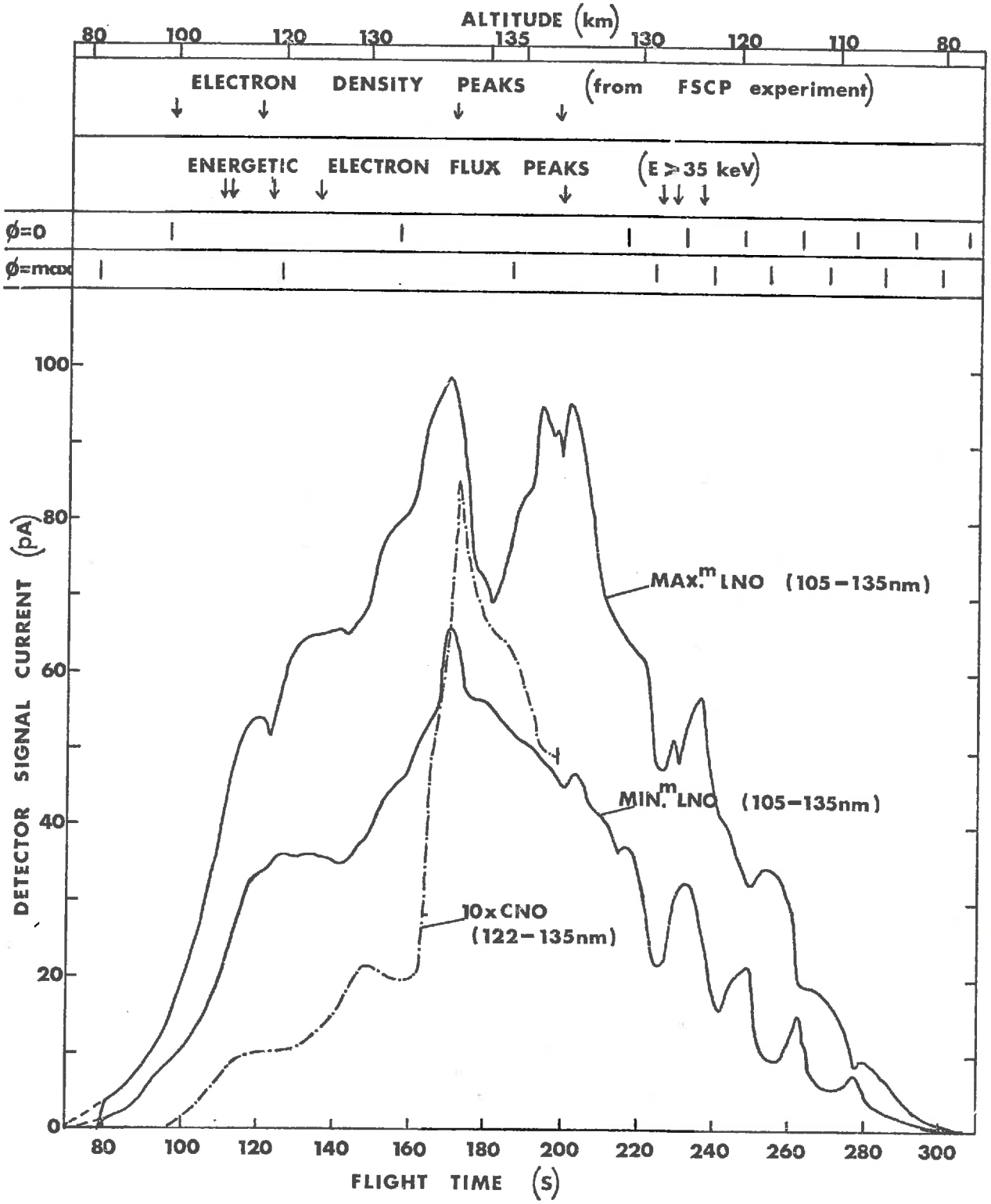

FIGURE 5·6 ULTRAVIOLET DETECTOR SIGNALS

for the intensity variation between +155 s and +185 s (Figure 5.6) as the rocket was approaching apogee during that period. After +173 s the signal declined steadily until +199 s when it suddenly dropped below the amplifier threshold. The rapidity and nature of the return to essentially zero signal level indicated a fault in an electral connection; the continued appearance of calibration pulses and the amplifier threshold level at the output showed that the fault must have occurred ahead of the calibration relay. No further ion chamber signals were recorded from this channel. The fact that no significant roll modulation of the CNO signal was observed at any time, suggested either that the detected radiation had become isotropic through multiple scattering, or that the amplifier response time was too slow at the low levels of signal current to follow the signal variations. Both of these effects could possibly have been effective in smoothing the signal waveform.

5.2.2 Time and altitude profiles

The maximum and minimum signals detected during roll-scans by the LNO detector, and the mean CNO detector signal, are shown plotted against flight time in Figure 5.6. An extrapolation of the LNO signal back from +82 s has been made to cover the period when the amplifier was recovering from the zero-clamped condition. Along the upper margin are shown the times when the rocket axis was parallel to the magnetic field ($\phi = 0$) and when the angle (ϕ) between the rocket axis and the field reached its maximum value. On the downleg

in particular, the dependence of the ratio of intensities (Imax/Imin) in the LNO channel on the magnetic aspect, ϕ, can be seen. Reference to the attitude solution showed that the minimum values of this ratio were reached when the rocket axis was vertical and the detectors were scanning around the horizon, with their fields of view below any local emission regions.

The signal levels from the LNO detector at times of comparable vehicle attitude are plotted against altitude in Figure 5.7. All of the points in part (a) were measured when ϕ was zero, and those in part (b) were taken at the times of maximum ϕ. To the lower parts of the curves have been fitted typical profiles for Lymanα airglow (Chapter 7 and 8; Opal et al., 1970) adjusted to match the data between 80 and 86 km altitude. The differences between the total signals and the airglow intensity profiles (that is, the auroral components) are shown in Figure 5.8 (a and b).

Figure 5.9 shows the altitude profile of the signal from the CNO chamber (122 to 135 nm). The maximum intensity was recorded 12 seconds before apogee was reached, which is consistent with the drop in visible intensities measured by the visible photometers around the time of apogee.

As an estimate of the auroral activity in the plane being scanned by the detectors, the 'scan-integral' of 557.7 nm emission was calculated for times coincident with each of the points plotted

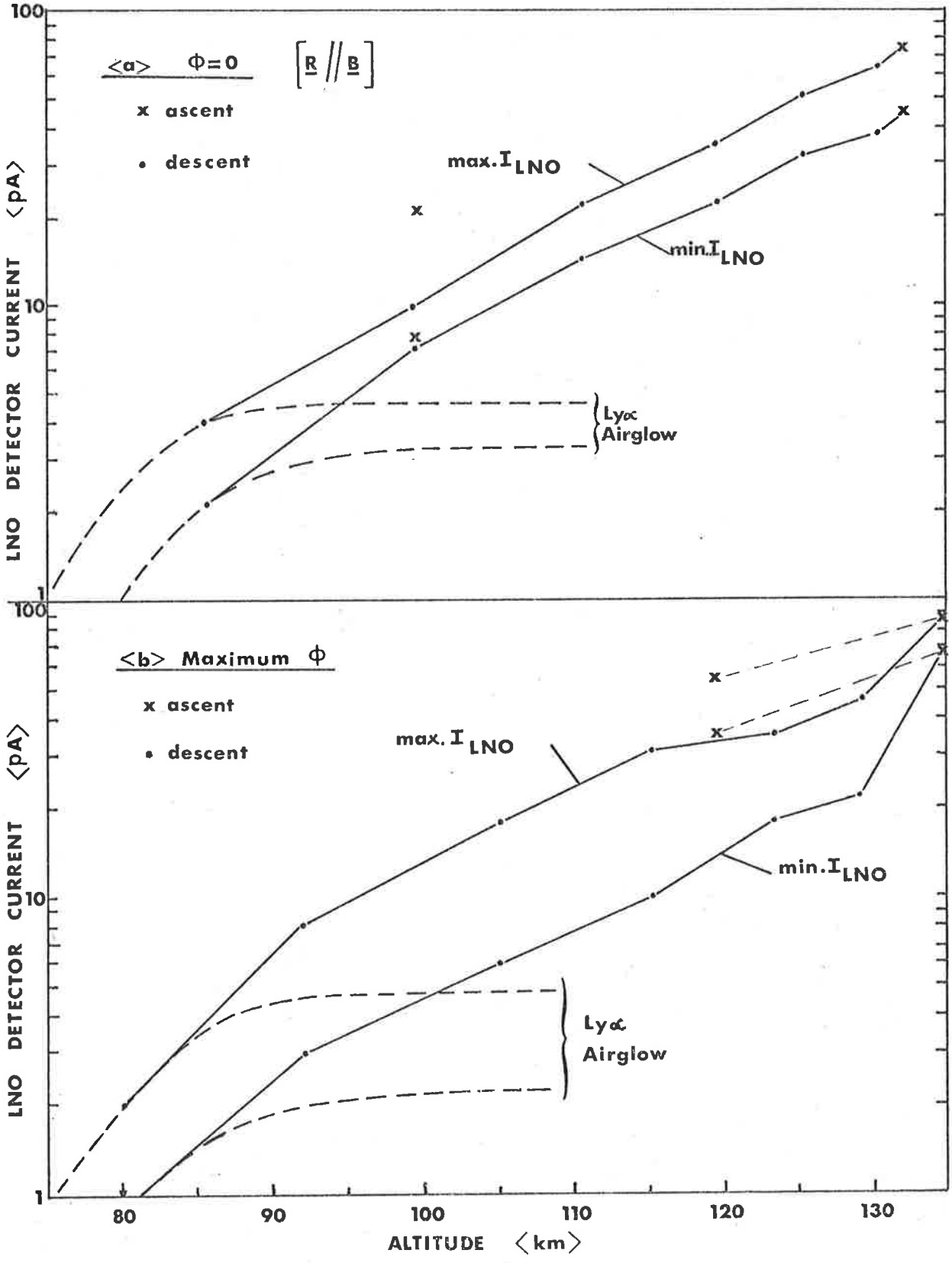

FIGURE 5.7 ALTITUDE DEPENDENCE OF LNO SIGNALS

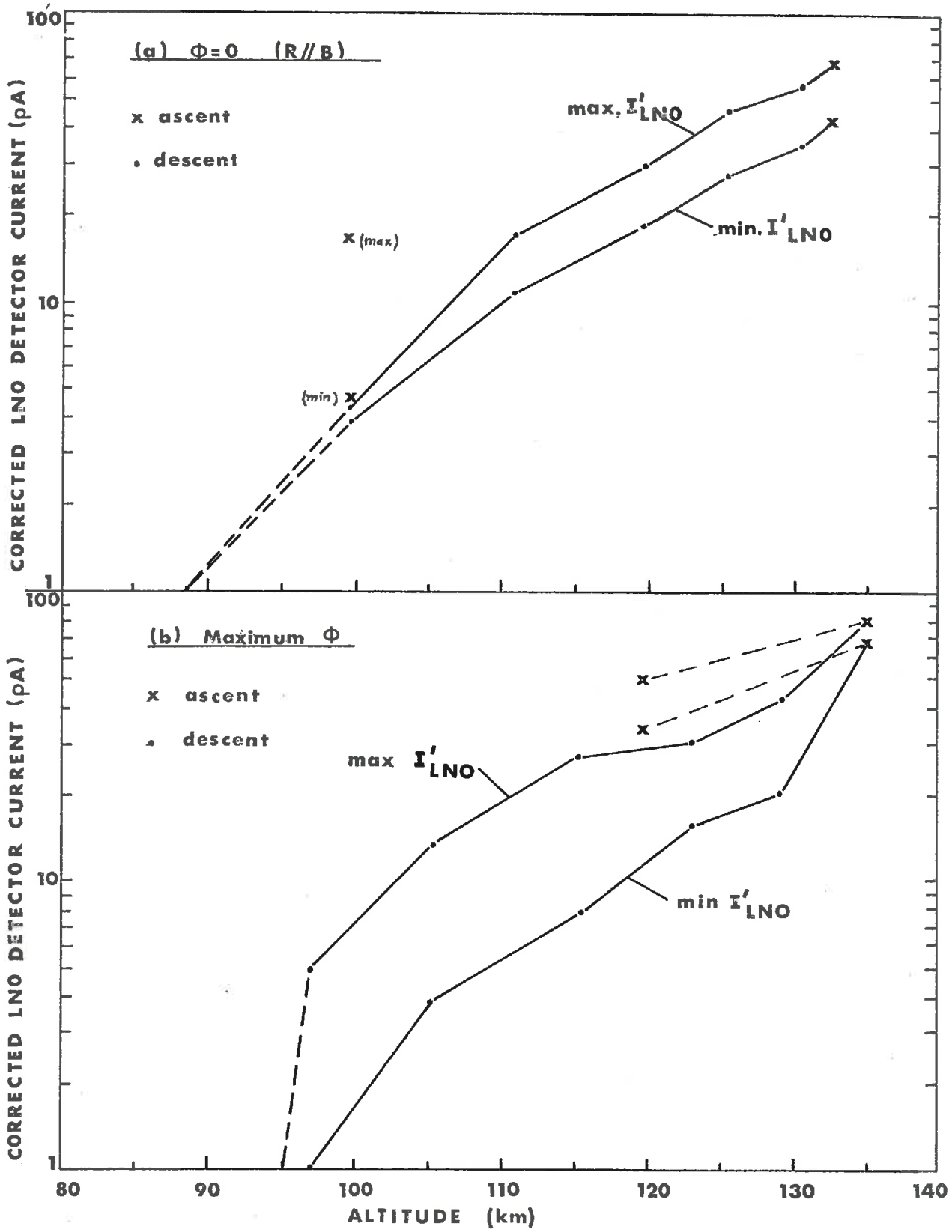

FIGURE 5.8 LNO DETECTOR SIGNAL WITH AIRGLOW CORRECTIONS

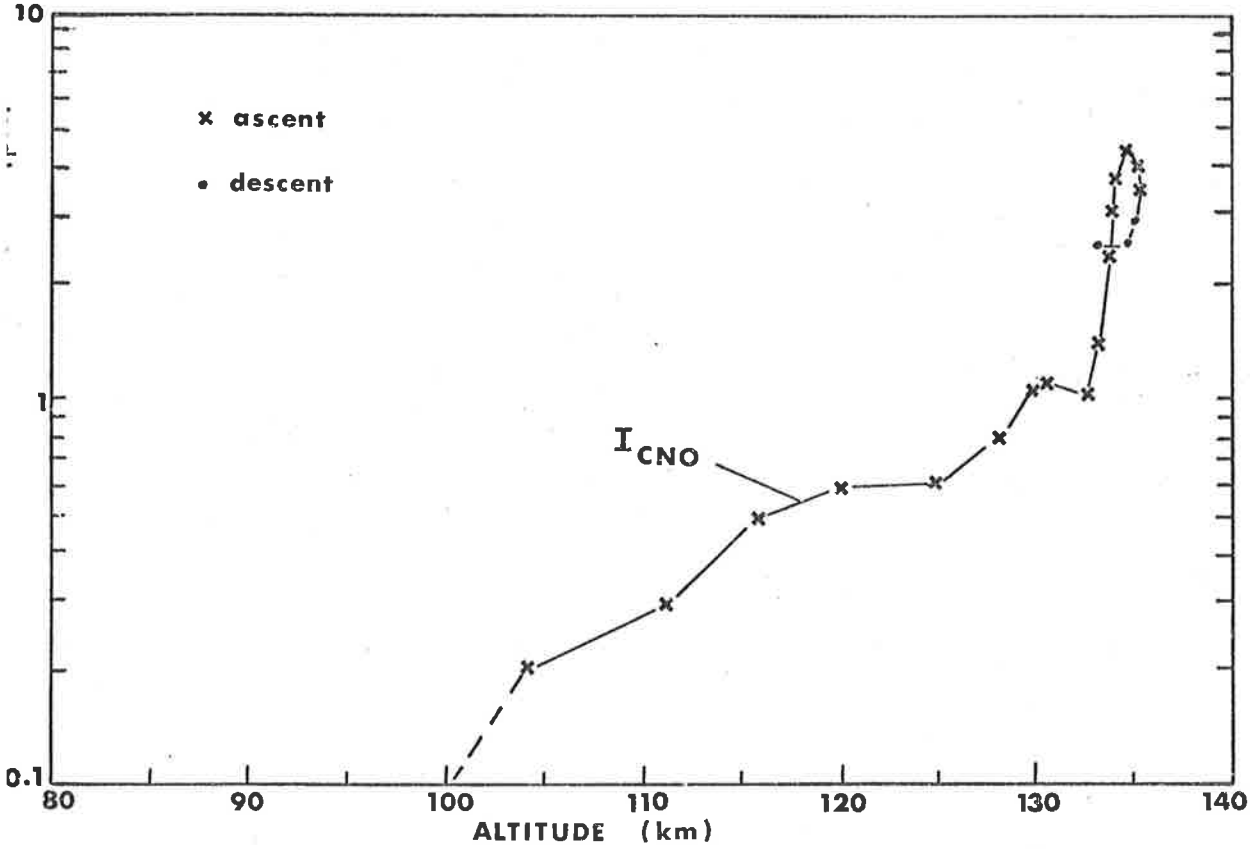

FIGURE 5.9 ALTITUDE DEPENDENCE OF CNO DETECTOR SIGNALS

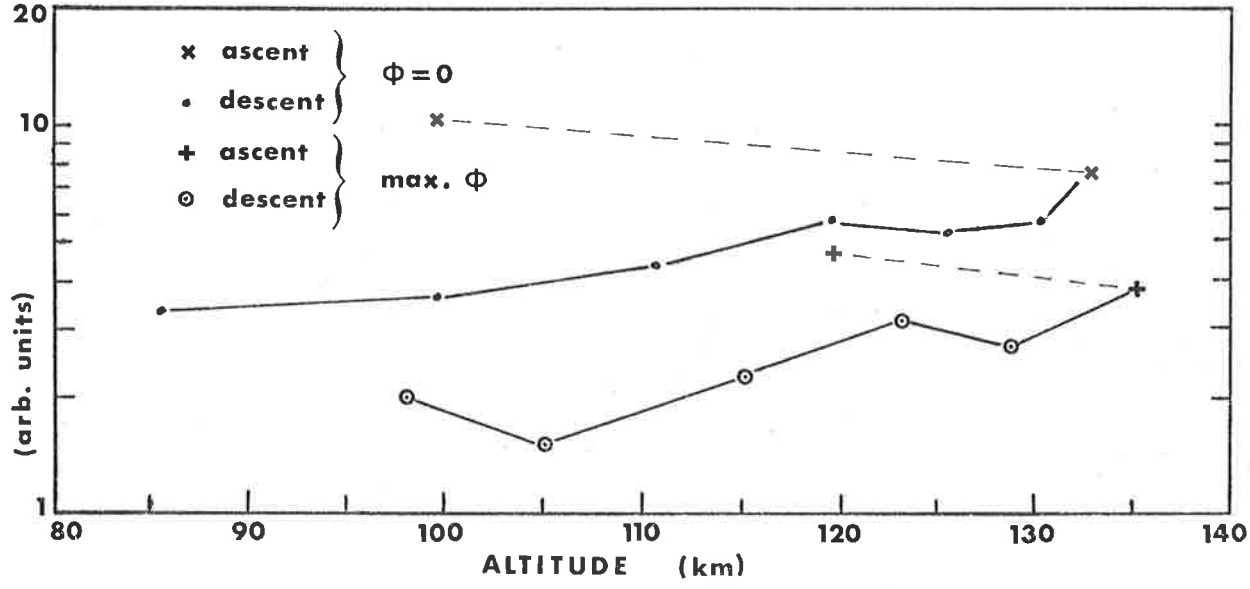

FIGURE 5.10 SPACE INTEGRALS OF VISIBLE (557.7nm) EMISSIONS

in Figures 5.7 and 5.8. A sum was formed of the visible intensity from ten equally spaced directions around the scan circle and the totals have been plotted (in arbitrary units) in Figure 5.10 to show the level of activity in the atomic oxygen emission line as seen from the rocket. The shapes of the curves of Figure 5.10 are reflected in the profiles of the ultraviolet intensities in Figure 5.8. All of the curves show a marked difference between the levels of activity during the up and down legs of the flight. Because there were so few measured points on the upleg (owing to the slow coning of the rocket), no attempt has been made to interpolate between those points in Figure 5.10.

5.2.3 Identification of spectral components

Previous measurements and model calculations (Chapter 3) had suggested several emissions as the most likely to be observed in the ultraviolet aurora. Miller et al., (1968) and Peek (1970) found that the 130.4 nm atomic oxygen emission was dominant in the range covered by the ion chambers, with significant contributions also from atomic nitrogen (120 nm), molecular nitrogen (L-B-H bands), and atomic oxygen (135.6 nm), as well as the Lymanα airglow.

Separation of the contributions from various emissions was made more difficult in the present case by the loss of data from the LEB detector, which would have made possible accurate separation of the NI (120 nm) contributions. With the available data, the N_2 (120 nm) and O_2 (130.4 nm) emissions could not be separated by

examination of altitude profiles, as the absorption profiles of the two emissions would be similar. The absorption coefficient of molecular oxygen is lower at 130.4 nm than at 120 nm, but resonance trapping would produce enhanced absorption of the 130.4 nm emission. Enhanced absorption is discussed more fully in Section 6.3.3, which refers more particularly to airglow radiation transport. The transport of auroral 130.4 nm radiation is analogous, although the source geometry is much more complex.

The level of the signals from the CNO detector was much lower than had been predicated on the basis of measurements such as those of Miller et al., (1968) and Murcray (1966). Signal differencing, using both CNO and LNO data, was used to separate the signals into 120 nm, 121.6 nm and 130.4 nm components. When the calibration sensitivities of the LNO and CNO detectors were used with the maximum total signal levels near apogee, the following partition was obtained:-

OI (130.4 nm)	6.8 kR
NI (120 nm)	18 kR
HI (121.6 nm)	1.8 kR (airglow extrapolated from 85 km)

The ratio of oxygen to nitrogen emissions was quite different from that found earlier (Miller et al., 1968; Peek,1970). In the case of this flight, however, no cross-check could be made with the LEB data to confirm the derived ratio.

It was possible that the chamber sensitivities could have

changed during the period between calibration and the flight. It has been observed that the sensitivity of chambers never increased during storage; any changes were invariably towards lower efficiency. This meant that if the chamber characteristcs had changed before flight, an analysis based on the laboratory calibration figures would provide a lower limit to the actual intensities. The airglow intensity measured by the LNO chamber was close to the value expected from the results of other flights, indicating that the LNO detector had remained stable. If the CNO chamber had lost sensitivity, as appeared likely on this flight, the above partition of the signal into spectral components would have given a lower limit for the OI (130.4 nm) intensity and an upper limit for the NI (120 nm) radiation.

An estimate was made of the probable loss of sensitivity of the CNO detector by assuming that the ratio of 130.4 nm to 120 nm intensities was 10 : 1, as found by Peek (1970). The partition of the total LNO signal, based on this ratio was:-

OI (130.4 nm)	40 kR
NI (120 nm)	4 kR
HI (121.6 nm)	1.8 kR

which was consistent with the absolute intensity measurements of Peek, when allowance was made for the difference between the visible intensities measured during the respective flights.

Auroral Lymanα emission produced by proton excitation would be

expected to be broadened and Doppler-shifted in the same manner as H_α emissions (Chamberlain, 1961a, p170). Resonance trapping in atmospheric hydrogen would be unimportant and pure absorption in molecular oxygen would determine the penetration of the radiation into the atmosphere. If auroral Lymanα had been present, the emitting regions would have been observable as discreet sources from well below 100 km. The absence of departures of the signals from the smooth airglow distribution indicated that the intensity of auroral Lymanα was less than that of the airglow, and therefore much less than the intensity of other auroral emissions.

5.2.4 Relationship between visible and ultraviolet emissions

Although the narrow-field photometers at the Auroral Observatory measured maximum intensities of both 391.4 nm and 557.7 nm emissions during the flight of about 25 kR, the activity was obviously very non-uniform and variable, and the ground photometers did not view the brightest regions. The strongest signals from the on-board visible photometers (10^0 field were equivalent to 459 kR (391.4 nm) and 520 kR (557.7 nm), while the filter wheel photometer at Fort Churchill Base registered up to 130 kR at 391.4 nm and over 200 kR at 557.7 nm. In the brightest parts of the sky the activity reached a level of IBC III^+, but only for the period around +240 s was the coverage of the sky extensive at this brightness level. Even with the assumption that the CNO detector was operating at reduced sensitivity, the resulting emission rate of OI (130.4 nm) was still

lower than the 557.7 nm emission rate ($I_{130.4}/I_{557.7} \simeq \frac{1}{4}$). With a larger N I (120 nm) intensity (5.2.3), this ratio became nearer 1/10, even further below the anticipated level.

The signal from the LNO detector showed roll modulation but not of very great depth, which is what would be expected if a large part of the detected radiation were resonantly trapped. Discreet features were seen at altitudes above 100 km, and of these, some were in the same direction as large fluxes of visible radiation, while others appeared in regions of low visible emission rates. Figure 5.11 shows a comparison between the outputs of the LNO and 557.7 nm detectors at selected times during the flight. A logarithmic scale has been used, and a one-decade span is marked below the trace for +117 s. The intensity from the bright ultraviolet region which could be seen at that time was 45% greater than that from adjacent parts of the scan.

While the brightest ultraviolet regions at +117 s and +140 s coincided with visibly active regions, the traces at +224 s and +241 s show ultraviolet enhancements from regions which were comparatively dark at visible wavelengths (Only traces from 557.7 nm detector are shown. The emission pattern at 391.4 nm was similar to that at 557.7 nm.) Because the CNO signal did not show roll modulation, it was not possible to determine the wavelength of the localized enhancements. The narrow apparent width and edge sharpness of some of the localized source regions indicated that

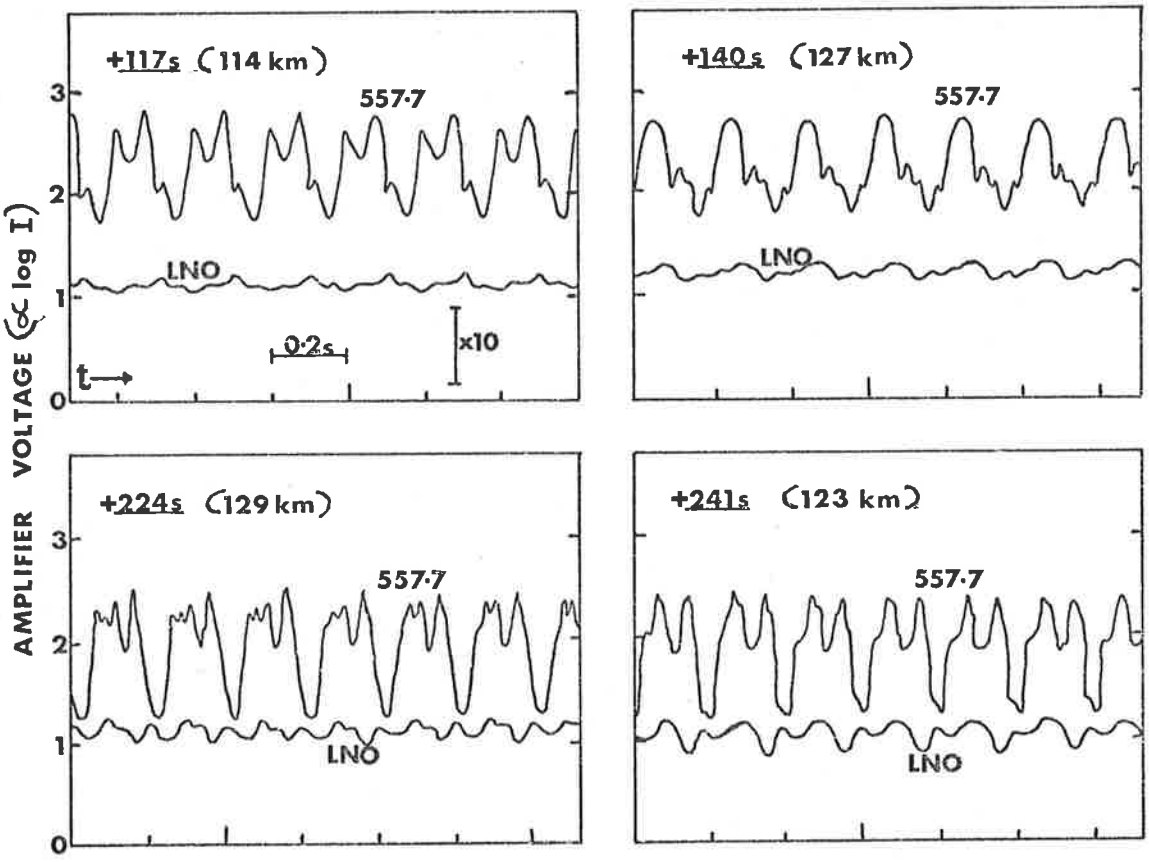

FIGURE 5·11 SPATIAL RELATIONSHIP BETWEEN VISIBLE AND ULTRAVIOLET EMISSIONS

the observed radiation from them was at least partly free of resonance trapping effects. Some possible sources of these emissions, for which the atmosphere above 110 km is optically thin, include the 135.6 nm oxygen line, the 120 nm atomic nitrogen line and the L-B-H bands of molecular nitrogen. All of these have been reported at significant strengths in auroras (Opal et al., 1970; Sharp and Rees, 1972).

That the ultraviolet emission can be enhanced in directions away from the visible forms is a significant observation and it was unfortunate that on this flight the limited data from the ion chambers precluded an identification being made of the wavelength(s) involved. An identification of the wavelength of the spatially separated emission component, together with more comprehensive data on the simultaneous particle fluxes would be a worthwhile objective for further work.

Some part of the observed roll modulation would have been due to the an-isotropy of the geocoronal airglow component of the signal (Chapter 8). Data from a complete set of ion chambers would be needed to separate the total Lymanα intensity from emissions at other wavelengths; once this had been done, the enhancement of the Lymanα auroral component above the airglow distribution pattern would be easily identified.

Another possible source of signal current enhancement from directions away from the visible emissions would be direct penetration

of high energy particles into the chambers. Analysis of the records showed, however, that the isolated enhanced regions which were observed did not bear the regular relationship to the magnetic field throughout the coning of the rocket which would have been expected for energetic particle fluxes. It is therefore considered that the contribution to the signals from direct particle penetration was small.

An approximate estimate, within the limitations of the data, was made of the total energy of the visible and ultraviolet auroral forms. At +233 s, the rocket axis was close to the vertical, while the visible activity was confined to relatively well defined regions of the sky (Figure 5.1). The rocket was at 125 km altitude, between the two bright arcs visible in the photograph taken at +240 s.

A model shape for the arc to the north of the rocket was based on dimensions taken from the all-sky photograph taken at +233 s, and is sketched in Figure 5.12(a). An assumed median altitude of 115 km was used to calculate the dimensions of the visible emitting region, which for the purposes of this calculation was assumed also to be approximately the source volume for the ultraviolet emission.

A column emission rate along the normal to the arc through the rocket was read as 52 kR (2.28 v from the telemetry records), and a uniform emission rate throughout the volume (3.5×10^{13} m^3) gave a total emission rate of 3.6×10^{24} ph s^{-1} ($\simeq 10^{11}$ ph s^{-1} m^{-3})

(a) Model of Visible Arc

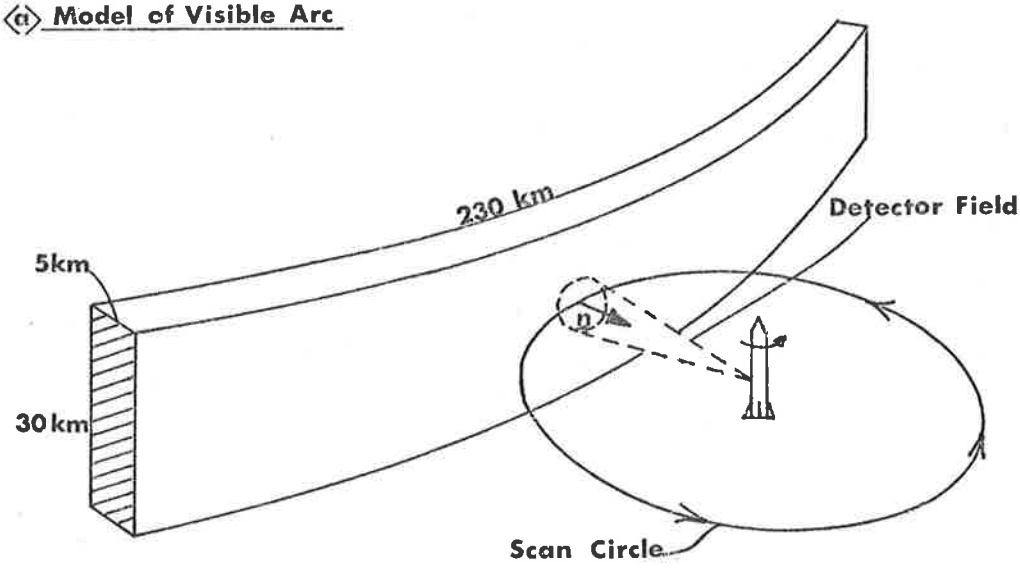

(b) Ultraviolet Transport Region

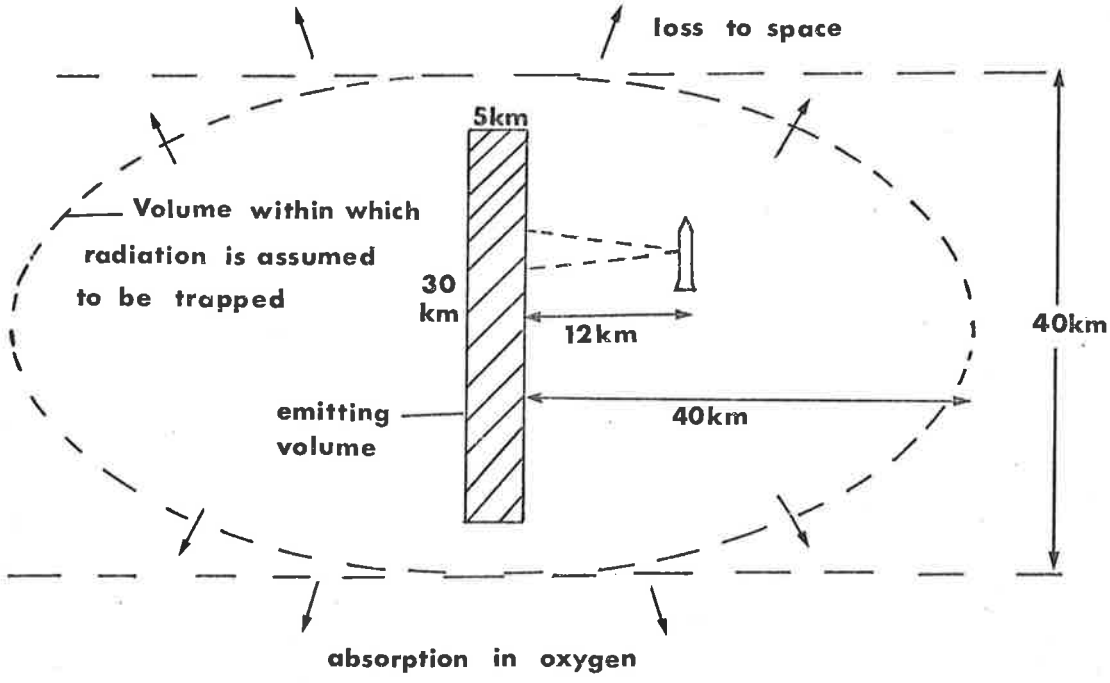

FIGURE 5.12 MODEL OF EMITTING REGION (ARC at +233s)

which corresponded to a power input of 1.3×10^6 watts at 557.7 nm.

The apparent brightness at 391.4 nm (52 kR) was the same as at 557.7 nm at +233 s, giving a calculated emission power of 1.8×10^6 W, and a total for the two major visible emissions of 3.1×10^6 W.

These two emissions, although the most intense in the visible region, constitute only a small part of the total visible radiation power. However, they do indicate the degree of excitement of two of the major constituents of the atmosphere at emission heights and should therefore be a good gauge of the total visible radiation power.

An estimate of the total ultraviolet emission rate was more difficult to derive because the coefficients for absorption and scattering of ultraviolet radiation cover a wide range over the altitudes where auroral emissions occur. Near the lower border of typical auroras, penetration of radiation is limited by absorption in molecular oxygen, while at the upper border absorption is relatively weak and, for 130.4 nm emissions at least, the transport properties of the atmosphere are dominated by resonance scattering in atomic oxygen.

A complete formulation of the effective horizontal transport from an auroral form such as the one being considered would have been extremely difficult to solve, so some simplifications were made in order to make the calculations tractable. Donahue and Strickland (1970) have made extensive calculations of the transport characteristics

of ultraviolet radiation in an aurora, based on a development of radiative transfer theory (Strickland and Donahue, 1970). Their calculations referred only to vertical transport of radiation from an assumed uniform overhead aurora, whereas the present problem concerns horizontal transport from a localized source. Because of the uncertainties in the data interpretation, the calculations given below were intended to give only approximate estimates of the relative emission rates at visible and ultraviolet wavelengths. It was considered that the assumptions and approximations used in the following calculation to formulate the emission model were sufficiently accurate for this purpose.

Because the contributions to the total intensity from different ultraviolet emissions was not precisely determined, all of the auroral ultraviolet radiation detected was assumed to be from the OI (130.4) transition. As indicated by the spectral scans of Miller et al., (1968) and Peek (1970), this emission forms the major contribution to the total intensity, so only a small error should be introduced into the calculations of apparent emission rates by this assumption. It was also assumed that, for this case of a well-defined visible emission region, the ultraviolet emission took place within the same volume.

The essence of the problem was to relate the photon emission rate within this volume to the intensity observed at the rocket, which was about 12 km from the emission region. The situation is depicted in Figure 5.12b. Because atomic oxygen in the vicinity of the detectors

resonantly traps photons at 130.4 nm, enhancement of observed intensities occurs and the measured intensities lead to an apparent emission rate rather than a true 'primary' or 'initial' emission rate.

An estimate was required of the distances which photons could propagate, under trapped conditions, from the emitting volume. In the upwards direction, the atmosphere becomes rapidly thinner, allowing photons to escape to the thermosphere. Below the emitting region, strong absorption by molecular oxygen efficiently removes photons from the radiation field. Trapped radiation propagating horizontally would be subject to losses into the regions above and below, and the effective extent of propagation would be expected to be approximately equal to the separation of the loss regions. Figure 5.12b shows the ellipse which was taken as the limit of the illuminated region. At the position of the rocket, the observed intensity would have approximated the mean intensity within the elliptical volume.

The mean intensity at the rocket (equivalent to 25 kR read from the telemetry output) corresponded to a radiation density of 8×10^5 ph m^{-3} so that the total number of photons within the illuminated volume of 5.5×10^{14} m^3 was 4.4×10^{20} ph. An apparent emission rate was deduced from this by dividing by the mean transit time through the region for untrapped photons. (If the actual transit time could be measured or calculated, this would give the primary emission rate directly; this interval cannot, however, be

measured.) With a direct transit time of 1.7×10^{-4} s, the apparent emission rate was 2.6×10^{24} ph s^{-1} corresponding to 4.1×10^{6} W.

Although this figure is useful for making comparisons with the measurements of other workers, and has been included in Table 5.1, it must be clearly distinguished from the true primary emission rate. The latter is the production rate of photons from particles excited by means other than resonance absorption; its relationship to the apparent emission rate is difficult to determine, particularly for complex auroral forms. Donahue and Strickland (1970) give ratios of their total source function to initial source function of between 10^3 and 10^4 in the centre of the emission range. This ratio would be equivalent to the ratio of the apparent to true emission rates in the case being considered. With a ratio as large as that calculated by Donahue and Strickland, the actual input power to the resonance radiation field would be quite small, and the greatest energy fluxes in the ultraviolet region would be carried by untrapped radiation. In order to determine the true energy flux in the ultraviolet region, an accurate measurement of the partition of the intensity between resonance emissions (such as at 130.4 nm) and untapped radiation would be required.

The apparent emission rates of total ultraviolet and visible (557.7 nm + 391.4 nm) radiation were of the same order (2.6×10^{24} and 7.2×10^{24} ph s^{-1} respectively), and the apparent emitted powers were approximately equal. This estimate of equal ultraviolet and visible photon

emission rates is comparable with the results of several of the workers mentioned in Section 3.4. The ratio found is, however, in contradiction with the results of Murcray (1966) who reported relatively much more ultraviolet radiation, and with the theoretical predictions outlined in Section 3.3. A more accurate determination of the total emission rates in each band would be obtained from vertical measurements in a large uniform emitting region, as analysis of such a configuration would not rely to the same extent as the above calculations on estimates of the effective emitting volume.

5.2.5 Comparison between particle and radiation fluxes

As was mentioned earlier, one of the objectives of the grouping of experiments in the vehicle was to allow the relationships between the instantaneous particle fluxes and emissions to be studied. Extensive data had been obtained on energetic particles from the earlier flights when no ultraviolet radiation was detected, but only limited data on particle fluxes was obtained on this flight, when both the visible and ultraviolet radiation levels were measured. The payload used on this flight did not include all of the experiments from the other groups. Only part of the 'energetic particles' package was flown in this payload, while an electronic fault blocked the data from the soft electron spectrometer experiment. The only data available for comparative purposes from other experiments were those from Geiger-tube high energy electron detectors ($E > 35$ keV) and the electron density measurements from the Frequency Shift Capacitance Probe.

Maximum fluxes of electrons with $E > 35$ keV normal to the

rocket axis were detected at +110 s and +112 s (each 2.9×10^7 electrons $m^{-2}s^{-1}sr^{-1}$); +122 s (3.2×10^7); +135 s (3.9×10^7); +198 s, +224 s, and +228 s (all 2.9×10^7); and +234 s (2.6×10^7) (J. Sharber, private communication). These times are identified in Figure 5.6, which shows that the ultraviolet intensities exhibited some increase around +135 s and +198 s, but no apparent response coincident with the energetic electron peaks at +224 s and +228 s. At the latter two times, however, the rocket was not actually in an active emitting region of the sky.

Peaks in the local electron density (also marked in Figure 5.6) were detected at +97 s, +129 s, +171 s and +198 s by the Frequency Shift Capacitance Probe experiment (N. Eaker, private communication). The second and fourth of these corresponded approximately with peak electron fluxes. In such a non-uniform pattern of auroral activity, when the rocket spent so little of the flight time actually within emission regions, the lack of correlation found between local electron density and fluxes, and emissions from distant parts of the sky was not unexpected. Further comment on the relationship between radiation and particle measurements is made in the following Section.

5.3 Discussion and Summary

An estimate was made in the previous Section of the ratio of emission rates in the ultraviolet region and at 557.7 nm in a bright auroral arc. The ratio referred to the 391.4 nm emission was approximately

the same because, in the bright regions at least, the emission rates at 557.7 nm and 391.4 nm were almost equal. Arriving at an estimate of the relationship between the visible and ultraviolet emission and the particle fluxes was difficult in the absence of most of the particle experiment data.

The total electron flux above 35 keV given by the formula of Hultqvist (1965) for an IBC III^{+} aurora is 2.5 x 10^{11} electrons m^{-2} s^{-1} $ster^{-1}$, which is much greater than the observed 2.6 x 10^{7} electrons m^{-2} s^{-1} $ster^{-1}$. At the time of the measurement, however, the rocket was approximately 12 km away from the active region, so that a low electron count would be expected. A more diffuse and uniform aurora would have been better suited to the radiation-particle comparisons.

Measurements such as those made by Evans (1968) have shown that most of the visible auroral emission would be expected to correlate better with low energy particle fluxes than with the electrons detected by the Geiger tubes. Calculations based on an estimate by Chamberlain (1961, p253) of the electron energy required to produce an IBC III aurora led to an estimated input power of approximately 1.2 x 10^{9} W for the arc examined at +233 s, while a relationship based on data from Evans (1968) gave an electron power of 1.4 x 10^{8} W.

Table 5.1 relates the estimates of radiation power from Section 5.2.4 to these two estimates of input electron power.

TABLE 5.1 RELATIONSHIPS BETWEEN INPUT AND RADIATION POWER

Input →		1.2×10^9 W (Chamberlain)	1.4×10^8 W (Evans)
λ (nm)	Power (W)	% of input	% of input
557.7	1.3×10^6	0.11	0.93
391.4	1.8×10^6	0.15	1.3
(557.7 + 391.4)	3.1×10^6	0.26	2.2
U.V. (105 to 135) (apparent only)	4.1×10^6	0.34	2.9

Comparisons between measurements on different events are, however, of limited value and a complete set of simultaneous measurements by both the photometers and particle detectors would be required before any detailed conclusions could be drawn concerning the imput - output energy relationship.

Several measurements of the ratio of ultraviolet to visible intensities have been summarized by Vreux (1971) for the L-B-H system of nitrogen. No measurements were obtained of the L-B-H system by the set of ion chambers on the flight reported here, although ion chamber which did cover longer wavelength regions were flown on some of the earlier flights in this program. Measurements of the relationship between other ultraviolet and visible emission intensities have been made by other workers under a variety of different conditions and with different types of instruments, and estimates of the relative emission rates have varied

widely (Miller et al., 1968; Opal et al., 1970; Peek, 1970; Murcray, 1966). Some of those measurements included uncertainties due to the unknown extent of the emitting region. The present measurements show a ratio of total ultraviolet to visible emission which is towards the low end of the range covered by other reports (approximately equal photoemission rates in the visible and in the ultraviolet). Further observations in a variety of auroral forms, with freshly calibrated detectors are needed to confirm and extend these results.

Ground-based monitoring of hydrogen emissions was not possible during the flight reported here because of the large amounts of scattered moonlight present in the sky. It is not known to what extent proton excitation contributed to the emissions observed during the flight, so that more measurements under better viewing conditions, and with a more comprehensive set of detectors would be worthwhile continuations of this work. The absence on this occasion of aurorally associated Lymanα radiation did, however, indicate that the event observed was dominated by electron excitation.

More complete measurements are also required to determine the spatial and spectral distribution of the ultraviolet emission which appeared to be, at least in part, separate from the visible aurora on the occasion reported here. Satellite observations (Joki and Evans, 1969) have also produced evidence of bright patches within diffuse ultraviolet auroras, and further studies, both from satellite and from rocket platforms, of the relationship between the emitting regions would be

valuable.

In future multiple-band photometry, as used in this work, advantage should be taken of the latest developments in electronic circuit techniques to enable the fields of view of the ion chambers to be made narrower, with the same acceptance angle as the photomultipliers (as in the original design of the photometer package). This would enable the bright emission regions to be more precisely located. Another prerequisite for a more detailed analysis of spatial relationships would be a more comprehensive set of attitude sensing devices to enable a full attitude solution to be generated.

The experiments described here form the basis for a more detailed and extensive study, with the inclusion of the suggested improvements, of auroral emissions. Instruments such as those described, with their good angular and time resolution and rapid scan rate, are well suited to the study of the temporal and spatial relationships between those emissions which can be separated by the limited spectral resolution obtainable. While a successful flight of ion chambers sensitive to the N_2 (L-B-H) emissions would be useful, it is considered that the most valuable results could be obtained in the study of proton auroras. To this end, conversion of one of the photomultiplier channels to monitor the very much less intense visible hydrogen emissions (e.g. H_β, 486.1 nm) would provide useful comparisons with auroral Lymanα emissions.

CHAPTER 6 ULTRAVIOLET AIRGLOW

6.1 Introduction

6.1.1 The region covered by this study

In the period since the first observation of geocoronal ultraviolet airglow (Byram et al., 1957), a number of measurements of this radiation have been made. The earliest experiments were restricted to the lower thermosphere by the limitations of the available rocket vehicles. With the development of high-altitude satellites and interplanetary probes, the emphasis in observations has moved to higher altitude regions which were previously inaccessible.

The experiments reported here were designed to be flown on small sounding rockets which carried the instruments to altitudes not far above the range in which Lymanα airglow radiation is absorbed. The results obtained from the measurements therefore concern the characteristics of the airglow radiation in the regions of its strongest interaction with the atmosphere.

Other measurements of the airglow from high altitude rockets and satellites have of necessity tended to exclude study of the lower-altitude interaction region. Workers formulating models of scattering in the hydrogen geocorona have usually considered the atmosphere to be totally absorbing at some selected altitude near 100 km. The consequences of assuming total absorption at a single height have been discussed by Meier (1969) and Meier and Mange (1970). This approximation to the actual absorption profiles is satisfactory for the calculation of scattered radiation intensities at high altitudes,

but is not appropriate when radiation near the absorption region is being considered. The determination of the actual absorption profiles of the airglow radiation was basic to this study of the interaction between the atmosphere and the radiation.

Although Lymanα airglow has been observed on both the day and night sides of the Earth, the observations reported here were all made at local night time. Measurements of the geocoronal airglow are generally made easier at night by the low intensities of other airglow emissions within the spectral range of simple ion chamber detectors, and by the absence of direct solar illumination on the instruments.

6.1.2 Molecular Oxygen

Molecular oxygen is responsible for most of the atmospheric absorption of radiation in the vacuum ultraviolet region around Lymanα, even though the Lymanα line lies in a deep 'window' where the cross-section of the oxygen molecule is much lower than in adjacent parts of the spectrum. In a mixture of gases with the composition of accepted model atmospheres (based on both measured and estimated constituent densities), all other constituents would account for less than 5% of the total absorption.

Measurements of molecular oxygen density profiles have been made on numerous occasions during daylight hours and by many workers. The oldest established technique involves reduction from measurements of the attenuation of solar ultraviolet radiation, as described by

(1e). A major advantage of this optical method over direct sampling techniques is the relative immunity to local contamination by the rocket vehicle. Because of the long absorption path involved (≃ 10 km effectively), even strongly absorbing gases in the vicinity of the rocket do not generally distort the measurements. The study of the altitude distribution of airglow radiation is a similar form of absorption spectroscopy, and also benefits from a high degree of freedom from the effects of local contamination.

It had been expected that the diurnal variations of the relatively inert major species (O_2, N_2) below 120 km would not be very large. The density profiles were thought to behave regularly, being defined by the local kinetic temperature, except for the effects of the photodissociation of oxygen. Some apparently significant variations have, however, been found. Weeks and Smith (1968) have observed quite rapid changes in the oxygen density profile near dawn. Roble and Norton (1972) have also given evidence of a substantial diurnal density variation at 120 km, while de Vries (1971) has found correlations of density with geomagnetic activity down at least to 140 km.

The number of properly co-ordinated measurements is as yet small, and the exact oxygen profiles applicable to night-time conditions (as distinct from sunrise - sunset configurations) is not well known. By measuring the atmospheric absorption in the ultraviolet spectrum of a star, Opal and Moos (1969) have estimated column densities of molecular oxygen above 120 km at night. Their

values showed no significant departures from daytime measurements.

In the lower part of the Lymanα absorption height range (below 90 km) the dissociation of molecular oxygen is negligible and effective mixing of the major constituents occurs; above 90 km a significant portion of the oxygen is in atomic form and diffusive separation starts to become evident. The molecular oxygen concentration derived from photochemical models of the atmosphere is sensitive to the assumed value of the eddy diffusion coefficient near the turbopause, which lies within the absorption range of Lymanα radiation. The empirical nature of the current diffusion models has been discussed by Hunt (1971), and it is apparent that more experimental measurements of atmospheric composition in the vicinity of 100 km are required.

The relevant density profiles given in the U.S. Standard Atmosphere Supplements, 1966, have been used here for the calculation of absorption corrections, and for comparison with the results of these measurements. The absorption cross-section of the oxygen molecule at Lymanα has been taken as 1.0×10^{-24} m^2 throughout this work. This is close to the measured value near the centre of the line (Ogawa, 1968). Although the cross-section is somewhat higher at the wavelengths of the 'wings' of the solar emission line, the spectral width of the airglow radiation is small enough for the cross-section at the line centre to be used without significant error.

6.1.3 Atomic hydrogen

Atomic hydrogen is an important active constituent in the upper mesosphere and the thermosphere. Although hydrogen is only a minor constituent in the mesosphere, the range of chemical reactions in which it participates makes a knowledge of the atomic hydrogen distribution important to the understanding of the photochemistry of the region.

Direct measurements of the atomic hydrogen density are difficult because of the relatively low density and the high chemical activity of the species. The density of hydrogen in the thermopause has usually been inferred from ground-based optical measurements (Tinsley (1963), and Meier (1969), based on measurements of Balmer α emissions), from the observed intensity and distribution of the Lymanα airglow (Meier and Mange, 1970), or from the altitude variations of the solar emission line profile (Jones et al., 1970).

Interpretation of the Lymanα airglow measurements is complicated by the large number of optical depths in hydrogen above 100 km. Because of the small weight of the atom, kinetic velocities are high and there is a significant escape flux upwards. Densities depart considerably from diffusive equilibrium profiles, and a suitable model atmosphere must be assumed in order to determine the density scales from measured airglow intensities.

Photochemical models have been used to predict the behaviour of the atomic hydrogen density in the mesosphere and lower thermosphere

and large diurnal variations are expected to occur, particularly below 85 km (Hunt, 1971). Direct measurements of the density profile in this region are however, extremely difficult. The maximum absorption of Lymanα radiation occurs in the region below 90 km, and the presence there of significant amounts of atomic hydrogen has important effects on the absorption process.

Atomic hydrogen at thermospheric densities re-radiates virtually all Lymanα photons which it absorbs (resonance scattering), so does not itself contribute to the absorption. Molecular oxygen is still responsible for the majority of the pure absorption. The resonance scattering by hydrogen has the effect of imprisoning (trapping) the radiation in the absorption region, thus modifying the absorption profiles. A treatment of this process is developed in full in Section 6.3.3.

6.1.4 The objectives of the present work

The experimental work was directed towards making measurements of the Lymanα airglow in the mesosphere and lower thermosphere. From the results obtained the composition of the transporting medium (atmosphere) could be inferred. The densities of both atomic hydrogen and molecular oxygen are reflected in their effects on the transport of the airglow radiation.

One payload (7.2.1) went to much greater altitude (166 km) than the others, and carried, in addition to Lymanα ion chambers, a detector to measure the extreme ultraviolet resonance airglow emissions of

the helium atom and ion. The helium airglow is not measurable at the heights reached by the other rockets.

Measurements of airglow radiation unavoidably include some sources which are not strictly airglow. The difficulty of distinguishing the airglow radiation from these other sources (particularly in the case of Lymanα radiation) has led to the examination of these non-airglow sources becoming an integral part of airglow studies. Some of these sources are mentioned in Section 6.4.

6.2 The Development of Airglow Studies

In this Section a brief summary is given of earlier airglow research in order to provide a background to the results and discussion in the following Chapters.

6.2.1 General features

The majority of airglow measurements have been done with ionization chambers which were basically similar to those described in Chapter 2. The instruments have therefore been spectrally broad-band, and even in those cases where grating dispersion was used, the resolution obtained was not sufficient to adequately separate the spectral components of the Lymanα airglow emission lines.

The first report by Byram et al., (1957) was followed by a series of flights by the same group to obtain more accurate data (Kupperian et al., 1958; 1959; Chubb et al., 1961). Some common features in their observations, which have generally been confirmed

by later work, include:-

1. Measurable intensities from both above and below the rocket at altitudes above 80 km.
2. A remarkable constancy of the ratio of zenith to nadir intensities above 120 km of near 2 : 1.
3. A fairly uniform overhead intensity distribution, with a slightly reduced intensity in the antisolar direction.

The experimenters thought that the source was solar radiation resonantly scattered from atomic hydrogen distributed in interplanetary space, and their views were supported by Brandt and Chamberlain (1959). Johnson and Fish (1960) then suggested that the hydrogen causing the scattering was moving with the Earth (a geocórona), and scattering by Earth-bound hydrogen has since been accepted as the source of most of the Lymanα airglow. It is interesting to note, however, that interest in the interplanetary medium has revived recently in connection with minor (extraterrestrial) components of the airglow which cannot be accounted for by geocoronal models (Tinsley, 1971).

6.2.2 The spectrum of the night airglow

The dominance of the vacuum ultraviolet radiation in the night sky by Lymanα emissions was demonstrated by several techniques. Spectrographic measurements by Morton (1962) showed no other strong emissions in the spectral region around Lymanα. Differential measurements making use of the sharp transmission cutoff of calcium

fluoride near 122 nm indicated that significant intensities of radition with $\lambda > 122$ nm occur only towards the solar direction (Moos) and Fastie, 1967), or in localized equatorial and auroral regions (Hicks and Chubb, 1970). Spectrophotometer experiments (Barth and Schaffner, 1970; Buckley and Moos, 1971) have also shown that, in the vacuum ultraviolet region, Lymanα is by far the most intense emission found in the night sky at mid latitudes.

One partly conflicting observation has, however, been reported. During one flight Chubb and Byram (1963) detected an airglow emission in the range 129 - 135 nm from part of the sky, but this feature was not seen on a second flight. They believed the radiation was in the 130 nm triplet (Figure 1.2) resonantly scattered by atomic oxygen above the sunwards horizon, but they were able to give only an approximate estimate of the intensity.

6.2.3 Geocoronal models

A number of models of the hydrogen distribution have been produced, incorporating in different ways the effects of the kinetic velocities of the thermospheric hydrogen (Chamberlain, 1963; Kockarts and Nicolet, 1963; Thomas, 1963). The atomic hydrogen in the thermosphere is not in diffusive equilibrium, and the high kinetic temperatures combinedwith the low atomic weight causes a considerable fraction of the atoms to be in satellite orbits or on escape paths. As the exospheric temperature varies with local time, the hydrogen distribution around the Earth is asymmetric to an extent which depends

on the degree of lateral flow (McAffee, 1967). A day-night assymmetry was found to be necessary to reconcile the optical depths of hydrogen found from solar observations (Purcell and Tousey, 1961; Jones et al., 1970) with the densities which the models required to produce the observed night airglow intensities.

6.2.4 The extraterrestrial background

An experiment employing an absorption cell technique (Morton and Purcell, 1962) indicated that some part of the night glow radiation was in the vicinity of the Lymanα wavelength, but outside of the approximately 1 pm absorption width of their cell, (1 pm = 10^{-12} m = 10^{-2} Å). This 'hot' or 'extraterrestrial' background component has been found to be consistent with the fitting of airglow spatial distributions to models developed by Meier (1969) and Meier and Manage (1970). With suitable background corrections, these models can be adjusted to fit closely the experimental observations made from satellites at altitudes where the lower boundary conditions of the radiation field are unimportant.

A more complete discussion of background radiation nature and sources is given in Section 6.5 because of its importance to the experiment described in Chapter 8.

Two approaches to the separation of the background components have been used in the past. Several satellites have carried vacuum ultraviolet photometers to large distances from the Earth. These photometers were intended primarily for studies of other planetary

atmospheres, but during transit have also provided useful data from regions where the direct geocoronal component is small.(Wallace et al., 1970; Mange and Meier, 1970; Bath, 1970). Alternatively, lower-altitude instruments have been fitted with absorption cells to separate the core radiation from that which is away from the line centre (Morton and Purcell, 1962; Winter and Chubb, 1967). An absorption cell was incorporated in the flight instrument described in Chapter 8, in an attempt to separate out the line centre component. Separation of the central component is desirable because of the different conditions governing its transport in the absorbing region. The following Section (6.3) outlines some aspects of the scattering and absorption of Lymanα, both in and away from the line centre, in the region of the atmosphere below 120 km.

6.3 Transport of Airglow Radiation through Atmospheric Gases

6.3.1 Solar radiation near the Earth

The vacuum ultraviolet solar spectrum is dominated by the Lymanα emission line. The complex spectral shape of this line was first observed by Purcell and Tousey, (1960). Their measured profile is shown in Figure 6.1. A series of line spectra of the direct solar radiation at different altitudes was obtained by Jones et al. (1970), showing a narrow core region from which the radiation had been apparently absorbed more strongly than in the side peaks of the line. Figure 6.2 shows the measured spectra superimposed on their model profiles from which they deduced hydrogen densities. Reduced intensities

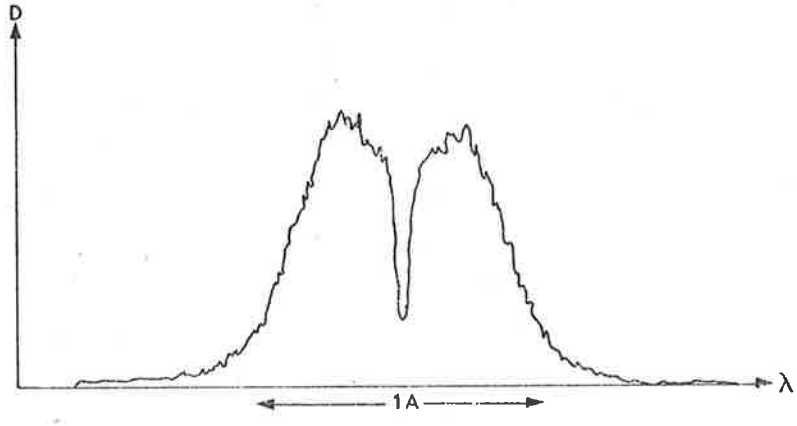

FIGURE 6·1 THE PROFILE OF THE SOLAR LYMAN « LINE
(FROM PURCELL AND TOUSEY, 1960)

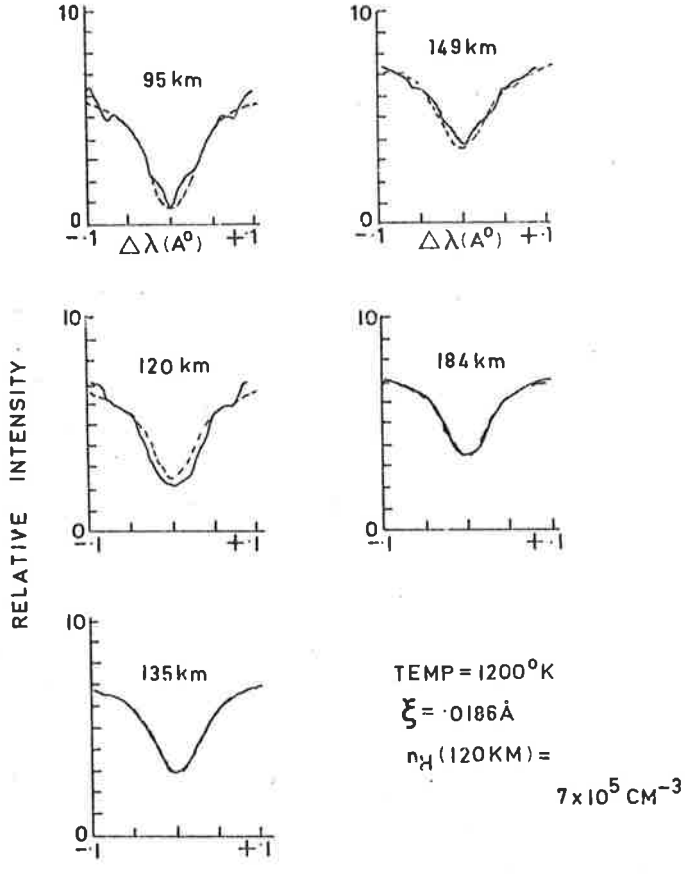

FIGURE 6·2 PROFILES OF THE LINE CENTRE REGION
(FROM JONES etal, 1970; based on their Fig 1)

were measured at the line centre because the radiation had been scattered away from the sun-Earth direction by the atomic hydrogen along the line to the sun.

Radiation sufficiently removed from the centre wavelength undergoes simple absorption without scattering, according to (1a), and only a small fraction of the total solar line energy is multiply scattered by atomic hydrogen in the atmosphere. Resonance trapping effects can therefore be ignored in daytime absorption profile measurements when the whole spectral width of the solar line contributes to measured flux. However, resonance trapping of radiation cannot be ignored in night sky measurements, as only the central part of the solar emission line contributes to the observed airglow intensity, and the fraction of the incident radiation susceptible to resonance scattering is therefore much larger.

The relative magnitudes of the scattered and unscattered components are easily estimated. The data of Bruner and Parker (1969) indicate a total Lymanα line strength of near 3×10^{15} photons m^{-2} s^{-1} over the line width of approximately 0.1 nm, and 3×10^{16} photons m^{-2} s^{-1} nm^{-1} at the centre of the line. Vidal-Madjar et al., (1972) give 3×10^{15} ph m^{-2} s^{-1} over the whole line and 5×10^{16} ph m^{-2} s^{-1} nm^{-1} at the centre. Assuming that the width of the core susceptible to resonance scattering is 1.2×10^{-3} nm (Section 6.3.3) gives an estimated 5×10^{13} photons m^{-2} s^{-1}, or less than 2% of the integrated direct solar line intensity, lying within the strongly scattered core

region. The errors introduced through assuming pure absorption by molecular oxygen in day-time profile analysis would thus be small. The equivalent fraction is nearer 20% in the night sky Lymanα radiation and resonance effects must be therefore taken into account (Section 6.3.3).

The total solar Lymanα flux has now been monitored by a number of satellite and rocket detectors over a period of about one solar cycle. The total line flux appears to be relatively constant, but the line core flux has been indicated to be more variable, (Meier, 1969) and it is this component which provides the source for the night airglow. Meier's measurements suggest a variation on a monthly scale of about 30%. Longer term variations could be greater than this, but there are uncertainties involved in comparing the absolute fluxes measured at widely spaced times and by different workers. By using an absorption cell instrument, Vidal-Madjar et al., (1972) found that the short-term variations in line core flux correlated with standard measures of solar activity, and that the range of the variations was close to 1.5 times the range in the total line flux measured. It appears that, despite this enhanced variability, the solar Lymanα core flux provides a reasonably constant excitation source for the night airglow, being predictable and stable to within a factor of two, at least over periods much shorter than a solar cycle.

6.3.2 Resonantly scattered radiation in the night sky

Solar radiation passing the Earth can be scattered into the vicinity of a detector in the night-side shadow region if its frequency is close enough to the Lymanα line centre. The forward scattered rays (from region FS in Figure 6.3) travel by a short path, but through high density regions, to form a source near the sunwards horizon from the detector. Rays at greater grazing heights pass through a larger volume of lower density hydrogen to be scattered down from near-zenith directions (BS). The data from the vehicle C1014 (Chapter 8) showed these two components as apparently distinct and readily separable. The spatial intensity distribution could be described as one source almost uniform over the upwards hemisphere, combined with another, centred on the sunwards horizon direction and extending over the sky about 60^0 from that direction. Further mention of this apparent separation into two sources will be made in Chapter 8 where the instrumentation and data are described.

Figure 6.3 shows the geometry of the geocoronal scattering region. Also shown beside the ray paths are sketches indicating the radiation spectral profile (I_ν) and the hydrogen absorption coefficient (k_ν) in several regions. The sketches are not based on accurate computations and are included only to indicate the relative changes in the two functions along the ray paths. The position of the detector (D) is shown at a point where the solar depression is 30^0, which was typical for the Cockatoo flights reported in this work.

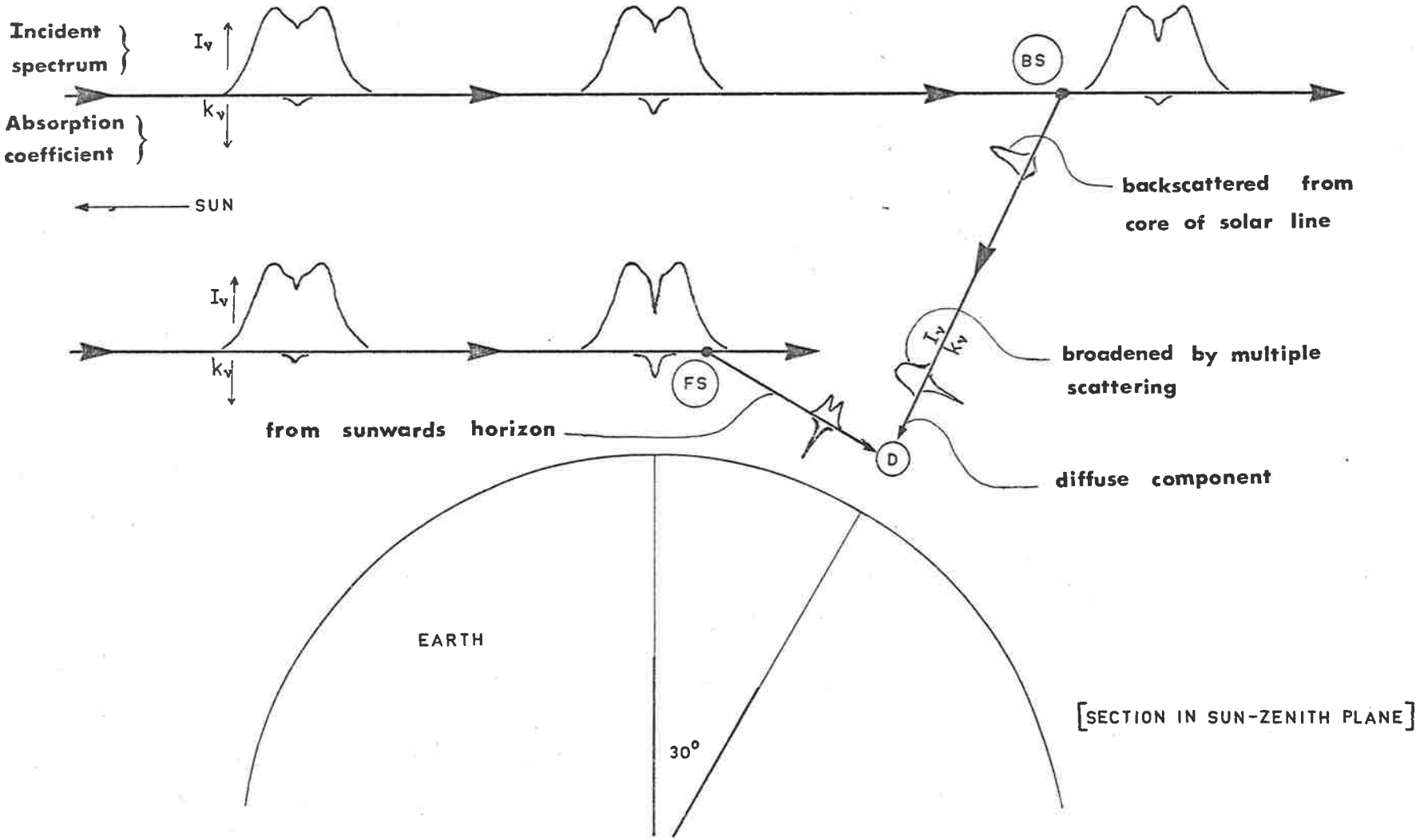

FIGURE 6·3 GEOCORONAL SCATTERING GEOMETRY

Geocoronal hydrogen strongly scatters the solar radiation within a narrow frequency range about the resonance frequency. The width of the (resonance) absorption range is determined by the natural and Doppler broadening of the absorption line of the atoms. The hydrogen atom, being simple, has no alternative energy dissipation mechanism, so absorbed photons are re-emitted and are not lost to the radiation field. This resonance absorption, or scattering, is in contrast with the pure absorption of Lymanα by molecular oxygen where the photons are permanently lost to the Lymanα radiation field.

The width of the solar spectrum subject to resonance scattering in the geocorona, and the corresponding absorption coefficient of the atmospheric hydrogen, can be estimated. Following the notation and theory of Mitchell and Zemansky (1961), the spectral width, $\Delta\nu$, will be written in terms of frequency, ν, rather than in wavelength. In any region of space over which the gas density is nearly constant, the reduction in the intensity of the radiation (the solar Lymanα radiation in the case of primary geocoronal scattering) can be described by:-

$$I_{\nu,\delta s} = I_{\nu,0} \exp\{-k_\nu ds\} \qquad (6a)$$

where δs is the path length through the region being considered, and k_ν is the absorption coefficient, in units of reciprocal distance. In the case of pure Doppler broadening of the absorption line due to the thermal motion of the atoms, the absorption coefficient has

the form:-

$$k_\nu = k_0 \exp\{-\left[\frac{2(\nu-\nu_0)}{\Delta\nu_D}\cdot\sqrt{\ln 2}\right]^2\} \qquad (6b)$$

where the Doppler width, $\Delta\nu_D$, $= \frac{2\sqrt{2R\ln 2}}{c} \cdot \nu_0 \cdot \sqrt{\frac{T}{M}}$ (6c)

k_0 = absorption coefficient at the frequency, ν, of the line centre

c = velocity of light

R = universal gas constant

T,M = temperature and molecular weight of the gas

The coefficient k_0 can be evaluated by integration over the width of the absorption line to give:-

$$k_0 = \frac{2}{\Delta\nu_D}\cdot\sqrt{\frac{\ln 2}{\pi}} \cdot \frac{\lambda_0^2}{8\pi} \cdot \frac{g_2}{g_1} \cdot \frac{n[H]}{L} \qquad (6d)$$

where g_2 and g_1 are the statistical weights of the upper and lower states in the resonance transition, L is the lifetime of the upper state, and $n[H]$ is the number density of the hydrogen atoms. For the case of natural line broadening only,

$$\Delta\nu_n = \frac{1}{2\pi L} \qquad (6e)$$

and the line has a different (Lorentz) shape. The relative importance of Doppler and natural broadening in the geocoronal case can be found by evaluating (6c) and (6e):-

$\Delta\nu_n = 1.33 \times 10^7 \text{ sec}^{-1}$

$\Delta\nu_D = 5.8 \times 10^{10} \text{ sec}^{-1}$ (for $T_H = 1000^0$K)

(A temperature of 1000^0 K is representative of the thermosphere between 500 km and 5000 km, where most of the primary scattering of the solar radiation occurs.) The absorption width is therefore determined almost entirely by the kinetic temperature of the gas, and corresponds to $\Delta\lambda$ = 2.8 pm (0.028Å) (full width half maximum). The total amount of radiation absorbed would be independent of gas temperature if the incident radiation intensity were independent of frequency, but the spectral distribution of the solar radiation incident on the region BS of Figure 6.3, is far from uniform. The intensity of radiation available for scattering near the Earth within a spectral width of the order of 2.8 pm will depend on the temperature and density of the scattering hydrogen along the ray pathfrom the sun. The primary scattered radiation which passes into the shadow region behind the Earth has an intensity determined by both solar activity and high altitude hydrogen density, and a spectral line width determined by the hydrogen temperature in the primary scattering region.

6.3.3 Transport and absorption of the resonance radiation

For any reasonable assumed hydrogen temperature and density profiles, the exosphere is optically thick to photons near the centre of the Lymanα line. Acceptable values of hydrogen density ($5 \times 10^{13} m^{-3}$) and temperature (200^0 K) at 100 km, combined with the large scale height give many optical depths above that altitude. However, the Doppler width of the absorption cross-section at rocket altitudes (at D in Figure 6.3) is narrower than the spread (2.8 pm) of the primary

back-scattered radiation from the region BS. The full-width-half-maximum of the absorption cross-section for 200^0 K atoms is, from (6c) 2.5×10^{10} sec^{-1} corresponding to $\Delta\lambda = 1.2$ pm. The core of the solar line, back-scattered from the region BS, is therefore a spectrally broad source compared with the absorption width of the cold hydrogen near 100 km. Radiation reaching the pure absorption region below 120 km will have been spread by multiple scattering over an even wider spectral range than the Doppler width of the primary scattering. The broadening by multiple scattering can be evaluated from the expression

$$W_D = \Delta\nu_D \left[\ln\left(\frac{\tau_o}{\ln 2}\right) \Big/ \ln 2 \right]^{\frac{1}{2}} \qquad (6f)$$

where W_D is the scatter-broadened width of a line with a primary width of $\Delta\lambda_D$ (Fastie et al., 1964). Taking a value of $\tau_o = 10$ at 100 km (i.e. 10 optical depths at the line centre in a vertical column above 100 km gives $W_D \simeq 2\nu_D$. The calculated spectral width of scattered radiation incident from above on the atmosphere at 100 km based on this figure is 1.1×10^{11} sec^{-1}, corresponding to $\Delta\lambda = 5.6$ pm.

The fraction of this incoming radiation near 100 km which is within two Doppler widths for 200^0 K hydrogen is subject to significant resonance scattering in the absorption region, while the photons in the wings of the incident spectrum pass through only small optical depths of hydrogen over the range in which pure absorption by oxygen occurs. These photons, with energy far enough removed from the centre of the resonance line, will be absorbed in a manner described approximately by (1a). For radiation being observed by a collimated

detector, the effective absorption occurs along the detector line of sight.

Those photons near the resonance line centre, being subject to scattering in the absorption space, will not be absorbed in such a simply described manner. Line core radiation reaching a detector in the absorbing space will not have followed the line of sight of the detector, and its effective path length will be longer than the direct path. The ratio of the mean photon path length to the direct path length will depend on the viewing geometry and on the relative absorption coefficients of the hydrogen and oxygen throughout the atmosphere. As can be seen from (6b), (6c) and (6d), the absorption coefficient of hydrogen is a function of the temperature and density of the hydrogen and of the photon wavelength, whereas the absorption coefficient of molecular oxygen near Lymanα, at the pressures prevailing, is a function of the oxygen density only. In this work the ratio of the absorption coefficients has been called R(ν, h)

$$\text{where } R(\nu, h) = \left(\frac{k_\nu [H]}{k_\nu [O_2]} \right)_{/h} \qquad (6g)$$

In the region of strongest oxygen absorption (near 85 km), the absorption coefficient of hydrogen at the line centre is greater than that of oxygen, and photons undergo many resonance scatterings in the absorbing region. The absorption coefficient of mesospheric hydrogen can be calculated from (6d) using a temperature of 200^0 K and a density of 8×10^{13} m^{-3} as reasonable values for night time conditions

at 90 km. This gives $k_0[H] = 1.9 \times 10^{-3}$ m^{-1}, while the effective absorption cross-section at the centre of the line, $\sigma_0[H] = k_0[H] / n[H]$, is 2.4×10^{-17} m^2. This can be compared with $\sigma_0[O_2] = 1.0 \times 10^{-24}$ m^2 for oxygen, which with a number density (U.S. Standard Atmosphere, 1966) of 1.3×10^{19} m^{-3} at 90 km, gives $k_0[O_2] = 1.3 \times 10^{-5}$ m^{-1}; $R(\nu_0, 90) = \{k_o[H] / k_o[O_2]\}$ 90 km would be about 150. Thus at the line centre the volume rate of resonance scatterings (m^{-3} s^{-1}) greatly exceeds the loss rate due to oxygen absorption. This condition also applies over the whole oxygen absorption region down to where the hydrogen density should drop rapidly with decreasing altitude. Model calculations (Hunt, 1971; Thomas and Bowman, 1972) suggest that this occurs at night near 80km, at which altitude $n[O_2] \simeq 6 \times 10^{19}$ m^{-3} and $k_o[O_2] \simeq 6 \times 10^{-5}$ cm^{-1}. Below the altitude where $R(\nu_0, h) \simeq 0.2$, i.e. where $n[H] \lesssim 5 \times 10^{11}$ cm^{-3}, the volume loss rate by oxygen absorption will greatly exceed the volume scattering rate by hydrogen, and the intensity will conform closely to the form (1d) of pure absorption. Figure 6.4 illustrates the relationship between the quantities mentioned above. With decreasing altitude, $k_\nu[O_2]$ increases continuously while $k_\nu[H]$ drops suddenly near 80 km. Where $R(\nu_o, h) >> 1$ there is also a finite spectral band within which $R(\nu, h) >> 1$.

Mathematical methods which have been developed for the treatment of diffuse radiation transport can be used to indicate the behaviour of the resonance-line core radiation in the absorption region.

In this treatment, the atmosphere is considered macroscopically

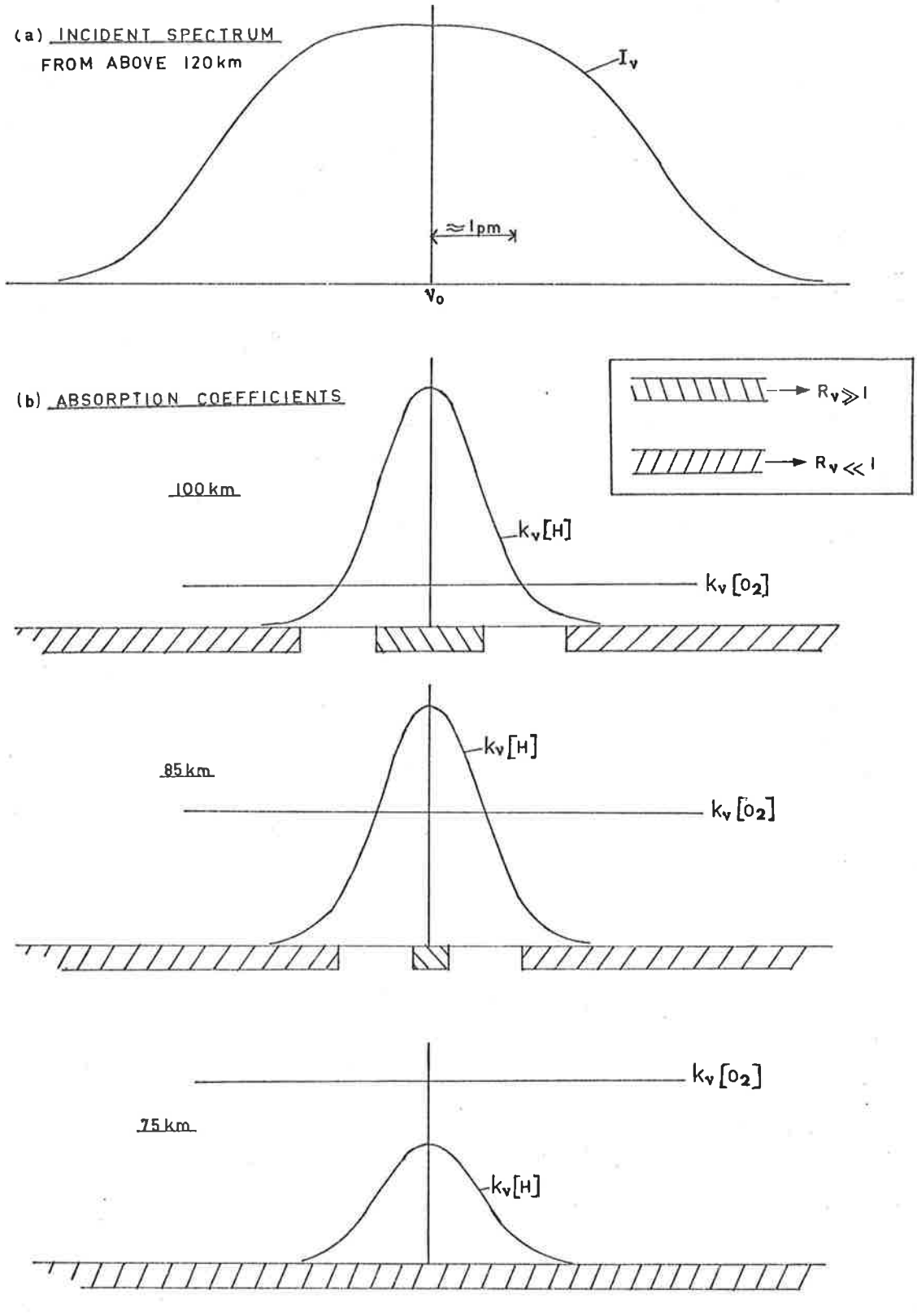

FIGURE 6·4 RELATIONSHIP BETWEEN ABSORPTION COEFFICIENTS OF H, O_2

as a gas made up of identical particles having absorption properties equivalent to a mixture of hydrogen and oxygen. These are the only species which have significant cross-sections for interaction with Lymanα radiation between 70 and 120 km. Only the central part of the airglow spectrum is affected by resonance scattering, and it is this line core radiation which is considered in the following theory; the line-edge radiation can be treated by simpler methods.

A mathematical treatment, based on one outlined by Chandrasekhar (1960) is given below for the following conditions:-

(1) isotropic, non-conservative scattering

(2) a plane-parallel, semi-infinite atmosphere

(3) axial symmetry of the radiation field about the zenith

The first condition does not strictly apply in this case to individual scattering events, but should be approximately valid in multiple scattering where $R \gg 1$; it is applied because of the worthwhile simplification it introduces to the treatment. The process is macroscopically non-conservative because a fraction of the photons interacting with the atmosphere are not re-radiated (i.e. those absorbed by oxygen). The mean free path of imprisoned photons is too short for curved Earth considerations to be important, while the large optical depths of hydrogen above the absorption region, and effectively infinite density of absorbing oxygen below, make the semi-infinite

approximation reasonable. Because there are many optical depths in H above the heights being considered, all photons have been scattered at least once, and the incoming radiation will be approximately symmetrical about the zenith.

The general radiative transfer equation

$$\frac{d I_\nu}{k_\nu \, ds} = I_\nu - J_\nu \tag{6h}$$

may be written, for the monochromatic plane-parallel, axially symmetric case as

$$\mu \frac{dI(\tau, \mu)}{d\tau} = I(\tau, \mu) - J(\tau, \mu) \tag{6j}$$

where $\mu = \cos\chi$

τ = optical depth = $\int_h^\infty k(h')\, dh'$

J = the source function (re-emitted radiation)

$I(\tau, \mu)$ is the intensity of radiation moving at an angle of χ from the zenith

For isotropic scattering, with an albedo = ω (i.e. the probability of re-emission after absorption) it can be shown that

$$\mu \frac{dI(\tau, \mu)}{d\tau} = I(\tau, \mu) - \frac{\omega}{2} \int_{-1}^{1} I(\tau, \mu')\, d\mu' \tag{6k}$$

This has a solution of the form

$$I(\tau, \mu) = g(\mu) \exp\{\kappa\tau\} \tag{6l}$$

where κ is a constant and $g(\mu)$ is a function of μ only. By successive substitution in (6k), the solution can be shown to have

the form

$$I(\tau , \mu) = \frac{C}{1 + \kappa\mu} \exp\{-\kappa\tau\} \qquad (6m)$$

where C is a constant and κ satisfies the relationship

$$\omega = \frac{2\kappa}{\ln [(1 + \kappa)/(1 - \kappa)]} \qquad (6n)$$

In the altitude range of interest, each Lymanα photon will be absorbed by either a hydrogen atom or an oxygen molecule. For the first case $\omega = 1$ (re-emission) and for oxygen absorption, $\omega = 0$. The mixture of gases behaves as a nonconservative scatterer with $0 < \omega < 1$. If the local absorption coefficient of hydrogen and oxygen are in the ratio R as in (6g), then

$$k_{[TOTAL]} = k [H] + k [O_2]$$

$$= (R + 1) k [O_2] \qquad (6p)$$

The quantities in (6p) are all functions of ν and h, and when broad-band measurements are being considered, an integral over ν should be formed to find the effective $k_{[TOTAL]}$ at each height. The process is very involved, and in this case only the centre wavelength, ν_0, will be considered. The treatment is then strictly applicable only to measurements made with absorption-cell instruments, but does indicate the general behaviour of radiation near the line core. For simplicity the subscripts $_0$, referring to ν_0, have been omitted below.

The attenuation of the radiation with decreasing altitude may

be found by differentiating (6m)

$$\frac{1}{I(\tau, \mu)} \cdot \frac{dI(\tau, \mu)}{dh} = \kappa \cdot k_{[TOTAL]} \qquad (6q)$$

$$= \kappa (R + 1) k[O_2]$$

$$= M k [O_2] \qquad (6r)$$

For the case of a pure oxygen atmosphere, $\omega = 0$, and

$$\frac{1}{I(\tau, \mu)} \cdot \frac{dI(\tau, \mu)}{dh} = k[O_2] \qquad (6s)$$

Therefore M is the factor by which the presence of the resonance scatter, hydrogen, increases the effective absorption coefficient of the oxygen which is present. M depends on R and therefore absorption measurements leading to values of M(h) can be used to derive R(h), which relates the densities of atomic hydrogen and molecular oxygen.

Table 6.1 lists calculated values of R, κ and M for a range of ω. The entries at the extreme top and bottom of the table are not relevant to the absorption of Lymanα in the atmosphere, but are included to show the trends as $\omega \to 0$ and $\omega \to 1$. Figure 6.5 shows ω, κ and M as a function of R. The values of R which would be expected to be relevant to this study lie in the range 10 to 1000.

The condition $R >> 1$ is not satisfied over the total spectral width of the Lymanα airglow, so the total line intensity could not be expected to be described fully by the mathematics of transport in an optically thick, isotropic scattering medium. The properties of the medium vary over the line width from optically thick to optically

TABLE 6.1 CALCULATION OF ENHANCEMENT FACTORS

R $= \frac{k[H]}{k[O_2]}$	ω (albedo for single scattering)	κ	M $= \kappa(1 + R)$
0	0	1.00	1.00
0.11	.1	≈1.00	1.11
0.25	.2	.9999	1.25
0.428	.3	.9974	1.43
0.666	.4	.9856	1.65
1.00	.5	.9575	1.92
1.50	.6	.9073	2.27
2.33	.7	.8286	2.76
4.00	.8	.7104	3.55
9.00	.9	.5254	5.25
19.0	.950	.3795	7.59
32.3	.970	.2964	9.87
49.0	.980	.2429	12.1
99.0	.990	.1722	17.2
199	.995	.1222	24.4
999	.999	.0548	54.8
1999	.9995	.0387	77.4
9999	.9999	.0187	187

(M is the absorption enhancement factor in a mixture with a ratio of scattering coefficient to absorption coefficient of R)

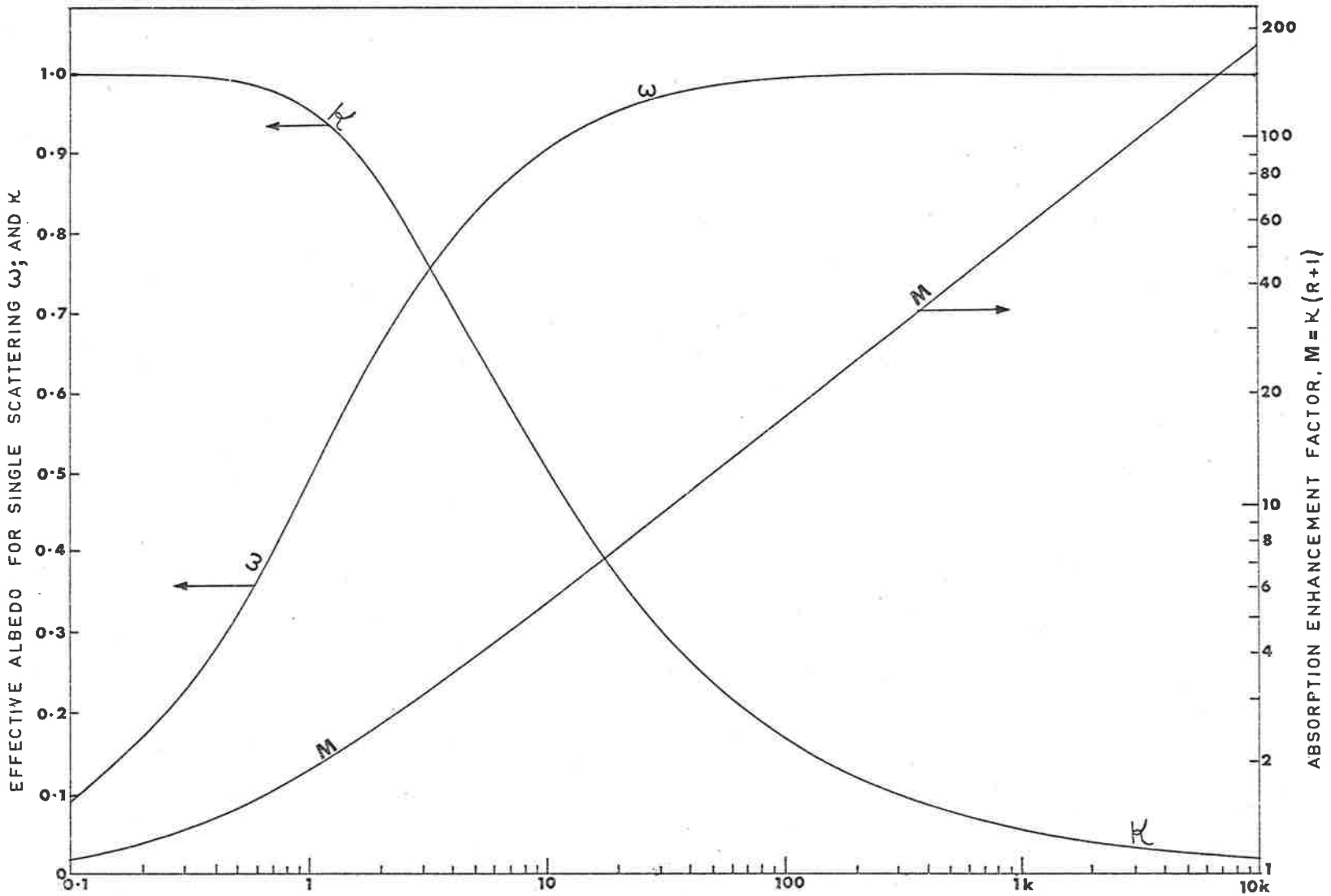

FIGURE 6·5 ABSORPTION ENHANCEMENT FACTOR

thin, and there is of course no sharp boundary separating these two extremes. As an aid to interpreting the experimental measurements, the assumption was made that the intensity measured can be divided into two components (one for which $R(\nu) >> 1$ and another for which $R(\nu) << 1$) so that the absorption profiles of the components could be considered separately. This might appear to be an extreme assumption, but it will be seen that, within the accuracy and intended application of this work, consistant results are obtained and useful observations can be made. This matter will be further discussed in Chapter 8 where the results of the flight of the rocket vehicle C1014 are presented.

Firstly, some of the other components of vacuum ultraviolet radiation in the night sky will be mentioned in (6.4) and in Chapter 7 the design, flight details and results of the night-airglow experiments preceding C1014 will be given. The earlier experiments did not provide such high resolution data as that from C1014 on which the discussion of radiative transfer is centred. However, as they led to the development of the C1014 experiment and payload, they are described before the contents of Chapter 8 are presented.

6.4 Non-airglow Radiation

6.4.1 Extraterrestrial Lymanα

Resonance scattering of solar Lymanα radiation by hydrogen within about 50,000 km of the Earth, as described in 6.3, can account for most of the vacuum ultraviolet radiation observed in the night sky.

A small part of the measured intensity does, however, come from other sources. Instruments such as those of Morton (1962) and Fastie et al., (1964) have indicated that in the vacuum ultraviolet region there are no significant emissions other than near the Lymanα line, at least when the signals are effectively integrated over a large area of the sky. However, the results of the absorption cell experiment (Morton and Purcell, 1962) which was done at the same time as the spectrograph measurements by Morton, showed that an appreciable fraction of the radiation from above in the Lymanα region was passed by their filter (15%). Some of this could have been in the wings of the broadened back-scattered source (6f) where the optical depth of the cell was small.

Measurements with detectors beyond the geocorona (Wallace et al., 1970; Barth, 1970) have shown that intensities of the order of several hundred Rayleighs originate beyond the extent of the geocorona. A review of the several measurements and interpretations has been published by Tinsley (1971). The proposed sources were:-

(1) the resonant scattering of solar Lymanα by interplanetary hydrogen, and

(2) emissions from galactic sources.

A model was proposed by Blum and Fahr (1970), and Fahr (1970) to predict a source function for interplanetary scattering. They considered the motion of neutral hydrogen atoms crossing the solar system as the sun moves through the interstellar medium towards the

solar apex. The neutral hydrogen density in the solar system would be asymmetric due to ionization losses, gravitational focussing and radiation pressure divergence of the hydrogen flow. The latter term, in particular, is difficult to assess because of the variability of the intensity of the solar radiation which can interact with neutral hydrogen.

Some measurements of intensity distributions (Chambers et al., 1970) support the prediction of enhanced intensities towards the solar apex (Right Ascension = 270^0; declination + $+30^0$) and the solar dependence of intensities (Mange and Meier, 1970), but there appears to still be some uncertainty concerning the exact direction and degree of the enhancement (Wallace et al., 1970; Barth, 1970). Conclusions are difficult to draw because the solar apex lies so close to the galactic plane from which there could be stellar enhancement. Bertaux and Blamont (1970) have found a symmetrical enhancement pattern, but with the symmetry axis displaced 45^0 from the solar apex. As Tinsley (1971) pointed out, more measurements with high spectral resolution are needed.

6.4.2 Stellar sources

As was mentioned in the previous section, direct radiation from hot stars could constitute part of the observed extraterrestrial background. Resonance scattering by interstellar hydrogen limits the direct viewing of distant sources at the centre of the Lymanα

emission line, but Doppler-shifted Lymanα and other line and continuum radiation from distant stars can still produce detector responses. The contribution to a Lithium Fluoride-Nitric Oxide (LNO) ion chamber detector signal from emissions other than Lymanα can be identified more easily if the field of view is small, as bright sources then appear as discreet peaks superposed on the diffuse Lymanα glow. The integrated intensity of weak, unresolved sources should be small, according to Kurt and Syunyaev (1968). Extensive surveys have been made of individual sources at wavelengths longer than Lymanα but shorter than the spectral response limit of LNO ion chambers (Smith, 1967; Code et al., 1969; Stecher, 1970). In instruments responsive between 105 and 135 nm, bright stars produce responses commensurate with the airglow signals when a narrow field of view ($\approx 10^{-3}$ steradiun) is used. Some such stars were scanned by the telescope in C1014 (Chapter 8), and the peaks were readily separable.

A detector with a wide field of view would integrate the intensities of a concentration of sources to give the appearance of a diffuse enhancement of the airglow similar to that predicted by the Blum and Fahr (1970) model of the interplanetary airglow, mentioned in the previous Section. Apparent galactic enhancement of intensities measured by detectors with large fields of view has been reported also in wavelength bands excluding Lymanα. Kurt and Syunyaev (1968) found on an enhancement in the Calcium Fluoride-

Nitric Oxide (CNO) chamber band (122 - 135 nm) from less than 1×10^{-10} W m^{-2} sr^{-1} from other directions, to 3×10^{-9} W m^{-2} sr^{-1} from near the galactic plane. They also reported an increase from 5.5×10^{-8} to 8.0×10^{-8} W m^{-2} sr^{-1}, measured by the detector which was sensitive to Lymanα as it scanned across the Milky Way. Barth (1970) reports that galactic plane enhancement was seen from Mariner 5, but was not seen by the spectrophotometer on Mariner 6.

As the background radiation is somewhat less intense than the geocoronal airglow in the Earth's vicinity, differentiation between possible sources of the background, such as interplanetary scattering and galactic contributions, requires particularly selective instruments. An absorption cell instrument has special properties suited to the separation of source components in the spectral range around Lymanα.

6.4.3 Airglow at wavelengths other than Lymanα

Just as galactic sources could produce ion chamber responses to non-Lymanα wavelengths, so could airglow from other atmospheric gases produce additional detector signals. In the wavelength range of interest the most likely emissions would be from atomic oxygen, which has its major resonance line at 130.4 nm and another transition to the ground state which is accompanied by emission at 135.6 nm (Figure 1.2). Night airglow at these wavelengths has indeed been detected. Hicks and Chubb (1970) and Barth and Schaffner (1970)

reported comparatively large intensities of night time oxygen emissions of up to 2 kR in bands near geomagnetic latitudes of $\pm 15^0$. These emissions were apparently restricted to narrow ranges of latitude, and no measurable intensities were reported for mid latitudes.

More recently, one set of rocket measurements of non-Lymanα airglow at solar zenith angles comparable with those in the present experiments has been reported (Buckley and Moos, 1971). They measured intensities of up to 70 R of λ = 130.4 nm radiation during a flight to 166 km altitude, with about 25 R at 120 km. They also measured up to 33 R near λ = 135.6 nm. No detailed spatial distribution was obtained. The measurements were made at mid-latitude (White Sands Missile Range, 32^0N). Buckley and Moos were able to place only upper limits on the nitrogen (N_2 : LBH and VK systems) emissions between 126 and 190 nm. The reported intensities are much smaller than those of the Lymanα airglow.

Some of the detector groups flown in this work included chambers with Calcium Fluoride windows to check on the level of contamination of Lymanα measurements by longer wavelength radiation. Knowledge, at the time, of the intensities of other possible emissions was not adequate to assume freedom from contamination.

6.4.4 Lunar radiation

The moon is another night-sky source which received special attention in this work. The backscattered solar Lymanα radiation from the moon would not be expected to make any measurable contribution

to airglow intensities, but for most photometry measurements a full moon situation would be normally avoided. However, included in the payloads with several of the airglow experiments described here were photomultiplier-filter detectors used for the determination of ozone density profiles (Carver et al., 1972). The profiles were deduced from the altitude dependence of the total lunar intensity at a number of wavelengths between 220 and 300 nm, where ozone is the major atmospheric absorber.

The ozone experiments were deliberately flown at times near full moon, with the lunar elevation between 20^0 and 30^0. This was done to optimise the intensities and absorption conditions. Absorption spectrometry also provides a measure of the source intensity above the absorbing atmosphere, and in this case the reflectivity of the lunar surface material can be assessed.

The airglow photometers were accordingly designed with a secondary objective of obtaining simultaneous measurements of the lunar flux at 121.6 nm. The measurements of Carver et al., (1966), Heddle (1962) and Lebedinsky et al., (1967a, b) had shown the optical behaviour of the lunar surface down as far as 200 nm, but no information was available at shorter wavelengths.

There were two reasons for extending the range of the measurements. First, to determine whether the steep reduction of lunar reflectivity in the 200 - 300 nm region continued down into the 100 - 200 nm region. The drop is sharper and more severe than

is usally found in measurements on terrestrial samples, and the extended curve would enable better matching of the characteristics of the untouched lunar surface to those of radiation-damaged samples which could be produced under controlled conditions in the laboratory. The second reason for making the measurements was to determine whether the total lunar flux is large enough to make feasible the measurement of night O_2 density by absorption photometry at Lymanα. This would not at present be feasible if the known downward trend in reflectivity did continue to 121.6 nm, but if the lunar reflectivity were flat, or showed a rise in the vacuum ultraviolet region, a usable flux might be available, at least near full moon. The lunar Lymanα should have a spectral line shape similar to that of the direct solar radiation, so that resonance scattering effects could then be safely ignored in height profile analysis, as they are in daytime oxygen measurements.

A discussion of the characteristics required in instruments suitable for lunar ultraviolet measurements and the design constraints are included in Chapter 8, where the C1014 payload is described. It is now known that the earlier flight instruments did not have adequate resolution to detect the lunar flux. This was due to a misinterpretation of some of the data which was used to calculate the required performance of the earlier instruments. The revised estimates, on which the C1014 instrument design was based, have now been proven by the data received to have been substantially correct.

CHAPTER 7 AIRGLOW EXPERIMENTS

7.1 Introduction

In the course of this work, four rocket payloads were designed, constructed and flown to make measurements of the night ultraviolet airglow. The main detectors in each payload were ultraviolet-sensitive 'telescopes' mounted to view along axes perpendicular (or nearly so) to the longitudinal axis of the rocket. Sideways viewing simplified the design and operation of the detectors and their protective covers, but relied on a suitable spin and coning motion of the rocket to scan the detectors through interesting regions of the sky. None of the rocket vehicles had an active stabilization and pointing system which could control the viewing directions.

The airglow detectors in each payload were lithium fluoride-nitric oxide ion chambers (Sensitive to $105 < \lambda < 135$ nm.). In two of the payloads, calcium fluoride-nitric oxide chambers were fitted to monitor contributions from the spectral region $122 < \lambda < 135$ nm.

The rocket flights spanned a period of slightly more than two years, and during that time considerable development was achieved in sensitivity, resolution and sophistication of the flight instrumentation. The first two systems to be flown used the windows of the ion chamber detectors as the collecting areas, with circular apertures in front to limit the fields of view (Sections 7.2.1 and 7.2.2). In the third payload there were lithium fluoride lenses in front of the ion chambers to give a larger effective collecting area, together with an accurately defined field of view (7.2.3). The latest instruments to be flown

(Chapter 8) used a side-entry, inverse-Newtonian form of telescope to give a greatly increased effective collecting area with a small field of view.

Three of the rocket vehicles were of a type designated 'Cockatoo' which was developed by the Australian Department of Supply. These vehicles carried the payloads, including ancilliary equipment and telemetry systems, to apogees between 96 km and 120 km. The other vehicle was an Aerobee-150 launched by NASA, which carried X-ray counters as the primary experiment for the University of Wisconsin. Space in the payload had been made available for the University of Adelaide experiments.

As the Aerobee launch was not programed for full-moon conditions, the objective of the measurements was simply a survey of the night-sky vacuum ultraviolet radiation to determine the spatial distribution of intensity at different altitudes, from the absorption heights up to apogee, which was well above the oxygen absorption region. A relatively wide field of view (8^0 FWHM) was used.

The three Cockatoo vehicles were launched at times near full moon to optimise conditions for the lunar-ozone measurements (6.4.4). The telescopes in each payload were designed to be able to measure vacuum ultraviolet lunar fluxes as well as airglow intensities. The detectors on the first Cockatoo (C104) had comparatively large fields of view (12^0 FWHM) as it was expected at the time that the lunar signal would have been detectable in a diffuse airglow field of that width. The

estimates are now known to have been in error and the lunar signal was below the noise level. For the last two flights the fields of view were reduced in accordance with revised lunar flux estimates, and were 4^0 x 1^0 rectangular (C105) and 2.5^0D circular (C1014). Both of these systems had high spatial resolution for the airglow measurements, and this proved to have important benefits in later analysis.

The design and performance specifications of the first three airglow experiments are given in parts of Section 7.2, and the data and results from C104 are presented in 7.3.

7.2 Experimental Payloads

7.2.1 Aerobee 4.301 UG

There were three ultraviolet radiation detectors in the Aerobee photometry package. Two were ion chambers operated in gas-gain mode with circular-baffle collimation in front. The third was a photomultiplier - thin film filter combination, also with baffle collimation, sensitive to extreme ultraviolet (EUV) radiation. The three detectors were aligned parallel, with their axes normal to the rocket axis.

The ion chambers were miniature gas-gain types (Section 2.4.1 and Figures 2.3 and 2.8). Both of the chambers were filled with nitric oxide andhad a long wavelength response limit of 135 nm. One had a lithium fluoride window, making it sensitive down to 105 nm, including the Lymanα line. The other chamber had a calcium fluoride window which limited the response band to $\lambda > 122$ nm. The

sensitivity of the calcium fluoride-nitric oxide (CNO) chamber to Lymanα radiation was much more than two orders of magnitude lower than that of the LNO chamber. The CNO chamber was included to determine how much of the LNO signal was due to radiation with $\lambda > 122$ nm.

The third detector was included to measure the night airglow intensities at wavelengths shorter than 60 nm. The existence of night-sky EUV radiation had been suggested by Friedman (1960), and Ogawa and Tohmatsu (1966). The major emissions expected were the 30.4 nm and 58.4 nm resonance radiation from He^+ and He respectively. A previous measurement of EUV night airglow had been reported by Young et al., (1968), who had found intensities approaching 10 R near 200 km in a spectral range which included both 30.4 and 58.4 nm.

Figure 7.1 shows diagrams of the detector systems and a brief description is given in Appendix A.

The payload was launched from Woomera, South Australia on 20th May, 1970 at 11.45 p.m. CST (1415 UT). A good trajectory and altitude was achieved, with the detectors making a series of slow scans across the sky. It appears, however, that the door of the compartment containing the instruments was lost shortly after launch. Aerodynamic heating produced abnormally high temperatures in the exposed detectors, and spurious outputs were produced. By studying the data in conjunction with the azimuth-elevation and right ascension-declination plots of the spatial scans, an attempt

(a) EUV Detector (2/3 actual size)

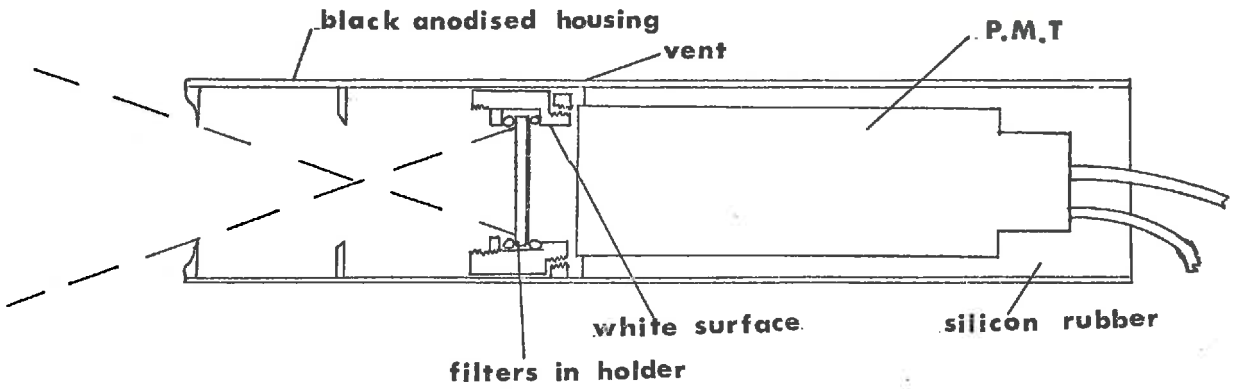

(b) EUV Filter Holder (1·5 x actual size)

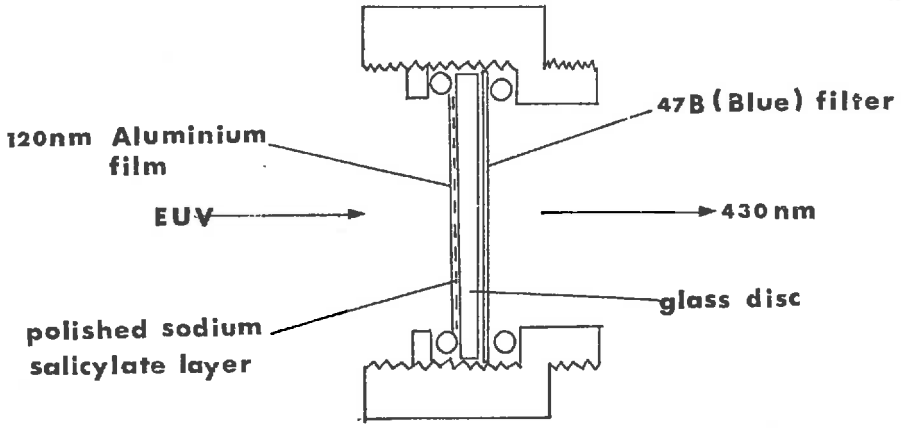

(c) Ion Chamber (2) (actual size)

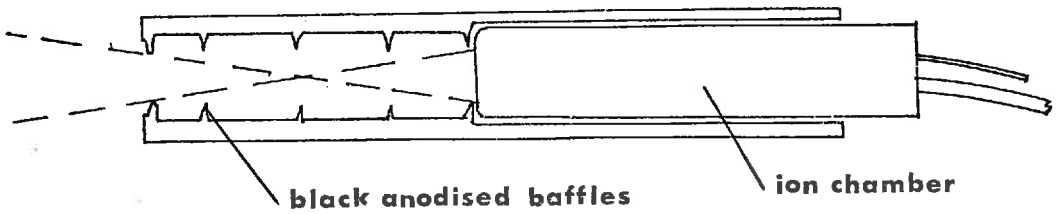

FIGURE 7·1 AEROBEE DETECTOR SYSTEMS

was made to determine whether some component of the outputs showed a repeatable spatial dependence. No such component was found and the outputs are assumed to have been due entirely to excessive dark currents, leakage current and temperature drifts in the electronic circuits.

7.2.2 Cockatoo C104

Another payload incorporating ion chamber detectors was launched soon after the Aerobee flight. This payload contained three ion chambers of the same type (LNO) sensitive to Lymanα radiation. It also carried mid-ultraviolet detectors for the measurement of the night ozone density profile (Carver et al., 1972) and so was launched close to the time of full moon.

The three ion chambers were mounted to view sideways from the rocket with their axes at 80^0, 90^0 and 100^0 from the vehicle axis, forming a fan-shaped array. The fields of view overlapped slightly and as the vehicle spun and precessed they scanned the sky in an interlaced pattern. The divergent array was chosen to give a more complete coverage of the sky during the short time that the rocket was above the region of strongest absorption of airglow by molecular oxygen. The orientation of the detectors during flight was deduced from the outputs of three orthogonal magnetometers and an optical moon-slit aspect detector.

Brief descriptions of the components of the C104 payload and their calibrations and operating specifications are given in the

following subsections. A view of the payload is shown in Figure 7.2.

(a) Detectors

The three Lymanα detectors in the array were miniature glass types, (Figures 2.3 and 2.8), operated at gas-gains near 100. Their fields of view were limited by circular apertures in front of the chambers. A measured angular response curve for one of the detectors is shown in Figure 7.3. The miniature chambers were developed and used in this vehicle to enable the angled array, with collimators, to be fitted in the available space. Because the range of gas-gain available with an adequate safety margin was not as great in these chambers as in the larger types, the operating gain selected for flight, and hence the absolute detector sensitivity, was lower than optimum. This meant that the full range of the telemetry system was not utilized, and some problems were encountered in the data analysis with noise and electrical drifts.

(b) Amplifiers

The signal currents were amplifed by F.E.T. input amplifiers operating in the current-feedback mode to give a fast response time. The amplifiers had a maximum gain of 10^{11} volts per amp, and fed low-impedance signals in the range 0 to 1.5 volts to the telemetry multiplexer.

FIGURE 7.2 INSTRUMENTATION SECTION OF C104

In order, from the top, can be seen the cover-release mechanism; the three mid-ultraviolet interference filters for the ozone experiment, flanked by amplifier modules; the slit pattern plate of the lunar aspect sensor; the three entrance apertures of the ion chamber array; the section containing the H.T. unit; the battery pack and umbilical connector.

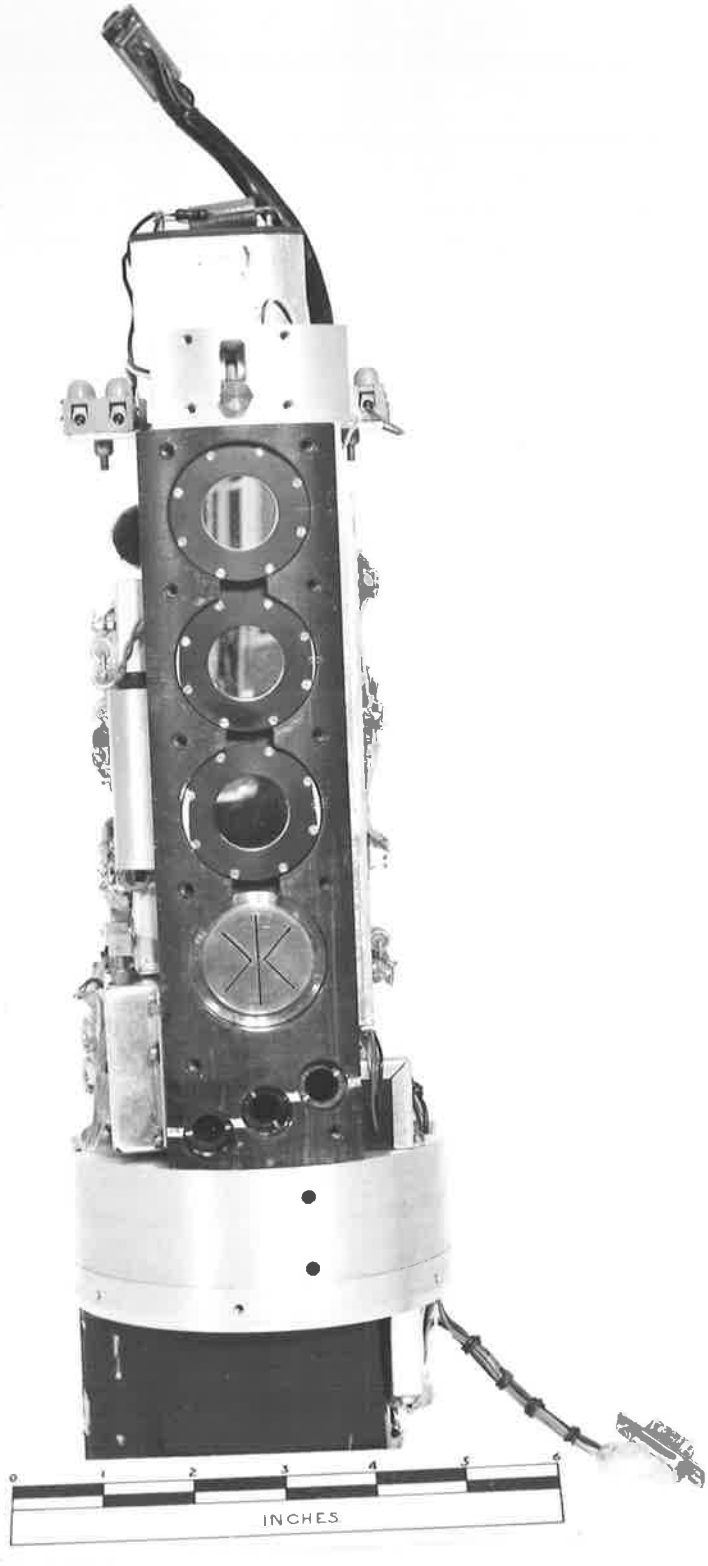
0
1
2
3
4
5
6
INCHES

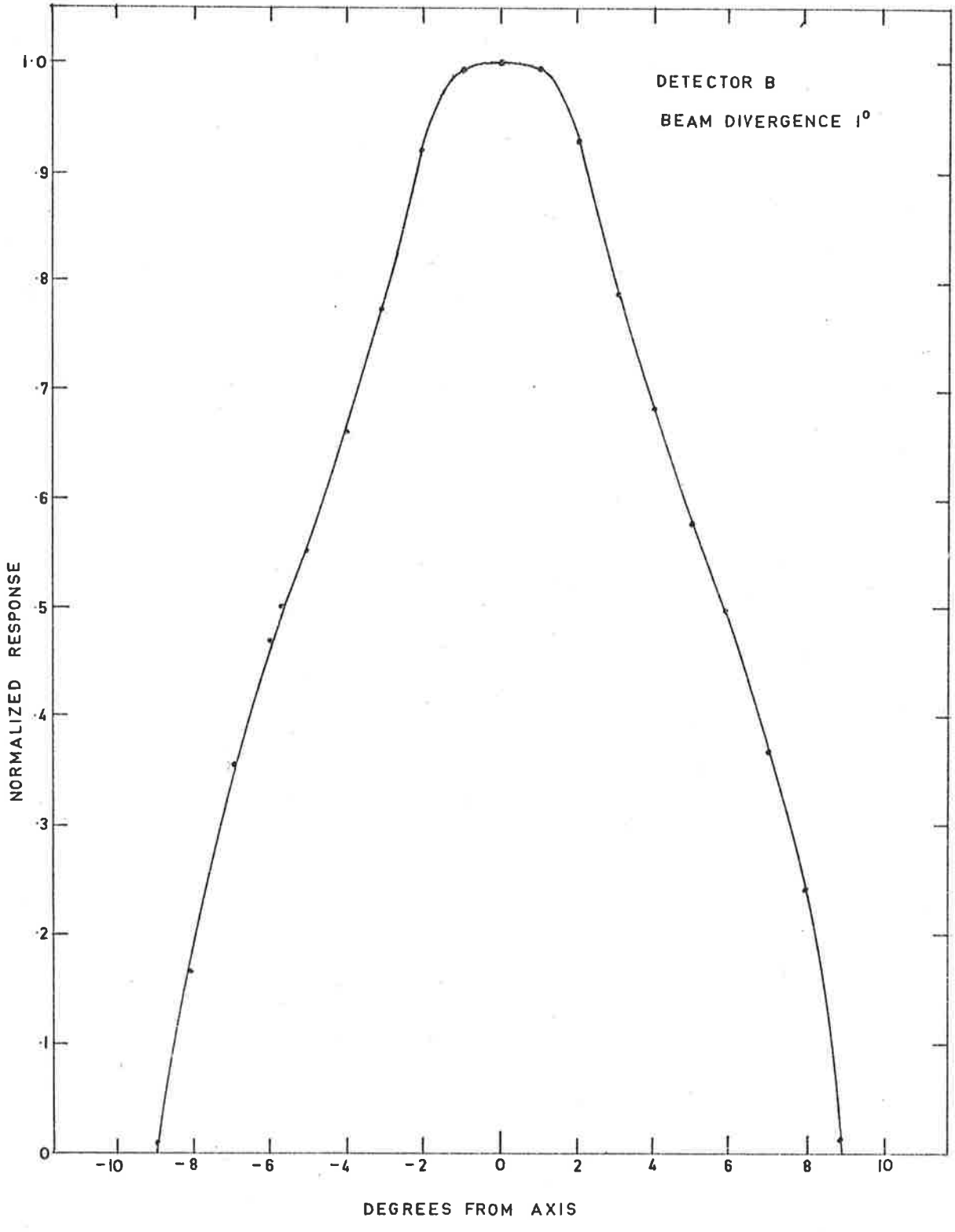

FIGURE 7·3 ANGLAR RESPONSE OF C104 LYMAN α DETECTOR

(c) High tension supply

The H.T. supply provided adjustable regulated voltages to the photomultipliers and ion chambers in the payload. A novel design of supply, particularly suited to the requirements of small rocket payloads, was developed and used in this and subsequent payloads. It is described in Appendix B.

(d) Photometric sensitivity

The ion chambers had been absolutely calibrated some time before launch by the method described in Section 2.7. Because a further calibration could not be done immediately before the chambers left the laboratory, the efficiencies at launch were estimated by combining the earlier figures with intercomparisons between flight chambers and the spares. The spares were absolutely calibrated again after the flight. The estimated limit of probable error in the flight chamber efficiencies is ± 25%. The uncertainties in the calibrations prior to flight contributed to the lower than optimum gains of the flight detectors. The detector characteristics are summarized in Table 7.1.

TABLE 7.1 C104 DETECTOR SPECIFICATIONS

Entrance Aperture Diameter	7.6 mm		
Chamber Window Diameter	6.5 mm		
Field of View (F.W.H.M.)	12^0		
Geometric Factor	1.0 mm^2 sterad		
Spectral Response Range	105 - 135 nm		
Detector	A	B	C
Quantum Efficiency at Lymanα	4	10	6 %
Operating Voltage	437	428	435 volts
Gas-Gain Factor	90	150	175
Channel Sensitivity	25	7	10 kR/volt

(e) Aspect sensor

The aspect sensor was housed and calibrated with the ozone experiment detectors. The sensor consisted of two parallel discs fixed approximately 5 mm apart, with their common axis perpendicular to the rocket spin axis. As the rocket spun, light from the moon passed through a pattern of slits in the outermost plate and through a small central aperture in the inner plate to fall on a photomultiplier cathode. The slit pattern was arranged so that the length and separation of the pulses detected during a revolution of the rocket uniquely defined the angle between the rocket

axis and the lunar direction. This angle was complementary to the lunar aspect angle, defined as the angle between the scan plane of detector B (aligned normal to rocket axis) and the lunar direction. The sense of the rocket spin could also be determined from the pulse pattern. The geometry of the attitude solution is shown in Figure 7.6, where the angles referred to later in the text are defined.

(f) Magnetometers

A set of three orthogonal search-coil magnetometers was fitted to provide data for the attitude solution (i.e. the directions of the rocket and detector axes throughout the flight). Unlike fluxgate magnetometers, the search-coils had no zero-frequency response, and read only the time-varying components of the field along their axes, down to a limiting frequency set by the signal processing integrators. The interpretation of the magnetometer data relied on regularity of the rocket motion and an acceptable roll rate.

The C104 payload was launched on 21st May, 1970. The vehicle performed satisfactorily, although the spin rate was somewhat high, and an apogee of 96 km was reached. The results of the data reduction are given in Section 7.3.

7.2.3 Cockatoo C105

The next experimental payload to be flown in this program was Cockatoo C105. This was similar to C104 in that it combined

vacuum ultraviolet detectors and middle ultraviolet ozone measurement sensors, but the arrangement of the airglow detectors was quite different.

The vacuum ultraviolet detectors were a pair of ion chambers, one LNO and one CNO, as in the Aerobee payload. The main difference was the amalgamation of the two detectors into a dual ion chamber to allow better matching of the detector characteristics. Figure 7.4 shows a cross-section of the dual detector system.

A miniature three axis fluxgate magnetometer unit (Figure 7.5) was designed and constructed for this payload to provide improved data over a wide range of roll rates for the attitude solution. The objectives of the experiments and the design of the payload are outlined in Appendix C.

The C105 payload was launched on 12th November, 1970 and the vehicle reached an apogee of 105 km. A fault common to both chamber channels developed during the launch phase and persisted throughout the flight. It was not possible to identify the fault with confidence, but the most likely course would have been a mechanical failure somewhere in the chamber structure. As the payload was not recovered, no further investigation of the fault could be made. Because of this fault, no usable data was received from the ion chambers during this flight. The investigations made and the experience gained during the development of this payload did,however, contribute to the design and development of the

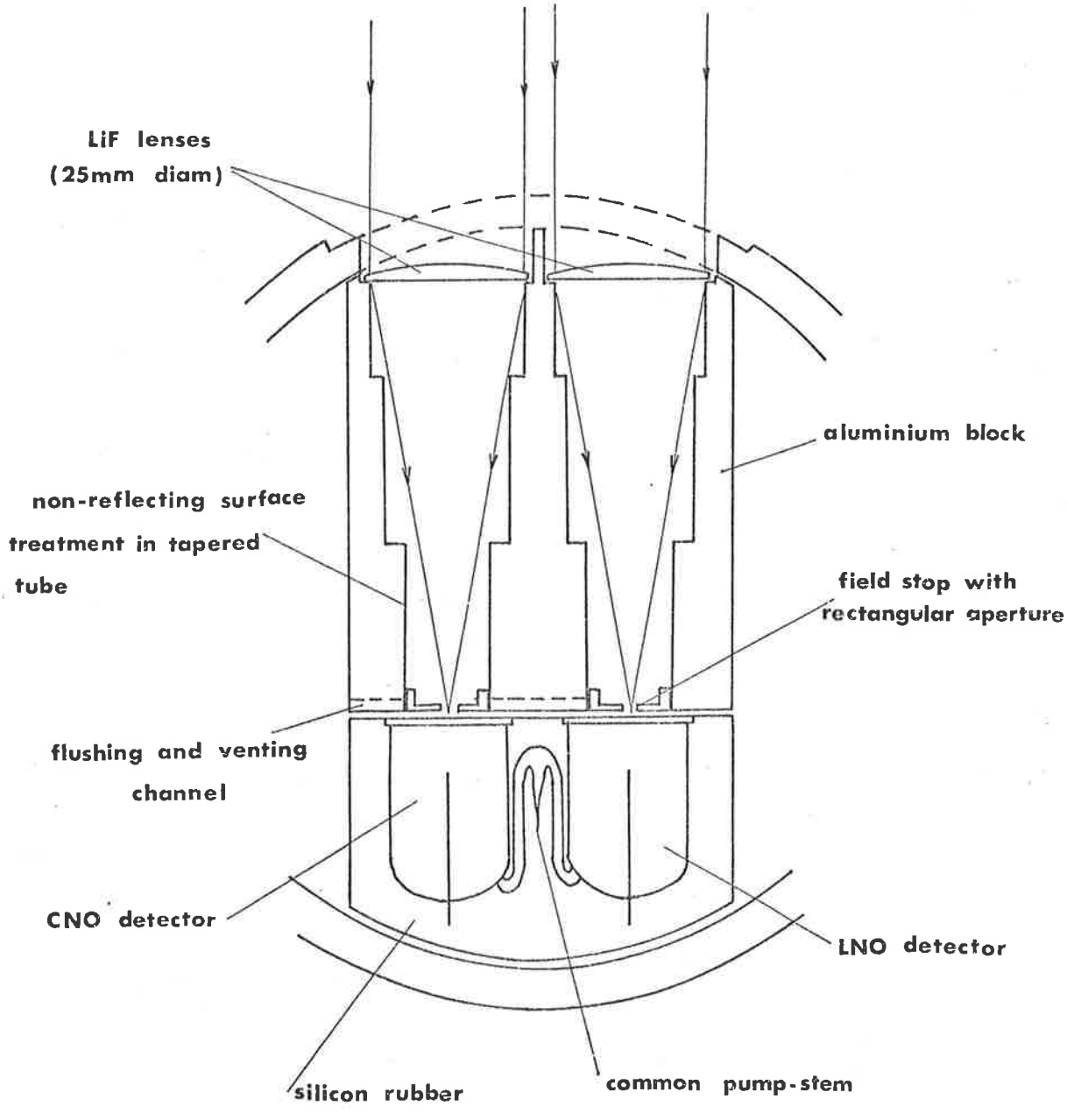

FIGURE 7.4 C105 DETECTOR SYSTEM WITH GLASS DUAL CHAMBER

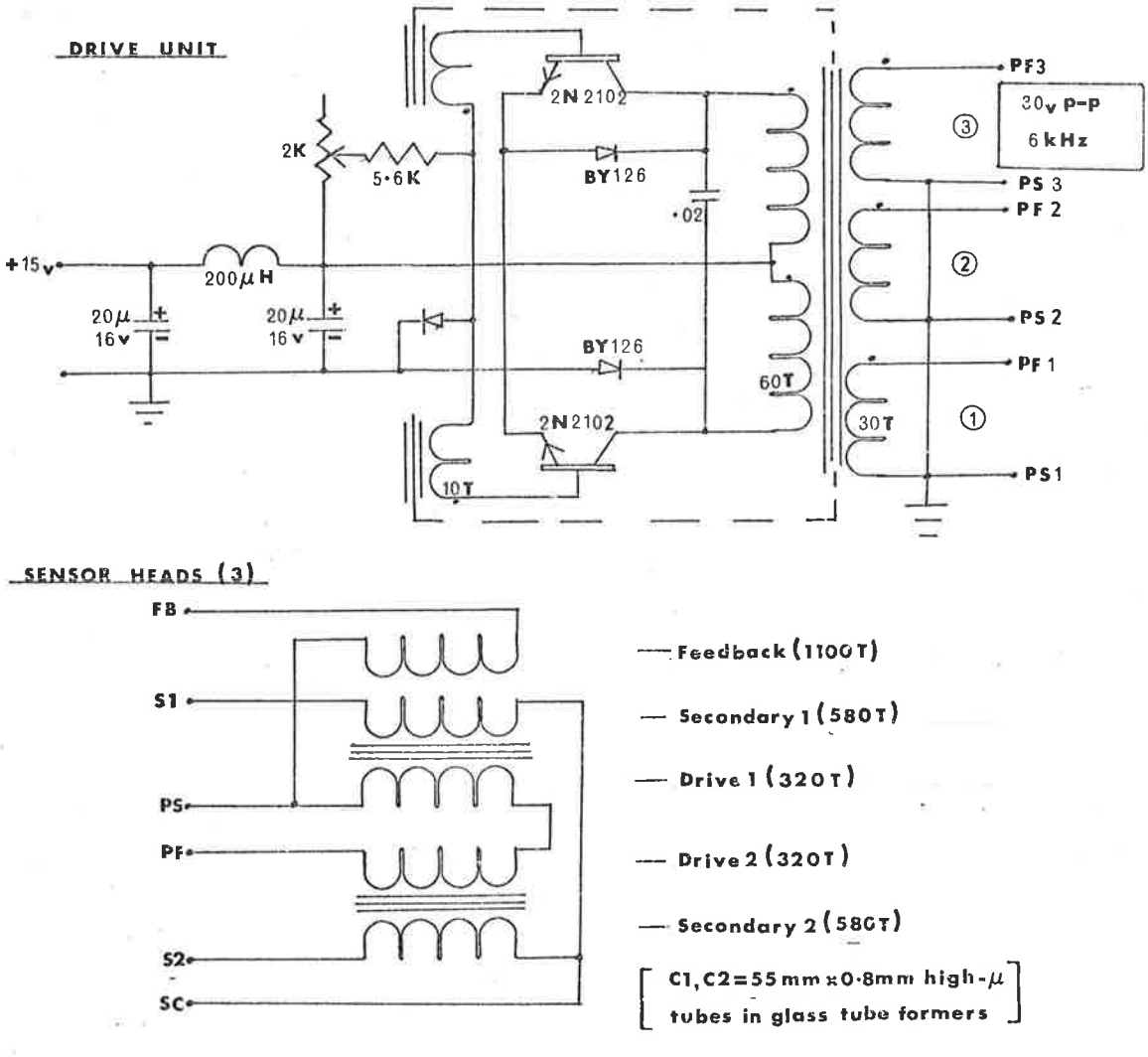

FIGURE 7·5 FLUXGATE MAGNETOMETER CIRCUIT

successful dual-telescope payload on C1014.

7.3 Results from the Flight of C104

7.3.1 Vehicle performance and attitude solution

The vehicle was launched from the Woomera Range on 21st May, 1970 at 1945 CST (1015 UT). Apogee was 96 km, with 147 seconds spent above 70 km (Figure 7.12). During the data-taking portion of the flight, the rocket rolled at 2.5 r.p.s. with a precession period of 23 seconds.

Figure 7.6 shows the angle notation used in the attitude solution. The lunar aspect angle is marked and the magnetic aspect angle, ϕ, is defined as the angle between $\underline{R}$ and $\underline{B}$. The magnetometer calibrations had not been done to a roll rate as high as 2.5 Hz, and the absolute sensitivity at that rate was unknown. An in-flight calibration was therefore derived from the data near the beginning and end of the flight when the rocket axis was aligned with the trajectory. The calibrations were cross-checked by reference to the lunar aspect readings near apogee, when the rocket was assumed to behave as a free spinning body.

The lunar aspect during flight is shown in Figure 7.7. The reading range of the sensor was only $\pm 30^0$ and the dashed portions of the curve were derived from a combined 3-D plot of lunar and magnetic aspect angles. During the period of 90 seconds centred on the apogee time (+150 s), the coning motion of the

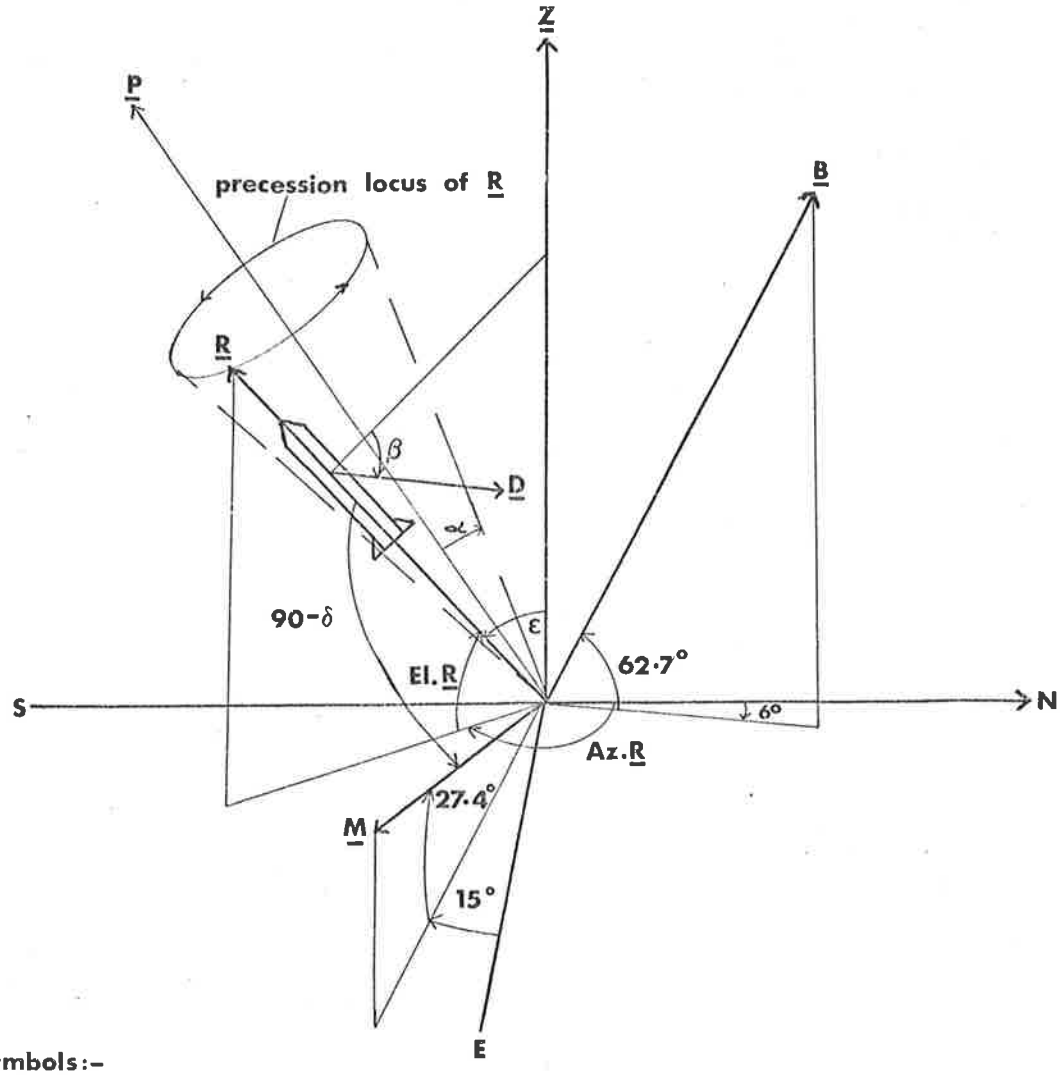

Symbols:-

R	Rocket axis
B	Magnetic field
M	Direction of moon
D	Axis of orthogonal detector
P	Axis of precession cone
α	Half-angle of precession cone
β	Roll angle of detectors from zenith plane
δ	Lunar aspect angle
ε	Zenith angle of roll axis $\equiv$ inclination of scan plane

FIGURE 7.6 GEOMETRY OF THE ATTITUDE SOLUTION

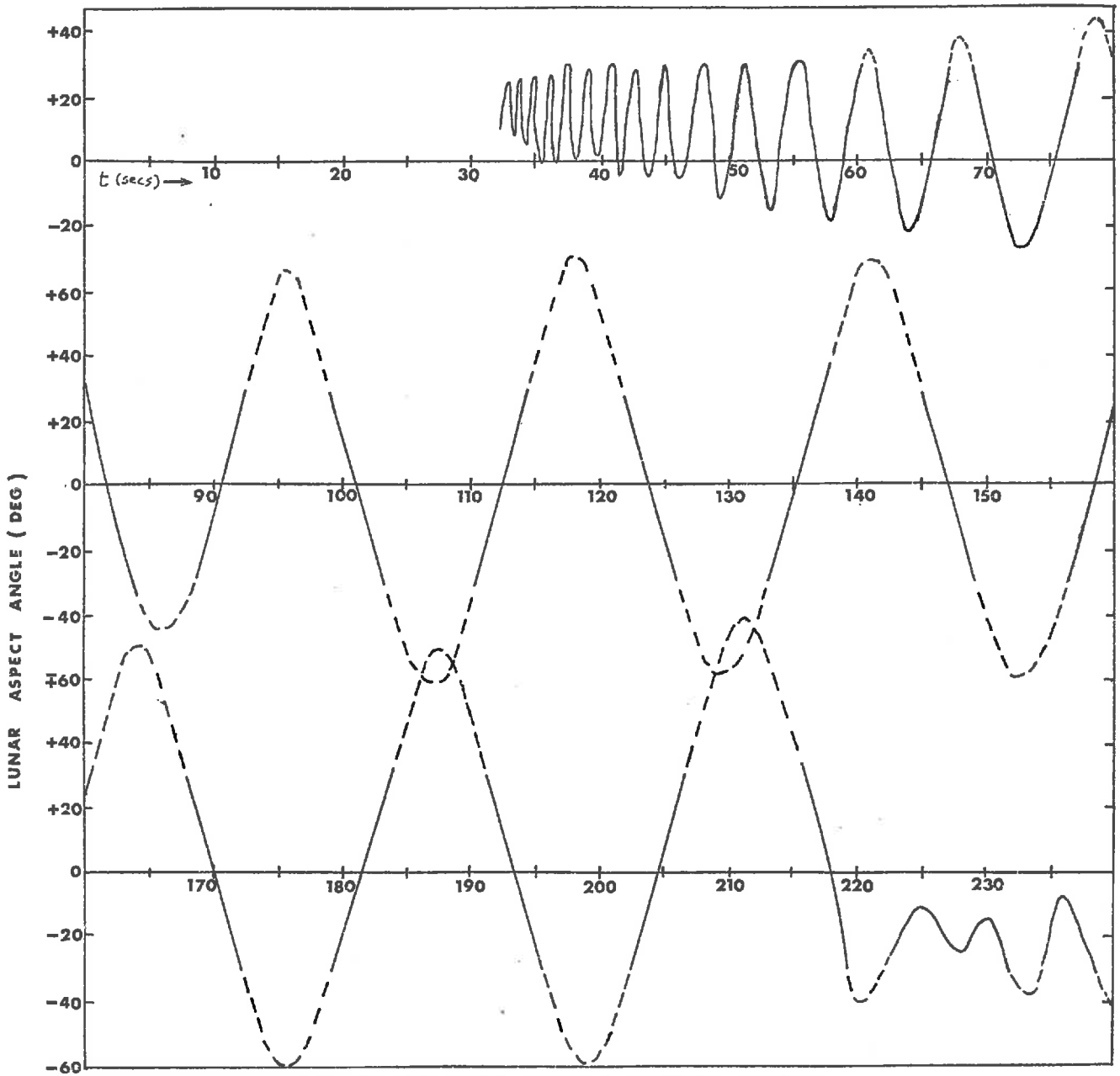

FIGURE 7·7 C104 LUNAR ASPECT ANGLE

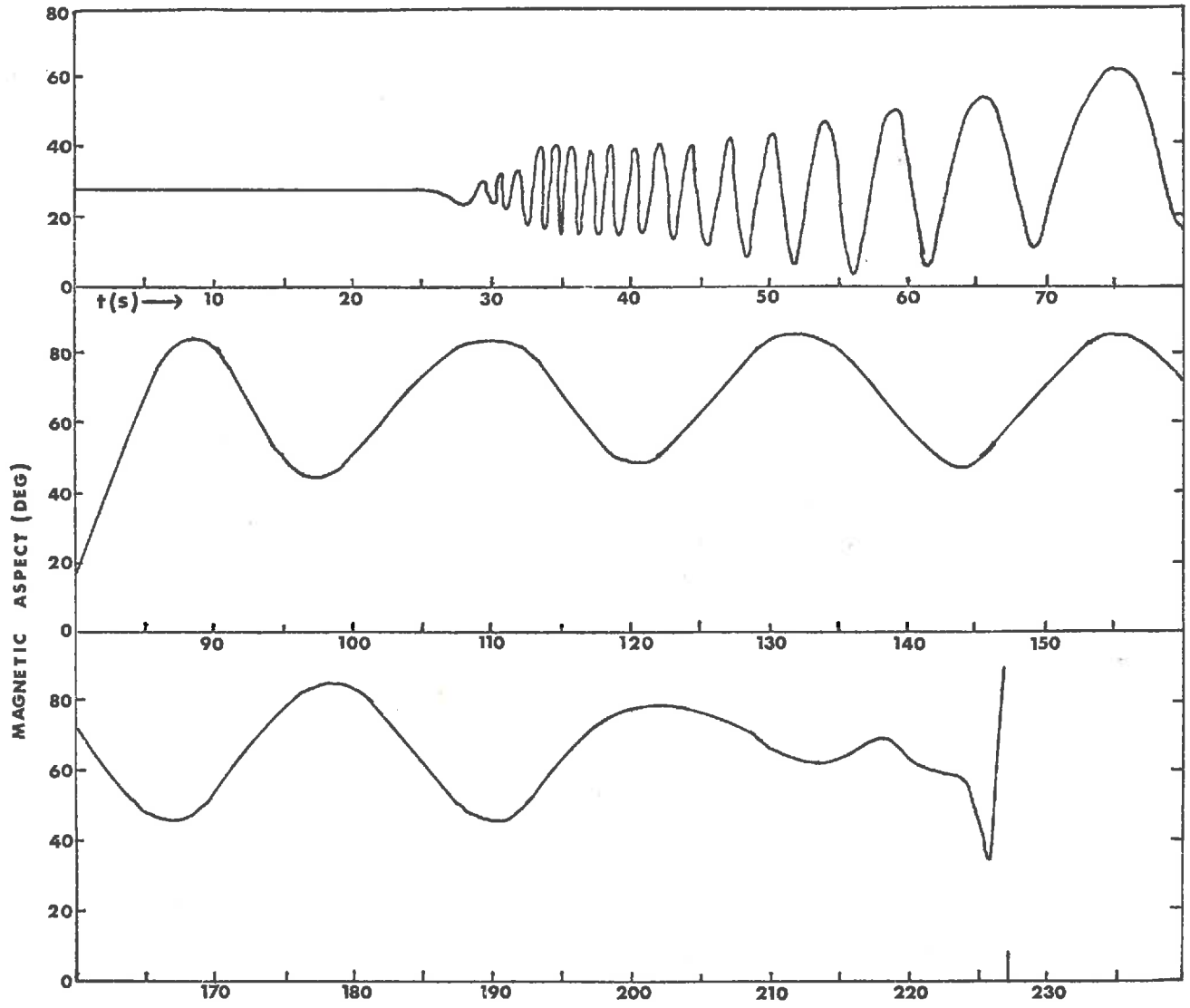

FIGURE 7.8 C104 MAGNETIC ASPECT

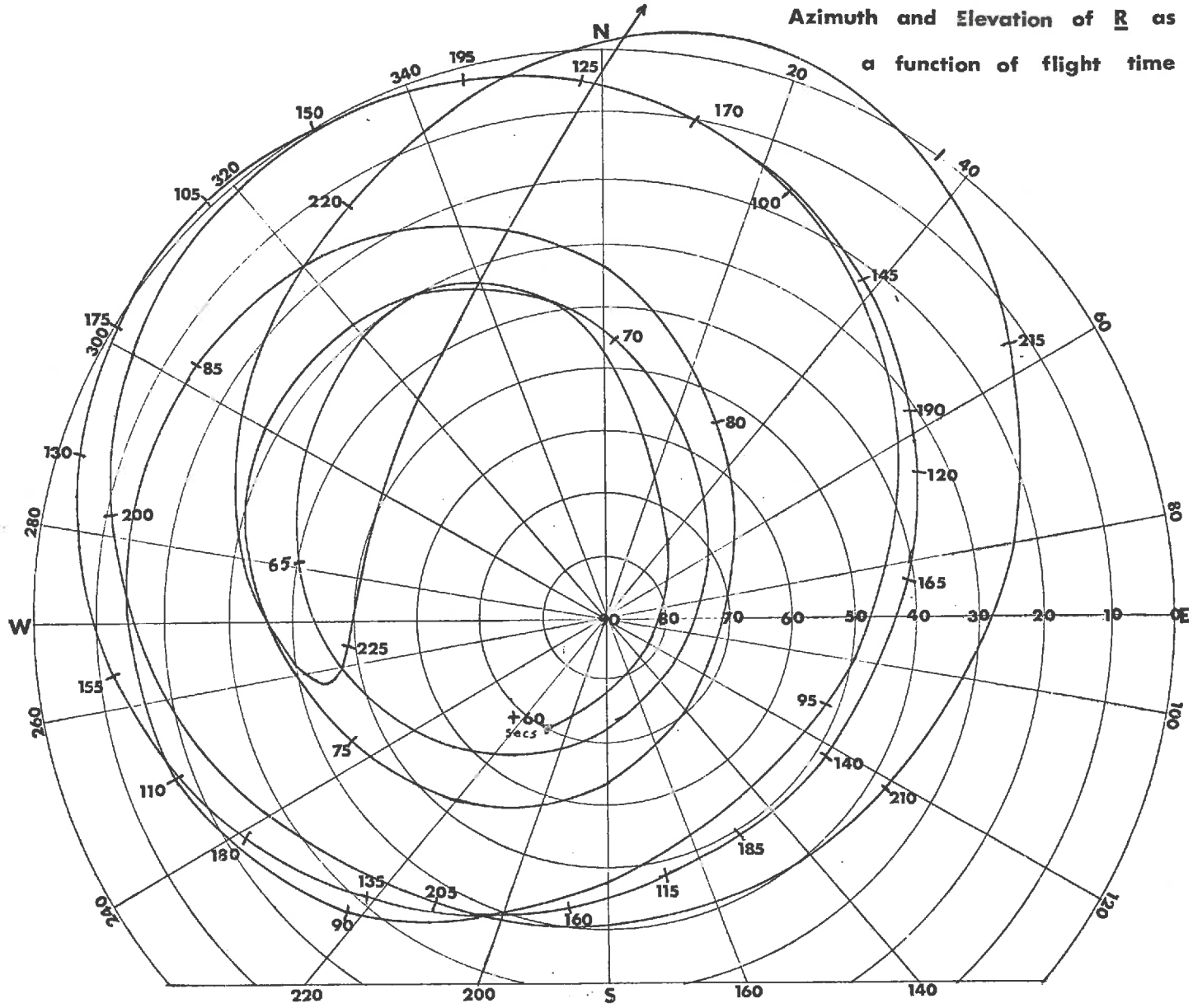

FIGURE 7.9 ATTITUDE SOLUTION FOR C104

rocket was repeated four times. It was assumed that during this period the roll axis described a closed cone, and from the rate of change of aspect angle within the ± 30^0 limits of reading, the half-angle of the cone was calculated to be 65^0. The magnetometer data (Figure 7.8) was used to determine the cone axis (P) as 290^0 Azimuth, + 64^0 Elevation.

The attitude solution (i.e. Azimuth and Elevation of $\underline{R}$ as a function of time) is shown in Figure 7.9 between + 60 s and + 227 s (inversion for re-entry). The detector scans gave several almost complete coverages of both the upper and lower hemispheres ($\chi<90^0$ respectively) between + 85 s and + 220 s.

7.3.2 Lymanα airglow measurements

Airglow radiation was detected at altitudes above 70 km on both the up and down legs of the flight. One detector had quite a low sensitivity, and the airglow signals from this detector were degraded by the comparatively high noise level. The central detector in the array was the most sensitive, but at several times during the flight it produced large spurious pulses. The signal between the pulses was rather noisy and it was considered that the data could not be analysed with confidence. The results given below are based on the signals from detector C which was at an angle of 80^0 to the rocket axis. As the vehicle spun, the viewing axis scanned around a cone of 80^0 half-angle. The signal levels measured from this detector are in most cases the mean of several

successive scans, combined to reduce the contributions from random noise.

The situation whenever the rocket axis $\underline{R}$ was coplanar with the solar and zenith directions is shown in Figure 7.10a. Because of the symmetry about the sun-zenith plane, both the detector-zenith angles (χ', χ''), and the detector-sun angles, (Y', Y'') where equal at times equally before and after the detector crossed the sun-zenith plane (β', β''). If the geocoronal hydrogen distribution was close to spherically symmetric, the observed airglow intensity would also be symmetrical about the local sun-zenith plane. The detector signals should therefore show symmetry about the times of zenith-plane crossing, and this was observed during the flight. Figure 7.11 shows traces taken from groups of scans when $\underline{R}$ lay in the sun-zenith plane. The zero levels are those used to derive Figure 7.13.

The overhead intensity appeared to be fairly uniform over the sky, to within about 20%. The intensity measured in the zenith plane, both upwards looking (I_{UP}) and downwards looking (I_{DOWN}), was read at those times when $\underline{R}$ lay in or near the sun-zenith plane. The zenith angle of the roll axis (ε) at these times covered the range 20^0 to 90^0 while the rocket was above 65 km. The measured values (I_{UP} and I_{DOWN}), together with the difference between them (ΔI) are plotted against flight time in Figure 7.13. Because some amplifier drift occurred during flight, the signal

[a] Orientation with sun–symmetry.

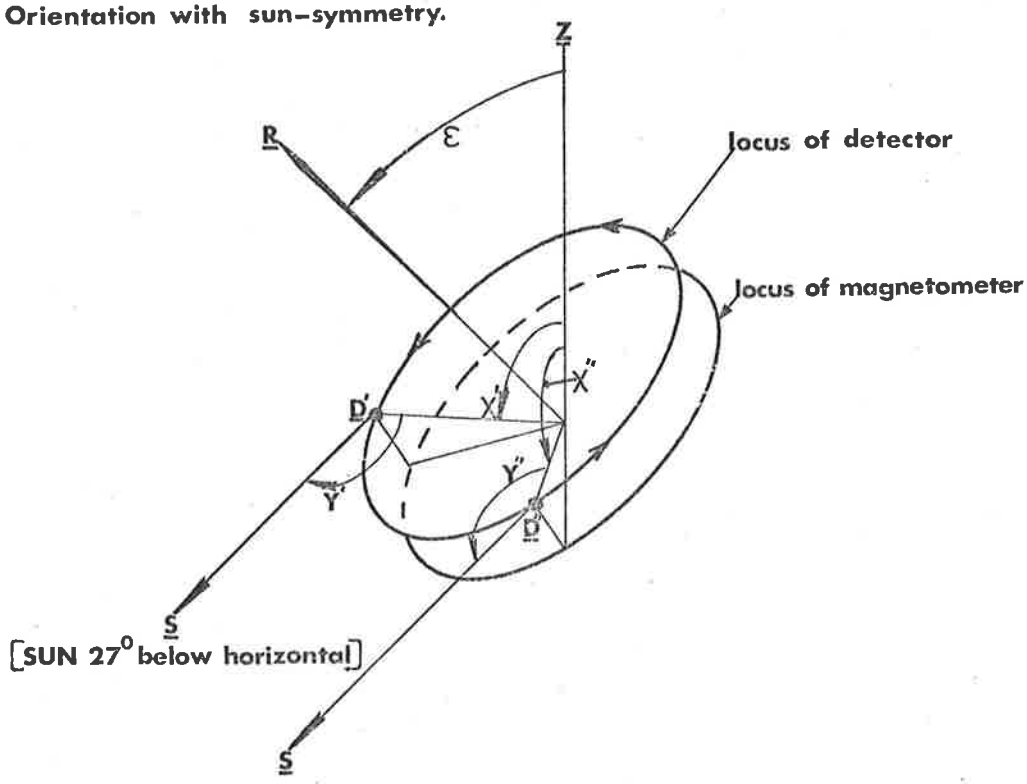

[b] Scanning towards moon and sunwards horizon

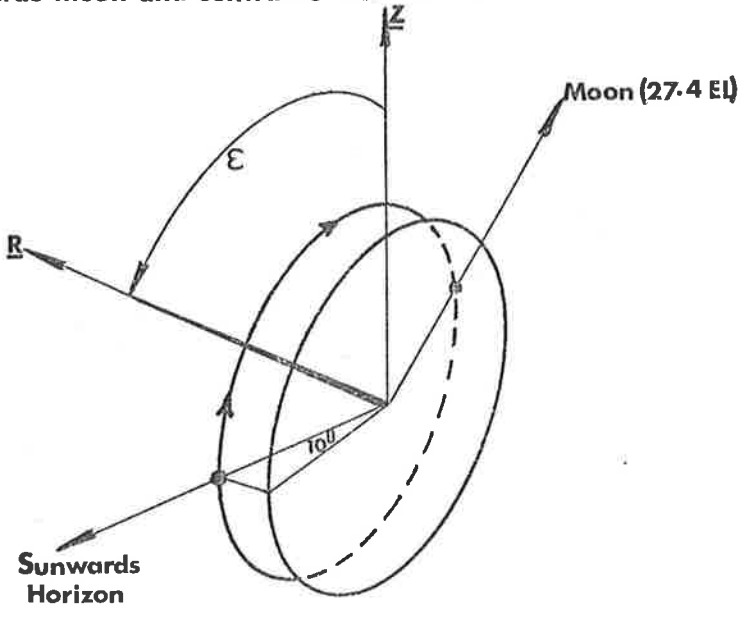

FIGURE 7.10 DETECTOR SCANNING GEOMETRY – C 104

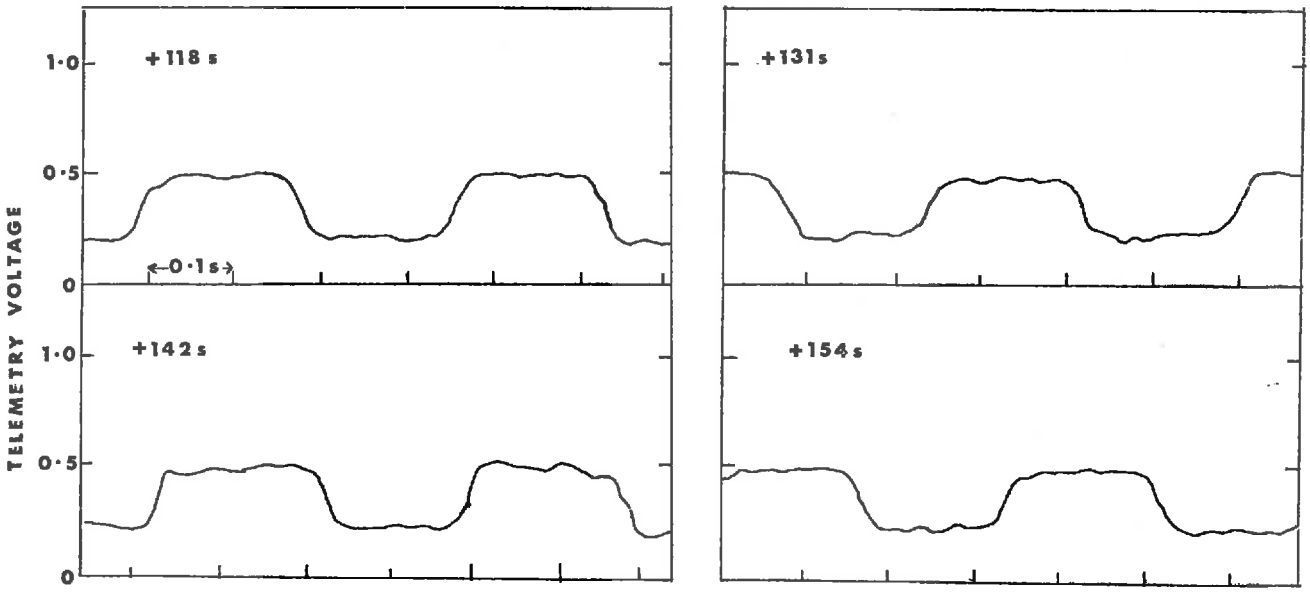

FIGURE 7·11 TELEMETRY TRACES WITH SUN-SYMMETRY (C104)

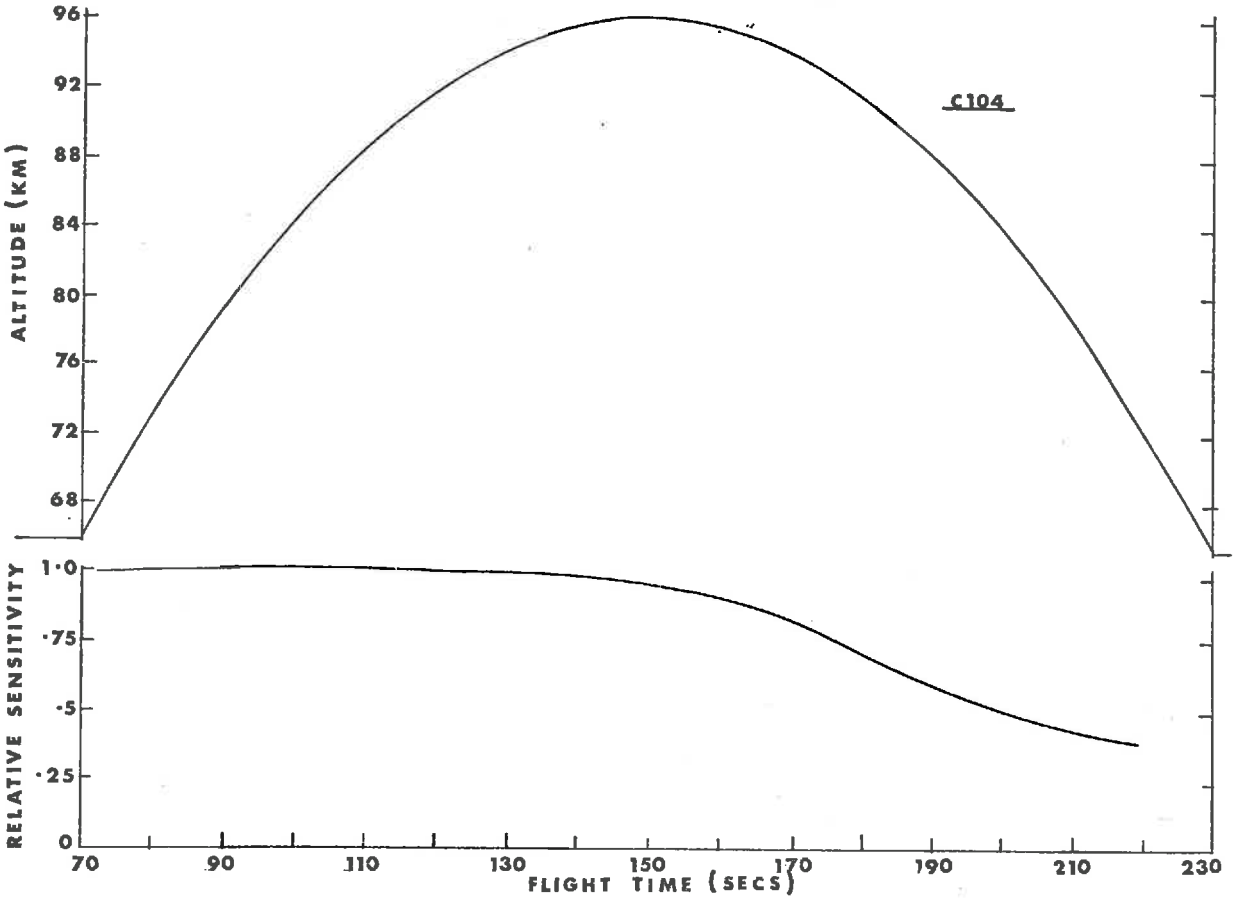

FIGURE 7·12 TRAJECTORY AND CORRECTION FACTOR

zero-levels for Figure 7.13 were obtained from the downward-viewing signals below 70 km, where no backscattered radiation could have been seen. Interpolation between the up-leg and down-leg zero levels gave a value from which the signals near apogee were measured.

Measurements were obtained with $\underline{R}$ towards the east and towards the west on both up and down legs. When $\underline{R}$ was in the west, I_{UP} was measured within 10^0 of the zenith, and when $\underline{R}$ was in the east I_{UP} was measured near 99^0 Azimuth, 52^0 Elevation; both the sets of data points lie close to the fitted curve. The curves in Figure 7.13 lack the symmetry about apogee which would be expected. The only feasible explanation of the asymmetry is that a reduction in the detector sensitivity began just before apogee, and continued throughout the rest of the measurement period. It is possible that temperatures in the payload rose higher than anticipated, causing the chamber walls to outgas. The result would have been a reduction in gas gain, together with increased water vapour absorption. The payload was not recovered, so no post flight calibrations could be done to test this hypothesis. It was assumed that a steady decrease in sensitivity did in fact occur, and appropriate correction factors were estimated. The downwards intensity (I_{DOWN}) is due to back scattered radiation, and would be expected to be almost independent of zenith angle for zenith angles greater than about 130^0. A sensitivity

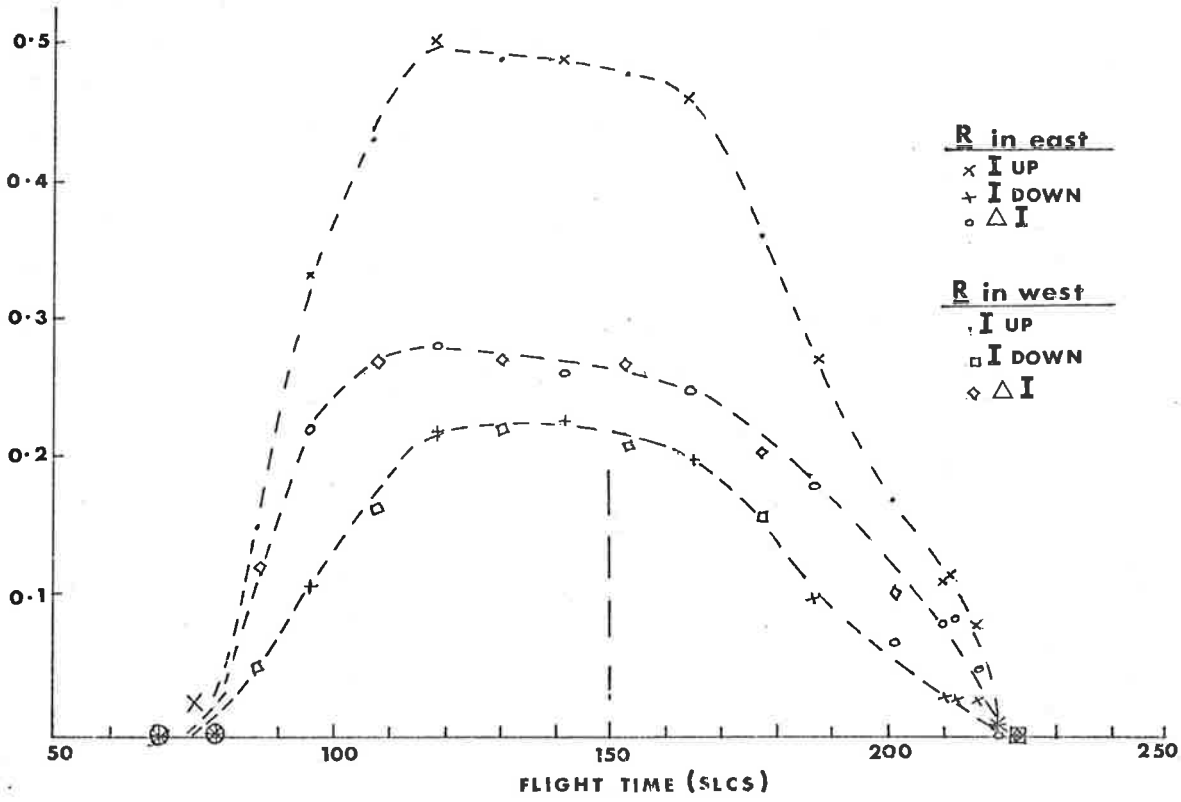

FIGURE 7·13 SIGNALS IN ZENITH PLANE (corrected for zero-level drift)

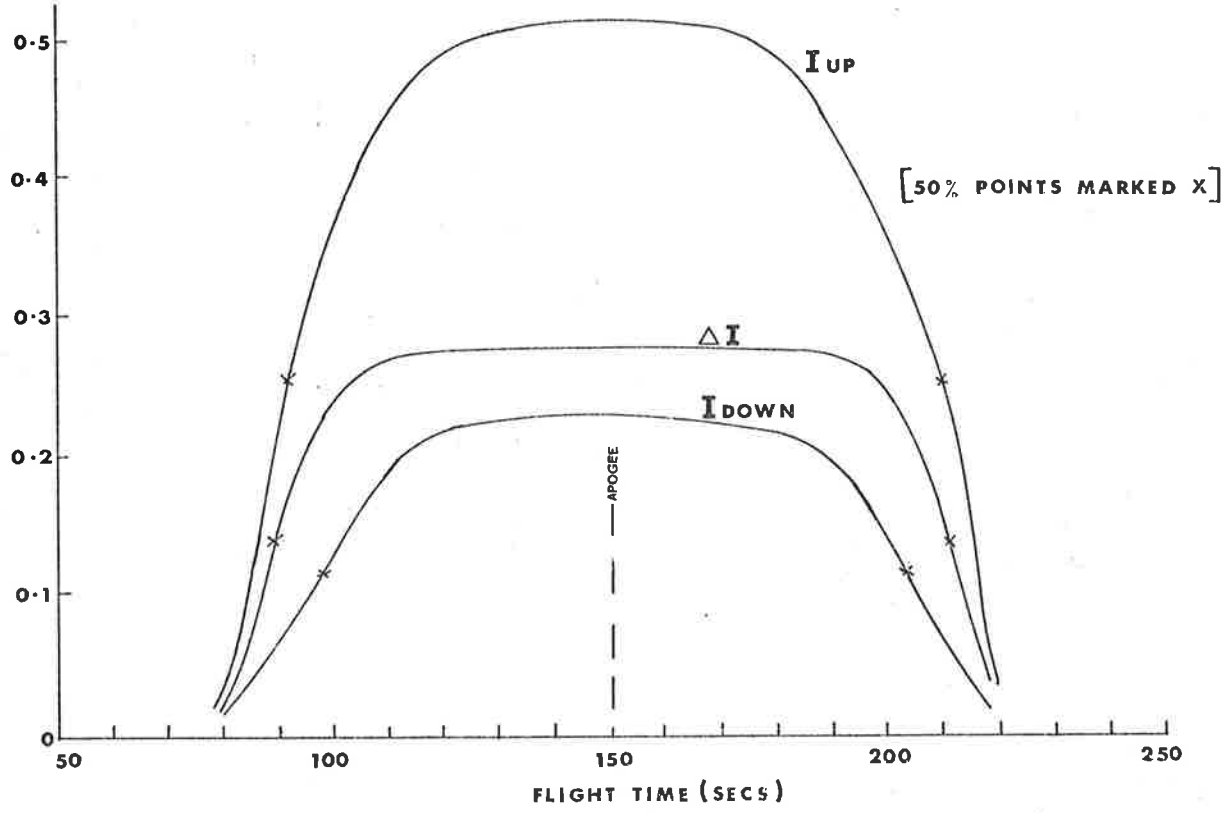

FIGURE 7·14 SIGNALS CORRECTED FOR GAIN-CHANGE

versus time curve was calculated to make the smoothed curve of I_{DOWN} match on the up and down legs. The correction factor is shown in Figure 7.12, and the corrected time - profiles are in Figure 7.14. All three curves are approximately symmetric, with the exception of the period +195 s — +215 s when R dropped to below horizontal and the signal from above exceeded the corresponding signal from the same altitude on the up leg.

Some of the data points were subject to appreciable corrections for zero drift and gain change, so that a very detailed analysis of the data was not justified. The data are good enough, however, to illustrate the general characteristics of the airglow radiation below 100 km. It was found that the corrected curves of Figure 7.14 do give results which are self-consistent within the limited accuracy which could be expected from the data.

Whenever the detector scanned close to the moon, a peak was produced in the output. The peaks were first observed at 40 km altitude, and are attributed to the photoelectric response of the ion chamber to the mid ultraviolet lunar flux. The pulses were clearly seen out to angles of 20^0 from the detector axis, which means that the photoelectric sensitivity was large at the edge of the field of view. Subsequent tests in the laboratory showed that, with the type of collimator used, some miniature chambers did have sufficient sensitivity at the edge of the field to have given an appreciable lunar signal. The photoelectric sensitivity on-axis

(where most testing had been done) was about two orders of magnitude lower than the sensitivity at the edge of the field of view of some chambers. Some scans showing lunar pulses (arrowed) are shown in Figure 7.15a. The scanning geometry for those times is depicted in Figure 7.10b.

Also to be seen in Figure 7.15a are enhanced signals from the western horizon, opposite to the moon. The intensity appeared to be greatest from the region round 10^0 elevation. (The direction of the sun was 279^0 Azimuth, -27^0 Elevation.) Enhancement of the airglow intensity above the western horizon was also observed during the flight of C1014 (8.4.3).

At those times when the detector was scanning to large positive and negative elevations (ε large), the horizon transition between the up-looking and down-looking signal levels was seen to be quite sharp. Figure 7.15b shows telemetry traces at a number of times during flight when ε was $\simeq 90^0$. The scans shown did not include the regions near the moon or the sunwards horizon. The sharpness of the horizon cross-over is discussed in Section 8.4.3 in connection with the higher resolution measurements from C1014.

Radiation which is resonantly trapped in a scattering medium becomes quasi-isotropic. In an optically thick layer, the degree of isotropy depends on the degree of absorption occurring in the scattering region, as described by equation (6m) in Section 6.3.3. Therefore, any radiation which was trapped in the region around the

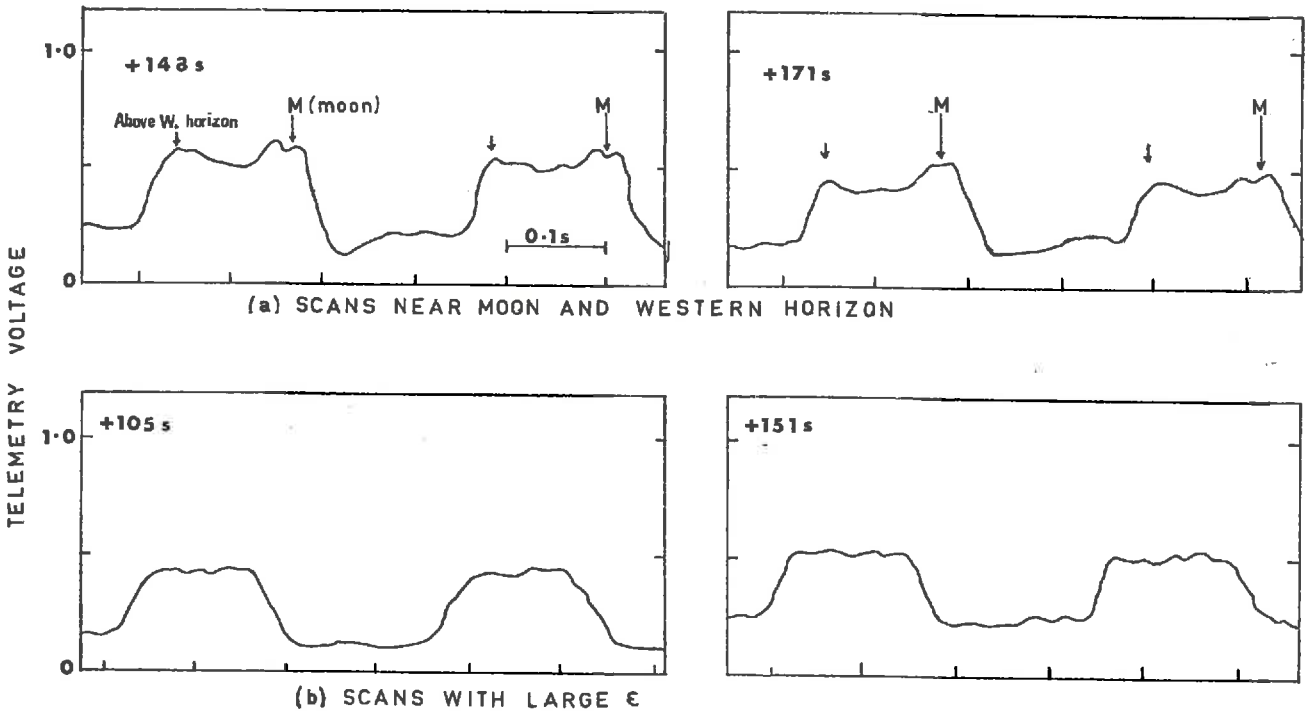

FIGURE 7·15 TELEMETRY TRACES—C 104

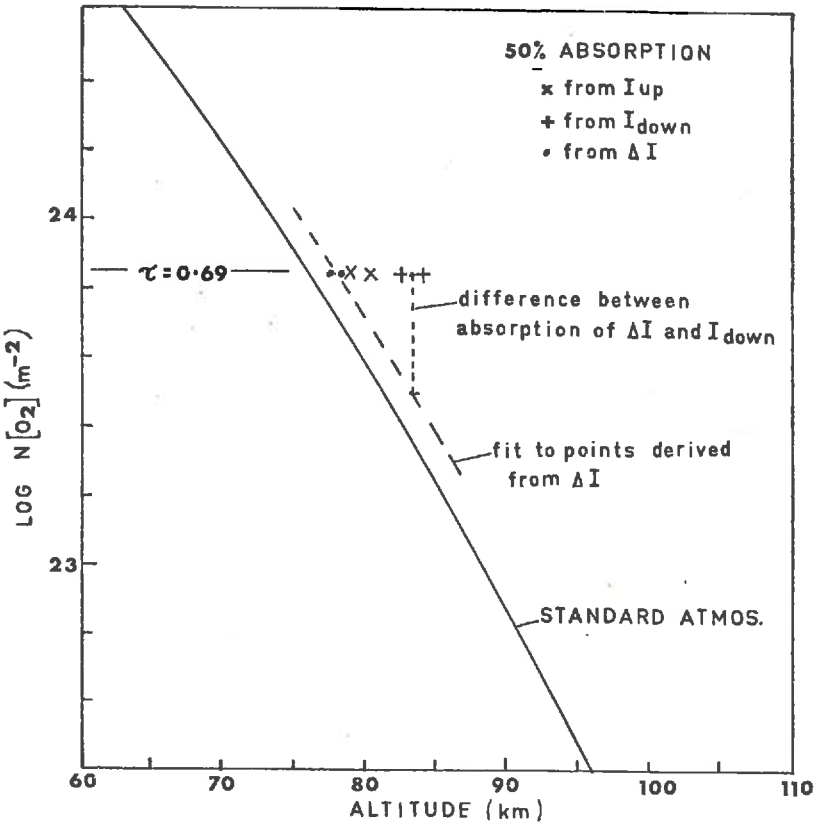

FIGURE 7·16 PARTIAL ABSORPTION HEIGHTS

rocket would have contributed almost equally to I_{UP} and I_{DOWN}. In the interpretation of the data from the airglow expriments, it was assumed that the total measured intensity could be considered as the sum of the two components - one trapped and the other untrapped - corresponding to the different shaded regions in Figure 6.4. Under this assumption, which is examined in greater detail in the next Chapter (8.4.2, 8.5.1, and Figure 8.15), the intensity of the backscattered radition (I_{DOWN}) was taken as a measure of the trapped component, and the difference between this and the total intensity from above ($\Delta I = I_{UP} - I_{DOWN}$) was interpreted as the untrapped component.

The attentuation of the radiation components (profiles in Figure 7.14) was used to estimate the molecular oxygen density. The data were not sufficiently precise for a complete density profile to be deduced, so only the points of 50% attenuation were considered. For (near) vertically incident untrapped radiation,

$$\frac{I}{I_0} = \exp\{-\sigma \int_h^\infty n(h')\, dh'\} \qquad (7a)$$

as in (1c). For absorption of Lymanα in molecular oxygen,

$$\frac{I}{I_0} = \exp\{-10^{-24}.N(h)\} \qquad (7b)$$

and at the altitude where $I = 0.5\ I_0$,

$$N(h) = 6.9 \times 10^{23}\ m^{-2} \qquad (7c)$$

An equivalent relationship for the trapped component, obtained

by substituting from (6r) into (7a), is

$$N(h) = \frac{(6.9 \times 10^{23})}{M} \; m^{-2} \qquad (7d)$$

Table 7.2 lists the altitudes corresponding to 50% absorption on both the upleg and downleg portions of the profiles in Figure 7.4.

TABLE 7.2 50% ATTENUATION POINTS

	UPLEG		DOWNLEG	
	t (s)	h (km)	t (s)	h (km)
I_{UP}	92	80.2	209	78.6
I_{DOWN}	98	83.2	203	82.4
ΔI	90	78.5	212	77.6

These points are shown in Figure 7.16 with a profile of N(h) from the U.S. Standard Atmosphere Supplements, 1966, for 30^0 latitude, SPRING/FALL (shown in full in Figure 8.17). The points derived from ΔI give a direct measure of N(h) $[O_2]$ while a comparison between these and the points based on I_{DOWN} gives an estimate of M, and hence the ratio of absorption coefficients of $[H]$ and $[O_2]$. As would be expected, the points based on the sum, I_{UP}, are intermediate. The results suggest a column density of molecular oxygen 1.5 x that of the model, and that the effective absorption cross-section (that is, the actual cross-section multiplied by M) for

trapped radiation was twice the cross-section for the untrapped radiation at 83 km. A similar difference between the absorption heights of I_{Up} and I_{DOWN} had been reported before (e.g. Kupperian et al., 1959); the enhancement of absorption by resonance trapping in the region is discussed in detail in Section 8.5. Because of the large corrections which had to be applied in the analysis of the data, the likely errors in individual intensity measurements are large. Even so, it is felt that the height given for 50% ΔI on the upleg is probably not in error by more than 2.5 km. It was found that the uncorrected data from the upleg also gave values close to those in Table 7.2, which indicated that the effects of the small corrections to the upleg data were not significant in the determination of the oxygen density profile.

The comparison between the plotted points and the standard curve in Figure 7.15 suggests that the standard atmosphere underestimates the oxygen density near 80 km at night, but, considering the quality of the raw data, such a conclusion must be regarded as tentative. The results are, however, an indication that more refined measurement of airglow profiles could yield useful measurements of atmospheric density.

The intensity of the airglow seen in the zenith, based on the corrected profiles of Figure 7.14, was 5 kilo-Rayleighs. This is slightly higher than most values which have been reported for $h \simeq 100$ km, but commensurate with the results of Paresce et al., (1972),

obtained ten weeks before the flight of C104. Paresce et al., measured intensities almost four times the model predictions of Meier and Mange (1970) and offered several reasons for the apparent discrepancy. It is possible that the airglow intensity at low altitudes was indeed higher than normal during the period spanning these two flights, although the data from the satellite absorption cell experiment (described by Vidal-Madjar et al., 1972) suggests that the Lymanα line core emission from the sun was not particularly strong at the time of the C104 flight. The exospheric temperature, calculated by the method detailed in the U.S. Standard Atmosphere Supplements, 1966, was 1190^0K, and the magnetic activity for the day was not particularly high. The intensities measured by C104 were certainly much higher than those measured by C1014 which was launched under similar conditions, almost exactly two years later.

7.3.3 Summary

Despite several disappointing aspects of the performance of the C104 payload, enough results were obtained to outline some of the characteristics of the Lymanα airglow field in the absorption region. The data obtained indicated the type of instruments which would be required to study the observed characteristics in detail. The absorption profiles observed pointed to the value of airglow measurements in the study of atmospheric properties, but it was clear that more sensitive instrumentation with greater resolution was required to make more detailed measurements.

CHAPTER 8 MEASUREMENTS OF LYMANα AIRGLOW AND LUNAR FLUX (C1014)

8.1 Introduction

8.1.1 The C1014 experiment

The ultraviolet airglow measurements made by the C104 instruments (7.3) had indicated several interesting features of the airglow distribution and absorption below 100 km, but the spatial and temporal resolution, and the signal to noise ratio were not adequate for detailed conclusions to be drawn. A further payload was designed to include much larger optical systems which improved each of these limiting characteristics.

Two airglow telescopes viewed in opposite directions normal to rocket axis, so that as the rocket rolled their fields of view scanned the same regions of the sky within a fraction of a second. Because of the advantages of the resonance absorption cell technique (8.1.2) in discriminating between the airglow line core and wings, an absorption cell was fitted into one of the telescopes. The absorption cell was arranged to be switched off periodically, so that comparisons might be made between three sets of measurements closely matched in space and time, viz:- Telescope 1, cell on; Telescope 1 cell off; and Telescope 2.

Spherical mirror optics enabled large collecting areas to be combined with narrow fields of view. Small fields were required to give good spatial resolution of airglow intensities near the horizon, and to enable lunar radiation to be detected against the airglow foreground. The payload was flown near full-moon and included another

lunar-ozone experiment. The intention was again to simultaneously measure mid and far ultraviolet lunar fluxes during the period near apogee. Because the absorption cell was virtually transparent (apart from window losses) to the broad lunar-reflected Lymanα line, both telescopes could be used to measure the lunar flux, while the inclusion of the cell in one telescope would enable the airglow radiation transport to be studied in more detail than before.

8.1.2 Resonance absorption filters

The properties of the upper atmosphere relevent to its interaction with ultraviolet radiation are strongly wavelength dependent in the vicinity of the Lymanα line. From the calculations in 6.3.3, it can be seen that large variations of the hydrogen scattering cross-section occur over a spectral range which is small compared with the resolution of most rocket borne instruments. This is particularly true of instruments which can be flown in small rockets. Even the data from such large systems as the double dispersion instrument of Bruner and Rense (1967) require significant corrections for instrument broadening. There are considerable technical difficulties in achieving greater resolution at night-time intensity levels by using dispersion methods.

There is, however, one simple technique which can be used to give an instrument an effective resolution sufficiently fine for measurements of the central component of the Lymanα airglow spectrum. The method uses the resonance scattering of radiation by atomic

hydrogen within an absorption cell in the instrument light-path. The line core radiation, for which the cell is optically thick, is scattered out of the beam passing to the detector, and can be measured by signal-differencing.

The technique has been applied extensively in laboratory measurements, and was first used in ultraviolet airglow measurements by Morton and Purcell (1962). They found that at 176 km more than 98% of the radiation from below the rocket, but only 85% of that from above, lay within the absorption width of their filter. The remaining 15% which was outside of the filter width was far enough removed from the line centre to be free of scattering from below the rocket.

A more sophisticated version of the absorption cell experiment was flown with a variable absorption width (Winter and Chubb, 1967). The current through the dissociating filaments was varied during flight to give a range of optical depths in the filter. Approximate airglow line profiles were generated to match the observed variation of signal with cell optical thickness. The observed albedo (nadir intensity/zenith intensity) was 35% with the cell switched off, for a solar depression angle of 43^0.

Bertaux and Blamont (1970) reported the results from a satellite-borne absorption cell experiment. Their instrument had a variable thickness absorption cell. From the attenuation factors measured, they estimated the temperature of the primary geocoronal

scattering hydrogen for several assumed levels of the extraterrestrial background. This same group also applied the absorption cell technique to the measurement of exospheric hydrogen densities by monitoring the absorption of direct solar radiation (Vidal-Madjar et al., 1972).

8.2 Experiment and Instrumentation Design

8.2.1 Lymanα Telescopes

In order to increase the collecting area of the detectors while retaining a small field of view, reflecting telescopes were used to focus the radiation onto the ion chamber windows. The configuration of the complete payload is shown in Figure 8.1. Covers over the entrance apertures of the telescopes on opposite sides of the rocket were released at approximately 50 km altitude. The telescopes were fitted closely back-to-back to reduce the overall length, and the amplifiers were mounted close beside their respective ion chambers to keep the low-level signal leads to a length less than 3 cm. Figure 8.2 is a cross-section of one telescope (T2).

The first reflecting surface was a flat glass plate, inclined at 45^0 to the entrant beam, and having a hole near the centre through which the focussed light passed to the field stop and detector. The second mirror was also glass, with a concave front surface having a radius of curvature of 140 mm. A thin metal disc with a circular central hole acted as the field stop in Telescope 2 while in Telescope 1 the field was defined by the entrance window of the absorption cell. The cell window opening was equivalent in size and position

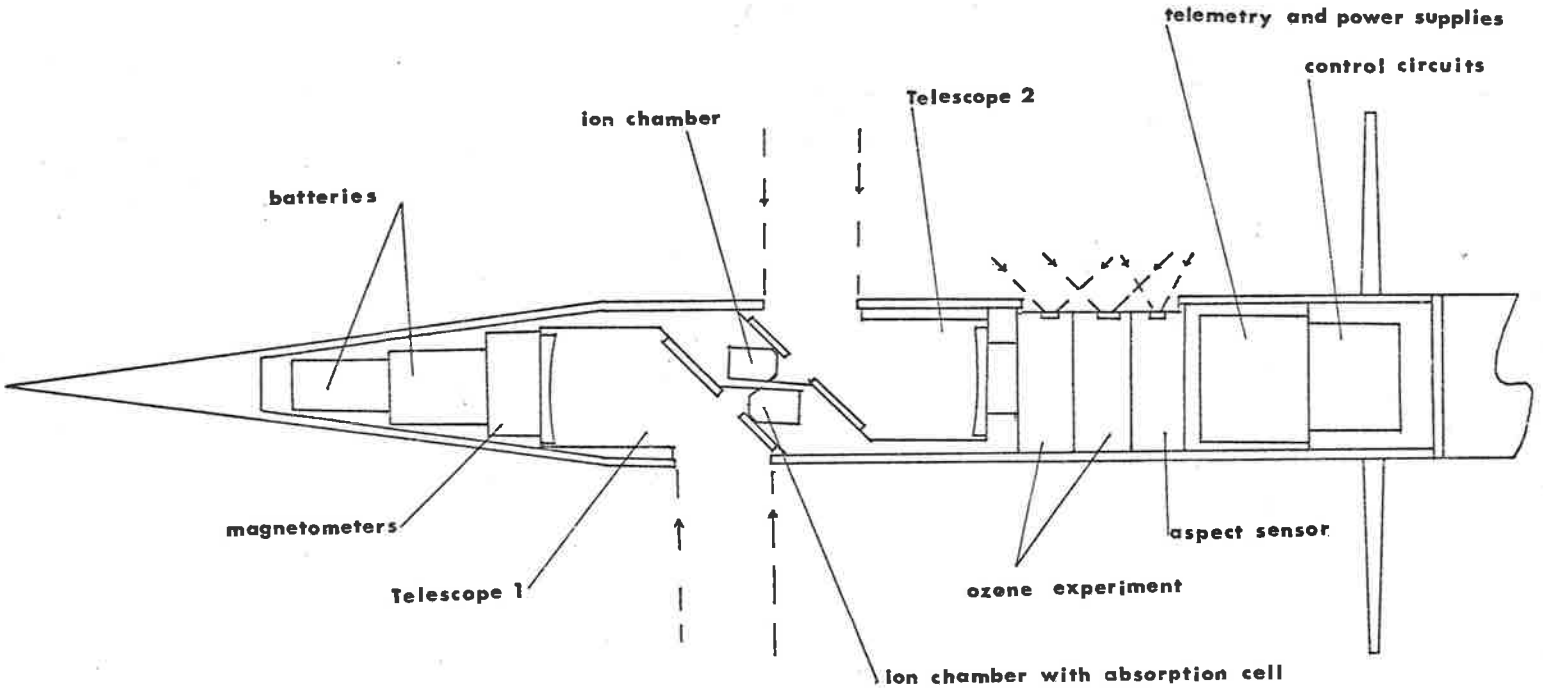

FIGURE 8·1 C1014 PAYLOAD CONFIGURATION

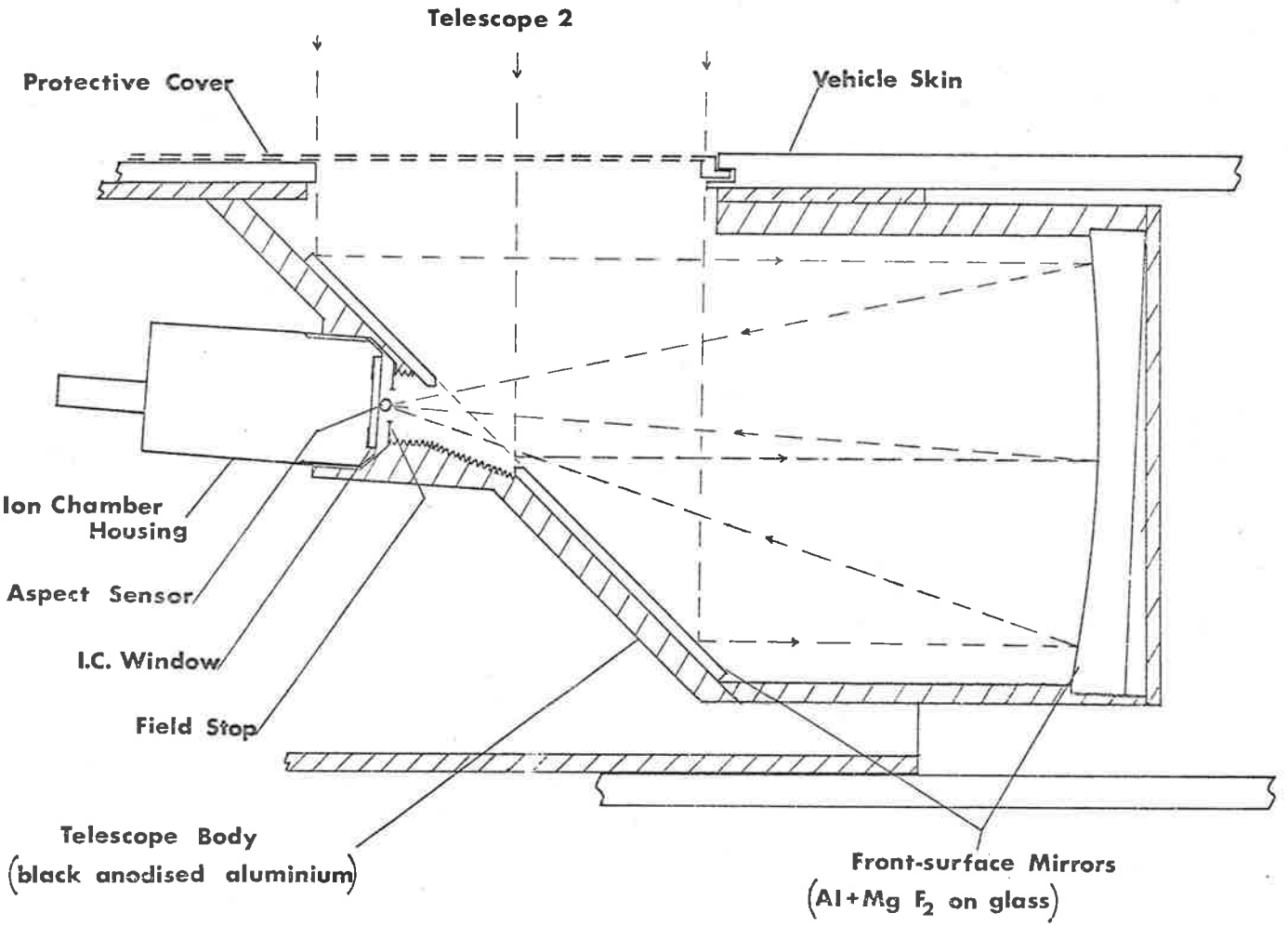

FIGURE 8-2 LYMAN ∝ TELESCOPE - C 1014

to the aperture in the field stop plate of T2. The field of view of each telescope was circular, with a diamter of 2.5^0. All of the collected light entered the ion chambers at less than 16^0 from their central axes. Within this acceptance angle the sensitivity of the chambers was quite uniform, and not much below the on-axis figure measured during calibration (Figure 2.16).

The mirrors were front-surface coated with evaporated aluminium covered with a protective layer of magnesium fluoride. The vacuum ultraviolet reflectivity of unprotected fresh aluminium decreases rapidly with exposure to air due to surface oxidation, so the reflectors were given a protective coating with a thickness selected to take advantage of constructive interferance effects (Canfield et al., 1966). Because the coating is much less transparent at 121.6 nm than in the visible region, the optimum thickness is less than a calculated quarter-wave layer. Optimum coating thicknesses were found to be about 25 nm of magnesium fluoride over 80 nm of aluminium, confirming the findings of Canfield et al., (1966) and Hunter et al., (1971). The latter group had reported extensive measurements of the reflectivity of mirrors at angles of incidence other than 90^0 which were applicable to the first reflecting surface. The evaporations were done at pressures between 10^{-7} and 10^{-6} mm of mercury.

The reflectivity of the mirrors was measured in a reflectometer attached to the ½ meter monochromator which was used for ion chamber

calibrations. A photomultiplier viewing a sodium salicylate deposit was used to measure the ratio of the direct beam flux to the reflected fluxes at 10^0 and 45^0 angles of incidence on the mirrors. Typical measured reflectivity curves of good mirrors are shown in Figure 8.3. The best mirrors used in the flight instruments had reflectivities, when fresh, of 74% and 67% at 10^0 and 45^0 incidence respectively. Good coatings were found to deteriorate only slowly with time when stored in a clean atmosphere of air.

8.2.2 Ion chambers

The ion chambers were constructed in the manner described in 2.4.3. They had 19 mm diameter windows of cleaved lithium fluoride bonded with apoxy to blown glass bodies. Each window had a series of stripes and a circular band of evaporated aluminium on the inner surface. These helped to prevent the distortion of the internal electric field by charge build-up on the window surface.

The glass chamber body was potted inside a brass shell which gave mechanical, electrical and thermal protection to the chamber itself. Ion chambers of this type, both with and without the protective shell, are shown in Figure 2.9. The chambers which were made for Telescope 1 had the absorption cells fixed directly to the front surface of the lithium fluoride windows. The wires to the absorption cell filament were taken down the side of each chamber to the rear of the brass shell. Tests were done in the assembled payload to ensure that the close proximity of the filament

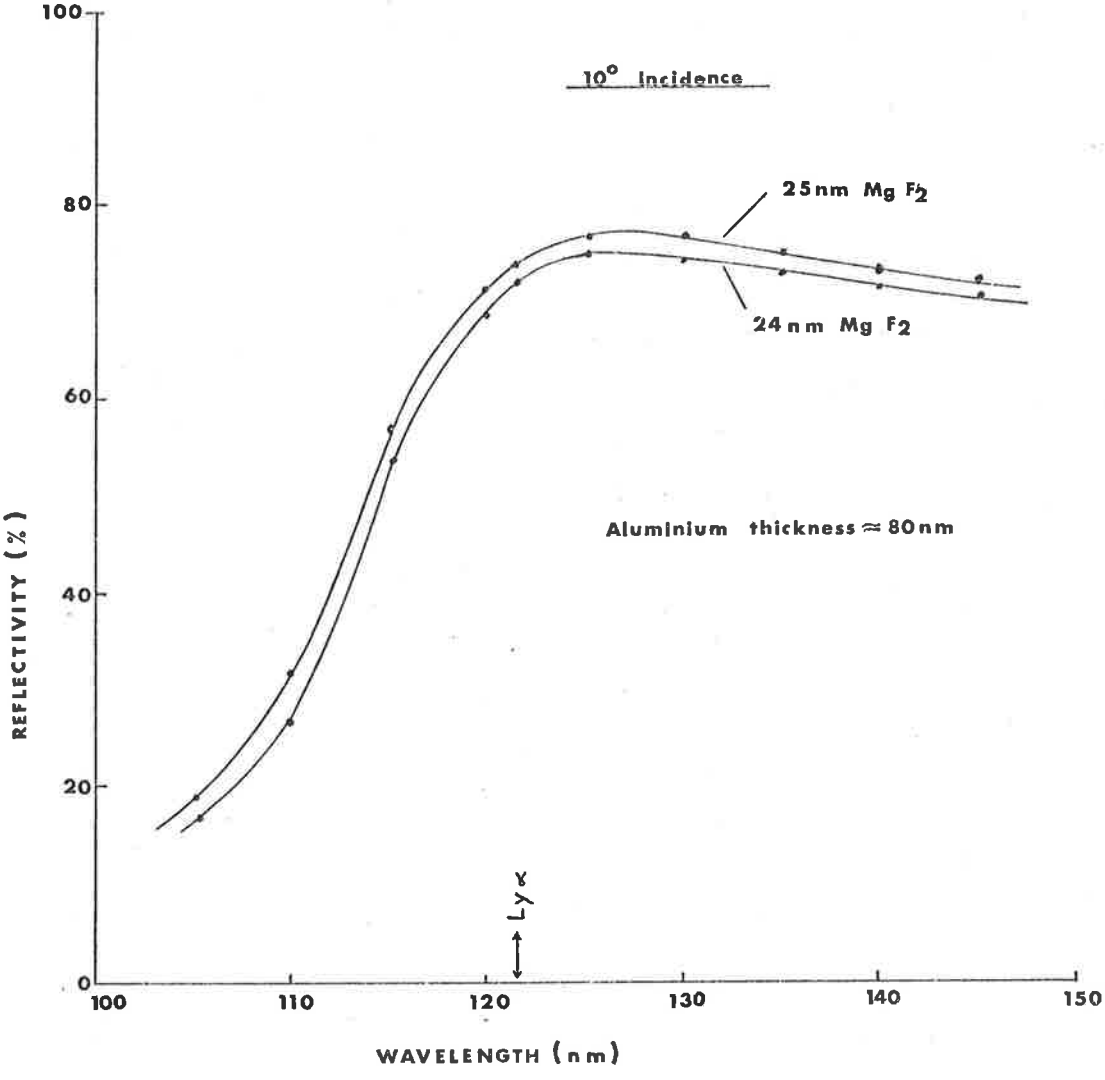

FIGURE 8·3 REFLECTIVITY OF COATED MIRRORS

leads did not introduce interference into the ion chambers. The absorption cell protruded from the potting material so that its front window lay in the focal plane of the telescope and acted as the field stop. Chambers with absorption cells attached are shown in Figure 8.4.

The ion chamber in Telescope 2 was operated at a gas gain of 100, while the other chamber was run at a higher gain (500) to compensate for the transmission loss in the cell window, and to give adequate signals from the part of the airglow spectrum which was passed by the absorption cell.

8.2.3 Resonance absorption cell

The atomic hydrogen absorption cell, which can be seen attached to the front of the ion chamber in Figure 8.4, had glass walls in the shape of a truncated cone.

Figure 8.5 shows two views of the cell. Although no usable data was received from the absorption cell detector on the flight reported here, the application of such devices has considerable potential in future work. Information on the design and construction of the cells which were developed has accordingly been included in moderate detail in Appendix D.

Scattering in the cell of the radiation from the line-core of the direct beam is analogous to the geocoronal scattering situation described in 6.3.2. Within the cell, atomic hydrogen is produced by thermal dissociation on the surface of a hot

FIGURE 8.4 ION CHAMBERS WITH ABSORPTION CELLS (C1014)

At right, both the chamber and the cell have been finally sealed: the chamber by flame and the cell by a cold-weld coated with epoxy. When potted into the brass sleeve, the window of the cell protruded slightly to form an aperture in the focal plane of the telescope.

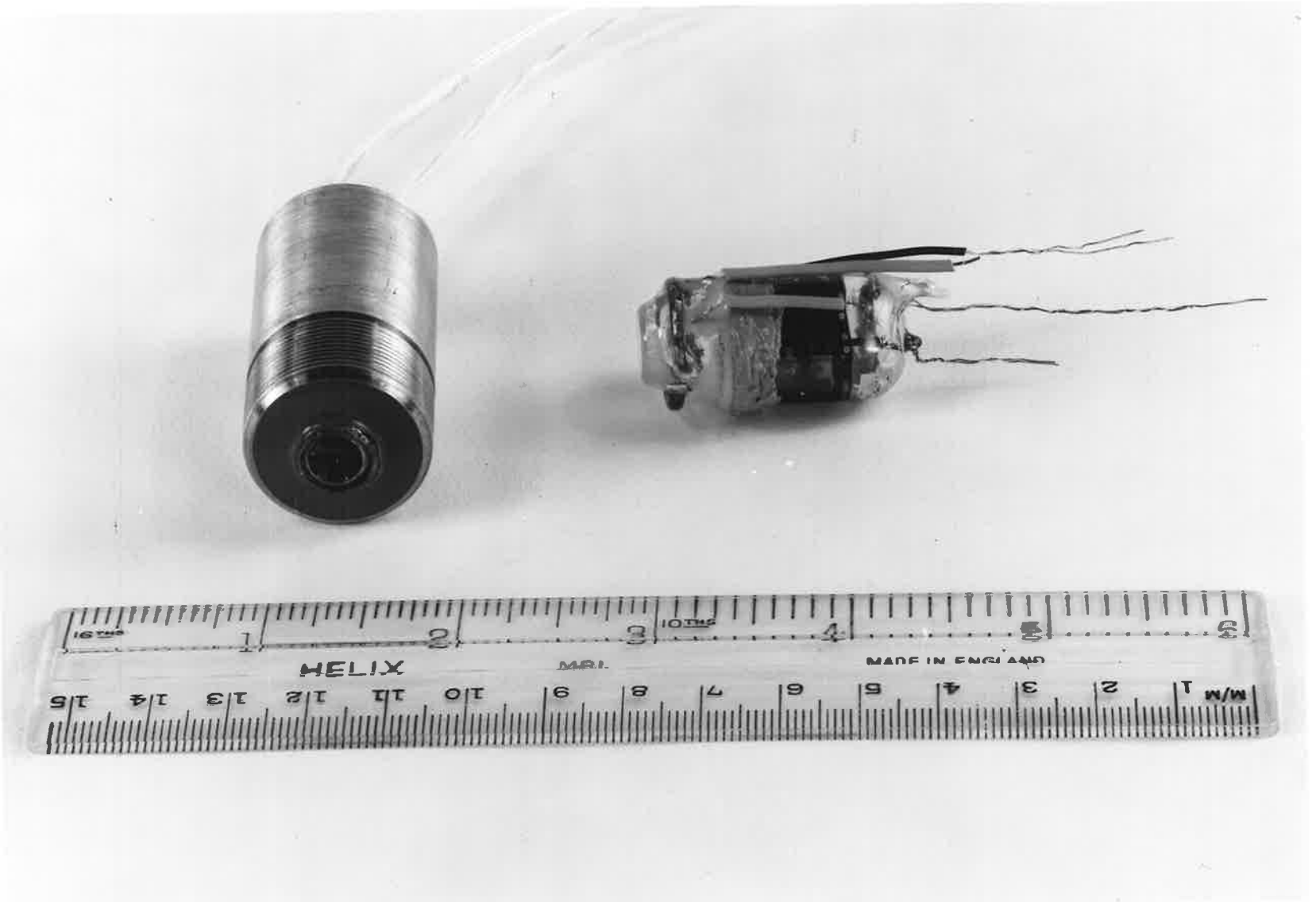
HELIX
MADE IN ENGLAND

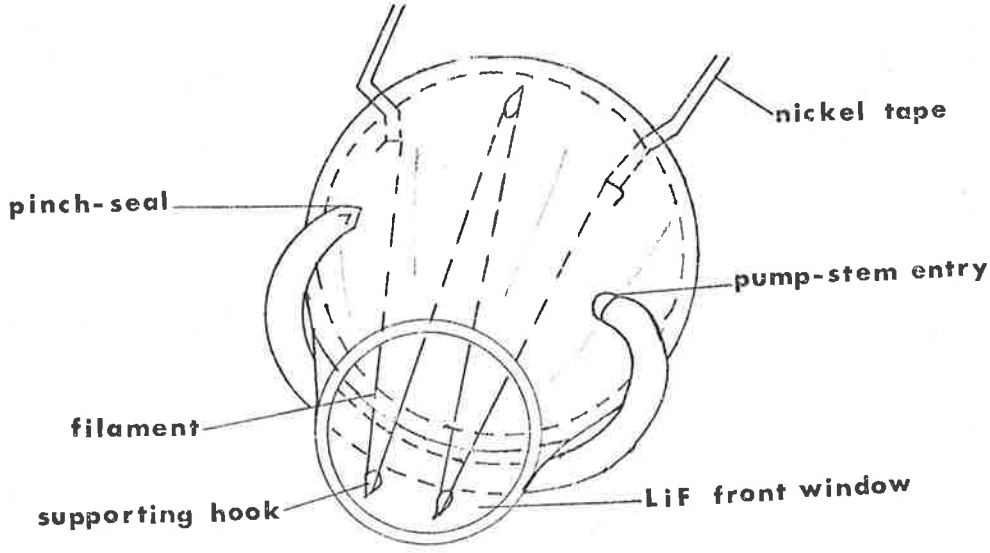

FIGURE 8·5a ABSORPTION CELL (PERSPECTIVE)

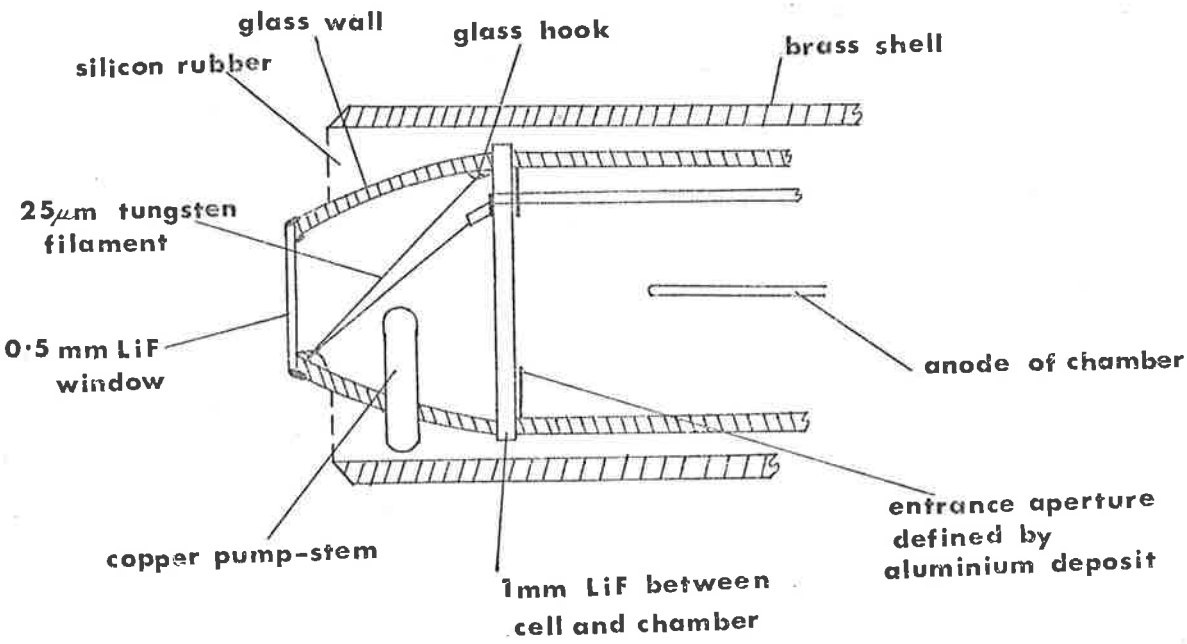

FIGURE 8·5b CELL AND CHAMBER IN SHELL (x2)

filament. The atoms become thermalized to the temperature of the molecular hydrogen filling as they diffuse through the cell. The temperature which determines the Doppler width for scattering (6c and 6f) is then close to that of the cell wall which provides an efficient heat-sink for the gas. The spectral response of an absorption cell instrument has a desensitized region, centred on the Lymanα emission line, and having a width comparable with the spectral spread of the back-scattered geocoronal radiation. The contribution to the detector signal from the central part of the spectrum can be found by comparison with a full-spectrum detector, or by noting the change in signal level when the absorption cell is periodically turned off, allowing the line-core radiation to reach the detector. Advantages of the absorption cell technique for rocket instrumentation include the relative compactness and simplicity of the hardware, and the intrinsic alignment of the filter band on the centre of the emission line without the need for delicate adjustment.

8.2.4 Amplifiers

If the rocket rolled about its axis at the expected rate, a point source would cross the field of view in only a few milliseconds. In order to be able to measure fluxes from point sources (e.g. the moon), the detectors and amplifiers had to have response times of 2 milliseconds or less. This speed had to be obtained with an amplifier gain of 10^{11} volts Amp^{-1}, and a suitably low random noise

level. The response time was achieved by using an electrometer feed-back amplifier. The feed-back resistor ($10^{10}\Omega$) was surrounded by a silver sleeve to reduce its self capacitance, and was mounted in an isolated shielded compartment. The random noise component in the output was minimised without compromising the response time by the inclusion of a second-order active filter to follow the main amplifier. The noise level at the amplifier output was 25 mV RMS for a 2 ms risetime. The signals passed through compression networks before being telemetered, as the signal from Telescope 1, in particular, was expected to approach the telemetry saturation level while the absorption cell was turned off. The circuit of the amplifier is shown in Figure 8.6 together with the aspect sensor amplifier which was mounted on the same circuit board.

8.2.5 Attitude sensors

The payload included a set of tri-axial fluxgate magnetometers and a lunar aspect detector to provide the data for the vehicle attitude solution. The lunar aspect sensor used the same type of slit pattern as had those on previous vehicles, but with modifications to extend the operating range to larger positive and negative aspect angles. Limitations of the acceptance angle of previous aspect sensors had complicated the aspect solution for earlier flights. A pattern of slits was formed on the surface of a cylindrical glass lens by vacuum-coating with nichrome through a mask. The viewing aperture for the photomultiplier was a ground indentation in the

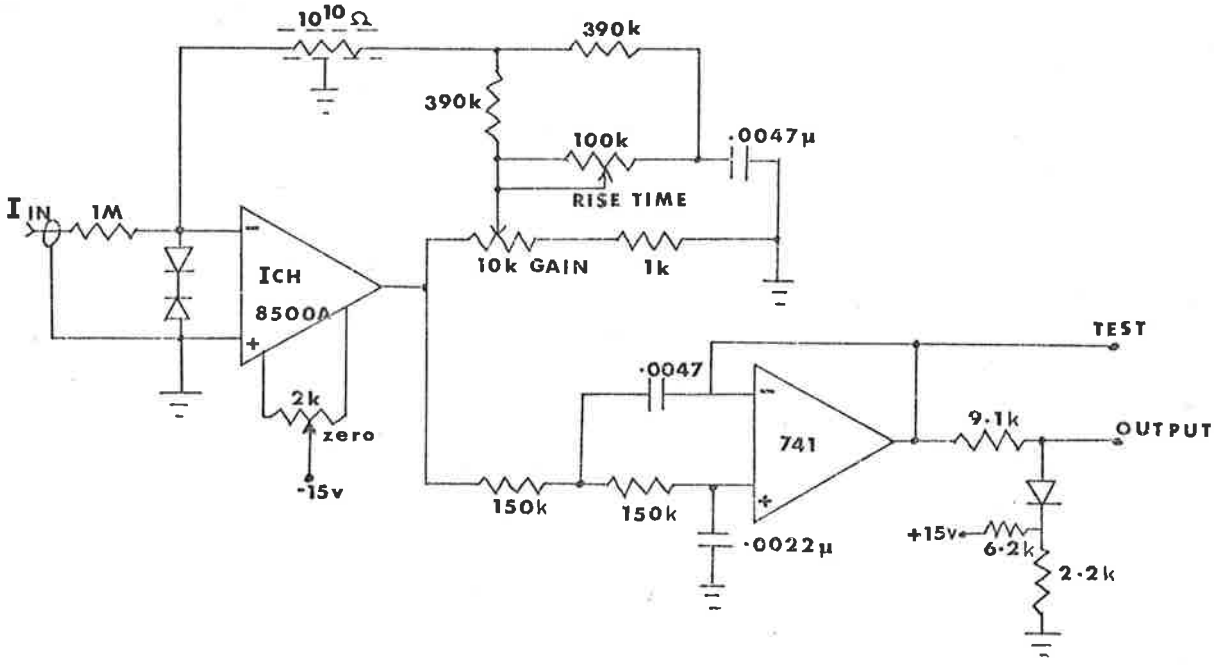

ION CHAMBER SIGNAL AMPLIFIER

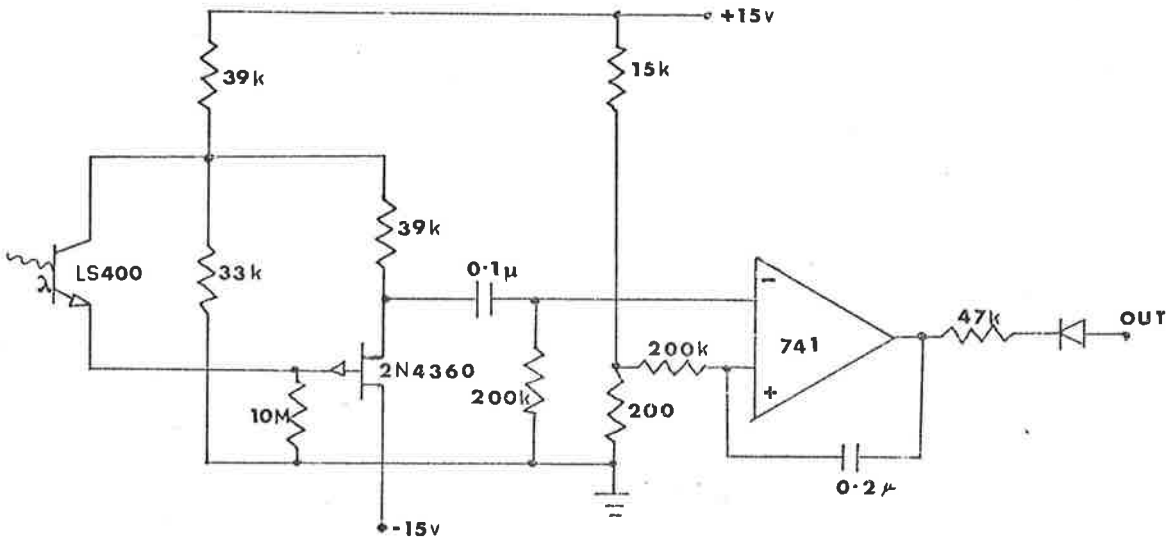

ASPECT SENSOR CIRCUIT

FIGURE 8·6 TELESCOPE ELECTRONICS C1014

coated back surface of the lens. Refraction at the front surface of the lens widened considerably the range of angles over which the detector operated.

It was required that the exact times when the moon crossed the telescope fields should be known. The detector responses to the lunar ultraviolet radiation could then be positively identified. If no response had been observed, an upper limit could confidently be placed on the flux with the knowledge that the moon had actually been scanned by the telescope(s). A detector sensitive to visible light was placed in the focal plane of each telescope. A photo-transistor viewed a reflecting strip along the edge of the aperture, and the associated circuit was arranged to generate a pulse whenever the moon's image crossed over the strip and into the telescope aperture. The visible aspect sensors were automatically compensated for diffuse background light and had thresholds set to ensure that the moon was the only source capable of producing the identifying pulses during flight. Because these aspects sensors were mounted on the telescope field stops, their optical axes were necessarily coincident with those of the ultraviolet detectors, and no ambiguities could be caused by misalignment.

8.2.6 Calibration of the telescopes

The design of the telescopes, with an aperture in the centre of the first reflecting surface, presented problems in the direct calibration of the complete unit. Accordingly, the properties of the

detectors and reflectors were measured separately using the half-metre monochromator as the source. The sensitivity of the complete system was then calculated by combining the measurements with the known geometric properties of the instruments. The factors included in the sensitivity calculations are listed in Table 8.1.

TABLE 8.1 FACTORS IN THE CALCULATION OF THE TELESCOPE SENSITIVITIES

Entrance Aperture	46 cm^2	
Effective mirror area	42 cm^2	
Telescope transmission (2 surfaces)	40%	
Field aperture diameter	6 mm	
	TELESCOPE 1	TELESCOPE 2
Ion chamber efficiency (axis)	7.2% (including cell)	32%
Gas gain of chamber	500	100
Amplifier gain	1.35×10^{11}	1.0×10^{11} Volt Amp^{-1}
Sensitivity (point source)	1.1×10^{-5}	7.4×10^{-6} Volt ph^{-1} cm^{-2} sec^{-1}
Sensitivity (extended source)	0.9	1.4 kR/Volt

The estimated likely errors in the sensitivity values, from quadrature addition of the components, are 20% (point source) and 30% (extended source). The greater error estimate for extended

sources is due to the degree of uncertainty in the effective field of view. The measurement of the lunar flux (8.6) included three additional factors which contribute to the error analysis. They are included in the error figure given in 8.6.3.

Figure 8.7 shows a view of the instrumentation section of the payload with the outer skin removed. From the bottom upwards can be seen the mid ultraviolet filters (2), the aspect sensor lens, the entrance aperture of Telescope 2, ion chamber 2 between the amplifier modules, and the magnetometers and battery compartment.

8.3 The In-flight Performance of the Telescope Payload

8.3.1 Launch conditions

Cockatoo C1014 was launched from the Woomera Range (30.9^0S, 131.5^0 E) at 2004 CST (1034 UT) on May 29, 1970. The apogee height of 120 km was reached after 170 seconds and the detectors were exposed above 75 km for 197 seconds. The H.T. was switched onto the ion chambers at +30 seconds, and the covers protecting the telescopes were released at +50 seconds.

At the time when measurements were commenced, the sun was at a zenith angle of 123^0 and at an azimuth of 277^0. The moon was at a zenith angle of 68^0 and at an azimuth of 108^0.

The exospheric temperature, T_∞, calculated from Jacchia's formulae, given in the U.S. Standard Atmosphere Supplements, 1966, was 1010^0K. The daily solar activity, indicated by the measured 10.7 cm radiation fluxes, was low ($F_{10.7}$ = 113). This was lower

FIGURE 8.7 INSTRUMENTATION SECTION OF C1014

From the top can be seen battery packs and magnetometers; Telescope 1; the ion chamber of Telescope 2 between the two telescope amplifiers; the entrance aperture and diagonal mirror of Telescope 2; the aspect sensor lens and ozone experiment filters , with amplifiers and the H.T. Supply on the sides of the photomultiplier block.

than the equivalent figure for the launch date of C104, even though the contribution to the exospheric temperature by the geomagnetic activity component was greater.

8.3.2 Attitude solution

The outputs from the attitude sensors (8.2.5) were used to deduce the direction, in azimuth and elevation co-ordinates, of the axis of the rocket as a function of time. The in-flight characteristics of the magnetometers were derived from the readings obtained near the beginning and end of the flight, and when the rocket was perpendicular to the magnetic field. Figure 8.8 was derived from the magnetometer head which was parallel to the axes of the detectors and the lunar aspect sensors. Basing the attitude solution on this magnetometer minimised the errors caused by any misalignment between the longitudinal axis and roll axis of the rocket. The misalignment, as expected with a roll rate of 1.7 revs per second, was less than two degrees throughout the major part of the flight. The estimated error range in Figure 8.8, referred to the detector axis, is $\pm 1^0$.

The lunar aspect angle (defined in Figure 7.7) remained within the calibrated range of the aspect sensor ($\pm 45^0$) until +270 seconds, after the rocket had inverted on the down leg. Correct alignment of the aspect sensor and the telescopes was verified when they scanned the moon at +66, +70 and +237 seconds. The lunar aspect curve (Figure 8.9) has estimated error limits of $\pm 1.5^0$.

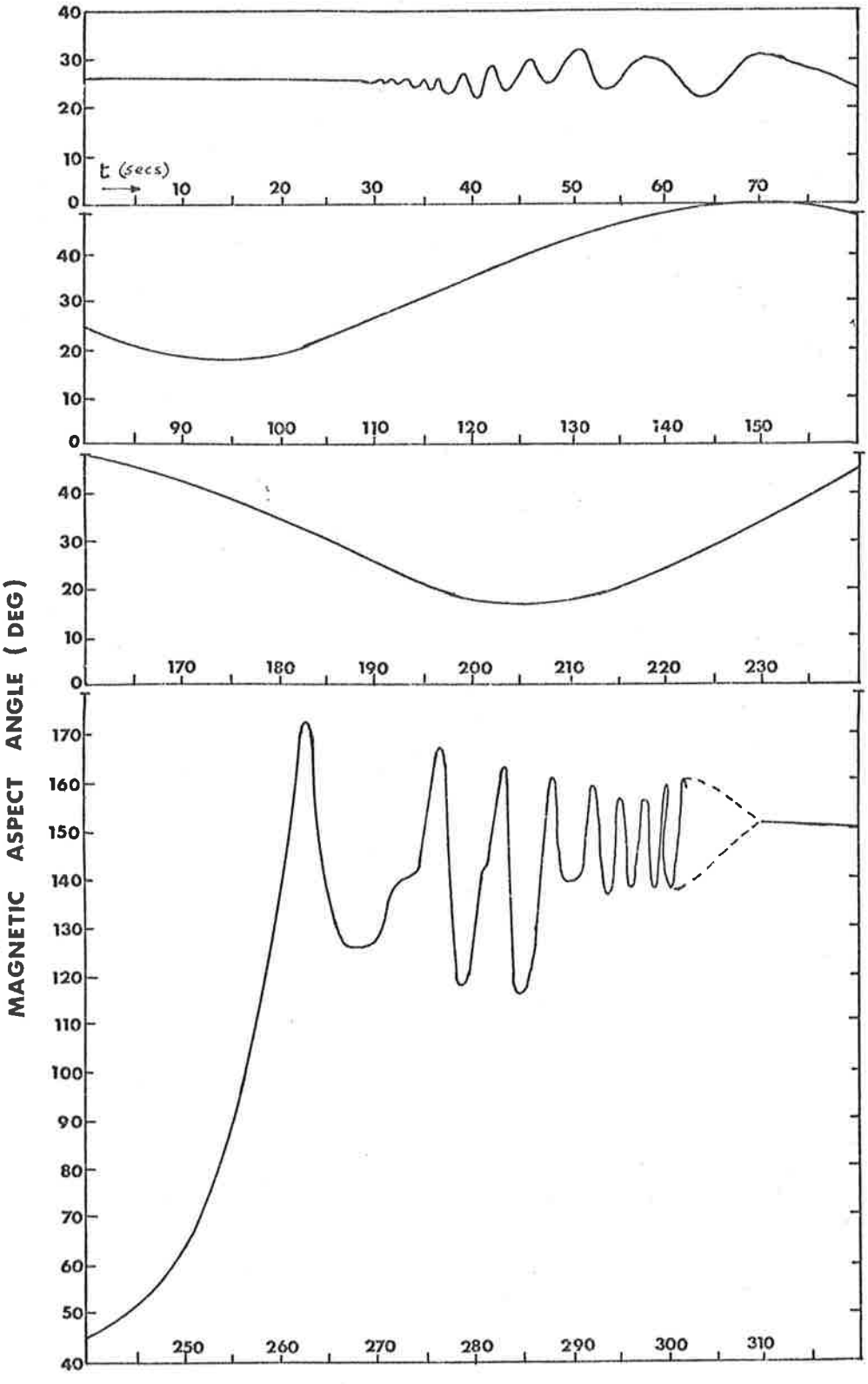

FIGURE 8.8 MAGNETIC ASPECT - C1014

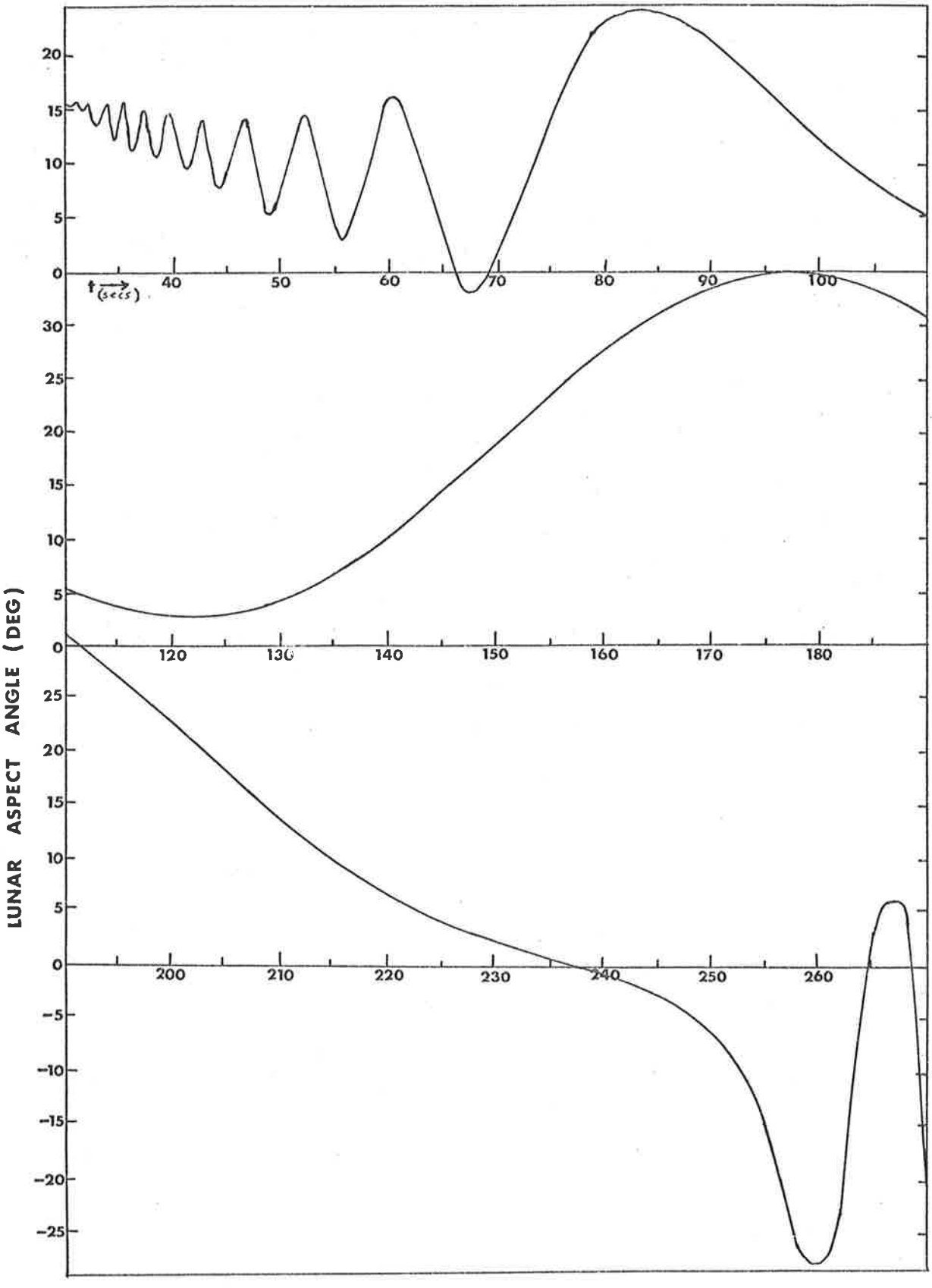

FIGURE 8.9 LUNAR ASPECT – C1014

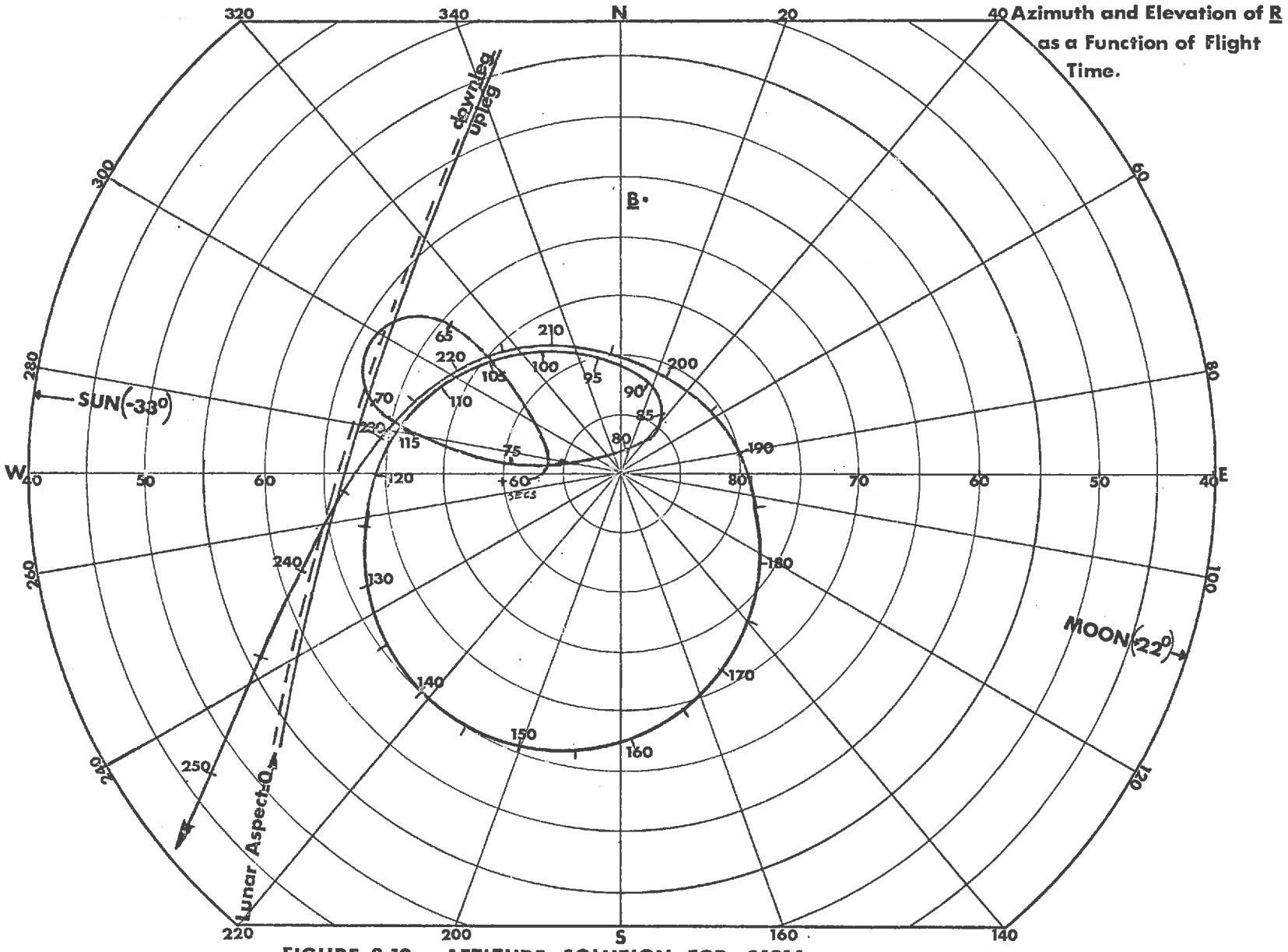

FIGURE 8.10 ATTITUDE SOLUTION FOR C1014

During the upleg of the flight, the angle between the directions of the moon and the magnetic field was 75.8^0. Up until the time of inversion during the downleg, the rocket axis did not deviate by more than 25^0 from the inital direction at launch, and within this solid angle the lunar aspect and magnetic co-ordinate frames are approximately orthogonal, allowing a derivation of attitude with minimum errors. The attitude solution (Figure 8.10) has an estimated error limit of 2^0.

From +95 s to +230 s the rocket motion closely approximated precession around a closed cone. Before +235 s the maxium inclination to the horizontal of the detector scan plane had been 25^0. The only occasion when the detector scan plane included the zenith was at +257 seconds. At +78 s the detector scan plane was within 2^0 of horizontal.

Figure 8.10 shows the direction of the magnetic field and the azimuth positions of the sun and moon. Also shown are the loci of attitudes having 0^0 lunar aspect for the upleg (centred on +70 seconds - solid) and downleg (240 seconds - dashed).

8.3.3 The absorption cell detector

When the H.T. voltage was applied to the ion chambers at +30 seconds, the output from Telescope 2 settled to zero volts within two seconds and remained stable. The Telescope 1 system, however, produced a series of pulses of sufficient amplitude to reach the full scale limit of the output circuit. Although the pulses ceased

at +42 s, they indicated that for some reason the stability of the Telescope 1 detector system was marginal.

The cover plates protecting the telescopes were explosively released at +50 s. Another series of similar pulses was produced, and again they showed no correlation with the viewing direction of the telescope. These random pulses stopped at +60 s, and from +62 s a different series of pulses was produced. They coincided with the times when the telescope axis swept to its greatest angle above the horizon. The length of the pulses increased until from +68 s the amplifier output remained in limit. This occured at 70 km altitude, where the telescope would first be expected to respond to Lymanα radiation. The detector appears to have been operating with extremely high gain so that even small radiation intensities produced full-scale outputs.

The reason for the sensitivity being higher than intended is not known. The characteristics of ion chambers had been found in earlier tests to be unchanged by the vibration levels which were expected within the payload. Because the payload was not recovered, the possibility that this particular detector suffered some physical alteration could not be eliminated; neither can the possibility of an error having been made in the setting of the voltage which the H.T. unit applied to this ion chamber during flight. No evidence to identify any particular cause could be found in the flight or pre-flight records.

Further evidence that the ion chamber was still functioning as a Lymanα detector was seen during the downleg of the trajectory. The amplifier output started to come periodically out of saturation from 81 km altitude downwards. The length of the periodic saturation periods reduced as the rocket moved down to 68 km, and the amplifier read zero output from there down. Figure 8.11 is a plot showing the times for which the amplifier was saturated during the recovery period. Each sloping line represents a 540^0 (1.5 revolutions) scan of the telescope about the roll axis. The reference (0^0) for each scan was the central pulse from the lunar aspect detector. The solid lines show the times for which the amplifier was saturated, and the dashed curves indicate when the telescope was viewing above the horizontal plane. As the rocket moved lower in altitude, the saturation periods were restricted to higher elevation angles. It was found that the behaviour of the mark-space ratio (i.e. $\frac{\text{time saturated}}{\text{time unsaturated}}$) could be approximately modelled by assuming a critical radiation intensity for saturation, and calculating the attenuation of Lymanα radiation at various viewing elevations over the recovery height range (as in 8.4.4). Of course, no information on actual atmospheric absorption could be deduced by this procedure, but it was at least shown that the detector did continue to operate and remained sensitive to Lymanα radiation, but to a degree which was undetermined.

The lack of data from the telescope containing the absorption

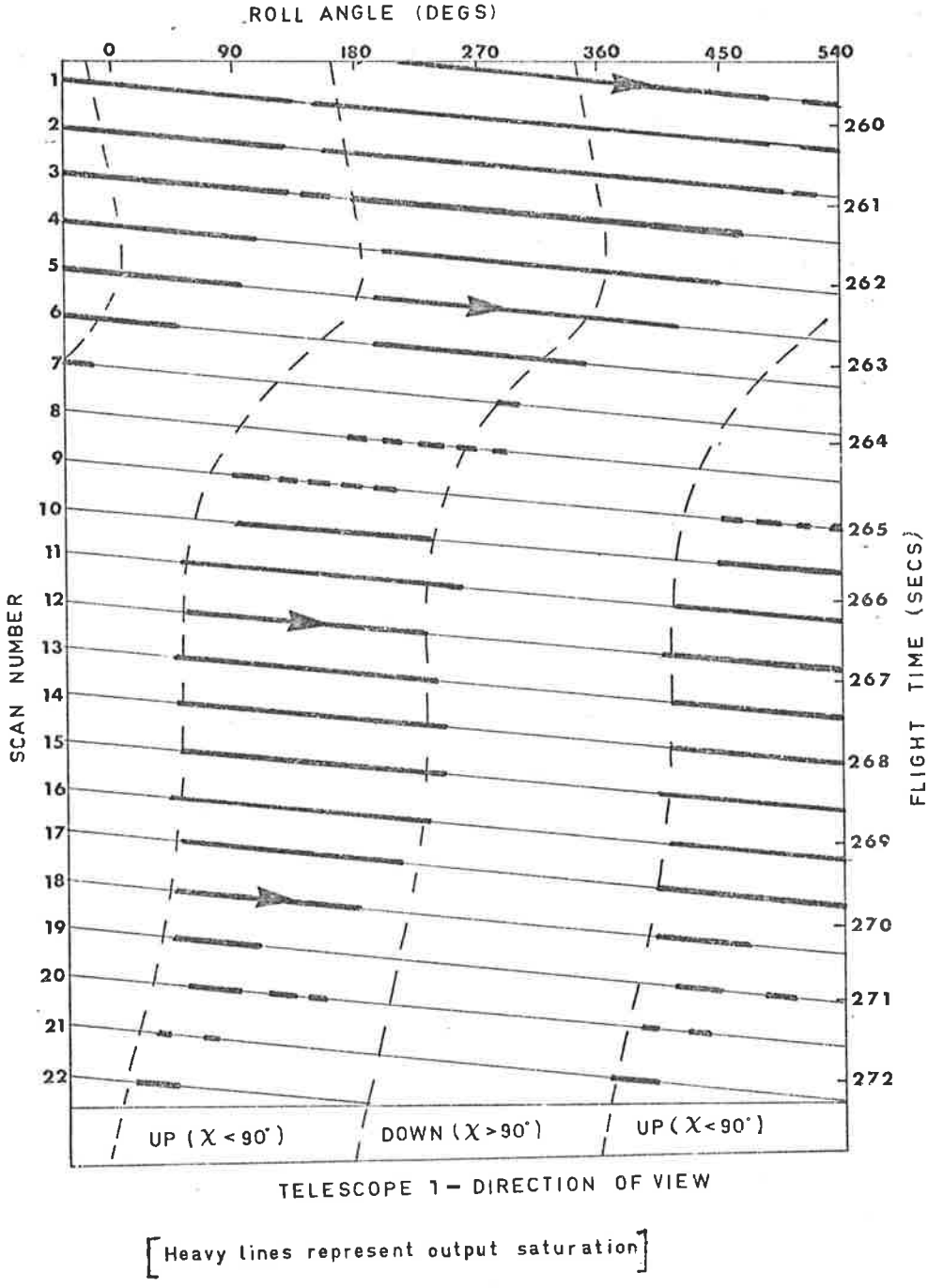

[Heavy lines represent output saturation]

FIGURE 8·11 OUTPUT OF TELESCOPE 1 DURING RECOVERY PERIOD

cell meant that the full potential of the instrumentation and experiment was not realized on this flight. It was not possible to separate unequivocally the 'hot' and 'cold' components of the airglow radiation, so that the planned study of extraterrestrial contributions, and the complete analysis of the low altitude transport could not be made. Despite this, a modified procedure was used to analyse the data from the other telescope, and useful results have been obtained, demonstrating the usefulness of measurements of this type. The measurements made with Telescope 2 are described and discussed in Section 8.4, 8.5 and 8.6.

8.4 Airglow Measurements

8.4.1 Introduction

The second telescope, which contained the ordinary ion chamber, continued to operate throughout the flight and showed no untoward effects associated with the saturation of the other detector. The following paragraphs outline in a general manner the nature of the signals received during the flight.

Between +75 s and +95 s on the upleg the rocket axis was within 10^0 of the zenith, so that the detector viewing direction was restricted to elevations between $\pm 10^0$ for this period. There were therefore no well distinguished measurements of up-looking and down-looking intensities as the rocket passed through the most strongly absorbing layers on the upleg. The first detection of ultraviolet radiation by Telescope 2 was +80 s, as the rocket axis

tilted away from the zenith (Figure 8.10). The telescope then scanned above the horizon and the strongest signals were received from the sunwards direction. By +95 s the detector was scanning up to an elevation of 10^0 above the southern horizon. The inclination of the scan plane (ε) did not get much lower than 10^0 for the rest of the flight until the time of re-entry inversion.

Radiation intensities increased as the vehicle moved upwards, but the general pattern of spatial distribution remained similar. There was a fairly uniform brightness over-head, separated by a rather sharp horizon boundary transition from the almost uniform intensity below the rocket. An enhancement of the intensity above the average upwards level was observed towards the sunwards horizon, and could be seen from 80 km upwards.

The intensities measured during the downleg followed the same pattern, but the inclination of the detector scan plane was much higher as the rocket moved through the altitudes of strongest absorption. The radiation from all directions had been reduced to the limit of detection at 72 km, when the detector was scanning between $\pm 35^0$ elevation. At this altitude Telescope 1 had almost completed its recovery from saturation.

Figure 8.12 shows examples of the output from the amplifier at several times during the flight. When the region of the sky towards the sun-horizon is excluded, the general zenith-symmetry and sharp horizon-step can be seen.

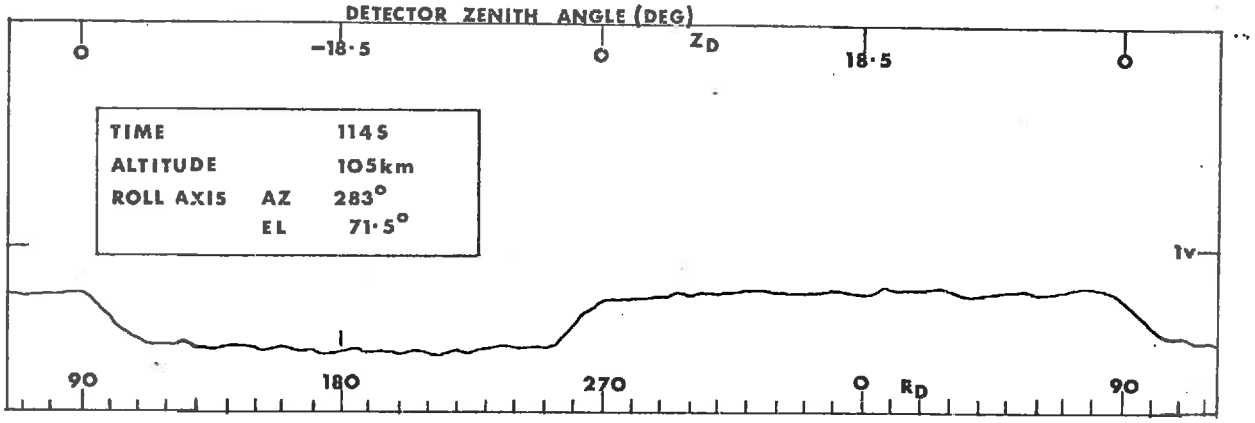

(a) Symmetrical scan:- upwards-looking towards east, away from sun.

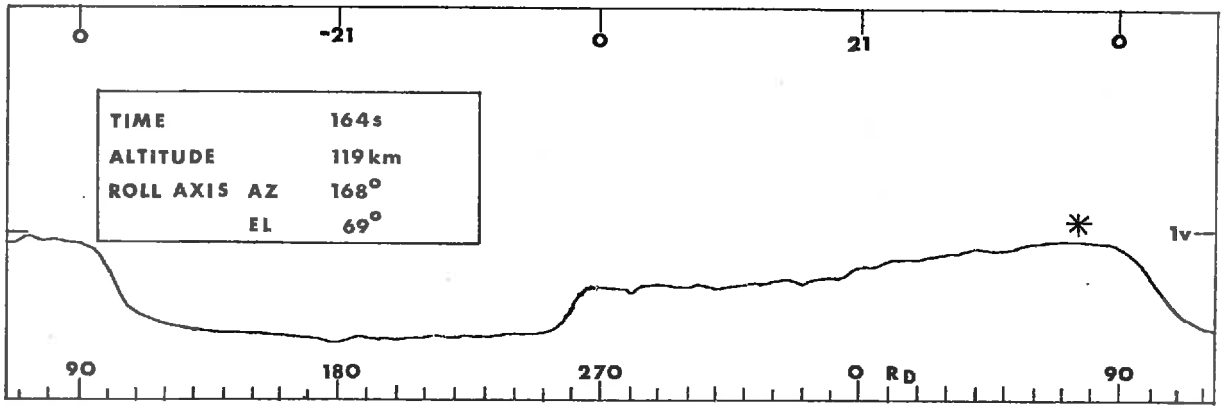

(b) Enhancement toward sun horizon: at * detector was 6° above sunwards horizon

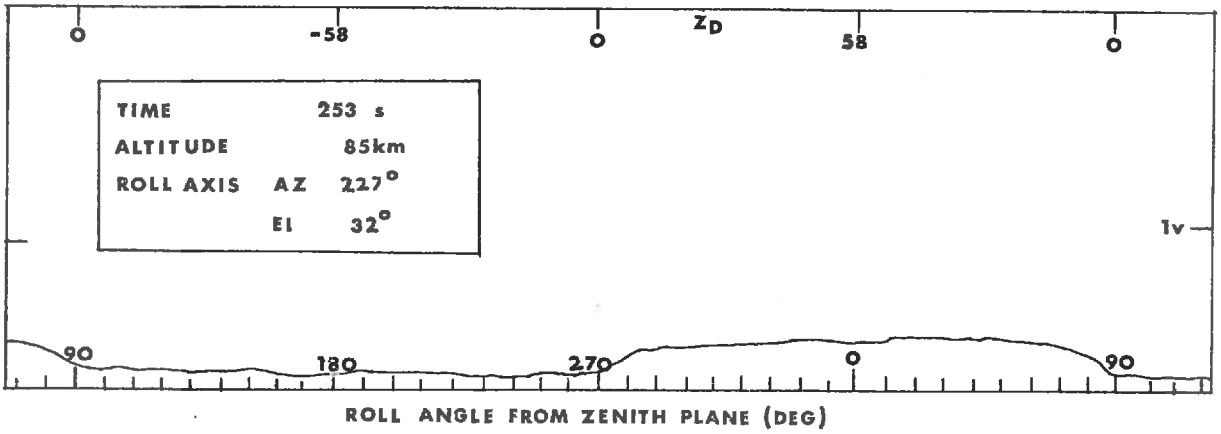

(c) Scan at lower altitude showing different mark/space ratio (P) and slight enhancement in north-westerly sky

FIGURE 8·12 TRACES TAKEN FROM TELEMETRY FILM RECORD OF LYMAN α TELESCOPE OUTPUT

8.4.2 Time and altitude profiles

Because it was not possible to separate properly the 'hot' and 'cold' components of the airglow intensities, a rigorous analysis could not be done, and the data from Telescope 2 was analysed on the basis of a simplifying assumption. The assumption was that the radiation could be considered as the sum of two separable components; one being trapped radiation for which R>>1, and the other, removed from the centre of the resonance line, for which R<<1 (see equation (6g) and Figure 8.15b). This was of course not a rigorously true picture of the actual spectrum, but when applied carefully, the separation of the components enabled a good fit of the data to model behaviour to be made. Only further, more complete, experimental measurements could show how closely this treatment approximated the results of a more rigorous analysis.

It was observed from the telemetry records that the detector output waveform was very much like an off-set square wave, particularly when the detector scan plane was inclined at a large angle to the horizontal. This shape can be seen in Figure 8.12, excepting the scans towards the western (sunward) horizon. The transition from UP (up-looking) to DOWN (down-looking) intensities occured over a small range of zenith angles. A detailed analysis of the changes of the wave-shape with inclination of the scans and with height (8.4.3 and 8.4.4) suggested that the intensity could indeed be approximately described as the sum of a quasi-isotropic, trapped

radiation field and a non-trapped flux propagating downwards through a pure absorbing medium (molecular oxygen) from an almost uniform overhead source. The trapped radiation component would not be expected to be a rapidly varying function of zenith angle of observation, whereas the other component would very rapidly as a function of zenith angle in the vicinity of the 'Lymanα horizon' (Figure 8.14a).

The Earth's atmosphere was considered to have an albedo for single scattering of zero for the untrapped component and an albedo not very much less than 1 for the trapped component. The intensity seen by the detector when viewing sufficiently below the horizon would then approximate the trapped component, whilst that seen from well above the horizon would approximate the sum of the trapped and untrapped components (with the latter modified by the zenith-angle function for the pure absorption). The difference between the two intensities ($I_{UP} - I_{DOWN}$) would therefore approximate the intensity of the untrapped component (Figure 8.15).

In Figure 8.13, the three parts (a), (b), (c), are plots of the upwards-viewing and downwards-viewing intensities, and the difference between them, as a function of flight-time. The maximum and minimum intensities during the rocket rotation were measured as an average over about four consecutive rotations at those times of flight where these intensities were varying slowly. The averaging was done to reduce the contributions from random noise.

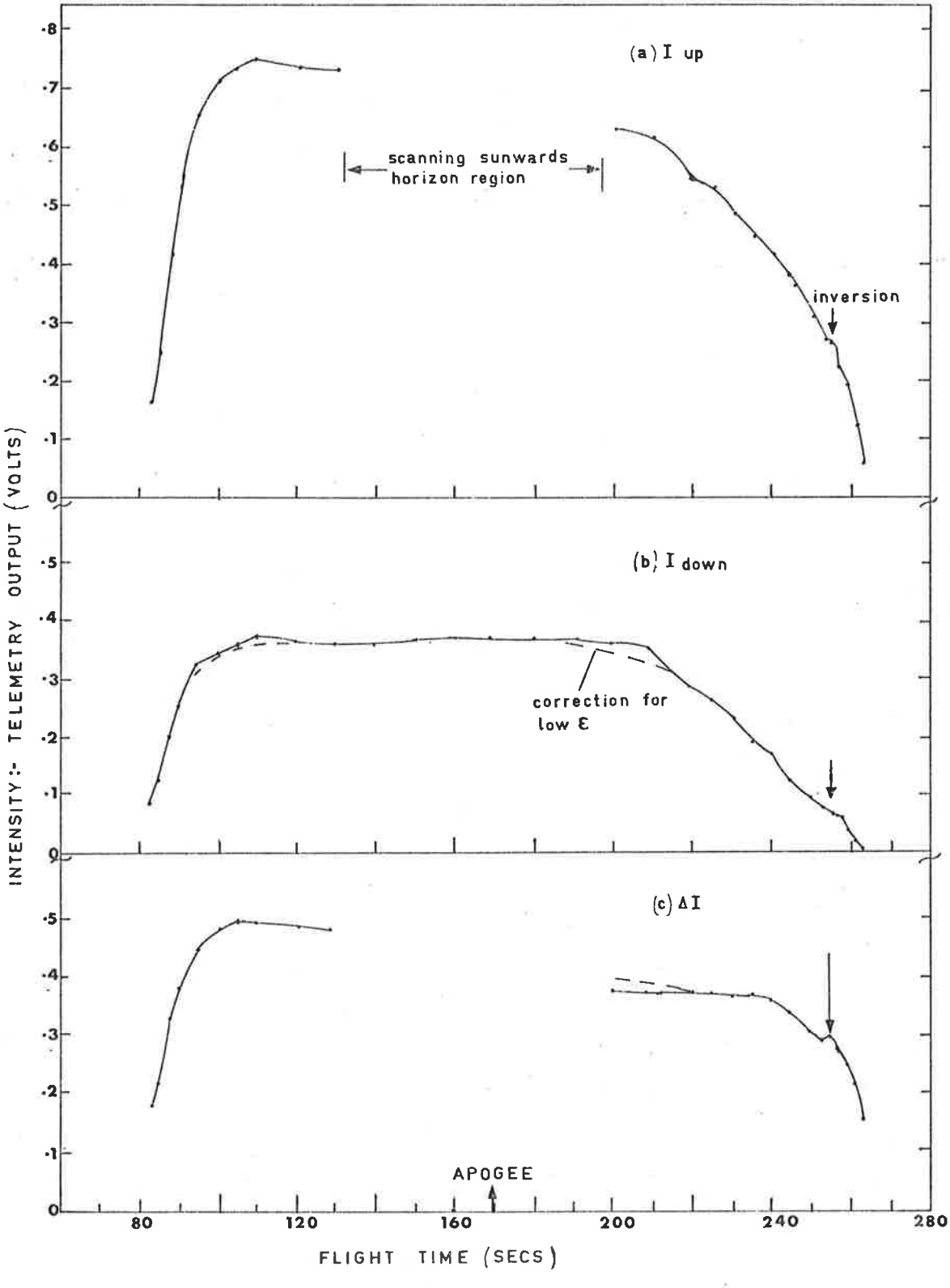

FIGURE 8·13 AIRGLOW INTENSITIES AS FUNCTION OF TIME

The curves are incomplete near apogee because the rocket attitude was such as to cause the upwards-viewing signals to be strongly influenced by the bright region above the western horizon. The dashed curves around +105 s and +205 s will be referred to later. At +255 s a discontinuity occurred as the rocket inverted rapidly during the downleg.

It will be observed that the curves in Figure 8.13 lack symmetry about the time of apogee (+170 s). This is partly attributable to the differences between the rocket attitude on the ascent and descent legs of the trajectory. Between +75 s and +85 s, the detector was scanning near the horizon from below the height range of strongest absorption, causing the UP signal to be reduced by strong absorption. Near 105 s, the scan plane crossed the western sky and the intensities were enhanced. For a period near +250 s, horizon scanning from a higher altitude produced enhancement of the DOWN signal in accordance with the predictions of the two-component model of the radiation field.

The same data points are plotted in Figure 8.14 as a function of altitude. The differences between the upleg and downleg are even more apparent than in Figure 8.13. Inversion of the rocket occured at 85 km and is marked by the arrow in the Figure.

It is possible that some attenuation of the radiation in the early part of the flight could have been due to outgassing of the payload. The payload had been flushed for some time prior to the

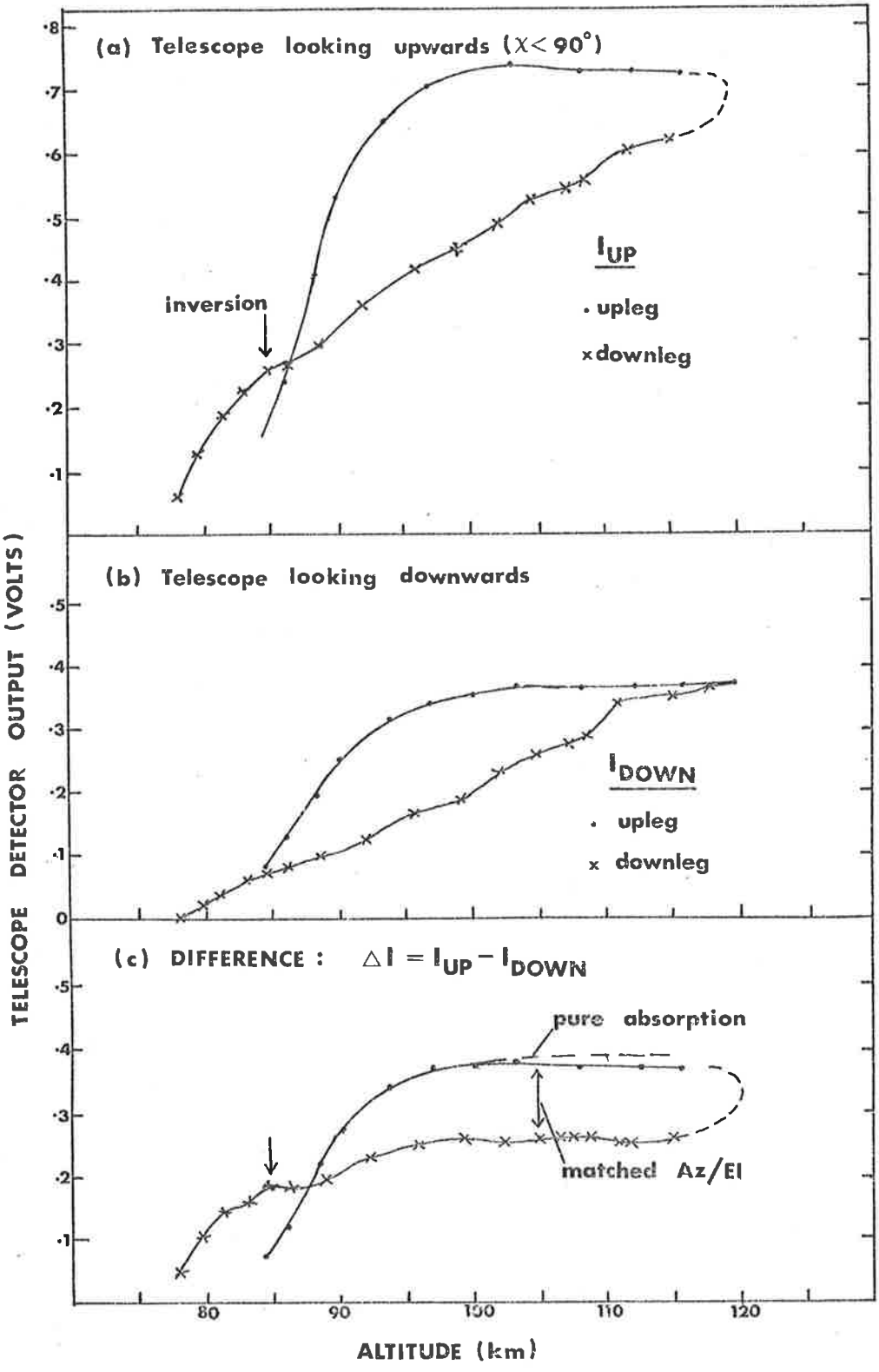

FIGURE 8.14 TELESCOPE SIGNALS AS FUNCTION OF ALTITUDE

flight with high purity dry nitrogen, but as this problem has affected the experiments of other workers (e.g. Fastie et al., 1964) the possibility of some local absorption cannot be excluded. No estimate of the extent of out-gassing effects before +90 s could be made because of the vehicle attitude, and after that time no such effects were apparent.

It seems that a reduction in the telescope sensitivity occurred in the period between about +105 s (100 km) and +200 s (115 km). During this period the rocket went through apogee (120 km) and the total height range included was only 20 km. Because the atmospheric absorption in this range is small, the intensities should have shown only variations due to non-uniform brightness of the overhead source. The scans included the sunwards horizon for some time near apogee, so it is difficult to assess the uniformity of the sky brightness, but scans at other times during the flight indicated that the overhead brightness was uniform to within about 10%.

That the observed discrepancies could not have been due to source non-uniformity alone can be seen from the data at +113 s and +225 s. At these times the rocket was at the same altitude (104.7 km) and the roll axis was aligned in the same direction to within approximately 1 degree. The geometry at the times of the two measurements was therefore the same, except for a downrange translation of the rocket and a shift in the relative sun position

during the 112 s interval. (These two effects partly offset each other.) By calculation of the ratios of the signals at the matched observing altitudes, a loss of sensitivity of 30% between +113 s and +225 s was inferred. Figure 8.14(c) indicates that most of this change had occurred by +200 s and that the system was stable after that.

The cause of the degradation is unknown. The ion chamber casing had reached only 18^0C by +200 s, so thermal effects on the chamber would have been negligible. There was no monitor of the temperature of the mirrors, however, and it is possible that their surfaces could have been damaged by excessive heating.

Whatever may have been the cause of the change, for the purpose of the data analysis it has been assumed that a drop in sensitivity of 30% occurred between +113 s and +200 s, and that the system was sufficiently stable both before and after that period. Such a change in sensitivity would have no effect on the analysis of absorption profiles, provided the system was stable during the movement of the rocket through the strongly absorbing height region.

8.4.3 Zenith angle dependence of intensity

As had also been observed from C104, at some times during the flight the telemetry output waveform assumed a symmetric shape with sharp rising and falling edges. This occurred at times when the rocket axis lay in the sun-zenith plane (Figure 7.10a) and when the detector scan-plane was sufficiently inclined to the horizontal.

It can be seen from Figure 8.10 that for most of the time when the detector was at a high enough altitude to detect Lymanα radiation, the inclination of the detector scan-plane (ε) was less than 25^0. The inclination exceeded this value only as the rocket started to invert. Even at low inclinations, however, the waveform had quite sharp edges.

A more detailed study of the waveform (i.e. the zenith dependence of intensity) was made for two selected times during the flight. At +118 s and +231 s the rocket axis lay in the sun-zenith plane, and the signal waveform had a symmetrical appearance. The measured intensity distributions at these times were compared with calculated distributions based on the two-component model of the airglow spectrum (Figure 8.15). The trapped component of the radiation was assumed, for simplicity, to be strictly isotropic. This component could then be separated by subtraction of I_{DOWN} in the experimental curves (Figure 8.15a).

The computed curve in Figure 8.18 was based on an assumed altitude profile of the molecular oxygen density from the appropriate U.S. Standard Atmosphere. The parameters of the assumed atmosphere are depicted in Figure 8.17. The sec χ in equation (1c) was replaced by an optical depth factor (or Chapman function), F(h, χ) of the type described by Swider (1964). The absorption equation, in terms of the vertical column density above the grazing height, was

$$I(h) = I_0 \exp\{-F\sigma \int_{h_g}^{\infty} n(h')dh'\} \qquad (8a)$$

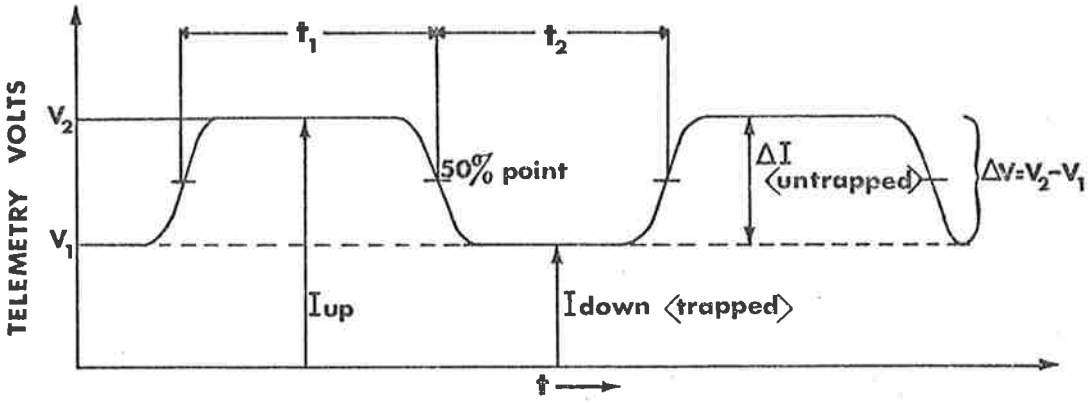

FIGURE 8.15 (a) SCHEMATIC OF TELEMETRY WAVEFORM

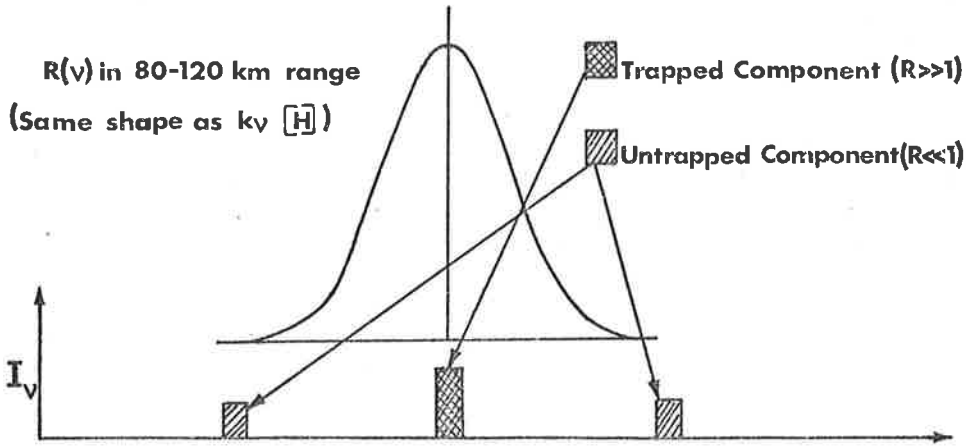

FIGURE 8.15 (b) THE TWO-COMPONENT SPECTRUM MODEL

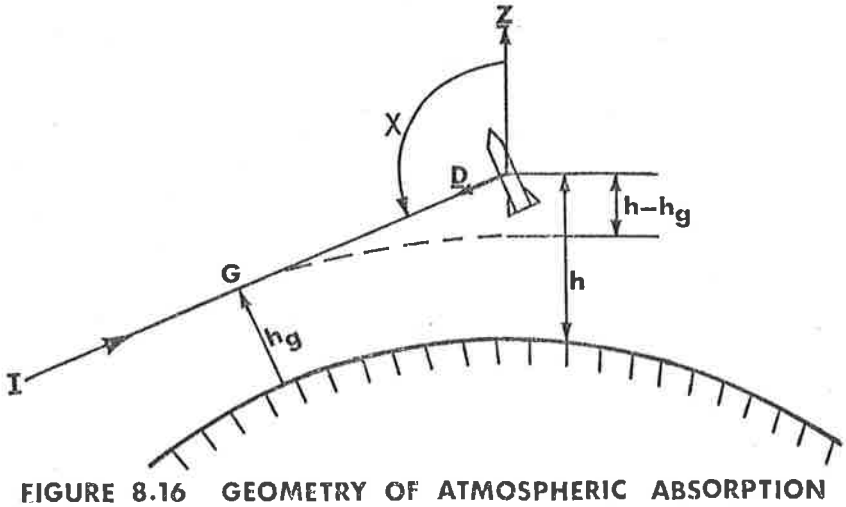

FIGURE 8.16 GEOMETRY OF ATMOSPHERIC ABSORPTION

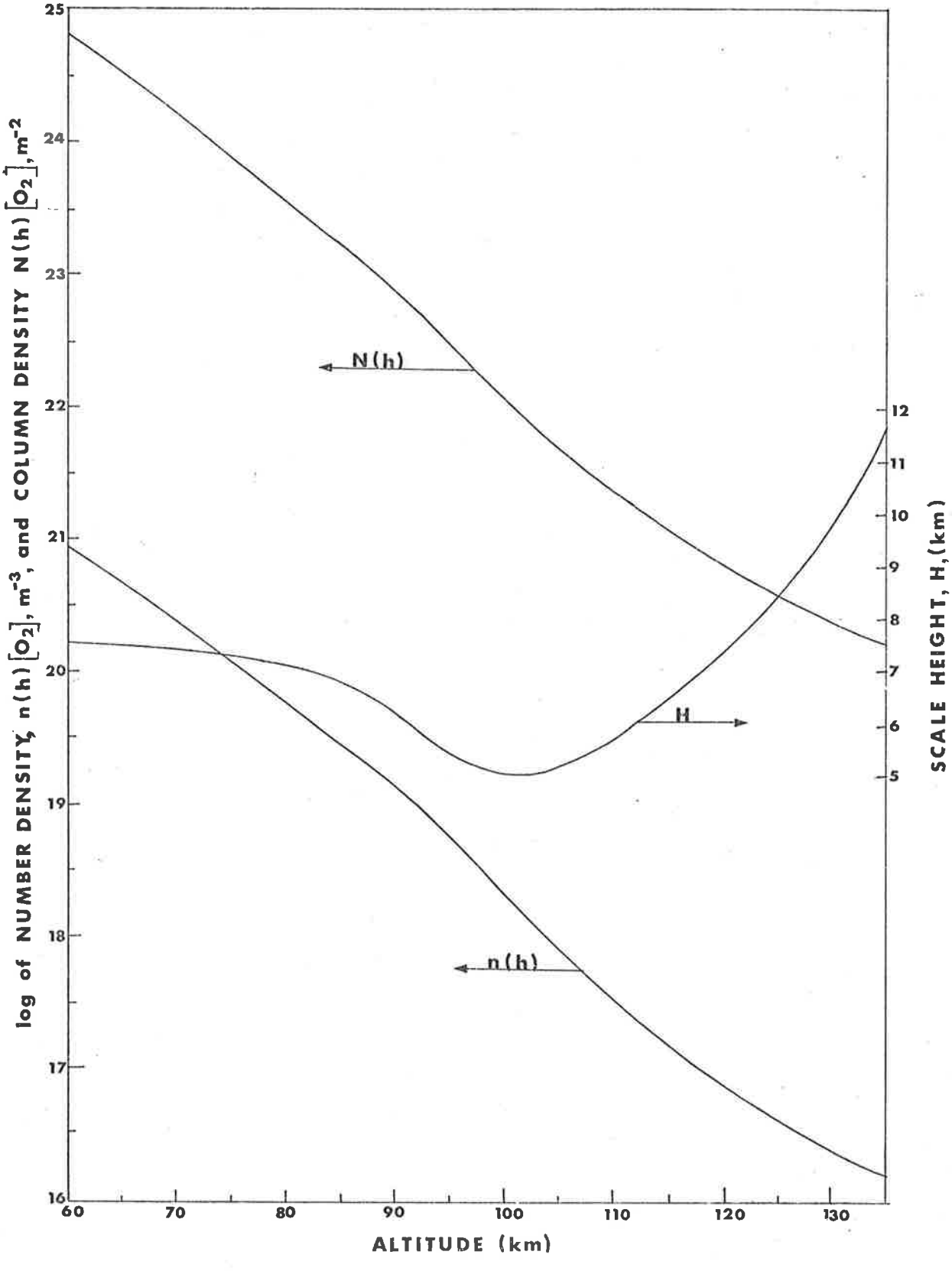

FIGURE 8·17 STANDARD ATMOSPHERE PROFILES

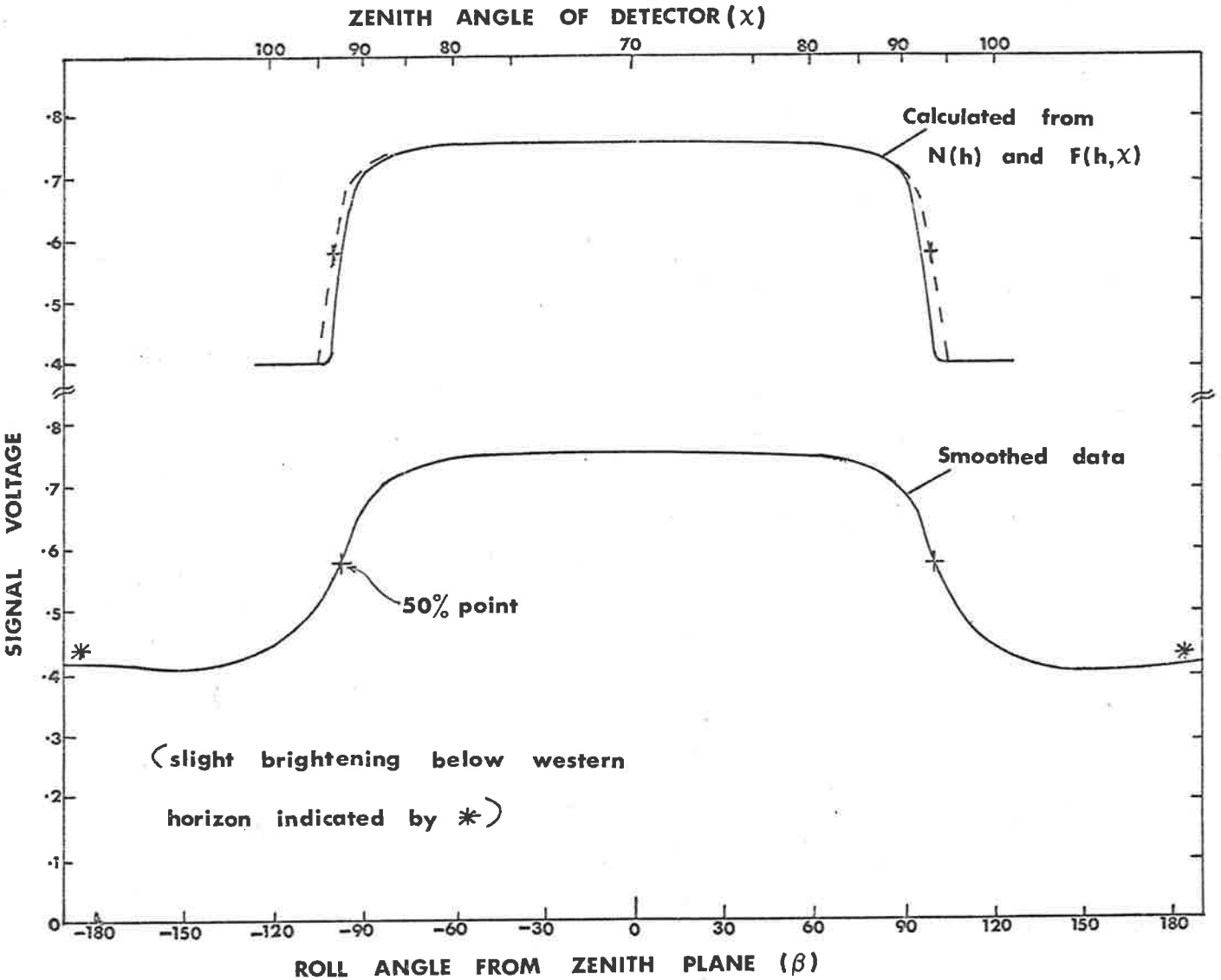

FIGURE 8.18 SPATIAL DISTRIBUTION OF INTENSITY (107·5 km)

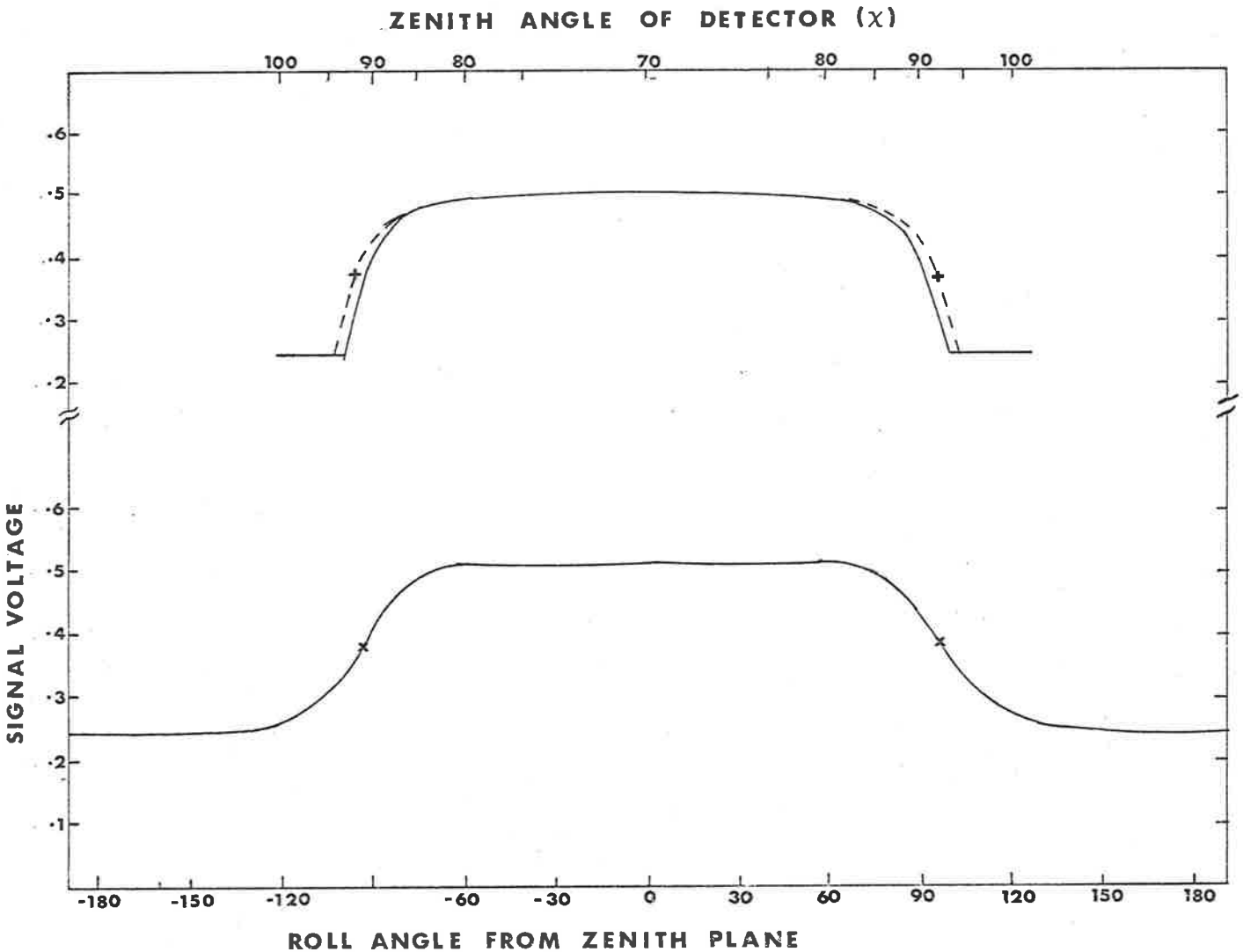

FIGURE 8·19 SPATIAL DISTRIBUTION OF INTENSITY (101 km)

The geometry of the absorption path is shown in Figure 8.16. In (8a), the rocket altitude (h) was substituted for the grazing height (h_g) for values of χ less than 90^0. At +118 s and +231 s the rocket altitude was 107.5 km and 101 km respectively. The factors in the calculation of the zenith angle dependence of intensity at these two altitudes are listed in Table 8.2. The values of $F(h, \chi)$ were obtained by interpolation in the tables given by Swider.

The lower curve in Figure 8.18 was obtained by overlaying the data points from two successive scans of the detector at +118 s (107.5 km). The horizontal axis is graduated in degrees of rotation in the detector scan circle, measured from the plane containing the zenith (β in Figure 7.9).

The upper curve in Figure 8.18, was based on the values in the last column of Table 8.2, with vertical scaling to match the amplitude of the lower curve. The dashed portions of the computed curve show the broadening caused by the finite field of view of the flight instrument. The zenith angle of the detector line of sight for the appropriate value of ε (20^0) is marked across the top of the figure.

Figure 8.19 is the equivalent set of curves for +231 s (101 km). The shapes are similar to those in Figure 8.18, but of reduced width, and at this altitude there is no evidence of the enhancement below the sunwards horizon which can be seen in Figure 8.18.

TABLE 8.2 ZENITH ANGLE DEPENDENCE OF ABSORPTION

h (km) detector height	χ^0 viewing direction	h_g (km) grazing height	H_g (km) scale height	F depth factor	$\int_{h_g}^{\infty} ndh'$ depth to grazing pt.	$F\int_{h_g}^{\infty} ndh'$ slant opt. depth	$\frac{I}{I_0}$ atten.
107.5	80	107.5	5.5	5.6	.004	.022	.98
	85	107.5	5.5	10.4	.004	.042	.96
	90	107.5	5.5	52	.004	.17	.84
	92	103.5	5.2	78	.009	.62	.54
	94	91.5	6.0	81	.059	4.8	.01
101	70	101	5.0	3.0	.012	.036	.96
	80	101	5.0	5.6	.012	.067	.93
	85	101	5.0	10.5	.012	.13	.88
	90	101	5.0	43	.012	.52	.60
	92	97	5.4	77	.021	1.62	.20
	93	92	6.0	78	.54	4.21	.015
	94	85	6.8	75	.18	13.5	$\simeq$.0

On the measured curves, the transitions between the UP and DOWN intensities are not as sharp as is indicated by the calculated curves. The width of the upper portion of the measured curves, and the variation of this width with altitude are, however, well matched to those of the calculated curve shapes. More will be said of this in the following Section (8.4.4.).

The difference between the shapes of the measured and calculated curves can be attributed to two causes. Firstly, the actual distribution of radiation in the airglow spectrum is continuous and there is therefore some intermediate radiation which is neither strongly trapped, nor completely free of resonance scattering effects, and so has a zenith angle distribution intermediate between those of the two components of the model. Secondly, the trapped radiation component would be anisotropic to a degree determined by the local value of $R(\nu_0, h)$, defined by (6g). The zenith angle dependence of the trapped component $\left(\propto\left[\frac{1}{1 + \kappa\mu}\right]\right.$ from (6m)$\left.\right)$ would account for some of the difference between model and measured curves near $\chi=110^0$.

The dashed portions of the curves in Figure 8.13 which were mentioned earlier show the estimated intensities which the detector would have seen if the field of view had moved away from the horizon region. The corrections were calculated from the zenith angle dependence measured at other times during flight in the form shown in Figures 8.18 and 8.19.

The enhancement of intensity seen in the western sky was first observed at about the same altitude (≈82 km) as the glow from the rest of the horizon. The increase in the amount of enhancement with altitude appeared to be similar to the profiles in Figure 8.14 (Upleg). It is suggested that this radiation was essentially 'hot' Lymanα scattered by a fairly direct path (Figure 6.3). The directional localization of the source indicated that the radiation was removed to some degree from the centre of the absorption line, and not subject to much multiple scattering. Because the forward scattered radiation passed through a larger optical depth than the radiation from the region BS (Figure 6.3), the spectrum would have been broader, with possibly some degree of self-reversal of the core.

Only Lymanα radiation could have been responsible for the observed enhancement of intensity. The degree of enhancement observed (up to 470 R at 119 km) was too large to be consistent with the measurements of Buckley and Moos (1971) and Meier (1971), of the 130.4 nm emission from atomic oxygen. Also, at altitudes below 100 km the contribution to the signal from the oxygen emission would have been negligible because the absorption cross-section of molecular oxygen at 130.4 nm is much larger than at Lymanα, giving a greater absorption height (Figure 1.1).

8.4.4 The ultraviolet horizon

The output of the detector as a function of time had approximately a 'square-wave' appearance during a large portion of the period of

measurement. The mark-space ratio of this wave form (i.e. t_1/t_2 in Figure 8.15a) varied considerably with rocket altitude. The periods t_1 and t_2 were measured between the points at which the output voltage of the telescope amplifier was half-way between the adjacent maximum (V_2) and minimum (V_1) values (defined in Figure 8.15a). This method of reading the time ratios was selected because of the ease and accuracy with which the 50% cross-over points could be read from the records.

On the basis of the same assumptions concerning the radiation spectrum as were used in 8.4.3, the values of zenith angle at which the cross-over points should occur were computed. The model atmosphere of Figure 8.17 and the optical depth factors from Swider (1964) were again used. An infinitely small detector field of view was assumed in the calculation, as the complication introduced by the inclusion of broadening by the instrument field of view was not warranted.

The intensities ($I(h)$, I_z, I_m) referred to in this Section are those of the untrapped component of the radiation only, i.e. with the component producing V_1 subtracted.

Substituting $\tau_g = \int_{h_g}^{\infty} \sigma\, n(h')dh'$ $\left[\begin{matrix}\text{vertical depth}\\ \text{to grazing point}\end{matrix}\right]$ (8b)

in (8a) gives $I(h) = I_0 \exp\{-F.\, \tau_g\}$ (8c)

Taking the ratio of the intensity at any zenith angle, $I(h, \chi)$ to

the maximum intensity during the scan (I_m), for scan plane inclination ε (Figure 7.6) gives

$$\frac{I\ (h, \chi)}{I_m\ (h, \chi_{min})} = \frac{\exp\ \{-\ F(h, \chi).\tau_g\}}{\exp\ \{-\ F(h,\ 90 - \varepsilon).\tau_h\}} \qquad (8d)$$

Under the assumption of a laterally homogeneous atmosphere, the maximum intensity should be observed in the plane defined by the rocket axis and the local zenith direction ($\beta = 0$). The horizon cross-over points were defined by the condition $\frac{I}{Im} = 0.5$ (8e)
(these are marked + in Figure 8.15a)
Substituting into (8d) and taking logarithms , gives

$$0.7 = -\ \tau_h\ .\ F_0 + \tau_g\ F_c \qquad (8f)$$

$$\text{or } F_c = (0.7 + \tau_h\ .\ F_0) \Big/ \tau_g \qquad (8g)$$

where $F_0 = F_{(\beta\ =\ 0)} = F(h,\ 90 - \varepsilon)$

and $F_c = F(h, \chi_c)$ at the horizon crossover points.

Figures 8.18 and 8.19 indicate that reasonable estimates of the values V_2 and V_1 could be read from the data whenever ε was greater than about 11^0. This condition was satisfied except for the period +187 s to +208 s in which ε went as low as 9^0. During this period, V_2 and V_1 were measured at zenith angles where, as can be seen from Figure 8.18, the observed intensity distribution is not well described by the model.

Because in general the maximum intensity, I_m, is less than the intensity in the zenith, the zenith angle of the horizon crossover, F_c, satisfying (8g) depends on the instantaneous value of ε, which

varied throughout the flight. So that measurements of F obtained at different flight times could be related in a manner independent of vehicle altitude, the values of χ_c' satisfying $\frac{I}{I_z} = 0.5$ were plotted in preference to those for which $\frac{I}{I_m} = 0.5$ (read from the data). $I_z = I(h, 0)$ is the maximum intensity which would have been measured had the detector scan passed through the local zenith. The difference between I_z and I_m was significant only for the first few measured points (Figure 8.20). The crossover angle χ_c' calculated from the zenith-corrected intensity corresponded to

$$F_c' = \frac{0.7 + \tau_h}{\tau_g} \qquad \left[\text{because } F(h, 0) = 1\right] \tag{8h}$$

and the difference between χ_c and χ_c' was taken as the correction to be applied to the measured values of χ_c at low altitudes in order to compare them with the altitude-independent calculated values of χ_c'. Table 8.3 lists the assumed atmospheric densities, and the corresponding values of χ_c' and χ_c, computed at a number of different heights.

The measured values of the ratio t_1/t_2 were used, together with vehicle attitude data, to calculate the points plotted in Figure 8.20. The solid curves is drawn through the computed values of χ_c' from Table 8.3. The first three points on the upleg were the only ones for which $(\chi_c' - \chi_c)$ was significant, and they are shown with their corrected positions.

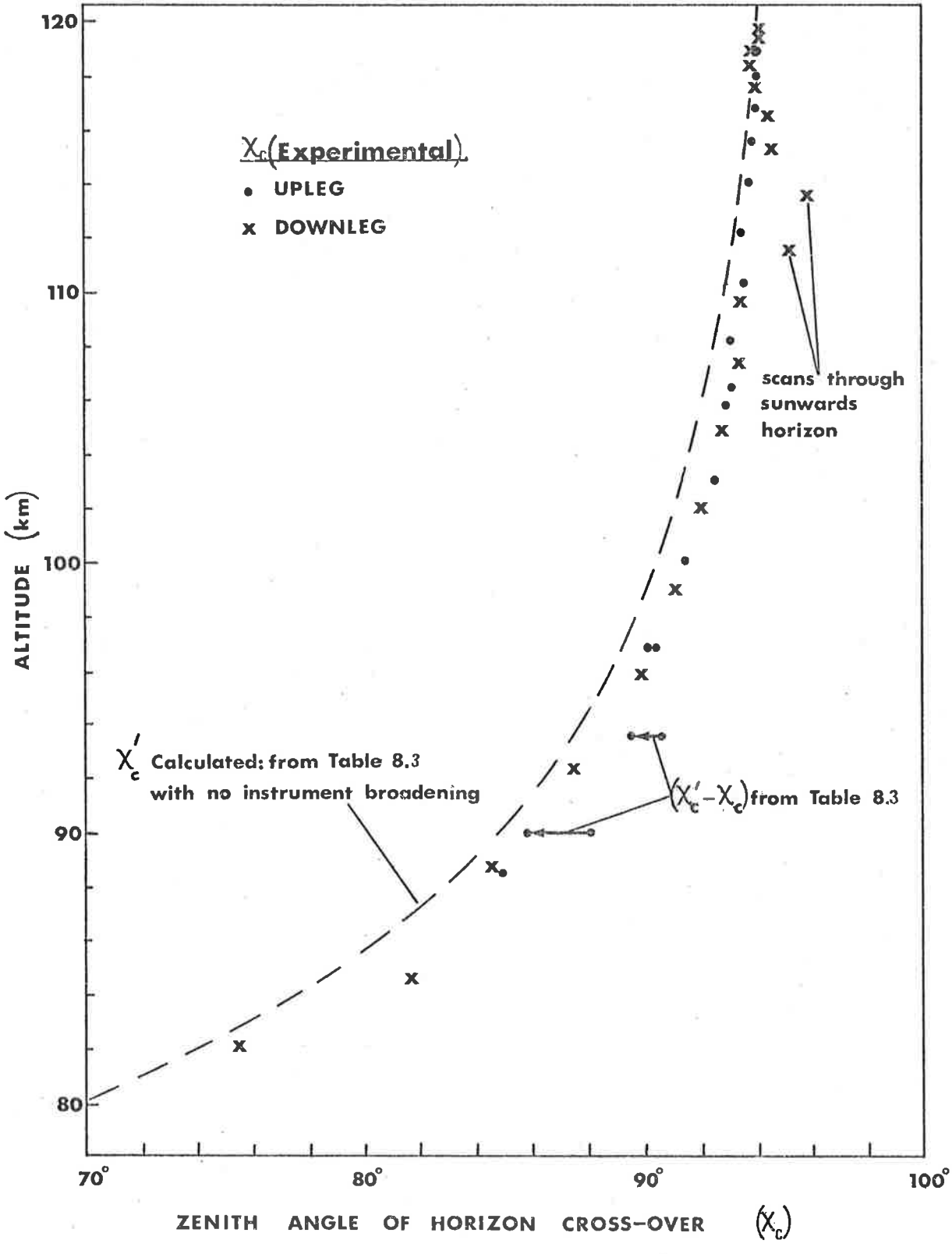

FIGURE 8·20 ULTRAVIOLET HORIZON ANGLES

TABLE 8.3 CALCULATION OF HORIZON CROSSING ANGLES

h (km) rocket hgt	(vertical) τ_h to rocket	(vertical) τ_g to grazing pt	χ_c' (deg)	χ_c (2) at	ε
80	.37	(1)	70		
85	.17		79		
90	.077		85	87.5	8^0
93.6	.040		87.5	88.3	10^0
95	.031		88.4		
96.9	.022		89.3	89.7	12.7^o
100	.013	.013	90.6	(3)	
105	.0062	.0089	91.9		
110	.0032	.0087	92.9		
115	.0017	.0086	93.5		
120	.0009	.0084	94.1		

Notes: (1) $\tau_g = \tau_h$ for h < 100 km where $\chi_c < 90^0$

(2) Required for correction of experimental points

(3) $\chi_c' \simeq \chi_c$ for h > 100 km

The agreement between the calculated curve and measured points in Figure 8.20 is quite good, considering the simplicity of the two-component model of the airglow spectrum. The bulge in the downleg measured cruve is in a period when the detector was scanning near the sunwards horizon, and where also the angle ε was less than the required minimum of 11^0. If the rocket attitude had been more favourable, the downleg curve would probably have followed closely the upleg curve.

No attempt has been made to include the effects of a finite field of view in the calculated curve, but the correction would move this curve about 1^0 to the right, at least for $h < 100$ km. The agreement between the two curves would then be good except for large h. Near the apogee of the flight, the distance between the grazing point (G) and the detector (D) (Figure 8.16) was quite large ($\simeq$ 200 km). Over such long path lengths the assumption of pure absorption without scattering, as applied to this spectral component, would be less applicable to the real spectrum than it is over short paths. The small divergence between the curves at the top of Figure 8.20 is therefore not surprising, and it is concluded that the two component model of the airglow spectrum allows a good description of the ultraviolet horizon curves to be made. The 50% points in Figures 8.18 and 8.19 are marked +, and the corresponding zenith angles agree well with Figure 8.20.

8.5 Discussion of the Airglow Measurements

8.5.1 Separation of the trapped and free radiation

The measured intensities, on which the results in Section 8.4 were based, must be considered with the limitations on their accuracy in mind. The attitude of the rocket was not ideal for observations during some parts of the flight; in particular, the closeness of the rocket axis to the vertical during the upleg did not allow very good measurements of the UP and DOWN intensities until about +100 s. The apparent change in sensitivity in mid-flight could not be observed clearly because of the similtaneous scans of the enhancement region of the sky. The results in 8.4.3 and 8.4.4 are not affected by the change which occurred, however, and the altitude profiles (8.4.2) appear to be normal when reasonable corrections are applied for vehicle attitude. The profiles will be considered in more detail in 8.5.2 and 8.5.3.

The zenith angle dependence and the horizon angle measurements appear to match closely the predictions of the two-component model, with one component isotropic, except for the lack of sharpness in the horizon cutoff (Figure 8.18, 8.19). The horizon blurring could be partly explained by the departures of the trapped component from isotropy (equation (6m)).

The treatment of the radiation as two distinctly separate components with $R \gg 1$ and $R \ll 1$ respectively is a simplification of the real situation, where there is a continuous variation between

these extremes of R across the width of the airglow spectrum. There will, therefore, be limitations to the usefulness of this two component spectral model. A value of $R(\nu_0) = 120$ is representative of the range of altitudes being considered (6.3.3). Using the values of Doppler and natural widths from 6.3.2 and 6.3.3, it can be shown that, for combined Doppler and natural broadening,

$$|\nu - \nu_0| = 1.3\ \Delta\nu_D = 3.3 \times 10^{10}\ s^{-1}, \text{ or } |\lambda - \lambda_0| = 1.6 \text{ pm}$$

satisfies the conditions $R(\nu) = 1$. These frequencies lie within the line width of the incident spectral width given by (6f), so the need can be seen for instrumentation with high spectral resolution to accurately make measurements of the type described.

If the spectrum incident on the absorbing region is assumed to be a simple sum of the Doppler and Lorentz components with a width of $1.1 \times 10^{11}\ s^{-1}$ as given by (6f), the fraction of the total energy within the above limits ($|\nu - \nu_0| = 3.3 \times 10^{10}\ s^{-1}$) can be calculated to be ≈45%.

This is the part of the total incident intensity which in the model is subject to resonance scattering with $R >> 1$. The value is close to the albedo (I_{DOWN}/I_{UP}) which is observed near 100 km. Allowance should be made for the enhanced intensities which are observed in optically thick resonance scattering regions, and for the fact that there is certainly radiation present for which $R \approx 1$, but the closeness of the calculated and observed ratios suggests that the line widths given in 6.3.2 and 6.3.3 are reasonable estimates.

8.5.2 The absorption profiles of radiation from the nadir

The measured variation of UP and DOWN intensities as a function of altitude are shown in Figure 8.14. Because of the unfavourable attitude of the vehicle, and the loss of data from Telescope 1, it was not possible to derive accurate density profiles of either O_2 or H from this experimental flight. The data from Telescope 2 was analysed by the same method used in 7.3.2, and the results indicate that the method has potential for measurement of the densities of the two species (O_2 and H) with which Lymanα mainly interacts between 120 and 75 km.

The equivalent form of equation (1e) for a mixed atmosphere of O_2 and H is

$$n(h)\ [O_2] = \frac{1}{M.\sigma[O_2]} \cdot \frac{\partial}{\partial h} \ln I(h) \qquad (8j)$$

which can be seen by comparison of (6r) and (6s). It was assumed in the analysis that the nadir intensity was a measure of the resonantly trapped radiation which interacts with H as well as O_2. A smooth curve was fitted to the DOWN intensity measurements from the downleg and is shown in both linear and logarithmic form in Figure 8.21. A set of points with estimated corrections for unfavourable vehicle altitude was also plotted for h > 105 km. The corrections were based on the results in Section 8.4.3 on zenith angle dependence. Values of $\frac{\partial}{\partial h} \ln I$ were measured from the curves.

The values of $n(h)\ [O_2]$ from the Standard Atmosphere (Figure

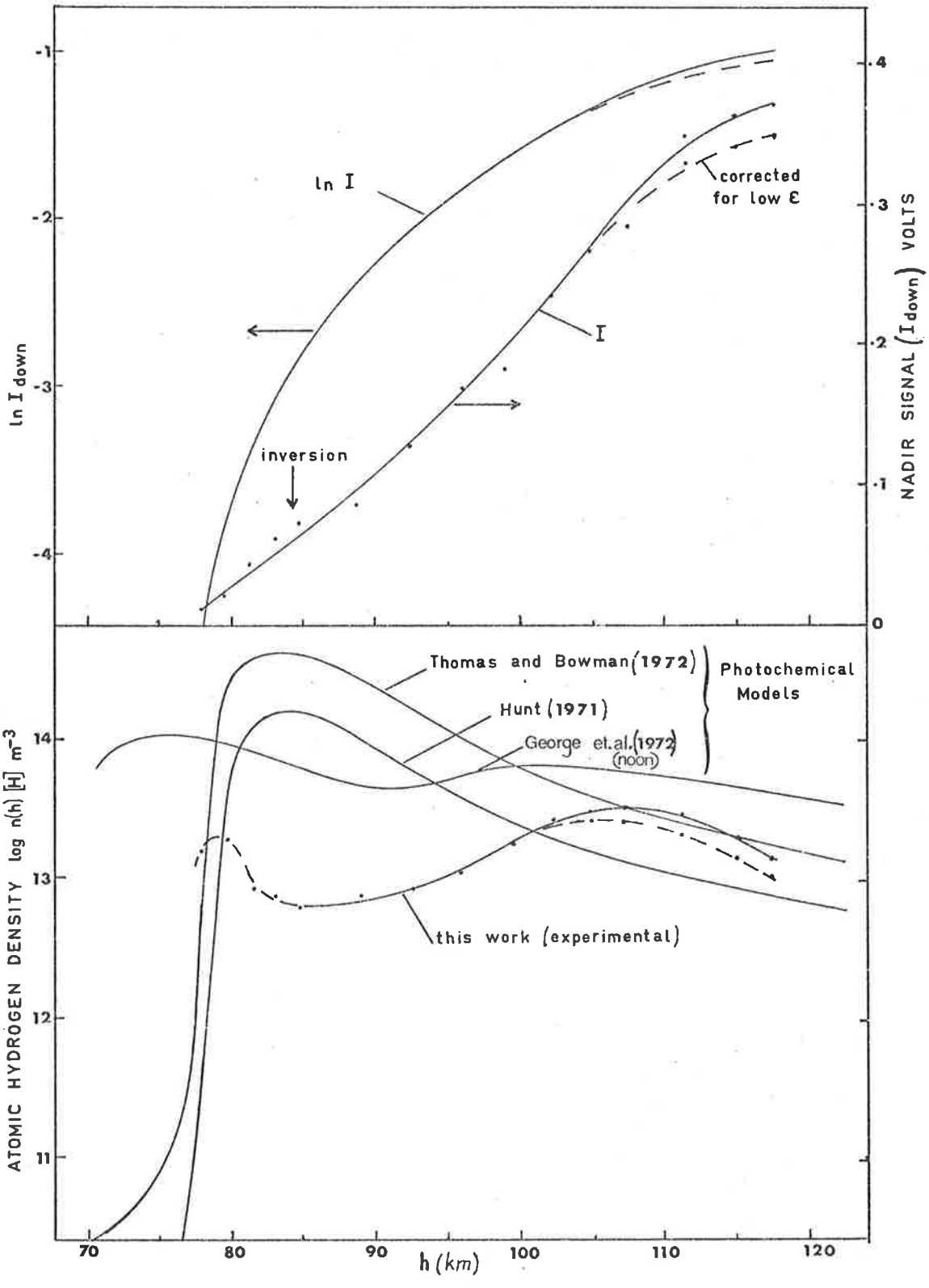

FIGURE 8·21 NADIR SIGNAL AND DERIVED HYDROGEN DENSITY PROFILE

8.17) were then used in (8j) to derive M(h) (Table 8.4). In the calculation of n(h) [H] from M(h), the temperature was assumed to be constant over the height range. The inclusion of a temperature profile was not warranted in the approximate analysis. The value of $\sigma[H] = 2.5 \times 10^{-17}$ m^2 was taken as an appropriate effective cross-section for the analysis of intensity measurements made with an unfiltered detector, and n(h) [H] was computed between 78 and 120 km.

In the lower part of Figure 8.21 the derived hydrogen density profile is compared with the photochemical model profiles of Thomas and Bowman (1972) and Hunt (1971). The computed curve of George et al., (1972) in the figure actually refers to local mid-day. The other two models show diurnal variations only below 85 km, so the mid-day curve is probably applicable to night-time conditions above that height. The data points from which the curve below 85 km was derived were measured at low signal levels during a period when the rocket attitude was changing rapidly, and the accuracy of that section of the profile is lower than in the centre of the height range covered.

A series of measurements from a more stable vehicle with high gain telemetry channels would improve the data obtainable in the important region near 80 km. Near 90 km the derived densities are much lower than predicted by the models. A complete set of measurements with an absorption cell instrument would be required

TABLE 8.4 DERIVATION OF HYDROGEN DENSITY PROFILE

t (secs)	h (km)	lnI (fitted curve)	lnI (m^{-1})	M (from 6r)	R (from Fig.6.5)	n H (m^{-3})
190	117.6	-0.99 *(-1.05)	1.1×10^{-5} (9.8×10^{-6})	100 (89)	3.2 k (2.5 k)	1.4×10^{13} (1.1×10^{13}
200	115.1	-1.02 (-1.08)	1.5×10^{-5} (1.3×10^{-5})	100 (86)	3.2 k (2.3 k)	2.0×10^{13} (1.4×10^{13}
210	111.6	-1.05 (-1.11)	2.4×10^{-5} (2.0×10^{-5})	92 (77)	2.8 k (2 k)	3.1×10^{13} (2.2×10^{13}
220	107.4	-1.20	3.5×10^{-5}	67	1.5 k	3.3×10^{13}
225	104.7	-1.32	4.4×10^{-5}	51	850	3.1×10^{13}
230	102.1	-1.45	5.0×10^{-5}	36	470	2.8×10^{13}
235	99.1	-1.71	6.0×10^{-5}	23	170	1.8×10^{13}
240	95.8	-1.77	6.7×10^{-5}	13	52	1.1×10^{13}
245	92.4	-2.06	7.7×10^{-5}	8.1	22	8.8×10^{12}
250	88.8	-2.46	9.6×10^{-5}	5.7	11	7.8×10^{12}
255	84.7	-2.60	1.2×10^{-4}	4.0	5.0	6.0×10^{12}
257	83.1	-2.74	1.4×10^{-4}	4.0	5.0	7.5×10^{12}
259	81.3	-3.17	1.9×10^{-4}	3.9	4.8	8.2×10^{12}
261	79.6	-3.86	2.9×10^{-4}	4.8	8.0	2.0×10^{13}
263	78.0	-4.51	3.0×10^{-4}	4.0	5.0	1.6×10^{13}

* values in parentheses corrected for low ε

to determine whether the difference between the observed and predicted profiles was caused by limitations in the instrumentation, in the models, or in the technique itself (e.g. in neglect of redistribution between the components of the spectrum.) The estimated limits of errors in the densities due to transmission and reading of the data are (+50%, -30%) between 85 km and 105 km, increasing towards each end of the range covered, as is normal for absorption profile measurements. To this must be added a contribution due to the deviations of the Standard Atmosphere molecular oxygen profile from the actual profile at the time.

Despite the stated limitations of the present measurements, the results indicate that the absorption method has potential for making useful measurements of the atomic hydrogen density in an otherwise inaccessible region.

8.5.3 The absorption profile of the unscattered component

The difference between I_{UP} and I_{DOWN} was assumed to represent the component of the spectrum which was not subject to multiple scattering ($R \ll 1$). Absorption factors, taking into account the vehicle attitude, were derived from the tables given by Swider (1964). A series of values of the column density (Ng) at the grazing height h_g, was calculated from the relation

$$Ng = \frac{1}{\sigma . F(h, \chi)} \ln\left(\frac{I_0}{I(h)}\right) \qquad (8k)$$

where I_0 was obtained from the measurements on each leg at about

100 km, corrected for the small amount of residual absorption by using the profiles in Figure 8.17.

The values obtained are shown in Figure 8.22, together with the Standard Atmosphere profile. Owing to the low inclination of the scans during the upleg, large values of the zenith correction factor ($F(h, \chi)$ were involved, and the accuracy of the derived densities was not as good as would have been obtained from direct zenith measurements.

The consistency of the data on the downleg indicates that the detector sensitivity had stabilized by +230 seconds when the downleg profile measurements were started.

The errors in the derived densities due to intensity measurement errors are estimated to be less than a factor of two in the centre of each profile (85 to 95 km on the upleg, and 80 to 95 km on the downleg).

The degree of error introduced by the assumption that the trapped and untrapped components were separable is as yet unknown, and further measurements would be required to show how valid the reductions for a broad-band detector might be. The estimated limits of errors in the central values on Figure 8.22, due to limitations in the detection, transmission and reduction processes above, are about a factor of 2, larger or smaller.

8.5.4 Absolute intensities

The general level of the intensities measured by Telescope 2

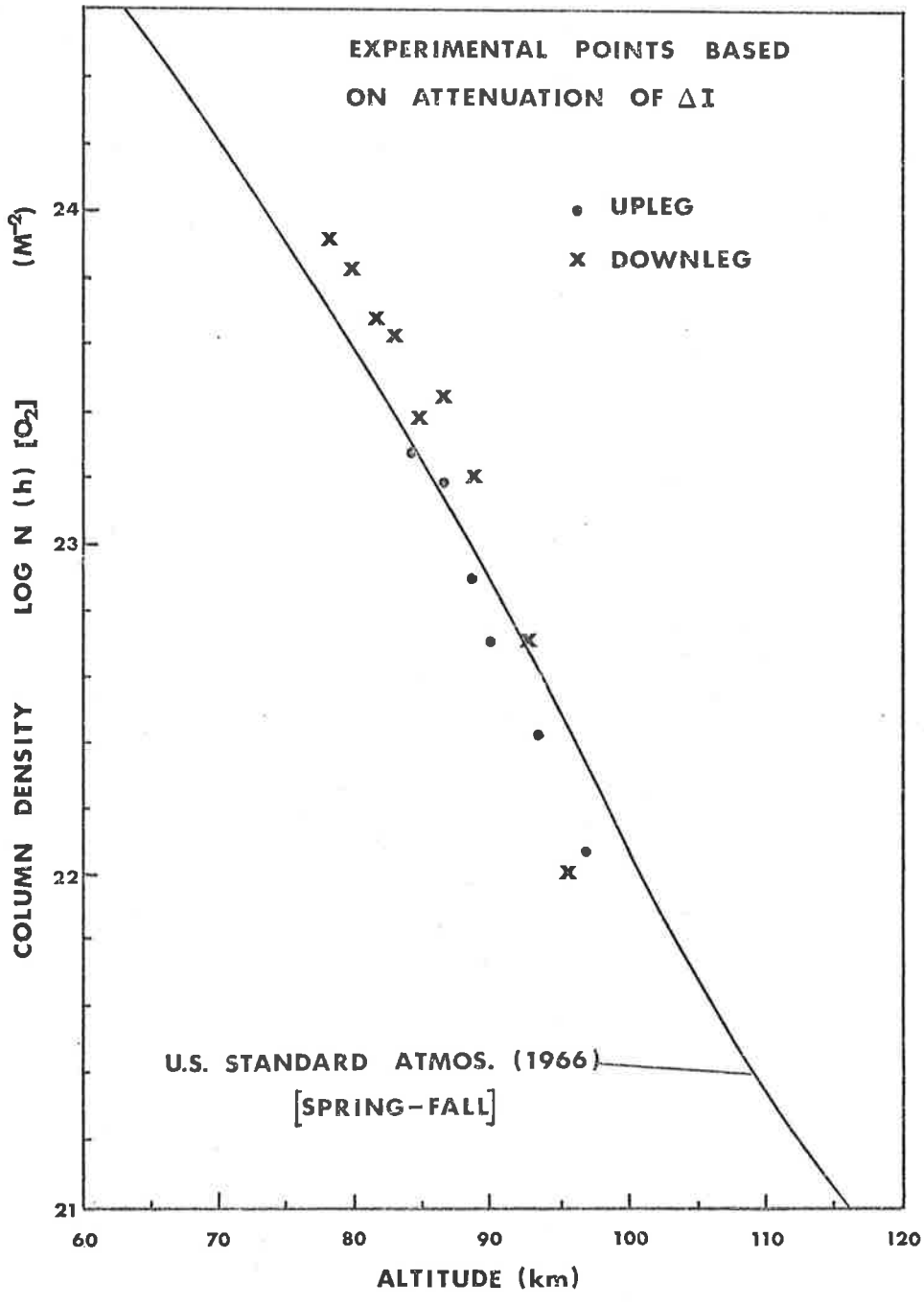

FIGURE 8·22 MOLECULAR OXYGEN DENSITY PROFILE

throughout the flight was lower than had been expected. The maximum signal detected corresponded to 1.4 kR (1.8μW m^{-2} sr^{-1} at the calibrated sensitivity. This was seen at +165 s, as the detector scanned above the western horizon. The loss of sensitivity by that time was probably about 6%, giving a corrected maximum of 1.5 kR. When the detector scans were clear of the western enhancement region, the maximum signal was equivalent to 1.1 kR (1.4μW m^{-2} sr^{-1} at +110 s. At that time the Telescope still appeared to be operating at the calibrated sensitivity.

As has been mentioned already, the calculated exospheric temperature at the time of the rocket firing was 1010^0K. Geomagnetic activity for the day was moderate, but the solar activity (based on 10.7 cm flux measurements) was lower than the monthly mean, which itself was rather low ($F_{10.7}$ = 130). The 10.7 cm flux on the day of the flight was only 66% of that on the day of the flight of C104, which measured much higher airglow intensities. Both the total solar Lymanα flux and the line centre flux have been found to be positively correlated with short-term variations of solar activity (Meier, 1969; Vidal-Madjar et al., 1972). The radiation available for scattering increases with solar activity, but the corresponding reduction in thermospheric hydrogen density, resulting from increased temperatures, partly off-sets the effects of the flux increase.

The difference between the solar activity at the times of flight of C104 and C1014 would account for some of the difference

between the measured intensities, and calibration errors may also have contributed. Even so, the ratio of 4.5 in the maximum zenith intensities does not seem to be fully explained, unless the difference between the solar zenith angles on the two occasions (5^0) was responsible for a difference in the vicinity of a factor of two in the radiation intensities at the detectors.

8.6 Lunar Ultraviolet Radiation

8.6.1 Introduction

When the moon is visible in the night sky, the solar Lymanα radiation scattered from the lunar surface adds to the geocoronal airglow flux reaching the mesopause. The lunar flux is small compared with that from the geocorona, and the spectrum should be similar to the spectrum of the solar emission. The telescopes in C1014 were designed to be capable of measuring the lunar flux during the period near rocket apogee.

Although much has been learned from the examination of samples returned from the lunar surface, photometric methods enable measurements to be made of the surface properties over the whole surface, either from the total disc or from selected regions. An important feature is that the surface can be examined in an undisturbed condition, with the emphasis more towards physical rather than chemical structure of the surface layer.

Measurements of the ultraviolet reflectivity of the lunar surface have been made by several workers, (Heddle, 1962; Carver

et al., 1966; Lebedinsky et al., 1967a,b). The measured fluxes between 200 and 300 nm showed that the lunar reflectivity drops sharply through this range down to 200 nm. Extrapolations of the observed trends indicated that the Lymanα flux from the moon should be observable and measurable with moderate accuracy by the telescopes in C1014. The lunar measurements were a secondary objective of the flight, but did require some compromises to be made with the airglow experiment. The main penalty was an increased noise level resulting from the requirements for spatial and temporal resolution of the lunar measurements.

8.6.2 Lymanα radiation from the moon

Because the lunar spectrum was known to be weak in the vacuum ultraviolet, care was taken to ensure that the lunar signals would be due only to Lymanα and would not be spurious responses to the longer wavelength part of the spectrum. From laboratory measurements it was known that the most troublesome spectral region in this respect was around 240 nm. Measurements of the detector sensitivity in this region indicated that the in-flight photoelectric response would be negligible, and confirmation of this was obtained during the flight. The telescopes made three series of scans of the moon, as indicated by the aspect sensors, at +66 s, +70 s and +237 s. The slant optical depths in molecular oxygen at these times were 4.8, 3.1 and 0.05 respectively for Lymanα radiation (from the model of Figure 8.17). The corresponding atmospheric transmissions

were 0.8%, 4.5% and 95% respectively. The transmission at 240 nm was almost 100% at each of these times. No significant lunar signal was detected during the first two series of scans, confirming that the photoelectric response of the detector was indeed negligible. The radiation detected during the third series of scans was therefore entirely within the photoionization range of the chamber response. In this range the strong Lymanα line from the solar spectrum is the dominant radiation which is absorbed between the altitudes of the second and third series of scans, so the signal has been attributed entirely to Lymanα radiation.

The relationship between the airglow and lunar signals can be seen in Figure 8.23, which is a trace of the telemetry output in the middle of the third series of lunar scans. The lunar signals were about 10% of the airglow background. A mean of the two groups of the data points before and after each lunar scan was used as the estimate of the airglow component which had to be subtracted from each peak value. The data points within each pulse were plotted on a large scale and a smooth curve was fitted to reduce the contributions of high-frequency noise. Because there was a significant level of mid-frequency (≃ 200 Hz) noise still present, the smoothed pulse shapes were not all exactly identical. The height of each peak above the nearby background was measured and combined plot of these amplitudes is shown in Figure 8.24. The pulse height when the moon crossed the centre of the field of view

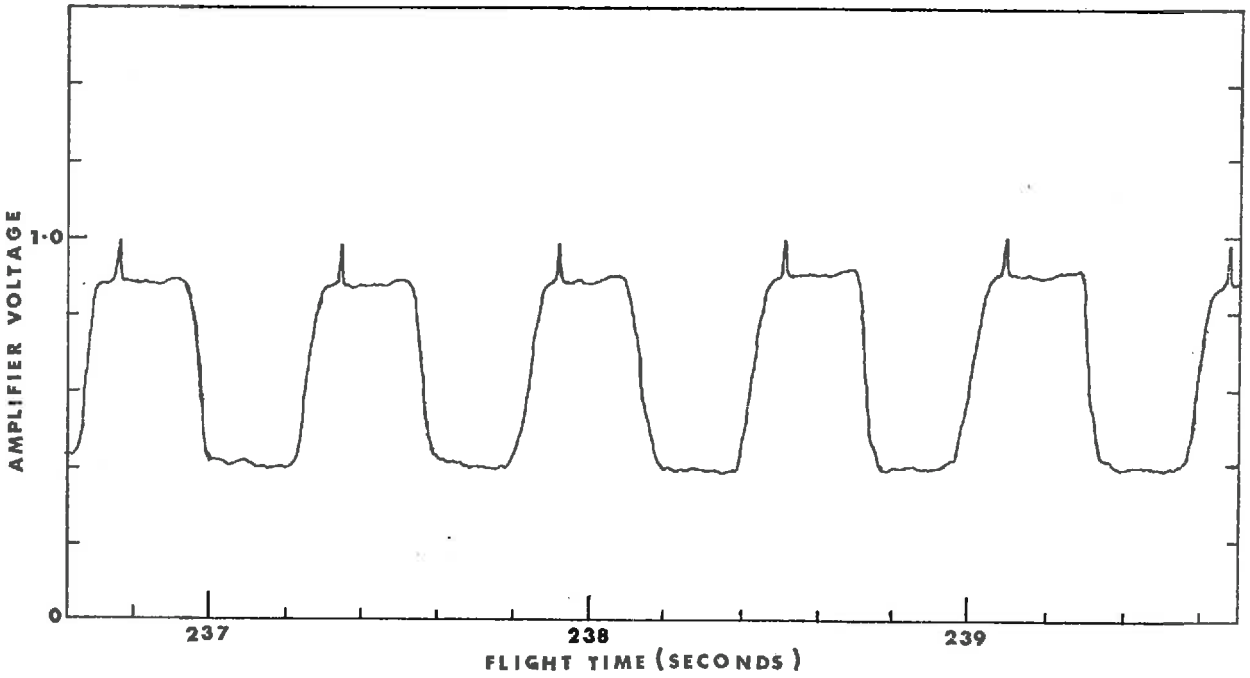

FIGURE 8·23 LYMAN α SIGNAL WITH LUNAR PULSES

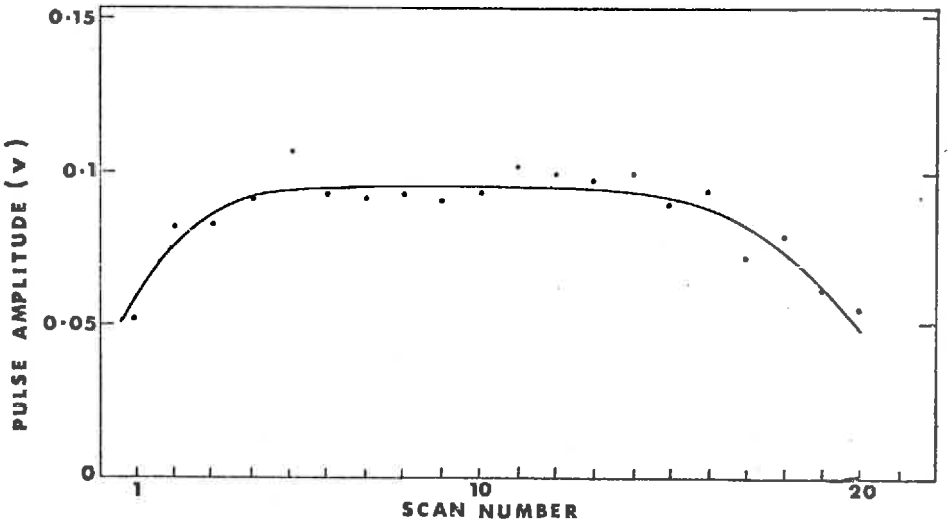

FIGURE 8·24 AMPLITUDES OF THE LUNAR PULSES

was read from the fitted curve.

The shape of the individual pulses suggested that at the high scan-rate (600^0/sec), the amplifier was not reaching the proper pulse height as the moon crossed the field. By fitting the known rise-time to the pulses it was estimated that a +10% correction was appropriate. Based on the analysis of the airglow signals, the assumed telescope sensitivity at +238 s was 30% lower than the pre-flight calibration figure.

The lunar flux measured was 3.1×10^{-10} watts m^{-2}. The measured flux was adjusted to the mean lunar orbital radius (3.84×10^5 km) and was corrected to a full-moon value by assuming that Rougier's phase law (Kopal, 1969) can be applied in the ultra-violet region. The phase law correction factor was 1.56. A further correction of 4.5% was made for the slant path absorption by the molecular oxygen above 97 km.

The corrected zero phase lunar flux at Lymanα was calculated to be $5.0 \pm 1.5 \times 10^{-10}$ W m^{-2}. The estimated limits of error included contributions to the total error from ion chamber calibrations, telescope transmission, data reading, phase law correction and the atmospheric absorption correction.

8.6.3 The lunar albedo

Measurements of the lunar flux at different wavelengths can be related to the albedo (integrated reflectivity) of the lunar surface by taking into account the incident solar spectrum. If the

fluxes at the Earth from the sun and the full moon are denoted by L_s and L_m respectively, the spherical (Bond) albedo is given by (Kopal, 1969)

$$A = 0.585 \frac{L_m}{L_s} \left(\frac{r}{a}\right)^2 \qquad (81)$$

where r is the mean Earth-moon distance, a is the radius of the moon, and the factor 0.585 comes from the integration of Rougier's phase law function.

At the altitude and elevation that the measurement of L_m was made, the only radiation within the detector pass-band penetrating effectively to the rocket from the moon would be Lymanα. A value of 4.5×10^{-3} W m $^{-2}$ (±10%) was assumed for the solar Lymanα flux. The resulting albedo was $A = 3.2 \pm 1.3 \times 10^{-3}$ at 121.6 nm.

Measurements of the lunar flux at wavelengths between 200 and 300 nm had been made by other workers from some of the rockets described in the preceding Chapters. Calculations of the lunar albedo based on these measurements and the solar spectrum of Brinkman et al., (1966) had been made. The results are shown together with the above measurement in Figure 8.25, which was taken from Carver et al. Included in the figure are the measurements of Stair and Johnston (1953), Heddle (1962), Lebedinsky et al., (1967a, b; 1968), and Ahmad and Deutschman (1972). The results from the last reference have been multiplied by the phase integral (0.585) to make them compatable with the definition of albedo used

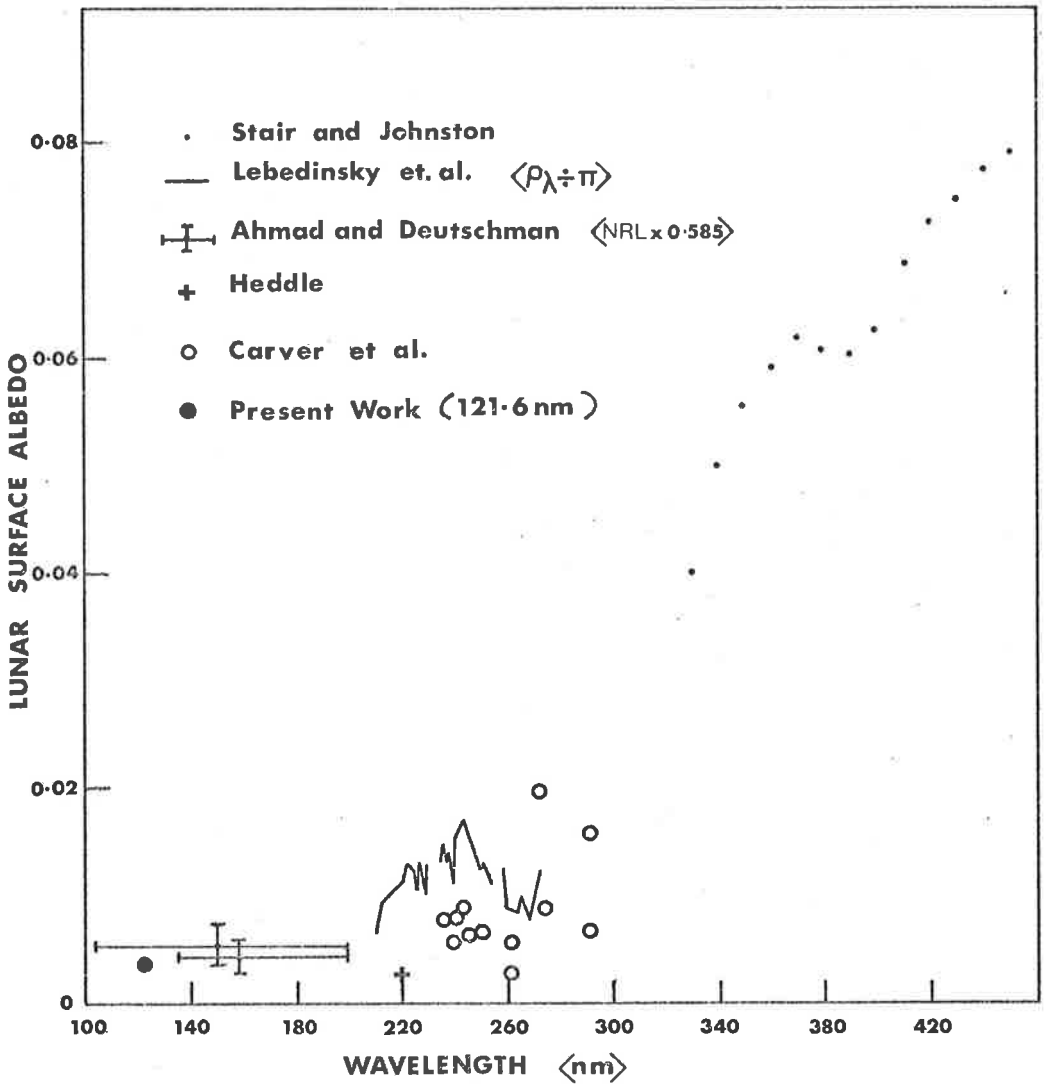

FIGURE 8·25 MEASUREMENTS of LUNAR ALBEDO

by other workers. The measurements of Lebedinsky et al., which were essentially of a unidirectional flux from a small area of the lunar surface, evaluated in terms of a Lambertian reflector, are shown as their $\rho\lambda$ divided by π to make their results more comparable. Even so, their measurements were of a continental area which could have a reflectivity somewhat higher (as in the visible) than the total disc to which all of the other measurements refer.

The sharp drop in albedo towards shorter wavelengths between 200 and 300 nm, which had been observed before, has been shown not to continue down to 121.6 nm. Ahmad and Deutschman's results also indicate a flatter curve below 200 nm, but their measurements cannot be related to a specific known wavelength as can the value of A (121.6) found in this work.

8.7 Conclusion

8.7.1 Summary of results

The series of airglow investigations culminating in the flight of C1014 has illustrated several properties of the Lymanα night airglow in the region below 120 km. The altitude and zenith angle dependence of the radiation intensity has been examined in detail. The results have been shown to be well described by the behaviour of a simple two-component model of the incident spectrum. The measurements of the resonantly scattered component, although not as extensive and detailed as planned, did nevertheless indicate the potential of such measurements for the determination of the

night time atomic hydrogen and molecular oxygen density profiles.

Measurements were also made of the lunar flux at 121.6 nm, enabling a considerable extension to be made to the range of photometric measurements of the lunar surface.

8.7.2 Further work

Because of the loss of data from the absorption cell detector, it would be worthwhile to repeat measurements with instruments similar to those flown in C1014. If lunar flux measurements were not included in the experiment objectives, modifications could be made to the detectors to make them better suited to airglow measurements. Through a more rigorous analysis, the improved and complete data should allow a more detailed model of the airglow spectrum to be verified, with consequent better measurements of the atmospheric constituents.

The lunar flux measurements could be continued as a separate series of experiments. The indications of a relatively flat lunar reflectivity over the 100 to 200 nm range suggest the possibility of using the moon as a source for absorption spectroscopy at other wavelengths in this range, as well as at Lymanα. Absolute flux measurements with improved angular resolution through this band could provide valuable data for comparison with measurements on samples under different conditions in the laboratory.

APPENDIX A

Aerobee Detector Systems

The field of view of each ion chamber in the Aerobee payload (7.2.1) was defined by a series of knife-edged baffles positioned in a tube in front of the ion chamber so that no surfaces could reflect radiation at near grazing incidence into the chamber window (Figure 7.1c). The fields of view of the ion chambers were 8^0 FWHM, similar to those in the C104 payload which was launched two weeks after the Aerobee. The entrance aperture of each chamber was circular and 6 mm in diameter. Both ion chambers were operated at gas gains near 100.

The spectral response range of the Aerobee EUV detector (Figure 7.1a) was determined by a thin film filter which consisted of a layer of aluminium (120 nm) over a phosphor layer (sodium salicylate) on a glass substrate. A quartz-window photomultiplier viewed the back of the filter through a Wratten 47B filter which narrowed its sensitivity range to the emission band of the phosphor.

The construction and properties of thin film metallic filters has been described by Linke and Palumbo (1965). Some filters using a double layer (80 nm tin over 20 nm aluminium) were made, as the bandpass of this combination would have allowed discrimination to be made between the 58.4 nm and 30.4 nm emission lines. The compound filters were not used as it was found that they deteriorated too rapidly, apparently due to reaction between the two metals. Experiments were also made with vacuum evaporated para-terphenyl as the phosphor, but low conversion efficiencies and apparent persistence effects led to its abandonment in favour of sodium salicylate.

The detector had a field of view of 15^0 FWHM defined by knife-edge apertures, and its spectral response range included both the He^+ (30.4 nm) and He (58.4 nm) emissions.

The detector currents were fed into logarithmic amplifiers, similar to those described in 4.2.3, and Figure 4.5, which were automatically calibrated at 60 second intervals during flight from constant current sources.

APPENDIX B

Regulated H.T. Power Supply

The central part of the circuit (Figure B.1) is a standard push-pull converter with voltage doubler rectification. The main feature is the control circuitry. Instead of the usual feed-back to a separate regulator controlling the input voltage to the converter, the feed-back is used directly to control the drive to the power transistors in the inverter. Tr1 generates a feed-back error signal which, via Tr2, determines the base current of the conducting transistor (Tr3 or Tr4). The power transistors are not driven into saturation unless the input voltage is below the regulation range. The excess power at high input voltages is dissipated by the two inverter transistors themselves, making far easier mounting in payloads where proper mounting of extra regulators may be difficult. Thermal bonding of the marked pairs of components ensures good temperature stability.

When an output of opposite polarity, or a floating output is required, a low-voltage secondary can be included with resulting input output isolation and greater efficiency, but with slightly worse regulation performance.

This discreet circuit was flown in the ealier payloads. An improved circuit using an integrated circuit regulator (μA723) in place of Tr1, Tr2 and the reference, has been used in later payloads.

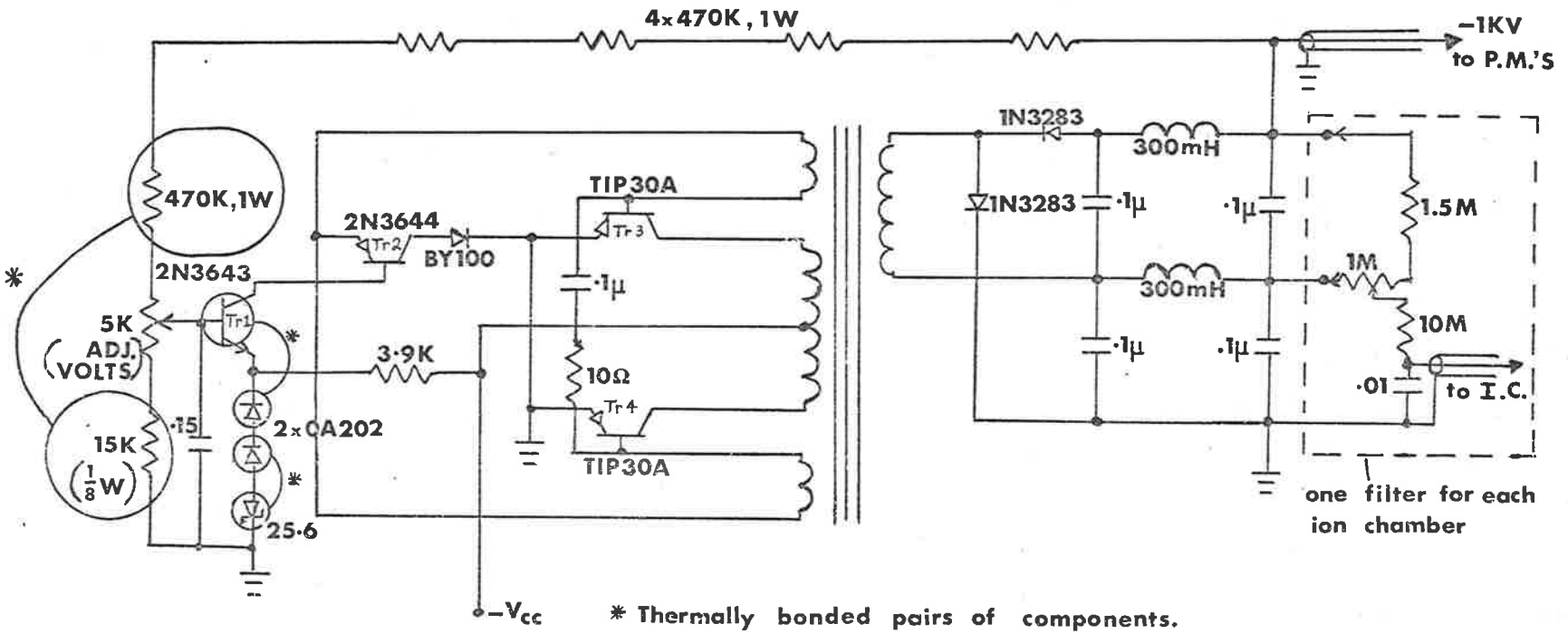

FIGURE B.1 REGULATED H.T. POWER SUPPLY.

APPENDIX C

The C105 Detectors and Payload

The data from the flight of C104 had shown that improvements were necessary in the supression of the off-axis photoelectric response of the ion chambers, so larger working volumes were adopted. The change to larger chambers involved foregoing the advantages of the triple array in gathering data during the short time near apogee. A compensating advantage was the increased effective sensitivity resulting from the larger window area and the higher absolute efficiencies obtainable in a larger volume. In the smaller chambers, at the gas pressures required for gas gain, complete absorption of radiation across the dimensions of the chambers could not be achieved and the large diameter central electrode unavoidably occupied an appreciable part of the active region behind the window. As a result of these two factors, the chambers had a low absolute efficiency, as indicated in Table 7.1, and the signal to noise ratio of the chamber-amplifier combination was degraded.

The payload for vehicle C105 included a second detector sensitive in the 122 to 135 nm spectral range, as in the Aerobee experiment (7.2.1). The signals from this chamber could then be used to subtract contributions to the Lymanα airglow detector signal from any hot stellar sources or oxygen/nitrogen airglow.

The accuracy with which corrections can be made by channel differencing depends on the accuracy to which the relative channel sensitivities are known at the wavelength of the radiation being separated out. When the radiation is broad-band, or when its wavelength is unknown, the sensitivity

of the two channels must maintain a constant known ratio over the whole wavelength range in which difference correction is to be applied. A dual ion chamber was developed with two windows (LiF and CaF_2), two anodes and a common gas volume to give better matching of the detector characteristics (Section 2.4.2). This arrangement was chosen to most closely approach the above requirements for the application of channel differencing. The efficiencies of the two sections were related in the same way as the corresponding pair of chambers shown in Figure 2.14, and the shapes of their spectral response curves were matched down to 124 nm.

In order to improve the angular resolution of the detectors and also their ability to detect the lunar ultraviolet flux, a field stop plate was fitted in front of each chamber at the focal plane of a 25 mm diameter lithium fluoride lens. The fields of view were rectangular, approximately 1^0 x 4^0, aligned parallel to the rocket axis to give better coverage of the sky than square fields. The arrangement is depicted in Figure 7.4.

A small triaxial fluxgate magnetometer system was developed to fit within the confines of the payload volume. This performed well during flight and gave much more useful and accurate attitude data than had the search-coil system on C104. The circuit of this compact unit is shown in Figure 7.5.

The ion chamber current amplifiers were similar to those in the C104 payload, except that adequate input protection was provided to prevent the zero-level shifts which had been observed during the earlier flight. A compression circuit was included to extend the usable range.

APPENDIX D

The Resonance Absorption Cell

The objective in the design of the absorption cell was to provide the lowest transmission into the ion chamber of Lymanα emission core radiation, while conforming to the constraints imposed within the payload. The most severe limitation was of physical size. Because the collecting optics had an aperture of f/2, the exit beam was strongly divergent, and a long path length of hydrogen in the cell could not be used. The cell had to be fitted close to the chamber window so to minimise the transmission losses a common window plate was used. Limitations on the electrical power available for the dissociation filament meant that the filament had to be placed in a position where maximum effect could be obtained from the dissociation which was produced. The following paragraphs outline the design of the cells which were produced to operate within the above constraints.

The gas volume of the cell was approximately 1 ml; the internal diameter of the cell at the junction with the ion chamber window was 14 mm, and the diameter of the front window opening was 6 mm. The distance between the two lithium fluoride windows was 12 mm (Figure 8.5).

The filament was approximately 55 mm of tungsten wire of 25 microns diameter. This was spot-welded to fine nickel terminating ribbons and was supported in the shape of a W by small glass hooks which protruded from the cell walls. The nickel ribbons were passed out of the cell against the front surface of the ion chamber window. The pump-stem of the cell was annealed copper tubing which spiralled around the circumference of the cell from the side entry opening to a point where a cold-weld seal could

be made. All joints in the cell were bonded with epoxy resin.

After the cells had been baked under vacuum, hydrogen was admitted through a hot palladium filter and a liquid-air trap, and the filaments were flashed in this hydrogen atmosphere. The gas was replaced and the cells were removed from the filling system by forming a pinch-seal. The final filling pressure was 0.8 mm of mercury, at which pressure the filament took 165 ma at 9 volts (1.5 w). The filament surface temperature, as measured by an optical pyrometer, was approximately 1800^0K.

There was not sufficient information available for a rigorous calculation of the required filament temperature to be made. Neither the temperature dependence, nor the absolute value, of the dissociation rate of hydrogen on an open tungsten surface was known. The operating temperature was selected by referring to data on dissociation in a tungsten oven (Teubner, 1967), and to the published details of the cells successfully flown by Morton and Purcell (1962) and Winter and Chubb (1967).

The mean free path of hot hydrogen atoms leaving the filament would be approximately 0.6 mm. Therefore the atoms should have a temperature close to that of the molecular gas for most of their lifetime until they struck the cell structure. At this temperature, a number density of $n[h] > 2 \times 10^{19}$ m^{-3} would be required to produce an optical depth in the cell of at least 2. The fraction of hydrogen molecules dissociated at any time would be 0.5% for this optical depth with 0.8 mm filling pressure. As the longitudinal cross-section of the filament was approximately 1% of the cell cross-section, the requirement for adequate optical

depth was equivalent to having 5% of all molecules which hit the filament being dissociated. No direct measurements could be found to justify making this assumption, but the data on closed dissociation sources suggested that the condition should be reasonably well satisfied. Calculations made to compare the properties of the cell with that of Winter and Chubb also indicated that an adquate atomic hydrogen concentration could be produced.

It was estimated that, providing an optical depth of two could be generated within the cell, the fraction of photons at the Lymanα line centre frequency which would pass through the aperture into the ion chamber would be only 5% of those entering the cell from the telescope. The filter would not then be perfectly opaque to this radiation, but a correction could be readily made for its effective 5% 'leakage'. A longer cell would have been better in this respect, but would have required the telescope focal length to be longer, which was unaccceptable.

As is apparent from the report of Winter and Chubb, the task of directly measuring the spectral transmission of resonance absorption cells is very difficult. A vacuum monochromator with sufficient resolution for the measurements was under construction in the laboratory, but was not operating at the time that the cells described here were being constructed. An attempt was made to produce a resonance-scattering source in a hydrogen filled chamber attached to the half metre calibration monochromator. Even when a low pressure discharge in Helium was used as the primary source, the total energy flux entering the test chamber within the resonantly scattered band was too small. No usable resonantly scattered radiation

was detected by the ion chamber in the test-mounting and the cell transmission could not be measured directly. It was therefore necessary to assume on the basis of the previous estimates that sufficient absorption would be produced by the cell during the flight. The validity of the assumption could be checked by examination of the ion chamber signal when the telescope looked downwards from altitudes above 100 km.

An electronic timer was included in the payload to switch the cell filament power supply in a 30 seconds ON - 2 seconds OFF cycle during flight. The switching was done to allow more accurate estimates to be made of the signal attenuation by the cell over a range of zenith angles.

During testing it was found that the presence of the hot filament in front of the ion chamber modified the gas-gain characteristics of the chamber. The gain at each applied voltage was lowered. In the flight chamber the reduction was 35%. The photoelectric response of the chamber to the hot filament had been estimated previously, and measurements verified that the chamber signal produced by the radiation from the filament was negligible. No definite cause of the gain change was found, but it is considered that the change in the chamber characteristics was caused by photoemissive redistribution of the charge on the inside of the chamber window. Because no cure for the gain change effect could be found, the chambers were calibrated at gas gain while the cell filments were switched on. It was accepted that no accurate comparisons would be able to be made between signals detected with the cell hot and with it cold, as the gain recovery was not sufficiently rapid during the 'CELL OFF' period. Comparisons

would be then valid only between Telescope 1 (with the cell on) and Telescope 2.

In order to obtain the maximum amount of information from absorption cells used for the type of measurements described in this work, the chamber gain should be made completely independent of cell operation so that rapid mode-switching can be used. Although it would require a considerable increase in power consumption, the simplest solution to the problem of cell-chamber interaction would be to ensure that in future instruments, direct radiation from the filament could not strike the ion chamber window. Such a modification would, however, limit the usefulness of the cell in small payloads. Perhaps a better approach would be the development of a more elaborate screening structure within the ion chamber to electrically isolate the window surface, together with less drastic changes in the cell structure. The potential usefulness of simple absorption cell detectors for compact rocket experiments would justify a program of further development of cell and chamber designs.

BIBLIOGRAPHY

AHMAD, I.A., AND DEUTSCHMAN, W.A. Astronomical J., 77, 692, 1972

AKASOFU, S-I., HONES, E.W., MONTGOMERY, M.D., BAME, S.J., AND SINGER, S. J. Geophys. Res., 76, 5985, 1971

ALBERT, R.D. J. Geophys. Res., 72, 5811, 1967

ANDERSON, K.A. J. Geophys. Res., 65, 551, 1960

BAME, S.J., ASBRIDGE, J.R., FELTHAUSER, H.E., HONES, E.W., AND STRONG, J.B. J. Geophys. Res., 72, 113, 1967

BARTH, C.A. Astrophys. J., 161, L181, 1970

BARTH, C.A., AND SCHAFFNER, S. J. Geophys. Res., 75, 4299, 1970

BERTAUX, J.L., AND BLAMONT, J.E. Space Research, 10, ed. T.M. Donahue, P.A. Smith, L. Thomas, North Holland Pub. Co., Amsterdam, 1970, p591

BLUM, P.W., AND FAHR, H.J. Astron. Astrophys., 4, 280, 1970

BOND, F.R., AND JACKA, F. Aust. J. Phys., 16, 514, 1963

BRANDT, J.C., AND CHAMBERLAIN, J.W. Astrophys. J., 130, 670, 1959

BRINKMAN, R.T., GREEN, A.E.S., AND BARTH, C.A. N.A.S.A. Tech. Report No. 32-951, 1966

BRUNER, E.C., AND PARKER, R.W. J. Geophys. Res., 74, 107, 1969

BRUNER, E.C., AND RENSE, W.A. J. Opt. Soc. Am., 57, 709, 1967

BUCKLEY, J.L., AND MOOS, H.W. J. Geophys. Res., 76, 8378, 1971

BYRAM, E., CHUBB, T.A., FRIEDMEN, H., AND KUPPERIAN, J.E. 'Threshold of Space", ed. M. Zelikoff, Pergamon, London, 1957, pp203-210

CANFIELD, L.R., HASS, G., AND WAYLONIS, J.E. App. Opt. 5, 45, 1966

CARVER, J.H., HORTON, B.H., AND BURGER, F.G. J. Geophys. Res. 71, 4189, 1966

CARVER, J.H., HORTON, B.H., O'BRIEN, R.S., AND O'CONNOR, G.G. (to be published)

CARVER, J.H., HORTON, B.H., O'BRIEN, R.S., AND ROFE, B. Planet Space Sci., 20, 217, 1972

CARVER, J.H. AND MITCHELL, P. J. Scient. Instruments, 41, 555, 1964

CARVER, J.H. AND MITCHELL, P. J. Opt. Soc. Am., 57, 738, 1967

CHAMBERLAIN, J.W. 'Physics of the Aurora and Airglow', Academic Press, N.Y., 1961a

CHAMBERLAIN, J.W. Mem. Soc. Roy. Sci. Liège, (5), 4, 606, 1961b

CHAMBERLAIN, J.W. Planet. Space Sci., 11, 901, 1963

CHAMBERS, W.H., FEHLAU, P.E., FULLER, J.C., AND KUNZ, W.E. Nature, 226, 435, 1970

CHANDRASEKHAR, S. 'Radiative Transfer', Dover, N.Y., 1960, p18

CHUBB, T.A., AND BYRAM, E.T. Astrophys. J. 138, 617, 1963

CHUBB, T.A., FRIEDMAN, H., KREPLIN, R.W., AND MANGE, P. Soc. Roy. Sci. Liège (5) 4, 437, 1961

CODE, A.D., HOUCK, T.E., McNALL, J.F., BLESS, R.C., AND LILLIE, C.F. Sky and Telescope, Nov. 1969

COLE, K.D. Space Sci. Rev. 5, 699, 1966

CROSSWHITE, H.M., ZIPF, E.C., AND FASTIE, W.G. J. Opt. Soc. Am., 6, 643, 1972

DAVIS, T.N. J. Geophys. Res., 68, 4447, 1963

DAVIS, T.N. 'Aurora and Airglow'; ed. B.M. McCormac; Reinhold Pub. Co., N.Y., 1967, p41

DE VRIES, L.L. Paper presented to COSPAR Conference, Seattle, 1971

DONAHUE, T.M., AND STRICKLAND, D.J. Planet. Space Sci., 18, 691, 1970

EATHER, R.H., AND SANDFORD, B.P. Aust. J. Phys., 19, 25, 1966

EVANS, D.S. J. Geophys. Res., 73, 2315, 1968

FAHR, H.J. Nature, 226, 435, 1970

FASTIE, W.G., CROSSWHITE, H.M. AND HEATH, D.F. J. Geophys. Res., 69, 4129, 1964

FASTIE, W.G., CROSSWHITE, H.M., MARKHAM, T.P. Ann. Geophys., 17. 109, 1961

FRIEDMAN, H. 'Physics of the Earth's Upper Atmosphere', ed. J. Ratcliffe, Academic Press, N.Y., 1960, p133

GARTLEIN, C.W. Trans. Am. Geophys. Union, 31, 18, 1950

GEORGE, J.D., ZIMMERMAN, S.P., AND KENESHEA, T.J. Paper presented to COSPAR Conference, Seattle, 1971

GREEN, A.E.S., AND BARTH, C.A. J. Geophys. Res., 70, 1038, 1965

HEDDLE, D.W.O. Nature, 193, 861, 1962

HERZBERG, L. 'Physics of the Earth's Upper Atmosphere'; ed. C.O. Hines, I. Paghis, T.R. Hartz and J.A. Fejer; Prentice-Hall, N.J., 1965, p40

HICKS, G.T., AND CHUBB, T.A. J. Geophys. Res., 75, 25, 1970

HONES, E.W., ASBRIDGE, J.R., BAME, S.S., AND SINGER, S. J. Geophys. Res., 76, 63, 1971

HULTQVIST, B. Space Res., 5; ed. D.G. King-Hele, P. Muller, G. Righini, North Holland Pub. Co., Amsterdam, 1965 p91 et seq.

HUNT, B.G. J. Atmos. Terr. Phys.,33, 1869, 1971

HUNTER, W.R., OSANTOWSKI, J.F., AND HASS, G. App. Opt., 10, 540, 1971

ISLER, R.C., AND FASTIE, W.G. J. Geophys. Res., 70, 2613, 1965

JOHNSON,F.S., AND FISH, R.A. Astrophys. J., 131, 502, 1960

JOKI, E.G., AND EVANS, J.E. J. Geophys. Res., 74, 4677, 1969

JONES, R.A., BRUNER, E.C., AND RENSE, W.A. J. Geophys. Res., 75, 1849, 1970

KOCKARTS, G., AND NICOLET, M. Ann de Geophys. 19, 370, 1963

KOPAL, Z. 'The Moon'; D. Riedel Pub. Co., Holland, 1969

KUPPERIAN, J.E., BYRAM, E., CHUBB, T.A., AND FRIEDMAN, H. Ann de Geophys. 14, 329, 1958

KUPPERIAN, J.E., BYRAM, E., CHUBB, T.A., AND FRIEDMAN, H. Planet. Space Sci., 1, 3, 1959

KURT, V.G., AND SYUNYAEV , R.A. Soviety Physics - Astronomy (Eng. Trans.) 11, 928, 1968

LEBEDINSKY, A.I., ALESHIN, G.N., IORENAS, B.A., KRASNOPOLSKY, V.A., SELWANORE, A.S., AND ZASETSKY, V.V. Moon and Planets, 7th COSPAR Conference, North Holland Pub. Co., Amsterdam, 1967b, p65

LEBEDINSKY, A.I., KRASNOPOLSKY, V.A., AND AGANINA, M.V. Moon and Planets,II COSPAR Conference, North Holland Pub. Co., 1968, p47

LEBEDINSKY, A.I., KRASNOPOLSKY, V.A., AND KRYSHKA, A.A. Moon and Planets, 7th COSPAR Conference, North Holland Pub. Co., 1967a, p59

LINKE, R., AND PALUMBO, G. App. Opt. 4, 1677, 1965

MANGE, P., AND MEIER, R.R. J. Geophys. Res., 75, 1837, 1970

McAFEE, J.R. Planet. Space Sci., 15, 599, 1967

McILWAIN, C.E. J. Geophys. Res., 65, 2727, 1960

MEIER, R.R. J. Geophys. Res., 74, 6487, 1969

MEIER, R.R. J. Geophys. Res., 74, 3561, 1969

MEIER, R.R. J. Geophys. Res., 76, 242, 1971

MEIER, R.R., AND MANGE, P. Planet. Space Sci., 18, 803, 1970

MEINEL, A.B. Phys. Rev., 80, 1096, 1950

MILLER, R.E., FASTIE, W.G., AND ISLER, R.C. J. Geophys. Res., 73, 3353, 1968

MITCHELL, A.C.G., AND ZEMANSKY, M.W. 'Resonance Radiation and Excited Atoms', Cambridge, 1961, p92 et seq.

MOOS, H.W., AND FASTIE, W.G. J. Geophys. Res., 72, 5165, 1967

MORTON, D.C. Planet. Space Sci. 9, 459, 1962

MORTON, D.C., AND PURCELL, J.D. Planet. Space Sci., 9, 455, 1962

MURCRAY, W.B. J. Geophys. Res., 71, 3353, 1966

O'BRIEN, B.H., LAUGHLIN, C.D., AND GURNETT, D.A. J. Geophys. Res., 69, 1, 1964

O'BRIEN, B.J., AND TAYLOR, H. J. Geophys. Res., 69, 45, 1964

OGAWA, M. J. Geophys. Res., 73, 6759, 1968

OGAWA, T., AND TOHMATSU, T. Rep. Ionos. Space Res. Japan, 20, 395, 1966

OGAWA, M., AND YAMAWAKI, K.R. App. Opt., 9, 1709, 1970

OPAL, C.B., MOOS, H.W., AND FASTIE, W.G. J. Geophys. Res., 75, 788, 1970

PARESCE, F., KUMAR, S., AND BOWYER, S. Planet. Space Sci. 20, 297, 1972

PEEK, H.M. J. Geophys. Res., 75, 6209, 1970

PRAG, A.B., AND MORSE, F.A. J. Geophys. Res., 75, 4613, 1970

PURCELL, J.D., AND TOUSEY, R. J. Geophys. Res., 65, 370, 1960

PURCELL, J.D., AND TOUSEY, R. Space Research 1; ed. H.K. Bijl; North Holland Pub. Co., Amsterdam, 1960, p590

PURCELL, J.D., AND TOUSEY, R. Mem. Soc. Roy. Sci. Liège, 4, 274, 1961

ROBLE, R.G., AND NORTON, R.B. J. Geophys. Res., 77, 3524, 1972

SAMSON, J.A.R. J. Opt. Soc. Am., 54, 6, 1964

SHARBER, J.R. AND HEIKKILA, W.J. J. Geophys. Res., 77, 3397, 1972

SHARP, W.E., AND REES, M.H. J. Geophys. Res., 77, 1810, 1972

SMITH, A.M. Astrophys. J., 147, 158, 1967

STAIR, R., AND JOHNSTON, R. Nat. Bur. Stand. J. Res., 51, 81, 1953

STECHER, T.P. Astrophys. J., 159, 543, 1970

STOBER, A.K., SCOLNIK, R., AND HENNES, J.P. App. Opt. 2, 735, 1963

STOLARSKI, R.S., AND GREEN, A.E.S. J. Geophys. Res., 72, 3967, 1967

STÖRMER, C. 'The Polar Aurora', Oxford University Press, London, 1965

STRICKLAND, D.J., AND DONAHUE, T.M. Planet. Space Sci., 18, 661, 1970

SWIDER, W. Planet Space Sci., 12, 761, 1964

SWINGS, P., BOSMAN-CRESPIN, AND ARPIGNY, C. Mem. Soc. Roy. Sci. Liège (5), 4, 583, 1961

TEUBNER, P.J.O., Ph.D. Thesis, University of Adelaide, 1967

THOMAS, G.E. J. Geophys. Res., 68, 2639, 1963

THOMAS, L., AND BOWMAN, M.R. J. Atmos. Terr. Phys. 34, 1843, 1972

TINSLEY B.A. Rev. of Geophys. and Space Phys. 9, 89, 1971

VALLANCE-JONES, A. Space Sci. Rev., 11, 776, 1971

VEGARD, L. Nature, 144, 1089, 1939

VIDAL-MADJAR, A., BLAMONT, J.E., AND PHISSAMAY, B. Presented to COSPAR Conference, Madrid, 1972

VREUX, J.M. Ann. Geophys., 27, 493, 1971

WALLACE, L., BARTH, C.A., PEARCE, J.B., KELLY, K.K., ANDERSON, D.E., AND FASTIE, W.G. J. Geophys. Res., 75, 3769, 1970

WATANABE, K. J. Chem. Phys., 22, 1564, 1954

WATANABE, K., MATSUNAGA, M., AND SAKAI, H. App. Opt.,6, 391, 1967

WATANABE, K., AND ZELIKOFF, M. J. Opt. Soc. Am., 43, 753, 1953

WEEKS, L.H., AND SMITH, L.G. J. Geophys. Res., 73, 4835, 1968

WILKINSON, D.H. 'Ionization Chambers and Counters', Cambridge, 1950

WINTER, T.C., AND CHUBB, T.A. J. Geophys. Res., 72, 4405, 1967

YOUNG, J.M., CARRUTHERS, G.R., HOLMES, J.C., JOHNSON, C.Y., AND PATTERSON, N.P. Science, 160, 990, 1968